



HAL
open science

Seismicity of the Mid-Atlantic Ridge in the MoMAR area at a regional scale, observed by autonomous hydrophone arrays

Nuno Mendes Simao

► **To cite this version:**

Nuno Mendes Simao. Seismicity of the Mid-Atlantic Ridge in the MoMAR area at a regional scale, observed by autonomous hydrophone arrays. Geophysics [physics.geo-ph]. Université de Bretagne occidentale - Brest, 2009. English. NNT: . tel-00586976

HAL Id: tel-00586976

<https://theses.hal.science/tel-00586976>

Submitted on 19 Apr 2011

HAL is a multi-disciplinary open access archive for the deposit and dissemination of scientific research documents, whether they are published or not. The documents may come from teaching and research institutions in France or abroad, or from public or private research centers.

L'archive ouverte pluridisciplinaire **HAL**, est destinée au dépôt et à la diffusion de documents scientifiques de niveau recherche, publiés ou non, émanant des établissements d'enseignement et de recherche français ou étrangers, des laboratoires publics ou privés.



THESE / UNIVERSITE DE BREST
sous le sceau de l'Université européenne de Bretagne

présentée par

Nuno Mendes-Simão

pour obtenir le titre de
DOCTEUR DE L'UNIVERSITE DE BREST
Mention : Géosciences Océan
Ecole Doctorale des Sciences de la Mer

Préparée à l'Unité Mixte de recherche (6538)
Institut Universitaire Européen de la Mer
Laboratoire Domaines Océaniques

Thèse soutenue le (20 Novembre 2009)
devant le jury composé de :

Sismicité de la Dorsale Médio-Atlantique dans la région MoMAR à l'échelle régionale, observé par des hydrophones autonomes

Mathilde Cannat

Directeur de Recherche - Institut Physique du Globe de Paris, France / *rapporteur*

Nicolas Chamot-Rooke

Chargé de Recherche - Ecole Normale Supérieure, France / examinateur

Jean Goslin

Directeur de Recherche - Institut Universitaire Européen de la Mer, France / *Directeur de thèse*

Joaquim Luis

Professor Auxiliari - Universidade do Algarve, Portugal / examinateur

Jean-Yves Royer

Directeur de Recherche - Institut Universitaire Européen de la Mer, / *Président du Jury*

Deborah Smith

Senior Scientist - Woods Hole Oceanographic Institution, USA / rapporteur



THESIS SUBMITTED FOR THE DEGREE DOCTOR OF THE
"UNIVERSITE DE BREST"

**Seismicity of the Mid-Atlantic Ridge in the
MoMAR area at a regional scale, observed
by autonomous hydrophone arrays**

Author: Nuno Simão

Jury:

Dr. Mathilde CANNAT	Official Reader
Dr. Nicolas CHAMOT-ROOKE	Examiner
Dr. Jean GOSLIN	Advisor
Dr. Joaquim LUIS	Examiner
Dr. Jean-Yves ROYER	Examiner
Dr. Deborah SMITH	Official Reader

April 18, 2011

A PROBABILIDADE DAS COISAS

Desejos de um mundo com sede de vida.
Claros desafios nos destinos que possuis,
Corridos por feras numa estrada perdida
À procura de um oceano de águas azuis.

Momentos que passam e são especiais
Pelas lembranças que nos tocam.
Umás justas e boas, outras mais
Tristes que quase nos sufocam.

Dúvidas que todos tivemos e teremos,
Pois as escolhas são muitas e confusas.
Degraus, na construção do que seremos,
Com a incerteza de certezas difusas.

Incertezas que nos perdem no mundo.
Pois tudo lá fora dificilmente nos satisfaz.
Mas será que é preciso passar por tudo?
Tantas vezes se duvida do que se é capaz.

O que interessa é sentir-se aliviado
Convicto que o espírito se fortaleceu,
No caminho de um futuro reforçado
Por tudo aquilo que passou e se sofreu.

Sentir formar-se a dualidade nos lábios
Num sorriso de satisfação e tristeza,
Digno do mais elevado dos sábios,
Que impressionam pela sua certeza.

Nuno Mendes-Simão

Ce
mémoire
est dédié
à
Carole Cordier
parce que
un merci ce n'est pas
assez

Acknowledgments

Thank you to all members of the jury with a special thanks to Mathilde Cannat, Deborah Smith and Jean Goslin and their inputs that permitted me to improve this thesis. Thank you again to be present at my presentation.

Thank you to the people of the Cooperative Institute for Marine Resources Studies in Newport, Oregon for their hospitality and shared knowledge. Two special thanks, the first to Matt Fowler for risking his car and life dangerously driving through the Oregon forests through the worst storm in the history of Oregon so that I wouldn't miss my flight back to France, and also for the rafting and the warm and cosy Thanks Giving. The second of course to Joe Haxel and our scientific and not so scientific conversations.

Thanks to the ENS for welcoming me so kindly this last year and giving me the opportunity to teach and be in between the best of the best. 24, rue Lhomond is a special place.

Thanks to Javier Escartin, Delwayne Bohnenstiehl, Marcia Maia and Won Sang Lee for ideas shared and insights given into my work.

Big thanks to Marguerite Tarzia for the english editing and for all support given.

Big thanks to my parents, family and friends.

Contents

Résumé	v
Résumé étendu	vii
Abstract	xiii
Preface	xv
1 Introduction	1
2 Sound in the Ocean, <i>T</i>-phase and AuH	3
2.1 Sound measurements	3
2.1.1 Sound spectra	4
2.1.2 Sound source temporal properties	4
2.1.3 Waveform	4
2.1.4 Source level	5
2.1.5 Sound propagation	5
2.1.6 Ambient noise	9
2.2 <i>T</i> -phases	9
2.2.1 The down-slope conversion model	10
2.2.2 <i>T</i> -waves in the mode formalism	11
2.2.3 Scattering of <i>T</i> -waves in the mode formalism	12
2.2.4 <i>T</i> -phase waveform	14
2.3 Hydrophone Technology	16
2.3.1 Hydrophone and Mooring	16
2.3.2 Hydrophone servicing at sea	18
2.4 Data processing	20

2.4.1	Event location and source level	20
2.4.2	Location error analysis	24
2.5	Autonomous Hydrophone arrays	26
2.5.1	AuH detection thresholds and location accuracy	28
2.5.2	AuH and teleseismic data correlations	29
2.6	Conclusions	29
3	Mid Oceanic ridges and AuH data	31
3.1	Ridge segmentation and Morphology	31
3.2	Ridge Faulting	34
3.2.1	Detachment Faulting	37
3.3	Magmatic contribution Faulting and Morphology	38
3.4	Oceanic ridges seismic patterns	41
3.5	Land based arrays and OBS arrays	46
3.5.1	Teleseismic data	46
3.5.2	OBS data	47
3.6	Conclusions	47
4	MAR AuH seismicity analysis	49
4.1	Introduction	49
4.2	AuH array error field	50
4.3	MAR AuH Data	56
4.3.1	Time Distance Plots	56
4.3.2	Detection thresholds analysis	60
4.3.3	Mean error as a function of number of stations	62
4.4	Mantle Bouguer Anomaly	66
4.5	Analysis of the seismicity	66
4.5.1	Cluster analysis	68
4.5.2	Analysis of the seismicity at broad wavelength	70
4.5.3	Principal Component Analysis of the MAR Seismicity	74
4.6	Conclusions	90
5	Analysis of MAR AuH seismic clusters	93
5.1	Introduction	93
5.2	Catalog cluster identification using Single Link Cluster analysis	93

5.3	Mainshock-aftershock sequences	94
5.3.1	Modified Omori Law	94
5.3.2	Size-frequency relationship	95
5.4	Miami Parabolic Equation model	96
5.5	Previous analyses of seismic sequences along the MAR	97
5.6	Mantle Bouguer anomaly inversion and MAR segmentation	98
5.7	Mid-Atlantic Ridge seismic sequences	99
5.8	Transmission Loss analyses	105
5.9	Size Frequency analyses	109
5.10	MOL analysis	113
5.11	Conclusions	114
6	General Conclusions	117
	Bibliography	121
	Appendices	139
A	Figure of the MBA	141
B	Kolmogorov-Smirnov tables	142
C	Figures of the seismic sequences	144
	List of Tables	182
	List of Figures	185

Résumé

Le principal avantage des réseaux d'AuH, pour la surveillance sismique des dorsales océaniques, est leur faible seuil de détection. Cependant, les variations de seuil de détection entre les réseaux d'AuH déployés au voisinage de Açores, peut influencer le nombre de séismes enregistrés. Ces variations doivent donc être analysées avant interprétation de la sismicité. L'amplitude acoustique à la source (SL) d'un séisme dépend surtout de l'efficacité de la conversion séismo-acoustique mais aussi, dans une moindre mesure, des effets de propagation. Un autre avantage, la possibilité d'estimer l'erreur de localisation pour différentes géométries des réseaux et de topographie du fond, est présenté pour tous les réseaux d'AuH déployés sur la Dorsale Médio Atlantique (MAR). L'analyse de la sismicité de la MAR montre que la sismicité enregistrée par les AuH ressemble à celle enregistrée par les réseaux à terre au cours des 40 années passées. La distribution spatiale de cette sismicité est liée aux variations du régime thermique de la croûte le long de la dorsale. Des essaims de séismes, enregistrés par les AuH, sont liées à des télé-séismes et les sections où ils se produisent sont les plus actives. A l'échelle du segment, les essaims se groupent en extrémité et au voisinage de maxima de la MBA. L'analyse des distributions des SL et du taux de diminution du nombre des répliques indiquent que les failles de détachement produisent des essaims avec des diminutions plus rapides du nombre des répliques, que les failles normales. Cette observation serait associée à des contraintes plus faibles sur les failles de détachement et impliquerait un niveau de serpentinitisation plus important.

Résumé étendu

Ce mémoire, intitulé "Sismicité de la Dorsale Médio-Atlantique à l'Echelle Régionale dans la zone MoMAR, Observée par des Réseaux d'Hydrophones Autonomes" expose le résultat de la recherche effectuée dans le cadre du Groupe de Travail 1 du "Marie Curie Training Network - Monitoring deep sea floor hydrothermal environments on the Mid Atlantic Ridge (MoMAR-Net)". Le Groupe de Travail 1 était basé à l'Institut Universitaire Européen de la Mer à Plouzané, France. Le MCRTN MoMARNet m'a permis de participer à trois campagnes océanographiques, consacrée au déploiement et à la maintenance d'hydrophones autonomes dans la région de la Dorsale Médio Atlantique au sud des Açores, sur le chantier MoMAR. En outre, des levés bathymétriques multi-faisceaux ont été exécutés au cours de deux des trois campagnes sur la partie occidentale du Plateau des Açores entre l'Archipel des Açores et la Dorsale Medio Atlantique (MAR).

Dans le cadre de MoMARNet, j'ai pu bénéficier de deux formations d'une semaine chacune à l'Institut de Physique du Globe (IPG) de Paris et à l'Instituto Nazionale di Geofisica e Vulcanologia (INGV) à Rome. Ces formations m'ont apporté de nouvelles connaissances sur les processus géologiques et biologiques qui se produisent à l'axe des dorsales océaniques, ainsi que sur les méthodologies et instruments utilisés pour obtenir cette information. J'ai également passé trois mois au "Hatfield Marine Science Center" à Newport, Oregon, Etats-Unis où j'ai pu travailler en étroite collaboration avec le personnel du "Cooperative Institute for Marine Resources Studies". A Newport, j'ai pu me familiariser avec les techniques de construction et de déploiement des hydrophones autonomes.

Enfin, j'ai eu l'occasion d'assister à un atelier et aux réunions annuelles du MCRTN MoMARNet, au cours desquelles j'ai pu présenter mes recherches Lors du "fall Meeting 2006" de l'AGU à San Francisco, j'ai présenté un poster avec le titre "Analyse de la répartition spatiale et temporelle de la sismicité de la dorsale médio-atlantique en utilisant le SIRENA et les réseaux d'hydrophones autonome des Açores Sud".

En raison de la couverture spatiale limitée des réseaux mondiaux sismiques terrestres, seuls

les séismes de plus forte magnitude ont été observés par ces réseaux le long des dorsales océaniques. L'objectif principal du Groupe de Travail 1 et de cette recherche, était d'utiliser des hydrophones autonomes déployés dans le canal SOFAR pour la détection de séismes de faible magnitude qui se produisent le long de la Dorsale Médio-Atlantique, sur le chantier MoMAR, pour obtenir les distributions spatiale et temporelle de la sismicité de la région. L'analyse de ces distributions autorisera une compréhension plus approfondie des processus de déclenchement des tremblements de terre. On pourra ainsi espérer répondre à certaines questions concernant la dynamique des dorsales lentes.

Les hydrophones sont des instruments autonomes qui peuvent être déployés et récupérés par des navires. Les instruments, relativement simples, très fiables et peu coûteux ne permettent pas l'acquisition en temps réel. Les instruments sont aisés à déployer et maintenus en mer. Ils permettent d'acquérir des séries continues de données acoustiques échantillonnées entre 100 Hz et 250 Hz pour un période de deux ans maximum, autorisant la détection et la localisation des tremblements de terre sur de très vastes zones.

Une phase T ou onde T est une onde acoustique produite par un tremblement de terre sous-marin et qui se propage dans l'océan. Le T vient de "tertiaire", parce qu'elles se propagent plus lentement et ainsi arrivent en troisième, après les ondes P "primaires" et les ondes S "secondaires". Quand un tremblement de terre se produit dans la croûte terrestre sous l'océan, des phases P et S sont générées, et se propagent dans la croûte, où elles sont assez rapidement atténuées, mais une partie de l'énergie est convertie en énergie acoustique, l'onde T , au passage du fond. Les ondes T sont généralement enregistrés par des hydrophones, mais sont parfois enregistrés sur des sismomètres installés sur des îles, après que les signaux acoustiques de l'onde T aient été re-convertis en phases sismiques quand ils atteignent les pentes des îles. Ces phases T acoustiques se propagent sur de grandes distances dans le canal SOFAR avec peu d'atténuation. En raison de leur propagation efficace, les phases T d'événements de faible magnitude, dont les ondes P et S ne sont pas enregistrées par les réseaux sismiques terrestres, peuvent être détectées.

Le logiciel interactif de traitement des données acoustiques développé par le NOAA/PMEL pour l'analyse des données d'hydrophone autonomes se fonde sur des techniques développées pour l'acoustique sous-marine, plutôt que sur des techniques sismiques. Une seule application est utilisée pour accomplir toute l'analyse des séries de données. Un seul opérateur peut ainsi analyser les signaux de tous les hydrophones d'un réseau. Ce logiciel a été utilisé pour traiter les données enregistrées au cours de plusieurs déploiements d'hydrophones autonomes le long de la partie nord de la Dorsale Medio Atlantique.

Les erreurs attendues en latitude, longitude et l'heure d'origine pour l'ensemble du domaine

des observations peuvent être calculées pour différentes géométries et nombres d'hydrophones du réseau. L'erreur attendue permet de caractériser la précision de la résolution de la source de la phase T et sa répétabilité. Elle prend en compte la géométrie du système réseau/événements, la topographie du fond et les lois de célérité dans le canal SOFAR. Quatre simulations pour les configurations des réseaux de l'Atlantique Nord sont présentées. Les résultats indiquent que les erreurs de localisation sont inférieures à deux kilomètres à l'intérieur des réseaux et peuvent être plus importantes à l'extérieur de ceux-ci. L'erreur attendue augmentent systématiquement en dehors du réseau avec la distance entre le réseau et l'événement. Le champ d'erreur à l'extérieur des réseaux est également très déformé, avec, pour des réseaux "rectangulaires" allongés dans la direction NS, des erreurs très importantes en latitude le long d'un axe NS et d'importantes erreurs en longitude le long d'un axe EW passant par le centre des réseaux. Le nombre d'hydrophones déployé influence également les valeurs d'erreurs prédites : un nombre plus élevé d'instruments aide à diminuer l'augmentation des erreurs quand on s'éloigne du réseau.

L'interprétation des données des AuHs permettent de calculer l'énergie acoustique (le "Source Level" ou SL), qui résulte de la conversion des phases sismiques en phase-acoustiques à l'interface croûte-eau. En clair, cela signifie qu'on ne peut obtenir directement une estimation l'énergie du séisme et donc de sa magnitude, telle qu'elle est classiquement définie en sismologie. L'analyse de la relation fréquence-SL des événements (Loi de Gutenberg Richter) des réseaux AUH déployés sur la MAR révèle que le seuil de détection (le "SL completeness" ou SL_c) peut varier dans une fourchette de 15 dB, pour des séismes s'étant produits le long d'une section de la MAR qui s'étend sur plus de 5000 km, délimitée par les Zones de Fracture Marathon et Charlie Gibbs. Ces différences de SL_c peuvent avoir une influence considérable sur le nombre de tremblements de terre enregistrés par les réseaux d'hydrophones. Cela semble être particulièrement le cas dans la région entre la zone de fracture Oceanographer et les Açores. L'interprétation des distributions spatiales de séismes devra donc être menée en prenant soigneusement en compte les variations du seuil de détection.

L'inspection visuelle et une corrélation utilisant la technique Spearman-rang des distributions de sismicité en fonction de la latitude, obtenues à partir des catalogues "declustered" de l'ISC et de catalogues que nous avons obtenus en analysant les données acoustiques des AuH, présentent de fortes similitudes. Les expériences de surveillance acoustique de la MAR limitées dans le temps (à cinq années au maximum) peuvent révéler les tendances de la sismicité observées sur plus de 40 années d'observation telesismique. L'analyse conjointe des grandes longueurs d'onde des catalogues de l'ISC et de ceux des AuHs révèle un faible niveau de sismicité de la section de la MAR d'environ 200 km située à la latitude des Açores qui peut être liée à l'influence du

point chaud. Pour ces grandes longueurs d'onde, la valeur de l'anomalie de Bouguer réduite au manteau (MBA) se corrèle très bien avec les distributions de la sismicité, sur presque toute la MAR, à l'exception de la région qui s'étend depuis environ 200 km au sud des Açores jusqu'à la Zone de Fracture Oceanographer. Cette corrélation indique que la sismicité le long de la MAR est influencée par la variation de l'état thermique de la croûte, tel qu'il peut être caractérisé par la MBA. La section entre les Açores et la Zone de Fracture Oceanographer montre qu'une obliquité forte de la dorsale peut aussi avoir une grande influence dans les taux de sismicité observés le long de celle-ci.

Les séismes de plus forte magnitude, enregistrés par les stations terrestres, déclenchent des fluctuations du niveau de sismicité moyenne enregistrée par les AuHs. Cette connexion reste mal comprise. Les zones les plus actives de la MAR au nord des Açores sont les secteurs où ces fluctuations sont plus élevées. On peut également observer, pour la région de la MAR au nord des Açores, que les sections sismiquement actives et les sections inactives présentent des morphologies différentes. Les sections actives correspondent à des segments avec une morphologie plus asymétrique, le long desquels la vallée axiale est relativement plus large et plus profonde.

Nous avons également analysé en détail plusieurs séquences sismiques, en utilisant une Loi d'Omori Modifiée et l'analyse de la relation fréquence-SL des événements dans les séquences, afin de mieux contraindre les modes de formation des failles. Les séquences sismiques se produisent sur des segments avec des vallées axiales bien développées, ce qui renforce l'idée que ces segments sont dans un état thermique relativement froid. Les séquences sismiques peuvent être détectés au coeur de la vallée axiale ou sur les flancs jusqu'à une distance de 30 km de l'axe.

L'analyse de la relation fréquence-SL des événements et de la perte de transmission suggère que le niveau d'énergie de la source des phases T (Source Level) est plus fortement tributaire de l'efficacité de la conversion des ondes sismiques en ondes acoustiques que des conditions de son parcours dans l'eau et de son interaction avec la bathymétrie environnante. Cette dépendance n'est pas restrictive parce que, le nombre d'événements détectés pour chaque séquence ne dépend pas entièrement du seuil de détection SL_c et peut être représentatif des mécanismes de formation de failles.

Les localisations des séquences ont aussi été analysées par rapport à la segmentation de la topographie et de la MBA le long de la MAR. Les séquences ont toutes eu lieu sur des segments relativement froids avec des vallées axiales bien définies. Les séquences ont été enregistrées dans les régions où sont observées des failles, associées à des maxima de la MBA. Ceci suggère que les séquences sismiques sont plus susceptibles de se produire dans les régions de la MAR avec une croûte plus dense et plus mince. Le régime thermique de la croûte ne semble pas, par contre,

être le facteur qui contrôle le taux de décroissance du nombre des répliques sismiques . Ce taux serait lié à la rhéologie de la croûte là où se produisent les essaims. Il semble être plus dépendant du type de faille présentes dans la région : les taux de décroissance rapides seraient généralement associés la formation de failles de décollement créées par accréation asymétrique sur le MAR, alors que les taux plus lents seraient associées aux failles mises en place lors d'une accréation symétrique . Une telle dépendance peut résulter de la présence de serpentine le long des failles de détachement.

Abstract

Autonomous Hydrophones (AuH) arrays are excellent to seismically monitor mid oceanic ridges. One of their advantages is the ability of estimating, both for specific array geometries and specific oceanic regions around the globe, the error of the seismic locations. This has been implemented for all the AuH arrays deployed on the Mid-Atlantic Ridge (MAR). Another advantage of the AuH is its low detection threshold. An analysis of the detection thresholds of the AuH that were deployed in the MAR revealed that this feature can greatly impact the number of recorded events, and that this must be considered for further analyses. Transmission Loss analysis shows that the AuH Source Level of an earthquake is mainly due to the conversion from seismic to acoustic energy while the propagation paths play a smaller contribution. An analysis of MAR seismicity reveals that the AuH recorded seismicity mimics the longer time span of teleseismically recorded seismicity and that both are influenced by crustal thermal structure variations along the ridge. AuH recorded seismic clusters are directly linked with teleseismically recorded events and the sections where they occurred are the most active sections of the MAR. Seismicity generally clusters at segment extremities and at the segment scale, on MBA maxima. Size-frequency and mainshock-aftershock analyses of the clusters reveal that aftershock decay rate is influenced by the mode of faulting. Detachment faults produce seismic sequences with faster decay rate associated with a reduced strain release in comparison to normal faults. This implies the presence of higher levels of serpentinisation on detachment faults.

Preface

The following dissertation, titled "Seismicity of the Mid-Atlantic Ridge at a regional scale in the MoMAR area, observed by autonomous hydrophone arrays" is the final result of research within the framework of Work Package 1 of the Marie Curie Research Training Network - "Monitoring deep sea floor hydrothermal environments on the Mid Atlantic Ridge (MoMARNet)". The Work Package 1 was based at the "Institut Universitaire Europeen de la Mer" in Plouzane, France.

The work package permitted me to be onboard and participate in three oceanographic cruises. The first cruise onboard the "Arquipelago RV" based in the Department of Oceanography and Fisheries of the University of the Azores, Portugal while the following two cruises were onboard the "Le Suroit R/V" based at the IFREMER's center of Brest, France. Each of the missions were focused on the deployment and service of autonomous hydrophones in the Mid Atlantic Ridge region south of the Azores, called MoMAR. Bathymetrical soundings were executed in the Azores sector of the Mid Atlantic Ridge (MAR) aboard the "Le Suroit R/V".

As part of my involvement in the Research Training Network, I frequented two one-week training courses. The first of these took place at the "Institut de Physique du Globe" (IPG) in Paris, France, and was called "Hydrothermal environments at mid ocean ridges: biodiversity and geological/geophysical context". The second, at the "Istituto Nazionale di Geofisica e Vulcanologia" (INGV) in Rome, Italy, was called "Multidisciplinary Data Seafloor Observatories". These training courses provided me with new insights into the geological and biological processes occurring in mid oceanic ridges, as well as allowing me to gain knowledge about the methodologies and instruments used to obtain this information. Additional to this training, I spent three months in the "Hatfield Marine Science Center" in Newport Oregon, U.S.A where I was able to work in close collaboration with staff from the "Cooperative Institute for Marine Resources Studies" that aggregates people from the "National Oceanic and Atmospheric Administration (NOAA) Pacific Marine Environmental Laboratory (PMEL)" and from the "Oregon State University". There I learnt the process involved in setting up and mounting autonomous hydrophone arrays. I was also provided with the opportunity to assist and present my research at

the MoMARNet workshop and annual meetings as well as at the AGU meeting in San Francisco in 2006 where I presented a poster with the title "Analysis of the spatial and temporal distribution of the seismicity of the Mid-Atlantic Ridge using the SIRENA and the South Azores autonomous hydrophone arrays".

I will then present the final result of all these professional and scientific experiences on the following pages.

Chapter 1

Introduction

Two-thirds of the Earth's surface is made of oceanic crust, formed by magmatic and tectonic processes along mid-ocean ridges. Slow-spreading ridges, such as the Mid-Atlantic Ridge (MAR), are discontinuous and composed of ridge segments. Segments are thus fundamental units of magmatic accretion and tectonic deformation that control the evolution of the crust. The acquisition of geological and geophysical data improves our understanding of the mid-ocean ridge system. Earthquakes act as important tools in the pursuit of this knowledge. Earthquakes are the direct result of geological processes occurring within the Earth. Despite their importance, unfortunately few historic observations of earthquakes along mid oceanic ridges have been made. This is mainly due to the limited spatial coverage offered by the global seismological networks for remote regions of the oceans.

To address this deficit, scientists use Oceanic Bottom Seismometers deployed on the ocean seafloor and more recently, used Autonomous Hydrophones (AuH) moored within the oceanic minimum sound velocity channel known as the SOFAR channel. The main aim of this work was to use these SOFAR borne autonomous hydrophones to detect smaller magnitude earthquakes occurring along the MAR. With a more comprehensive catalog of earthquakes it is then possible to understand the spatial and temporal distribution of the seismicity in the region. Furthermore, a more in-depth understanding of the processes triggering these earthquakes could be achieved. There are a variety of influencing factors on these geological processes, for example the thermal, rheological and tectonic conditions of the ridge. Those factors that directly affect the morphology and modes of faulting and the volcanism at the segment scale, will then influence the ridge's seismicity. With this knowledge in mind the analyses of spatial and temporal distributions of the seismicity recorded by the AuH arrays in the MAR will provide us with a much clearer picture of the dynamics of slow spreading ridges.

The understanding of the MAR's geological can only be achieved with the concurrent understanding of the characteristics of the AuH dataset. This findings from this approach and insights on these characteristics will be presented and discussed in the following chapters.

Chapter 2

Sound in the Ocean, *T*-phase and AuH

This chapter has three objectives: introducing the concepts of sound propagation and measurement in the oceans, introducing the origin and propagation of *T*-phases in the oceans; presenting the hydrophones and the arrays of hydrophones deployed to record the MAR seismicity.

2.1 Sound measurements

For humans, sounds that are barely perceptible have intensities near $1\text{pW}/\text{m}^2$, where as those that are painful are near $10\text{W}/\text{m}^2$. The ear spans this wide range of intensities by means of a complicated nonlinear response (*Kinsler et al.*, 1982). In fact, in relating loudness of two sounds, our ears respond logarithmically. Therefore, acousticians adopted a logarithmic scale for sound intensities and scaled them in decibels (*dB*). In decibels, the intensity level or sound power per unit area of a sound intensity I is given by:

$$\text{Intensity Level (dB)} = 10\log(I/I_0) \quad (2.1)$$

Where I_0 is the reference intensity. Because intensity is proportional to pressure squared, the sound pressure level of a sound pressure P is given by:

$$\text{Sound Pressure Level (dB)} = 20\log(P/P_0) \quad (2.2)$$

Where P_0 is the reference pressure, e.g. $1\mu\text{Pa}$. The expression "sound pressure level" implies a decibel measure and a reference pressure used as the denominator of the ratio. When studying underwater sound, pressure (not intensity) is what is usually measured.

2.1.1 Sound spectra

The concept of power density spectrum is used to describe continuous sounds. Because measurements are usually in terms of pressure rather than power, a more common representation is the sound pressure density spectrum - the mean square sound pressure per unit frequency. To measure sound pressure, one could use one filter within the band pass of interest. The square sound pressure density spectrum is obtained by dividing the square sound pressure by the filter width. These data become sound pressure density spectrum levels when converted to decibels referred (*re*) to a unit pressure density expressed in $\mu Pa^2/Hz$.

Similarly, for pulsed sounds, an overall energy level in $dB re \mu Pa^2s$ can be decomposed into an energy density spectrum, with energy density spectrum levels at the frequency bandwidth in $dB re \mu Pa^2/Hz$.

2.1.2 Sound source temporal properties

A sound may be transient, of relatively short duration, having an obvious start and end, or it may be continuous. Transient underwater sounds include impulsive sounds from explosions, airguns, sonars, and earthquakes. An explosion produces a single transient sound, but airguns, pile drivers, earthquake sequences and many sonars produce repeated transient sounds. However, the distinction between transient and continuous sounds is not absolute. Sound emitted from a ship underway is continuous, but it is transient insofar as a stationary receiver is concerned. Also many sounds are not purely transient or purely continuous even at the source.

2.1.3 Waveform

In describing a transient sound it is useful to present the peak level as well as some description of how the sound varies with time (its waveform). The peak level may be described as being either a particular pressure or a mean square pressure averaged over a relatively short time interval. The terms phase, phase difference, relative phase and phase angle can be used in comparing two periodic waveforms with the same period. For example, sound components from one source that arrive at a given point via two different propagation paths may differ in phase. Phase refers to the difference in time, or the offset between two waveforms. If the difference equals the period, or any integer multiple of period, the two waveforms look the same and the phase difference is zero. Thus, it is possible to describe phase as an angle in the range $\pm 180^\circ$. For example, if phase difference is $1/4$ of the period, phase angle is $\pm 90^\circ$. The sign depends on whether the waveform of interest leads or lags the reference waveform. For continuous waveforms that are

random or non periodic, the phase concept generalizes to one of time delay, describing the time offset of a waveform and its replica.

2.1.4 Source level

Source Level is defined as the pressure level that would be measured at a standard reference distance from an ideal point source radiating the same amount of sound as the actual source being measured (Ross, 1976). This concept is necessary because sound measurements near large, distributed sources like seismic phases converted into T -phase depend strongly on source size and measurement location, and are difficult to relate to levels measured far away. This concept of source level introduces the dimension of distance into the description of sound. To compare different sound sources, it is necessary to adopt a standardized reference distance at which source levels will be determined. For underwater sounds, a reference distance of 1 m is usually used. Source level is estimated by adjusting the measured level to allow for transmission loss between a standard reference range and the range where the sound was measured. The standard units for source levels of underwater sound are dB re $1\mu Pa$ at $1m$.

2.1.5 Sound propagation

Discussions on sound propagation include two equivalent terms: transmission loss and propagation loss. Conceptually, a sound wave traveling from point A to point B diminishes in amplitude, or intensity, as it spreads out in space, is reflected, and is absorbed. If the source level is at $1m$ $160dB$ re $1\mu Pa$ at $1m$, the received level at range 1 km may be only $100dB$ re $1\mu Pa$ at $1m$; in this case transmission loss is 60 dB . Transmission loss is generally expressed in dB , representing a ratio of powers, intensities or energies of a sound wave at two distances from the source. The distance at which the denominator measurement is taken is the reference distance for transmission loss.

$$\log(P/P_0) = \log(P) - \log(P_0) \quad (2.3)$$

Because dB scales are logarithmic, transmission loss can be expressed as the difference, in dB , between the levels at the two distances.

Spherical spreading

In a uniform medium with no nearby boundaries and no absorption loss, sound from an omnidirectional source spreads uniformly outward with a spherical wavefront. Sound pressure de-

creases as the area of the wavefront expands. At distances that are large compared with the source dimensions (far field), sound pressure is inversely proportional to distance. Thus, transmission loss due to the spherical spreading is given by:

$$TL_{spherical} (dB) = 20 \log R \quad (2.4)$$

With spherical spreading, sound levels diminish by 6 dB when distance is doubled, and by 20 dB when distance increases by a factor of 10.

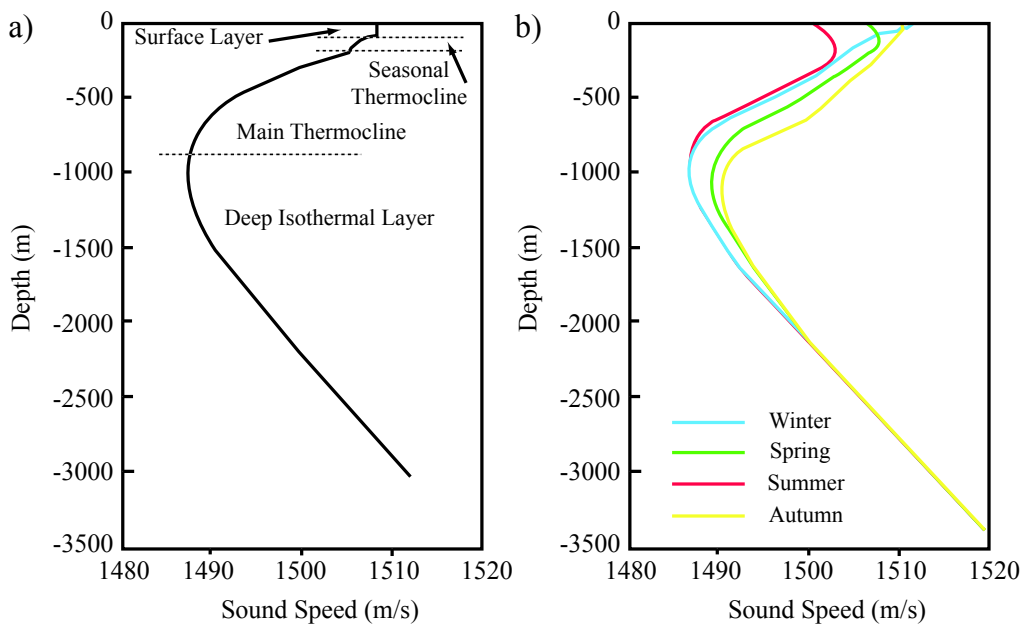


Figure 2.1: Typical deep-sea sound speed profiles. (a) Profile showing layer structure of the sound speed in the water due to temperature variations (b) Average sound speed profiles in different seasons in a area halfway between Newfoundland and Great Britain (modified from *Urick* (1983)).

Cylindrical spreading

Cylindrical spreading occurs when the medium is non-homogeneous. In shallow waters, sound reflects at the surface and bottom. At some distance from the source that is long compared to water depth, various reflected waves combine to form a cylindrical wave. A near cylindrical wave can also form as a result of refraction or ray bending. Sound rays are refracted in accordance with Snell's law when sound speed changes along the ray path.

Refraction is common in the ocean due to the temperature variation with depth and because

temperature has a major influence on sound speed (Figure 2.1). Variations in temperature and salinity with water depth affect the rate of propagation loss. The speed of sound increases with increasing temperature, salinity and pressure. This results in distortion of the wavefront as it propagates. This distortion is equivalent to the bending of the sound rays that trace paths of points on the wavefront. Refraction causes rays to bend towards the direction of slower sound speed, since the portion of the wavefront traveling in the region of higher sound speed advances faster than the remaining portion. Refraction of sound rays can result in convergence zones, which are regions of focused rays and higher sound levels, and in shadow zones, which are regions of very low sound levels.

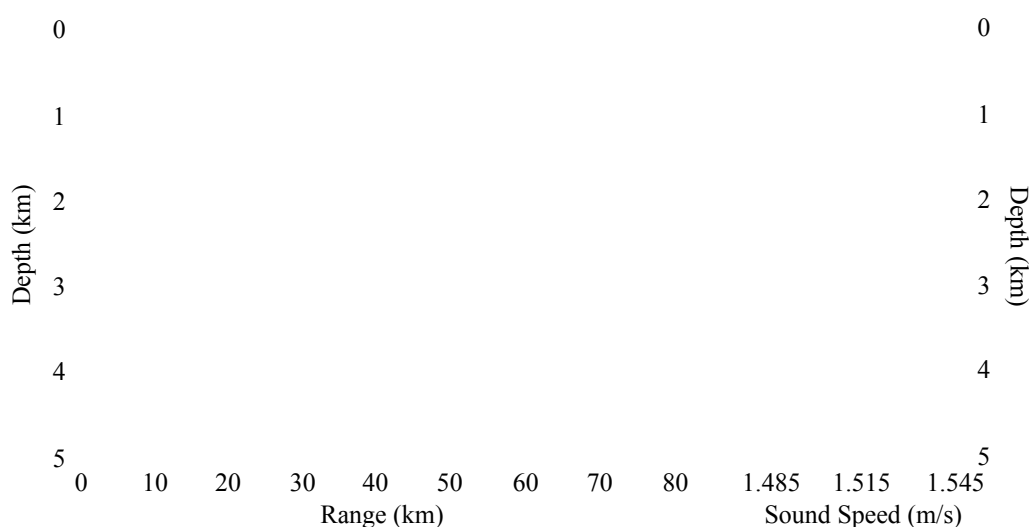


Figure 2.2: Ray diagram for sound transmission and sound speed profile at right from a source on the deep ocean sound channel axis (e.g. SOFAR channel) (modified from *Richardson et al.* (1995)).

One of the better known features of deep water propagation is the deep sound channel, also known as the SOFAR (Sound Fixing and Ranging) channel. The axis of this channel is at the depth of minimum sound speed: typically 600-1200 m at low and middle latitudes (Figure 2.1a), but approaching the surface in Polar Regions. The focusing effect of this channel causes sound rays from sources to be trapped, avoiding the losses that would result from bottom and surface reflections (Figure 2.2). The SOFAR channel then acts as a waveguide for sound, and low frequency sound waves within the channel may travel thousands of kilometers before being notably attenuated. When sound becomes trapped in a sound duct between horizontal refracting or reflecting layers, it is constrained to spread outward cylindrically rather than spherically. In these cases sound pressure varies as $1/\sqrt{R}$ in contrast to the $1/R$ that applies with spherical spreading.

Transmission loss of cylindrical sound is represented by:

$$TL_{cylindrical} (dB) = 10\log R \quad (2.5)$$

With cylindrical spreading, sound levels diminish by 3 dB when distance doubles, and by 10 dB when distance increases 10-fold. Thus, levels diminish more slowly with increasing distance with cylindrical than with spherical spreading.

Transmission loss

Sound spreading is usually more or less spherical from the source out to some distance, and then may be converted to cylindrical spreading. A useful equation for transmission loss (TL) with spherical and cylindrical spread is given by:

$$TL_{spherical+cylindrical} (dB) = 10\log(R_0R), R > R_0 \quad (2.6)$$

$$TL_{spherical} (dB) = 20\log(R), \quad R \leq R_0 \quad (2.7)$$

Where R_0 is a generic range at which spherical spreading (from the source point to the SOFAR) stops and cylindrical spreading (within the SOFAR) begins.

Absorption

When sound is transmitted through water, water molecules absorb a small portion. As a result, low frequency attenuation values vary with ocean location and can range from 10^{-2} to 10^{-3} dB/km for frequencies below 100 Hz (*Kibblewhite and Hampton, 1980*).

Sound energy loss due to absorption is directly proportional to distance between source and receiver and is usually given in dB/km. Absorption is weakly influenced by water temperature but is relatively strongly dependent on pressure, with absorption coefficients being reduced with increasing depth. Absorption of sound by seawater increases with increasing frequency; energy loss is approximately proportional to the square of frequency. At frequencies > 5 kHz, absorption causes significant (> 2 dB) transmission loss if the range is > 10 km. At frequencies < 1 kHz, absorption is not significant at ranges < 40 km. However, when the propagation path is thousands of kilometers long there is significant absorption even at frequencies below 100 Hz. Several empirical formulae have been published to calculate absorption versus frequency (*Urlick, 1983*). One that gives reasonable agreement with data over a wide range of frequencies (f in kHz) is $\alpha = 0.036f^{1.5}$ (dB/km). For example a 10 Hz acoustic wave yields a 0.25 dB loss for earth-

quakes 500 km from the hydrophone. Such a transmission loss is much smaller than transmission losses due to geometrical spreading.

2.1.6 Ambient noise

Ambient noise is the background noise. There is no single source, point or otherwise. In the ocean ambient noise can arise from wind, waves, organisms, earthquakes, distant shipping, volcanoes, fishing boats and more. At any place and time, several of these sources are likely to contribute significantly to the ambient noise. In the source-path-receiver model, ambient noise is present in the water along the path, and it is present at any receiver location. Ambient noise varies with season, location, time of day, and frequency. It has the same attributes as other sounds, including transient and continuous components. When the ambient noise level is x and there is a sound signal with level y , total sound level is:

$$L_x + L_y = 10 \log(10^{x/10} + 10^{y/10}) \quad (2.8)$$

2.2 *T*-phases

A *T*-phase or *T*-wave is an acoustic phase from an earthquake that travels through the ocean. The "*T*" stands for "tertiary", as *P*-waves stands for "primary", and *S*-waves for "secondary", because they travel the slowest and so arrive third (Figure 2.3). Basically, when an earthquake occurs in the earth's crust under the ocean, the usual crustal phases are generated (*P* and *S* waves), but in addition part of the energy goes into the ocean as acoustic energy, and that is the *T*-wave. It can basically be described as the seafloor rumbling. *T*-waves are typically recorded by hydrophones, but are occasionally recorded on some islands seismometers (Figure 2.3) when *T*-wave signals are converted to crustal phases when they hit the island.

These ocean borne acoustic *T*-phases propagate over great distances within the SOFAR channel with little transmission loss. Because of their efficient propagation, *T*-phases can be detected for low magnitude events that are not observable from land based seismic networks (*Dziak et al.*, 2004b; *Fox et al.*, 1995, 2001).

The mechanism for generating *T*-waves at the seafloor are not fully understood. Ray theory indicates that crustal seismic energy crossing the seafloor interface into the overlying water column experiences severe vertical refraction due to the large velocity contrasts between water and rock. This implies that SOFAR borne quasi horizontal *T*-waves have to be converted through some sort of mechanism.

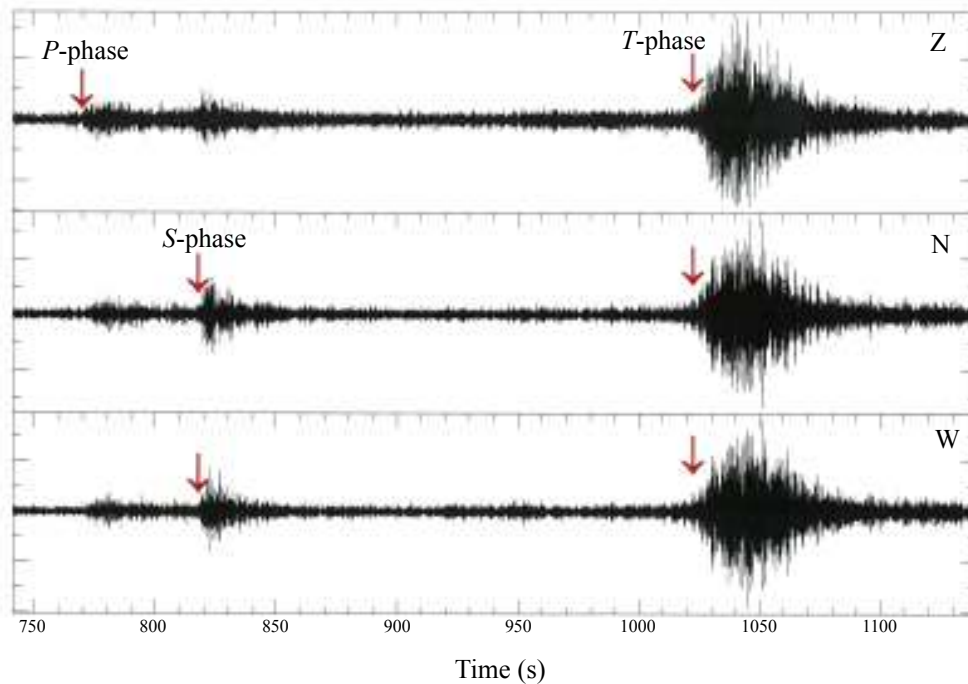


Figure 2.3: *P*-, *S*- and *T*-phases recorded by the three components of a seismometer.

T-phases generated by sub-oceanic earthquakes are classified into two types: "abyssal" *T*-phases, which are generated near the earthquake epicenter at seafloor depth far below the SOFAR channel, and "slope" *T*-phases which are generated at continental, or island slopes and ridges directly into the SOFAR channel at distances up to several hundreds of kilometers from the epicenter.

2.2.1 The down-slope conversion model

In the context of geometric optics, a slope interface provides a mechanism for the penetration of the SOFAR channel by the *T*-phases after a series of reflections in the liquid wedge between the sea surface and the sloping seafloor, which intersects the sound channel, gradually propagating more horizontally. This process known as "down-slope conversion" (Figure 2.4) (*Talandier and Okal, 1998*), successfully explains many characteristics of earthquake generated *T*-waves, but has severe limitations, notably regarding "abyssal" *T*-phases. In this instance, a small intra-plate earthquake occurring in a flat abyssal plain, far away from any documented shallow slope, generates a strong *T*-wave throughout the ocean, whose group times are compatible with generation at the time and epicenter of the seismic source.

Figure 2.4: P - T and S - T conversions in presence of a gently sloping beach. (a) and (b) show rays departing the focus at 1° and 10° incidence angles respectively. Each requires several reverberations to penetrate the SOFAR channel, and when combined in (c), this results in a wavetrain of longer duration. (d) shows similar characteristics for the S - T conversion for an 9° incidence angle (from (Talandier and Okal, 1998)).

2.2.2 *T*-waves in the mode formalism

The modal theory in the framework developed by *Pekeris* (1948) is a mechanism that envisions *T*-waves as the superposition of a discrete, albeit in principle infinite, number of modes of surface waves guided by the oceanic column, and in particular by the SOFAR channel. Figures 2.5a and 2.5b, adapted from *Park et al.* (2001), contrast, at a single frequency (in this case 5 Hz), the first overtone mode, with that of a higher overtone. The former has its energy concentrated around 1000 m depth, in the axis of the SOFAR channel, its phase velocity of 1483 km/s expresses propagation of the acoustic energy in the channel. Because its eigenfunction has become essentially negligible by the time it reaches the solid substratum, such a mode cannot be excited by any source in the solid Earth. By contrast mode 32 has a well developed eigenfunction both in the first 16 km of the solid Earth and in the water column. However its phase velocity of 3438 km/s indicates that its energy mostly reverberates at a steep incidence between the surface and the

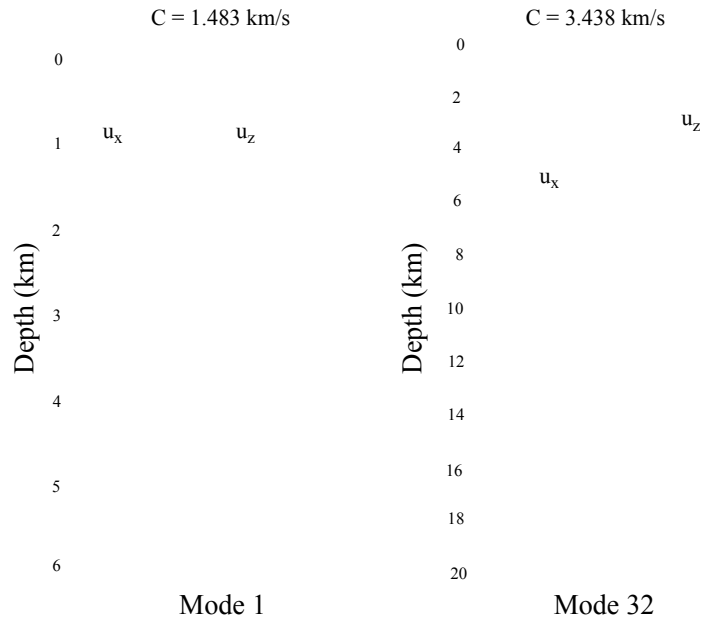


Figure 2.5: (a) First overtone solution of 5 Hz, computed by *Park et al.* (2001) for a 2.25 km deep ocean featuring a SOFAR channel; is the eigenfunction of the horizontal displacement, that of the vertical displacement. Note that the mode does not penetrate the solid earth. (b) Same as (a) for the 32nd overtone mode plotted using a different vertical scale. Note that energy is present both in the liquid and solid, but the larger phase velocity expresses the inefficient lateral propagation of the energy in the liquid layer (adapted from *Park et al.* (2001)).

bottom of the ocean and does not propagate laterally in the SOFAR channel. In summary, modal theory alone cannot explain the excitation of an "abyssal" T -phase in a flat-layered structure any better than geometrical optic dual ray theory.

2.2.3 Scattering of T -waves in the mode formalism

The third approach is based in the mode coupling induced by lateral heterogeneity of the layered structure under consideration, in this case a water column above a solid substratum. Generally two types of heterogeneity are considered: one involves two flat basins with different water depths, with a smooth transition extending over several wavelengths, the other a single basin with localized irregularities of the ocean floor, of an amplitude comparable to the acoustic wavelengths. *Odom* (1986) investigated a number of such scenarios and demonstrated that corrugated structures provide a mechanism to leak energy from modes with little if any ampli-

tude in the SOFAR channel (but strongly excited by underwater earthquake sources) into modes representing propagation of energy trapped into the channel (but not excitable by underground sources). This approach provides the key to a satisfactory explanation of the generation of the abyssal *T*-phase by scattering at the ocean bottom.

a) b)

Figure 2.6: (a) Initial excitation, at $f = 5$ Hz, of the various overtone modes of a flat layered structure by a double-couple source located at 9 km depth (the 2.25 km deep ocean layer, is shown in a darker tone). Note that only overtones of order 18-55 are substantially excited. In particular the lower overtones corresponding to propagation in the water column are not. (b) Mode excitation by sea bottom scattering. Note that the energy of the higher modes in (a) has been converted into the lower overtones (of order less than 20), propagating in the SOFAR channel (from *Park et al.* (2001)).

Park and Odom (1999) extended the concept to the case of a stochastic field of heterogeneity on the seafloor and *Park et al.* (2001) applied their results to a number of scenarios involving different geometries and depths of earthquakes under both a homogeneous ocean-bottom interface and a heterogeneous one, which could be deterministic (as is the case of the sloping interface) or stochastic (featuring random roughness). Figure 2.6a quantifies the seismic amplitude excited into the various overtone branches for a flat-layered structure and at a frequency of 5 Hz, and illustrates that only the overtone numbers 18 to 55 are significantly excited. Figure 2.6b similarly shows the kernel for conversion of the elastic field in Figure 2.6a by various scatterers located at the bottom of the ocean. Once multiplied by a scattering function expressing the density of heterogeneity, the kernels yield the cross over amplitudes converted into various modes. The horizontally propagating water modes 1 to 10 are now excited with finite amplitude. This expresses the key result of the model, namely that it can indeed predict the excitation of an abyssal *T*-phase. Using a simplified methodology, *de Groot-Hedlin and Orcutt* (2001) modeled the scattering into

a given acoustic mode by sea-floor heterogeneities as directly proportional to the product of the amplitude of the mode at the ocean-sediment interface and of the ground motion produced by the dislocation source at the relevant location. They emphasize that the bottom amplitude is strongly dependent on the depth of the water column, and that the scattering process generating the *T*-phase is thus strongly controlled by bathymetry. *Yang and Forsyth (2003)* later expanded this model by including the contribution of *S*-waves to the ground motion at the conversion point and by assigning only a small fraction of the incident amplitude to scattering in a horizontal direction. However, the effect of scattering when reverberating rays traveling quasi-vertically in the water column is also considered; hitting the ocean bottom at later times, thus contributing to the extended duration of the *T*-phases. This approach allowed *Yang and Forsyth (2003)* to produce very realistic synthetics of the envelopes of "abyssal" *T*-phases recorded at regional distances.

2.2.4 *T*-phase waveform

The *T*-phase waveform is strongly dependent on the conversion of the seismic waves into *T*-wave as described above. Multi-path propagation of the energy in the ocean wave-guide contributes some additional complexity to the recorded arrival waveform. Generally the spectral bandwidth of the *T*-phase arrivals is from ~ 2 to ~ 50 Hz. The low frequency cut-off is due to the mode cut-off of the geometry of the ocean wave-guide (*Richardson et al., 1995*).

A *T*-phase excitation and propagation model that explains all of the observed characteristics of *T*-phase arrivals (lens shape, rise time, multiple peaks, spectrogram behavior, etc.) does not exist. In general, there are two regions to consider: a relatively short excitation region where the *T*-phase characteristics are established, and a propagation region where the *T*-phase energy is totally trapped in the ocean sound channel (there have been occasional observations of basin scale multi pathing, with secondary scattering from continental margins, (*Shurbet and Ewing, 1957*)).

All *T*-phases by definition involve long-range propagation in the ocean. There is growing evidence however that *T*-phase propagation involves the coupling of energy between the ocean sound channel and the shallow oceanic crust including the almost ubiquitous sediment layers (*Butler and Lomnitz, 2002*). Recent observations have shown that the reciprocal process to excitation, getting energy out of the SOFAR channel into the crust, is commonplace even in deep water (*Butler and Lomnitz, 2002*). Hence scattering may also play a significant role in long-range *T*-phase propagation.

T-wave arrivals from large earthquakes are typically emergent, with a slow (>15 s) increase in amplitude to a maximum, followed by a long period (>30 s) decay (Figure 2.7). The maximum

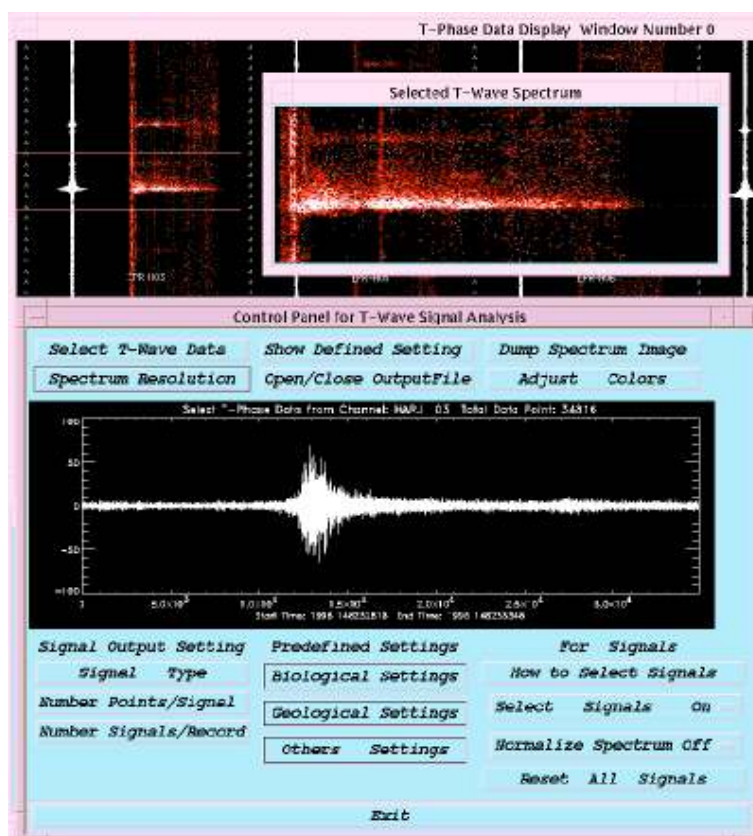


Figure 2.7: T-phase time series waveform and respective 0-50 Hz spectrogram.

amplitude of the T -wave signal is used as the arrival time of the earthquake. Although the process by which seismic energy is converted into acoustic energy is not well understood, it is assumed to be a scattering or diffusion process whereby the earthquake vibrates a region of the seafloor, coupling its energy into the water column over a large area (Dziak *et al.*, 1997; Schreiner *et al.*, 1995). The magnitude by which any point of the region is vibrated is a function of the distance from the epicenter. The largest vibrations occur at the epicenter and result in the maximum amplitude T -wave arrivals (Dziak *et al.*, 1997; Schreiner *et al.*, 1995; Slack *et al.*, 1999). Regions of vibration closer to the hydrophone will arrive earlier, since they have less distance to travel, but will have lower amplitudes resulting in the long rise time of the T -wave. Similarly, regions of vibration further away from the hydrophone than the epicenter will combine with other scattered signals from the event to create a long decay time (Dziak *et al.*, 1997; de Groot-Hedlin and Orcutt, 2001; Schreiner *et al.*, 1995; Slack *et al.*, 1999; Yang and Forsyth, 2003). In addition to producing well constrained earthquake locations, this hypothesis is supported by work that correlates T -wave rise time with event depth (Schreiner *et al.*, 1995). The deeper the event,

the larger the vibrated region and therefore the longer the rise time. There are exceptions to this rule as shown by *Williams et al.* (2006). The authors showed that onset time could also be a function of other variables such as efficiency of energy conversion from shallow topography and efficiency of propagation based on water depth of the event, reaffirming the complexity of the *T*-phase waveform.

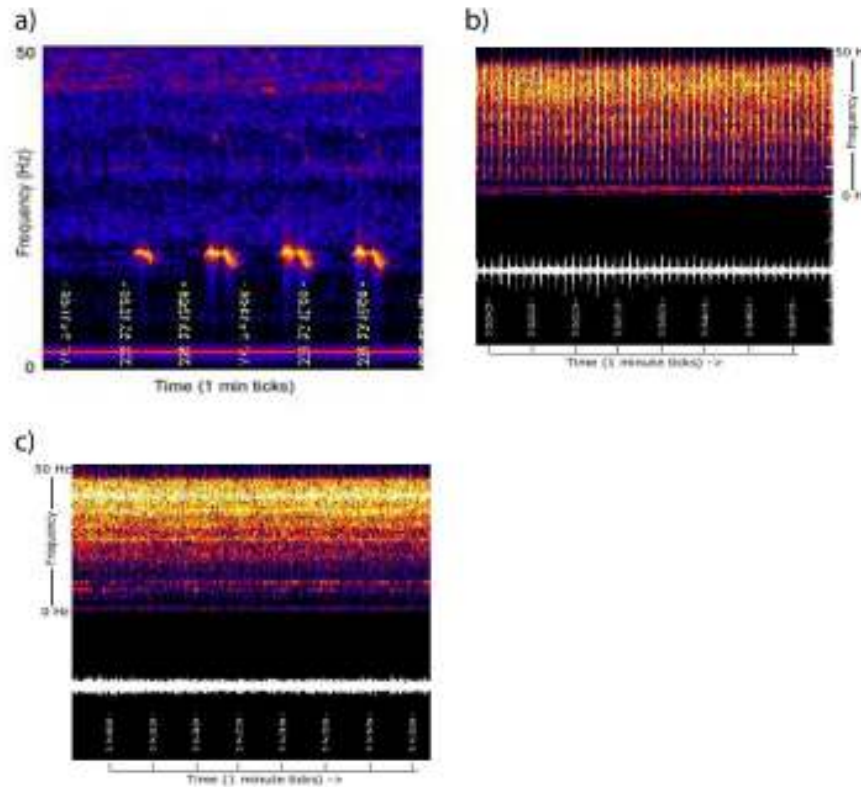


Figure 2.8: Hydrophone registered Atlantic Ocean ambient sounds. a) Blue whale calls. b) Air guns signal. c) Ship signal.

2.3 Hydrophone Technology

2.3.1 Hydrophone and Mooring

The hydrophone is a simple, autonomous recording package that can be deployed and recovered by surface vessels. This approach sacrifices real-time data collection for low cost, portability and is designed to be serviced at sea. The most recent model autonomous hydrophone instrument

diagram in Figure 2-8a, includes a single ceramic hydrophone, filter/amplifier stage designed to pre-whiten the ambient noise spectrum, an accurate clock drift (<1 s/yr), and a logging CPU computer. The instrument can be programmed to record the signal digitized from the hydrophone amplifier at 1-byte (8 bit) or 2-byte (12 or 16 bit) resolution data at a range of frequencies that goes from 100 Hz up to 5 kHz, for periods of up to two years (depending of the frequency range used).

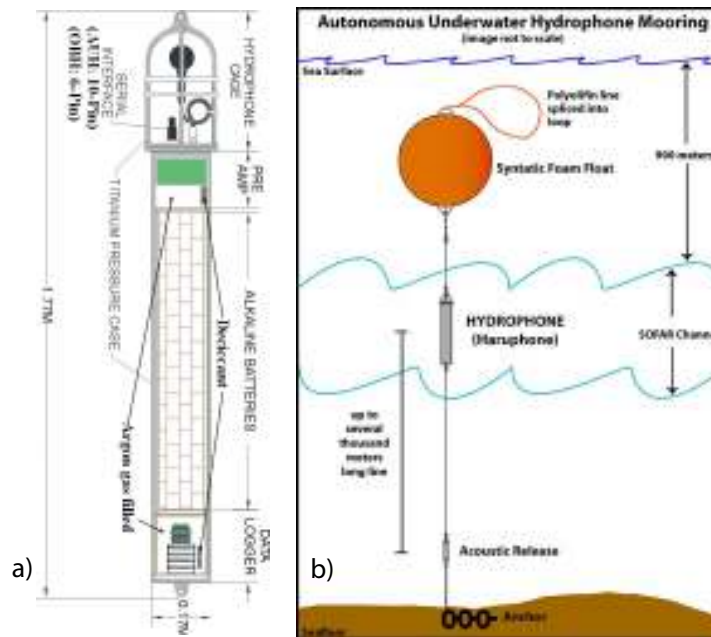


Figure 2.9: a) Current configuration of the Model 3 autonomous hydrophone. (b) Mooring diagram.

The digital section is based on a Persistor Peripheral Issues CF1 CPU computer with a compact flash card used as solid-state random access memory (RAM). It buffers the digitized data by using 20 Megabytes RAM until full, and then transfers the contents of the buffer to hard disk via IDE interface (approximately every 12 hours at 250 Hz sampling rate). To conserve power, the disks are only active during these transfer periods of approximately one minute twice per day, when the power consumption averages approximately 2 W. During the sampling and buffering stage, power consumption depends on the sampling rate, for example $\sim 50mW$ at 100 Hz, $\sim 60mW$ at 250 Hz, and $\sim 100mW$ at 1 kHz.

An additional circuit card allows writing to 2.5" FAT 32 formatted hard disks through an IDE interface. The logging computer monitors the number of files written and accesses the next disk when the current disk is filled. If all disks fill before the instrument is serviced, the system

is shutdown. Accurate timing is provided by a Q-tech Corporation model QT2001 MCXO microprocessor crystal oscillator that generally performs with an average drift of 200 ms during a 6-month deployment with a nominal consumption of 12 mW. The clock is synchronized to a GPS clock before and after each deployment.

The analog filter/amplifier section was developed at PMEL and designed to pre-whiten the ocean ambient noise spectrum over the frequency band of interest, as well as provide anti-aliasing for discrete sampling. Proper environmental filtering is critical to allow full digitization of the signal over the entire frequency band of interest. The creation of a flat spectrum allows the signal to be digitized at the desired resolution, conserving power consumption and storage space. The analog section is physically isolated from the digital section by the battery pack to avoid electrical interference. The electronics are powered by standard alkaline cell battery packs, which are replaced between each deployment. The total power consumption for the package during sampling is around 110 mW, 50 mW for the analog section and 60 mW for the digital section with a 250 Hz sampling rate. There are two types of batteries: one for the relatively slow sampling rate of 100 Hz and 250 Hz deployments for up to two years used mainly in earthquake detection, and one for faster sampling rates up to 2 kHz deployments for up to one year, used mainly in whale call detection.

The mooring package (Figure 2.9) is designed to minimize acoustic and mechanical noise, place the sensor within the SOFAR channel axis, and be serviced at sea. Custom pressure cases were manufactured at PMEL from aircraft titanium tubing and can be deployed to depths of $\sim 1000m$. The titanium construction minimizes corrosion and allows repeated deployments without onshore refurbishment of the case. The hydrophone is attached to the end of the pressure case in a welded cage. The instrument case is attached to a standard oceanographic mooring with anchor, acoustic release, and very low stretch 1 cm Yalex mooring line pre-measured to place the sensor at the proper water depth based on total water depth and depth of the SOFAR channel. Ideally, the instrument is deployed in at least $5^{\circ}C$ water temperature to reduce the chance of disk failure. Low stretch mooring line of small diameter is critical in reducing low-frequency hydrostatic noise associated with movements of the mooring and current related strumming noise. A rigid $\sim 1.5m$ diameter foam float suspends the mooring above the seafloor.

2.3.2 Hydrophone servicing at sea

A routine service of the most recent HARU-phone model requires a set of new batteries to replace the older ones, a GPS translator to have a real time measure of the GMT, PC to run the Crosscut software used to communicate with the GPS translator and the Motocross software with

PicoDos for the HARU-phone, a bottle of Argon gas (heavier than air) and specified connection cables. The GPS translator is a translator that converts the GPS satellite time into 1-pulse per second (pps) pulses that is used to synchronize times between instruments.

Logging program launch

Before launching the logging program it is necessary to be sure that there are no unnecessary files or programs in CF1's RAM and in each of the IDE disks. PicoDos is then used to check the logging settings and to determine if all the parameters were set correctly for the mission. Then the CF1 real-time clock is set close to the GPS time. The Crosscut program used to interact with the NOAA GPS translator system re-synchronizes the GPS translator clock with the satellites and Picodos reboots CF1 which starts a 10 second count down. After the reboot, it starts with a display of the logging parameters and permits the synchronization of the two internal times (Q-Tech and CF1's real time clocks) with the GPS translator time. This is done by connecting the 1-pps GPS translator output to the clock board and synchronization between the Q-tech clock and the GPS translator clock comes with an "Event trigger pulse" meaning that when the triggered pulse occurs the Q-tech clock time and GPS translator times are the same. When the clocks are synchronized the program spins up the first disk and writes the very first file. It also displays the logging parameters and goes into sleep mode for a predetermined number of hours. The container is filled with the argon gas just before closing. This, together with the installed desiccants removes all possible moisture.

After recovery

To prevent static electrical discharges that could damage the electronics, before opening the pressure housing its ground is connected to the ship ground with a jumper cable. Then the PC is connected with the autonomous hydrophone and with the Event/Time-tag of the GPS translator using serial cables. GPS program must be running and ready before ending the logging program. There are two possible scenarios how the logging may end. In the first scenario the logging program ended normally when the data logger finds no space left in the hard disks. When this happens it stops logging and goes into sleep mode until it receives a "break" signal from the operator. Second scenario: the hydrophone is still acquiring data, the "break" signal has no effect and the interrupt button on the serial cable connecting PC and hydrophone must be pushed instead to terminate the logging. This causes the A/D to stop and transfer whatever was written in the ping-pong buffer (stored in the Compact Flash Ram) to the current hard disk. This is the last file. It then goes to low power "sleep mode" as described above. When CF1 terminates the logging

without error, it asks how many seconds are needed to set up GPS and to measure the timing errors. The Crosscut window shows the time tagging from the GPS translator and waits for the pulse issued from the CF1 based on its real time clock. The time in the time-tag window is recorded and compared with the Q-Tech and GPS times. There should be no significant difference between Q-Tech and CF1 real time clocks. All time differences are recorded and the hydrophone is powered off to recover the drives and backup the data.

2.4 Data processing

The interactive data processing system developed by PMEL for analysis of autonomous hydrophone data is grounded in techniques developed for underwater acoustics, rather than standard seismic techniques. A single application program is used to accomplish the entire analysis of the multiple data sets (Figure 2.10). A single operator using a computer workstation analyzes signals from all available hydrophones.

2.4.1 Event location and source level

Individual acoustic signals from each hydrophone are initially decomposed into time versus frequency spectrograms by using fast Fourier transforms (FFT) techniques. Spectrograms as those shown in Figure 2.8 provide information on the character of the arriving signals and allow the analyst to distinguish different sources (seismic, marine mammal, man made) that might appear similar if only the hydrophone time series were used. It tapers a specified length of data using a 10% cosine and then determines the amplitude spectrum. The spectrum is then represented as a color-coded scan line (Figure 2-8) and the next window is processed. Varying the data window length and degree of overlap between windows controls the time and frequency resolution of the spectrograms. For seismic applications a windows length of 1 second that yields 1-Hz frequency resolution is considered sufficient (*Fox et al.*, 2001). Selected time resolutions (that is, the time periods represented by one scan line of the spectrogram) typically vary from 5 seconds to 0.1 seconds depending on the relative need to observe large portions of the data or to accurately pick the arrival. These time-frequency spectrograms for each hydrophone are scrolled down the graphics device either synchronized in time or independently along with the raw hydrophone time series.

The analyst visually identifies events of interest on the spectrograms and makes initial picks of the arrival times. Earthquake signatures are very distinctive, independent of their generating

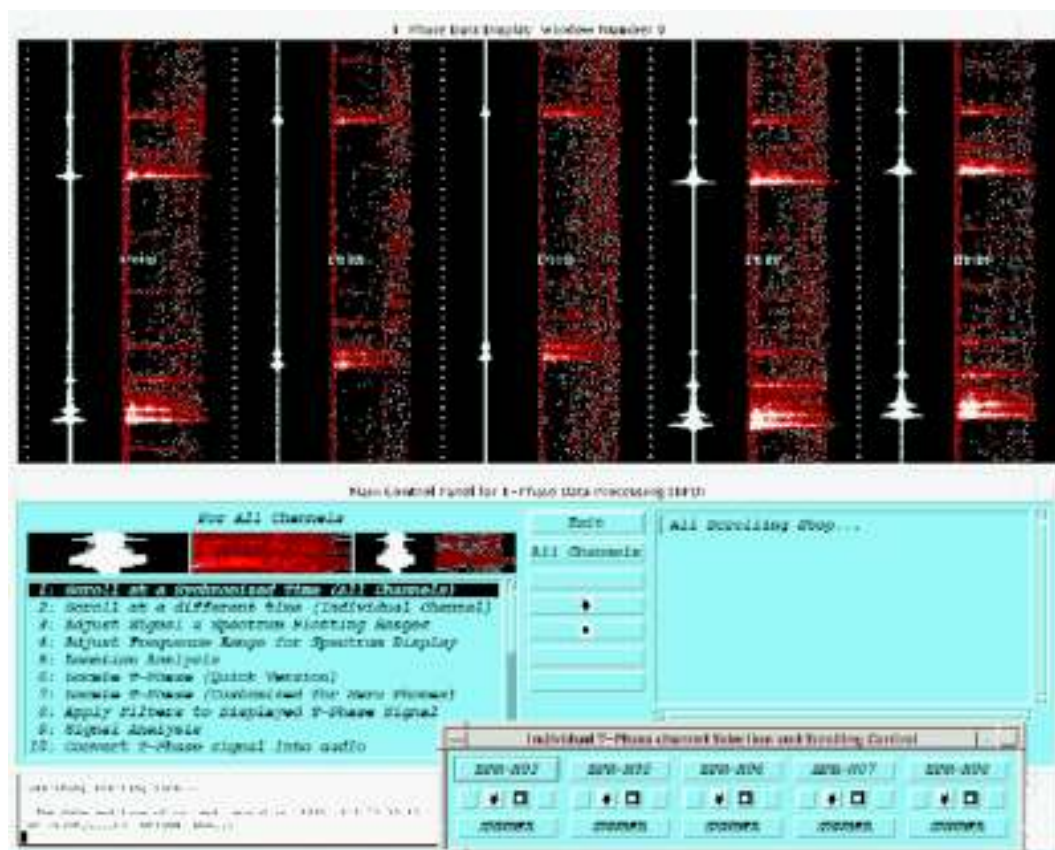


Figure 2.10: T-phase analysis software. The display shows the time series and corresponding frequency spectra for several earthquakes side by side. Time stamps are shown along the time series data. The diagram shows several minutes of hydrophone time series data sampled at 128 Hz. The frequency spectra range from 0 to 50 Hz and were estimated from consecutive 1-s windows of the time series data.

mechanism, and can be differentiated from other phenomena such as whale calls, seismic experiments, etc. (Figure 2.10). Normally, spectrograms from all hydrophones are displayed synchronized in time with each scan line representing 5 s. This allows earthquake arrivals from a single event over the entire array to be presented on a single screen. It is then possible to visually associate at least three arrivals as being from a common event and make a preliminary arrival time pick on each. Arrival times generally correspond to the peak energy arrival.

Given three arrivals, the software then derives a preliminary location from these initial picks and redisplay the spectrograms expanded in time and aligned on the expected arrival times for each instrument. At this point, a refined arrival time pick (based on a 0.1 to 5 s scan display) can be derived for each channel, if the alignment of channels appears correct or return to the

initial screen to re-pick the preliminary data in the case of a miss-association. Based on the refined display, arrival picks are determined for all sensors on which they can be detected and associated. Then the source location is calculated and saved to a file that contains the latitude, longitude, source time, the number of hydrophones (with identifiers) that recorded the event, the estimated error for location and time based on statistics from the least-square solution, the estimated acoustic source level at the source region and the error of the source level based on the variation of the source level determinations estimates from each instrument sensor.

The determination of the event location and source level is based on interactive nonlinear least-square method developed at PMEL in which the sound is propagated through the ocean medium by using digital sound speed models. The preliminary location and source time are used to predict arrival times. The difference between predicted and observed arrival times are iteratively minimized by using a modified Marquardt method (*Bevington and Robinson, 2003*).

For each hydrophone that recorded the signal, the data range that contains the peak recorded acoustic energy was selected in a delta time around the arrival time defined by the user (default is 5 seconds). The sound pressure density spectrum is then computed in a frequency range defined by the user (generally 2-35Hz for earthquakes) (*Fox et al., 2001*). The Received Sound pressure level is then computed using equation (2.2) plus the sensitivity value of the hydrophone. Following the determination of the position and source time, statistics are calculated and a simple spherical and cylindrical propagation equation is used to estimate propagation loss (equations 2.6 and 2.7) for each path. This factor is then summed to the Received Sound pressure level for each sensor and multiple independent estimates of the Source Level are obtained. Their average will then be the *T*-wave Source Level.

The technique used to localize earthquakes from hydroacoustic *T*-waves recorded on underwater differs from the methods used in solid earth seismology. Because digital models based on years of oceanographic measurements have accurately described the sound speed field of the ocean, direct calculation of location and origin time (both within and outside the hydrophone array) can be derived when there are detections on three or more sensors. Besides the known sound speed field, the other given parameters for each solution are the arrival times and sensor locations for all hydrophones that detect a given event. Since all of the measured parameters are subject to measurement error, the non-linear least-squares approach is applied to minimize estimation error. The nonlinear least-square method for estimating the source location and origin time requires the minimization of the following:

$$\min \sum_{i=1}^N w_i (a_i - b_i)^2 \quad (2.9)$$

Where w_i is the weight (1 for unweighted solution), a_i is the recorded arrival and b_i is the predicted arrival time on hydrophone i , and N is the number of hydrophones recording the event. The predicted arrival time is calculated on the basis of an assumed location and origin time as:

$$b_i = t + \frac{d_i}{c_i} \quad (2.10)$$

Where t is the origin time, d_i is the distance between the hydrophone i and the assumed origin, c_i is the sound speed along path from hydrophone i to assumed origin, and d_i/c_i is the travel time in seconds.

The distance d_i is calculated by using a geodesic algorithm with a spheroid Earth assumption. The sound speed estimate c_i along each path is derived through an implementation of the Generalized Digital Environmental Model (GDEM) of oceanic sound speeds (Teague *et al.*, 1990). GDEM provides seasonal sound profiles from the sea surface to the seafloor on a 30-minute grid. To allow rapid calculation, a single sound speed is pre-calculated from the complete profile for each 30-minute grid cell, using the harmonic mean sound speed weighted by layer thickness over all depths from the seafloor to the overlying conjugate depth (the depth at which the sound speed returns to the same value as at the seafloor). In high latitude cases, where the conjugate depth is never encountered, the entire water column is used. Since the sound propagates most efficiently in the slower sound channel axis, this method tends to produce a higher sound speed than observed, and therefore the resulting grid of mean sound channel sound must be modified by an empirically derived factor based on the calibration of arrivals from a known source.

The least-square solution is derived iteratively by providing measured arrival times and hydrophone locations and calculating travel times based on the initial estimate of the source location and origin time. The selection of an initial estimate can be critical to the stability of the solution. If the initial estimate does not fall within the general region of the actual event, it is possible that the solution converges to a local minimum on the solution surface and produces a grossly incorrect source location. The incorrect location can be easily recognized by the relatively high residual errors (assuming that more than three hydrophones were used), but an incorrect solution is obtained nonetheless. To improve the chances of deriving the global minimum solution, three cases are run for each determination using different initial conditions. The three initial estimates consist of (1) a location in the center of the array (assuming that the event is inside the array), (2) a location outside the array in the direction of the hydrophone that recorded the first arrival (assuming that the event is outside the array), and (3) the location of the minimum residual error of a coarse grid over the entire region. After the solution is derived for all three cases, the case

producing the lowest root-mean-square (RMS) residual error is selected as the source location.

The iterative least-square calculation is performed by using a gradient expansion algorithm derived from the Marquardt method, which combines the best features of the gradient search method with the method of linearizing the fitting function (*Bevington and Robinson, 2003*). The calculated mean sound speed for each travel path from initial source position to each receiver is calculated through a weighted harmonic mean based on the mean sound profile grid weighted by the length of each relevant segment along the path. These mean sound speeds are not recalculated during each interaction and no weighting ($w_i = 1$) is applied at this stage. Following the solution of all three cases, the best (lowest residual error) solution is selected and a final weighted recalculation is performed using the derived source location, origin time and where the weights (w_i) are equal to the inverse of the travel time. This allows hydrophones near the source, with presumably better record arrivals and better arrival time determinations, to be weighted more heavily than distant hydrophones. Also, the sound speeds for each of the travel paths are recalculated on the basis of this improved initial position. Finally, when four or more receivers are available, the standard error for latitude, longitude, and origin time is derived from the variance-covariance matrix as modified by the mean-square residual (*Fox, 1984*).

2.4.2 Location error analysis

Evaluating the error associated with the location methods described above requires a different approach than the direct calculation of standard errors or error ellipses from the variance-covariance matrix normally used in solid Earth seismology. An indirect method is needed because there are insufficient degrees of freedom to accurately calculate standard errors by using a least-square procedure. In most cases the procedure must solve for three unknown variables (latitude, longitude, and origin time) based on a maximum of only six hydrophone detections, allowing at most three degrees of freedom. A degree of freedom lesser than three may occur when an event is not recorded by all hydrophones owing to transmission loss, bathymetry blockage or instrument failure. With a small or null degree of freedom, the standard errors computed from the least-square procedure can be grossly inaccurate and the calculation of error ellipses even more suspect. An indirect method based on the standard Monte Carlo simulation techniques with calibration based on known sound sources is applied here. This method provides a robust prediction of error in each variable and provides these error estimates over the entire field of observation.

The objective of the simulation is to obtain standard error distributions of the estimated parameters (latitude, longitude and origin time) by generating multiple realizations of the location model and calculating the estimators in each case. This approach builds up the distribution of

the estimators relative to the predefined input values and allows a statistically robust estimation of the error distribution to whatever confidence levels desired (*Bevington and Robinson, 2003*). To estimate the error at any reference point, an event is defined in latitude and longitude and its origin time defined as zero (forcing the arrival times to be equal to the travel times for convenience). The hydrophone locations are also defined, and the GDEM-derived sound speed model is applied to compute the sound speed and arrival time of each path. Inversion of these arrival times through the least-square procedure yields the prescribed location and origin time. For each realization, however, a random error with normal distribution and defined standard deviation is added to each arrival time independently, before the location inversion. Weights can be applied at this stage to evaluate their effect. The least-square procedure is applied to determine the origin, and the calculated latitude, longitude and origin time are compared with those defined by the reference point and the result is saved. This procedure is repeated for 100 realizations per location, until the desired error distribution is obtained. The following are then calculated:

Observed bias

$$\Delta = \bar{x} - x \quad (2.11)$$

Mean Square Error

$$MSE = \frac{\sum_{i=1}^N (\hat{x}_i - x)^2}{N} \quad (2.12)$$

Root Mean Square

$$RMS = \sqrt{\frac{\sum_{i=1}^N (\hat{x}_i - x)^2}{N}} \quad (2.13)$$

Variance

$$Var = \frac{\sum_{i=1}^N (x_i - \bar{x})^2}{N} \quad (2.14)$$

Standard Deviation

$$\sigma = \sqrt{\frac{\sum_{i=1}^N (x_i - \bar{x})^2}{N}} \quad (2.15)$$

\hat{x} is the computed variable, either latitude, longitude, or origin time, N is the number of realizations per simulation, \bar{x} is the average for i , and x is either the true value of latitude, longitude, or origin time. The observed biases are generally very near to zero, and therefore only the standard errors are presented for each parameter. The analysis is repeated for a large grid of reference points, providing an error surface for each parameter (latitude, longitude, and origin time) over the entire study area. Note that normally distributed random errors are used for the study here. Since the primary source of error in the analysis is in picking the arrival time, the normal distribution assumption is reasonable.

2.5 Autonomous Hydrophone arrays

In October 1990, PMEL were granted access to the U.S. Navy's Sound Surveillance System (SOSUS) arrays in the North Pacific to assess their value in ocean environmental monitoring. The data collection systems developed by NOAA's VENTS Program have been in place since August 1991. Acoustic signals from the North Pacific Ocean are monitored and recorded at the Newport, Oregon facility of PMEL. This is the primary tool for both continuous monitoring of low-level seismicity around the northeast Pacific Ocean and real-time detection of volcanic activity along the northeast Pacific spreading centers. Real-time ridge crest monitoring potentially permits the timely on-site investigation of hydrothermal and magmatic emissions.

Following the successful use of the SOSUS for monitoring low-level seismicity on the Juan de Fuca Ridge, PMEL developed a strategy for monitoring remote areas of the world ocean not covered by fixed hydrophone, arrays using the autonomous hydrophones described above. In May 1996 one array was deployed in the eastern equatorial Pacific to begin the long-term monitoring of the East Pacific Rise between $20^{\circ}N$ and $20^{\circ}S$ that is still on-going. In February 1999 an autonomous hydrophone experiment started in the Northern part of the Mid-Atlantic Ridge (MAR) with several deployments of hydrophones and arrays configuration (Table 2.1 and Figure 2.11).

Table 2.1: AuH arrays on the MAR

Name	Starting Time	Ending Time	Latitude (N)	Longitude (W)
South Azores	February 1999	June 2005	$16^{\circ}30' - 34^{\circ}30'$	$49^{\circ}30' - 34^{\circ}30'$
SIRENA	June 2002	September 2003	$40^{\circ}30' - 50^{\circ}30'$	$49^{\circ}30' - 24^{\circ}30'$
MARCHE	July 2005	August 2008	$32^{\circ}30' - 39^{\circ}30'$	$42^{\circ} - 29^{\circ}$

Array geometry and hydrophone deployments are generally chosen in consideration of: the target regions for each study and the error field simulations; the optimization of ship time to keep within project budgets; a clear SOFAR path from the target region to the hydrophones; and a choice of deployment sites with relative bathymetric flatness to prevent the risk to miss the SOFAR channel axis. If the AuH is deployed on a slope, a small change in location can result in a large difference in bathymetry.

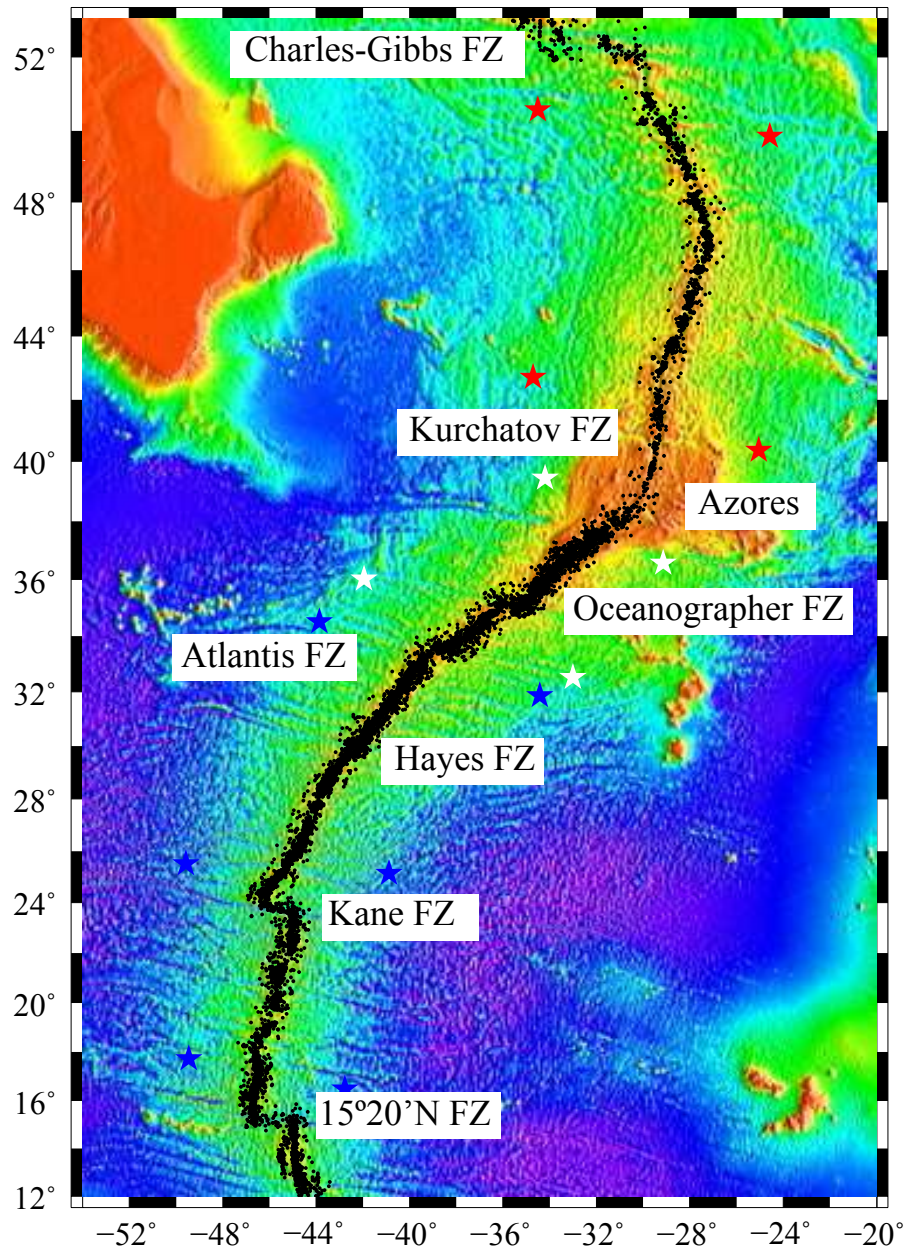


Figure 2.11: MAR seismicity recorded by AuH arrays. Blue stars represent hydrophones from the south Azores array, white stars represent hydrophones from the MARCHE array and red stars represent hydrophones from the SIRENA array.

The data from the four arrays were processed at the PMEL/OSU, Newport Oregon, USA and at the CNRS/UBO Domaines Oceaniques laboratory, in Brest, France. In total from February 1999 until August 2007 near 15000 (Figure 2-12) earthquakes were located in the northern part of the MAR in a region delimited by the Marathon Fracture Zone near $12^{\circ}N$, the Charlie Gibbs Fracture zone near $54^{\circ}N$ and within the recent domain of the MAR, as bounded by the magnetic anomaly 3A (5.69 Myr). The first three years of data were completely processed at Newport and were already interpreted, and providing valuable insight into the seismicity patterns along of the MAR (Bohnenstiehl *et al.*, 2002, 2003; Bohnenstiehl and Tolstoy, 2003; Dziak *et al.*, 2004a,b; Smith *et al.*, 2002, 2003).

2.5.1 AuH detection thresholds and location accuracy

Generally, mid oceanic ridges are far away from continents and therefore only high magnitude seismicity can be detected by terrestrial recording networks. The mooring of AuH hydrophones in the SOFAR channel is an effective way to improve the detection threshold of seismicity for these regions. For example, the Juan de Fuca Ridge (JdFR) was previously considered to be a relatively aseismic ridge, averaging only 1 event per year recorded by the global seismic networks with a detection threshold magnitude of 4.2. The analysis of SOSUS hydrophone array data for the JdFR (Fox *et al.*, 1995) showed that SOSUS data reduced the detection threshold to a magnitude of 1.8-2.1, with 1000 to 2000 events recorded per year (Figure 1). In the same way, AuH data analysis of the array deployed around the East Pacific Rise (EPR) indicated a detection threshold comparable to the SOSUS array for the JdFR (Fox *et al.*, 2001). The size frequency inspection of AuH data for the MAR, EPR and JdFR, showed an improvement of the detection thresholds to ~ 1.5 to ~ 2 orders of magnitude (Bohnenstiehl *et al.*, 2002). Dziak *et al.* (2004b) estimated a magnitude detection threshold of 3.0 by fitting source levels with seismic magnitudes of earthquakes recorded along the MAR by both AuH and land based networks. Finally, using the MAR AuH array, Helffrich *et al.* (2006) reported the detection of acoustic events in the vicinity of the Cape Verde Islands, where a land-based volcano monitoring network was in operation. The authors correlated hydro-acoustic events with earthquake locations determined by the network, finding that earthquakes of magnitudes as low as ML 2 can be hydro-acoustically located at ranges up to 2000 km. It appears that for broader regions detection threshold of AuH arrays are very similar. This raises the following question: are the detection thresholds comparable within smaller parts of the monitored region, or that the threshold is constant during the monitoring period of monitoring? Due to the characteristics of *T*-phases this seems highly improbable. It is therefore very important to take the spatial and temporal variation of the array

detection threshold into account in the AuH recorded seismicity interpretation. In consideration of this, the analysis of the MAR seismicity in the following chapters will examine the detection thresholds for smaller regions in a discrete manner.

Location accuracy was examined in a comparative study between AuH recorded seismicity from the EPR and the MAR, with the reviewed event bulletin produced by the International Data Centre (IDC). This study concluded that, AuH locations using four or more hydrophones are more closely associated with the plate boundary, relative to those obtained from land-based stations (*Bohnenstiehl et al., 2003*). A comparison between relocated International Seismological Centre (ISC) locations with the ones reported by hydro-acoustic monitoring of the north MAR concluded that AuH locations using four or more hydrophones can be used to confirm the mid-oceanic earthquake hypocenters (*Pan and Dziewonski, 2005*). For the ISC events associated with AuH locations, relocated location confidence ellipses based on teleseismic *P* phases are usually large enough to cover AuH locations and their error ellipses and lie in the same azimuthal direction (*Pan and Dziewonski, 2005*).

2.5.2 AuH and teleseismic data correlations

SOSUS locations of earthquakes recorded by the Pacific-Northwest broadband array in the Blanco Transform Fault Zone were used to reduce the number of unknown variables in CMT solutions (*Dziak et al., 2000*). This permitted the obtaining of improved fault information parameter and slip vector earthquake estimates for the study region. Within a comparative study, the Northeast Pacific Ocean earthquakes that had been recorded by ocean hydrophones were also analysed for their source parameters from land-based seismic networks (*Dziak, 2001*). Acoustic energy was compared with source parameters and suggested a relationship where, for a given magnitude, *T*-wave energy is lower for normal and reverse fault earthquakes than for strike-slip events and will often decrease as the component of dip-slip motion increases. AuH acoustic phases of converted upper mantle *P* arrivals from regional earthquakes were used to estimate the *P_n* velocity of 8.0 km/s along the east and west MAR flanks (*Dziak et al., 2004b*). *P* arrivals from earthquakes outside the Atlantic Ocean basin were reported/linked to body-wave arrivals from direct mantle *P* to outer- and inner-core reflected/refracted phases.

2.6 Conclusions

This chapter aimed to present the autonomous hydrophones and its methodology to monitor distant parts of the ocean. In this study case the targeted region were the oceanic ridges, more

precisely the MAR. The following work is based on the the latest five years of data obtained by the AuH arrays deployed on the MAR. This longer spanned data set is expected to give even more information about the dynamical processes occurring on the MAR and to clarify the open questions suggested by the earlier data set. The next chapter will then summarize the actual state of knowledge on the MAR and the role played by the AuH arrays in gaining that knowledge.

Chapter 3

Mid Oceanic ridges and AuH data

It is well recognized that seismicity distributions derived from the interpretation of hydroacoustic signals recorded by AuHs aids the scientific community to better understand the dynamic processes occurring along oceanic ridges. This chapter will then summarize the current knowledge of oceanic ridges and the AuH contribution to this knowledge.

3.1 Ridge segmentation and Morphology

The slow spreading MAR reveals systematic, along-axis depth variations from the segment ends to the segment center (*Detrick et al.*, 1995; *Hooft et al.*, 2000; *Lin et al.*, 1990; *Searle et al.*, 1998a; *Sempéré et al.*, 1995; *Thibaud et al.*, 1998). Segments have a typical length of 40 to 90 km (*Schouten et al.*, 1985) and are generally sub-perpendicular to the direction of relative plate motion.

Segments are laterally offset from each other by up to 30 km along "non-transform discontinuities" (NTDs), or by transform faults that normally accommodate larger offsets (*Fox et al.*, 1991; *Grindlay et al.*, 1991, 1992). The mechanism of NTD propagation requires the along-axis multiplication of dykes and extensional faults into the crust which are formed at the adjacent segments across the segment boundary. Large offsets (bigger than ~ 30 km) will result in a thicker, cooler and therefore stronger lithosphere across a discontinuity, thus stopping the propagation of dikes and faults across it. Similar plate-boundary segmentation can be observed at both intermediate and fast-spreading ridges, but without the major morphological and crustal thickness changes observed at slow-spreading ridges. Crustal thickness variations along fast-spreading ridges and away from major transform offsets are of much smaller amplitude than those observed at slow-spreading ridges (*Bazin et al.*, 1998; *Canales et al.*, 1998).

Slow-spreading ridges have characteristic tectonic patterns that demonstrate that both the seafloor morphology and the crust formed at the ridge axis undergo significant modification at the rift bounding walls (*Escartin and Lin, 1998*). Along the ridge axis, the shallowest point in the rift valley and the thickest crust are located at the segment center, which is considered to be an indication of focused magmatic accretion at the mid-point (*Lin et al., 1990; Gac et al., 2003*). The thinnest crust is found below the ridge discontinuities (Figures 3.1 and 3.2). Outside the rift valley, the shallowest points are commonly located in close proximity to the segment ends, at the inside corners of the ridge-transform or ridge-NTD intersections, while the thinnest crust is found under the elevated inside corners (*Escartin and Lin, 1995; Tucholke et al., 1997*). The outside corners are commonly more subdued topographically and tectonically, indicating asymmetric tectonic processes and uplift (*Severinghaus and MacDonald, 1988*).

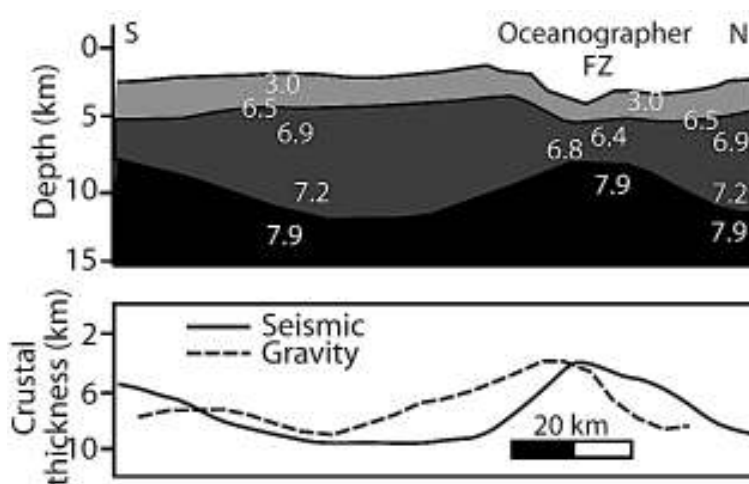


Figure 3.1: Along axis variation of crustal thickness based on seismic observations (top) and gravity modelling (bottom) after *Detrick et al. (1995)*. The gravity scale is reversed.

It is generally agreed that ridge segmentation is intimately associated with the pattern of melt delivery at mid-ocean ridges. While some models have suggested that segmentation may be controlled by focused mantle upwelling or mantle diapirs (*Gac et al., 2003, 2006; Lin et al., 1990; Lin and Phipps Morgan, 1992*), numerical modeling suggests that the characteristic size of diapirs exceeds the characteristic length of slow-spreading segments (*Magde et al., 1997; Magde and Sparks, 1997; Sparks and Parmentier, 1991*). Segmentation can also be controlled by brittle processes in the lithosphere (*Macdonald et al., 1991*), involving interaction and feedback as the melt is focused to the center of segments at slow-spreading ridges. The thinner crust at the ends of slow-spreading ridge segments results from along-axis dyke propagation from the segment center (*Hooft et al., 2000*). The crustal structure formed at the ridge axis is later modified (*Canales et al.,*

2000) by extensional faulting along the rift valley walls (*Escartin and Lin, 1998*) as the crust is rifted off its axis. The asymmetry in crustal thickness between the inside and outside corners may result from initial asymmetric crustal accretion (*Allerton et al., 2000*), possibly followed by asymmetric tectonic thinning (*Escartin and Lin, 1998*).

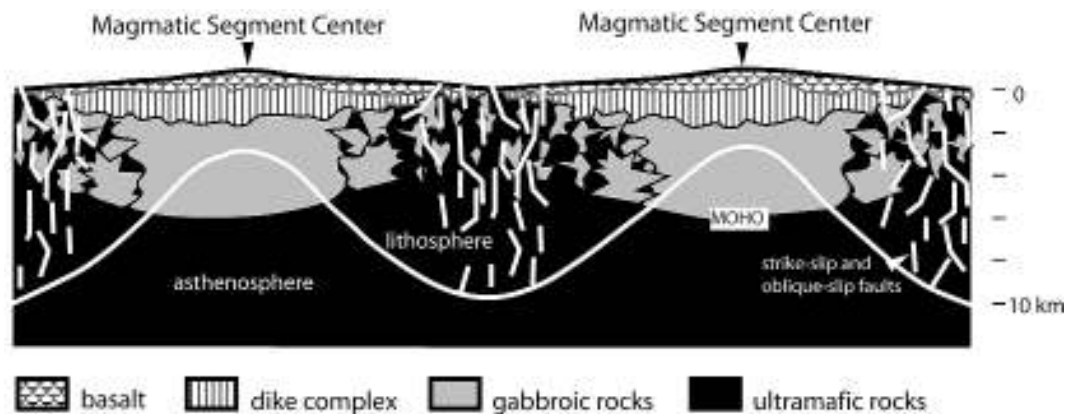


Figure 3.2: Along axis variation in crustal thickness and lithology after *Cannat (1993)*. Continuous white line represents the base of the lithosphere. White, sub-vertical lines represent mantle dykes.

Critical to the thermal state and rheological structure of the lithosphere under the ridge axis is the detailed pattern of hydrothermal circulation and the location and mode of emplacement and extrusion of magma in the crust. In addition to a thicker lithosphere, slow-spreading ridges appear to show a heterogeneous crust (Figure 3.2) that implies a non-steady state mode of magmatic accretion (*Cannat, 1993; Dick et al., 2000*). *Phipps Morgan and Chen (1993)* have modeled the general effect of hydro-thermalism and show that the yield strength of the lithosphere and its effective elastic thickness depend on the balance between the rate of heat input into the crust by magma injection and the rate of hydrothermal cooling.

Along many sections of slow-spreading ridges there is an axial rift, several kilometers wide and 1 to 3 kilometers deep, which is produced by stretching and necking of the lithosphere under horizontal tension as plates separate (*Chen and Morgan, 1990a; Lin and Parmentier, 1989; Tapponnier and Francheteau, 1978*). Along fast-spreading ridges the median valley disappears and is replaced by an axial high, which reflects dynamic viscous support and flexural bending of a thin plate over a hot axial region (*Buck, 2001; Chen and Morgan, 1990b*). Other effects, such as the presence of hotspots, also play a role in ridge morphology (*Canales et al., 1997; Searle et al., 1998b*).

Such a morphological transition is shown by simple rheological models that assume a brittle layer overlying a ductile layer with a power-law creep rheology, passive mantle upwelling driven

by plate separation, and incorporating the effects of both hydrothermal cooling and the latent heat of crystallization (*Chen and Morgan, 1990a,b*). Rift valley morphology is therefore a general indicator of the mechanical properties and overall thermal state of the lithosphere under the ridge axis. The behavior of the rheological models depends critically on the crustal thickness (*Chen and Morgan, 1990a*). A thinner crust predicts a wider and deeper rift valley. The mantle is inferred to be cold and to have a very low degree of melting. By contrast, a hotter mantle results in a thicker crust, as observed near hotspots and the lithosphere behaves in a similar manner to the fast-spreading ridges, producing an axial high (*Chen and Morgan, 1990b*).

The presence of a continuous magma chamber at fast-spreading ridges (*Sinton and Detrick, 1992*) and its absence at slow-spreading ridges (*Detrick et al., 1990*) demonstrates that the rheological structure of fast and slow-spreading ridges is fundamentally different. A magma lens at shallow crustal levels necessarily implies that the brittle layer above it is very thin and can be easily faulted or dissected by dykes. In contrast, the emplacement of discrete and ephemeral magma chambers in the thick lithosphere of slow-spreading ridges will result in large temporal variations of the rheological structure of the ridge axis. Over long periods of time, the thickness of the lithosphere at slow-spreading ridges can thus be assumed to be large and to vary gradually along the length of the ridge segments (*Gac et al., 2003*), as indicated by the gradual variation in rift valley width and depth along axis.

3.2 Ridge Faulting

Tensional stresses induced by plate separation results in disruption of the lithosphere by normal faults that dissect the ocean floor. In the slow-spreading MAR, the most active faulting occurs within approximately 10 to 15 kilometers of the ridge axis (*Searle et al., 1998b*). In comparison to slow spreading ridges, the width of the active tectonic zone in fast spreading ridges is not well constrained, with evidence suggesting that it can extend up to 30km off-axis (*Macdonald, 1998*). The faulting patterns occurring at both slow- and fast-spreading ridges differ substantially from each other and reflect the fundamental differences in the structure and thermal state of the lithosphere under the axis in these two environments. Variations in faulting patterns both regionally and locally (along individual segments) can therefore provide insight into the rheological structure of the lithosphere and its spatial variations.

Normal faults are typically orthogonal towards the spreading direction. Generally at the center of slow-spreading ridge segments the faults tend to define a symmetrical axial valley with similar fault size and strain distribution on each flank (Figure 3.3). In this case, mature faults

have throws of a maximum of a few hundred meters and are spaced 1 to 2 km apart. These faults grow from small individual faults that link together to form abyssal hill terrain (Cowie and Scholz, 1992; Cowie *et al.*, 1993; Searle *et al.*, 1998b). Furthermore, generally, the end of the segments are characterized by a marked asymmetry in topography and crustal thickness (Escartin and Lin, 1995; Severinghaus and MacDonald, 1988; Tucholke and Lin, 1994) that is also associated with profound differences in fault patterns, with larger throws and spacing than those nearer to the segment center (Shaw, 1992). This asymmetry which is most likely caused by asymmetrical tectonic strain can extend along the whole length of a segment, and may be associated with a complementary asymmetry in magmatic accretion (Allerton *et al.*, 2000; Escartin *et al.*, 1999; Searle *et al.*, 1998b). These variations in fault patterns have been interpreted to reflect broad variations in the overall strength of slow-spreading oceanic lithosphere, which in turn influences the lithosphere thickness (Behn *et al.*, 2002a,b; Jaroslow *et al.*, 1996; Shaw, 1992; Shaw and Lin, 1996). Other processes, such as fault weakening due to serpentinisation of the mantle can promote efficient strain localization and therefore influence the faulting patterns observed at the seafloor (Buck and Poliakov, 1998). Estimates of tectonic strain at the seafloor indicate that the majority of plate separation is taken up by faulting (Bohnenstiehl and Kleinrock, 1999; Bohnenstiehl and Carbotte, 2001; Carbotte and Macdonald, 1994; Carbotte *et al.*, 2002; Escartin *et al.*, 1999; Jaroslow *et al.*, 1996), while the remaining separation is taken up by magmatic emplacement or amagmatic accretion of mantle asthenosphere into the lithosphere.

Interpretation of AuH recorded data for the region of the MAR within 15° - 35°N, confirms the importance of tectonic activity and the role of faults on the MAR accretion. It shows that the highest degrees of clustering of AuH recorded seismicity are temporally associated with large main-shock aftershock sequences. In two of these mainshock-aftershock sequences, near 24°25'N and 16°35'N, Bohnenstiehl *et al.* (2002) propose that the sequences had occurred in a hot thermal regime along the ridge crest. North of the Azores, AuH SIRENA network recorded five sequences on the Reykjanes Ridge, each initiated by a moderate-to-large magnitude earthquake (Goslin *et al.*, 2005) and consistent with triggering by tectonic processes. The occurrence of several near-equal magnitude events distributed throughout each sequence may reflect the involvement of magmatic or fluid processes along this section of the Reykjanes Ridge (Goslin *et al.*, 2005). In the Endeavour segment of the Juan de Fuca Ridge (JdFR) a cluster of earthquakes was detected (Bohnenstiehl *et al.*, 2004) and interpreted as an indication that the western limb of the Endeavour - Cobb overlap zone has remained active (Dziak *et al.*, 2003). Near the northern edge of the Easter Microplate an aftershock sequence following a 7.1Ms thrust event, exhibits typical tectonic activity (Bohnenstiehl *et al.*, 2002). Aftershocks are located to the north of a

large topographic ridge, which may represent the surface expression of the shallow-dipping fault that ruptured during the main-shock (*Bohnenstiehl et al., 2002*). Two sequences on the Siqueiros and Discovery Transforms of the East Pacific Rise (EPR), suggest pure tectonic activity with a spatial distribution of aftershocks constrained by intra-transform spreading centers (*Bohnenstiehl et al., 2002*). Hydroacoustic earthquake data were used jointly with bathymetric data to evidence a shear zone extending as far south as the Cobb offset along the JdFR (*Dziak, 2006*). AuH technology also allows scientists to obtain more information regarding the location and size of active faults and the dynamic processes involved in ridge formation. For example: The major Blanco Transform earthquake sequence recorded by the SOSUS that was used to better limit the active transform fault location (*Dziak et al., 2003*) and understand its dynamics (*Bohnenstiehl et al., 2002*). A sign that the triple junction between the Pacific - Juan de Fuca - North American plates may be moving towards the Cobb offset (*Dziak, 2006*).

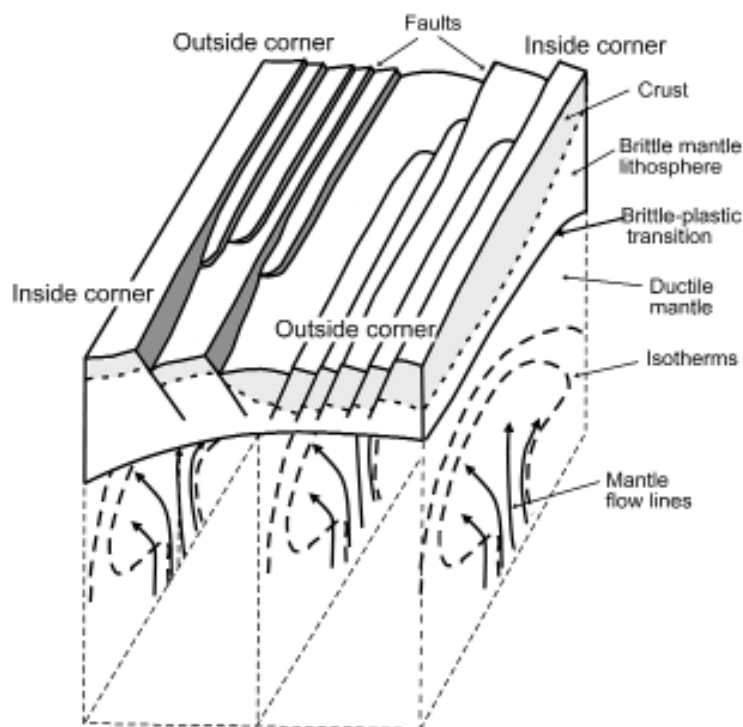


Figure 3.3: Block model of varying fault style along a spreading ridge segment after *Searle and Escartin (2004)*.

3.2.1 Detachment Faulting

Oceanic detachments were first unambiguously identified on the Mid-Atlantic Ridge at $31^{\circ}N$ *Cann et al.* (1997), as smooth, curved and sub-horizontal surfaces with corrugations lying parallel to the spreading direction. Numerous such structures have now been identified, surveyed and sampled along other sections of the MAR (*Dick et al.*, 2008; *Escartin and Cannat*, 1999; *Escartin et al.*, 2003a, 2008; *Fujiwara et al.*, 2003; *MacLeod et al.*, 2002; *Ranero and Reston*, 1999; *Tucholke et al.*, 1998, 2001), and the South West Indian Ridge (*Dick et al.*, 2000; *Searle et al.*, 2003) (Figure 3.4). Oceanic detachments can occur close to or away from ridge offsets (*Escartin and Cannat*, 1999; *Escartin et al.*, 2003a; *Fujiwara et al.*, 2003; *MacLeod et al.*, 2002; *Smith et al.*, 2006, 2008). The geometry of oceanic detachments, the conditions of formation, deformation, and linkage to the adjacent seafloor, are poorly understood. It has been proposed that these structures initiate as high-angle normal faults rooted deeply near the brittle-plastic transition faults that then rotate by flexure (*Buck*, 1988; *Tucholke et al.*, 1998). Other models propose that the faults flatten at depth and become sub horizontal, as proposed for Basin and Range detachments (*Karson et al.*, 1987). The presence of oceanic detachments implies that plate separation is accommodated mainly by tectonic extension in one flank of the ridge usually with lengths less than the length of the segment and with the presence of strain softening to promote localization of deformation during long periods of time (*Lavier et al.*, 1999). More recently the systematic study of the MAR between $12.5^{\circ}N$ and $35^{\circ}N$ revealed asymmetrical accretion along almost half of this section of the MAR involving active detachment faults along one ridge flank (*Escartin et al.*, 2008). This seems to suggest that much of the variability in sea-floor morphology, seismicity and basalt chemistry found along slow-spreading ridges can be attributed to the frequent involvement of detachment faults in oceanic lithospheric accretion.

Strong correlations between detachment fault morphology at the ridge axis and high rates of AuH recorded earthquake seismicity were observed in a region of the MAR near $13^{\circ}N$ (*Smith et al.*, 2006, 2008). This observation was later generalized for the Mid-Atlantic Ridge between 12.5° and $35^{\circ}N$. Asymmetrical accretion shows high levels of near- continuous AuH recorded seismicity (*Escartin et al.*, 2008). The authors associate the pattern of seismic gaps/stripes along the MAR observed by *Smith et al.* (2003) with high levels of seismicity being probably generated along detachment faults that accommodate a sizable proportion of the total plate separation, and lower levels of seismicity with symmetrical segments associated with symmetrical accretion, dominated by magmatic processes with high-angle faulting and the formation of abyssal hills on both flanks *Escartin et al.* (2008).



Figure 3.4: Shaded bathymetry of the detachment at $15^{\circ}45'N$ on the MAR after *Escartin et al.* (2003a). The detachment is sub horizontal and gently curved in the direction of the spreading, and has bathymetric corrugations at wavelengths of ~ 1 km. The exposed fault surface is up to 12 km wide. These detachment surfaces show lineations at shorter wavelengths and fault striations at rock outcrops.

3.3 Magmatic contribution Faulting and Morphology

Recently 2-D numerical models were produced to explore the thermal and mechanical effects of magma intrusion on fault initiation and growth at slow and intermediate spreading ridges (*Behn and Ito, 2008*). *Behn and Ito* (2008) proposed that fault development proceeds in a sequential manner, with deformation focused on a single active normal fault that initiates near the ridge axis and is subsequently rafted off-axis by continued magmatic accretion. This progresses until it becomes mechanically easier to break a new fault rather than continue deforming on the original fault. This new fault forms on the opposite side of the ridge axis to the existing fault, where tensile stresses are highest. As this process continues through time it generates sea-floor morphology similar to the abyssal hill topography seen at many slow and intermediate spreading

ridges.

Faulting is influenced by a number of competing factors including lithospheric structure, rheology, and the rate of magma accretion at the ridge axis. Fault heave and spacing decrease with increasing lithospheric thickness and increase with decreasing rate of off-axis lithosphere thickening (*Behn and Ito, 2008*). The dominant factor controlling fault growth is the ratio of magmatic accretion to the rate far field extension, with the largest, most widely spaced faults occurring for small ratios. Furthermore, fault growth generates a strongly asymmetric axial thermal structure, with elevated temperatures at the base of the lithosphere below the active fault. This asymmetry results from the advection of warm mantle material into the footwall of the active fault and is most pronounced for long-lived, large-offset normal faults. These across-axis variations in thermal structure will further stabilize slip on large-offset normal faults and offer a plausible mechanism for localizing hydrothermal circulation on the footwall of oceanic core complexes.

A good example of magma intrusion through dyking is that which occurred on the Manda Hararo-Dabbahu on the Afar ridge. More than 2km^3 of mafic magma were emplaced as a dike extended to maximum depth of 10 km (*Grandin et al., 2009; Wright et al., 2006*) with faults rupturing at the surface above the 65 km long dike (*Grandin et al., 2009*). On average, absolute subsidence reached 2 m between the faults, while the uplifted shoulders rose by 2 m (*Grandin et al., 2009*). Slip on faults is asymmetric, with a substantial amount of dilation occurring on the western side of the dike. This occurs where the dike is offset to the east with respect to the axial topographic depression, and is interpreted to result from dike injection below a mechanically anisotropic brittle crust (*Grandin et al., 2009*). This rifting event produced 163 earthquakes (*Wright et al., 2006*) and a volcanic eruption (*Grandin et al., 2009; Wright et al., 2006*) occurred within the magmatic segment of the Afar rift, a nascent seafloor spreading centre in stretched continental lithosphere. Simple elastic modeling showed that the magmatic segment opened by up to 8 m, yet seismic rupture can account for only 8% of the observed deformation. Much of the magma appears to have originated from shallow chambers beneath the Dabbahu and Gabho volcanoes. Thus, magma intrusion via dyking, rather than segmented normal faulting, maintains the along-axis segmentation throughout this sector of the Nubia-Arabia plate boundary (*Grandin et al., 2009; Wright et al., 2006*).

In oceanic ridges, frequent detection of seismic crises due to magmatic intrusions began as a result of the threshold detection of SOFAR deployed hydrophones. A magmatic cycle on the Axial volcano was identified in the JdFR (*Dziak et al., 1995; Dziak and Fox, 1999a,b; Fox et al., 1995; Fox and Dziak, 1998*). The cycle occurred along the summit caldera and flank rift zones with an increasing rate of swarm activity lasting approximately 7 years, followed by a one year

aseismic period. In all sequences, spatial migration of the seismicity in a fashion typical of dyke intrusion was clearly observed. Another cluster of earthquakes was detected in the Endeavour Segment in 1999 (*Bohnenstiehl et al.*, 2004). It extended along axis and migrated laterally to the south. This is consistent with a lateral dike propagation in a region known to have a shallow axial magma chamber. An analysis of the earthquake sequence decay constant failed (*Bohnenstiehl et al.*, 2002), due to the large number of earthquakes within the sequence and the absence of a clearly dominant main-shock. In the MAR the AuH recorded a seismic crisis created by a magmatic dike intrusion in the the Lucky Strike segment in 2001 (*Dziak et al.*, 2004a). The dike intrusion caused the largest teleseismic extensional earthquake swarm recorded at Lucky Strike segment. Hydrophone records indicate that the onset of the swarm was accompanied by 30 minutes of broadband intrusion tremor, suggesting the volcanic component (*Dziak et al.*, 2004a). Another volcanic sequence recorded by the AuH originated at the Walvis Ridge recorded by the AuH (*Haxel and Dziak*, 2005). Swarm locations were centered on the northern flank of a seamount, northwest of Wust Seamount. These events lend support to an extensional zone model, resulting in the recurrence of volcanic activity along older segments.

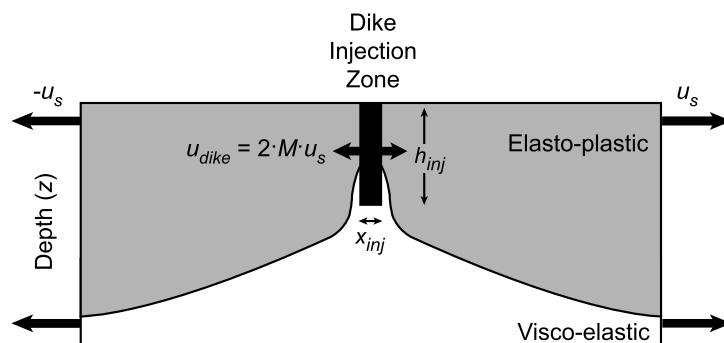


Figure 3.5: Model setup used for numerical simulations of magmatic spreading at a mid-ocean ridge from *Behn and Ito* (2008). The dike injection zone is illustrated with the thick black line. Gray region represents the portion of the model space that experiences brittle deformation, while the white region behaves viscously. Deformation is driven by applying a uniform half-spreading rate, u_s , to either side of the model space. The rate of magma injection u_{dike} is controlled by the parameter M , which is defined as the fraction of the total spreading rate accommodated by magma accretion.

3.4 Oceanic ridges seismic patterns

Most of the earthquake activity along the EPR is associated with transform fault zones (*Fox et al.*, 2001; *Bohnenstiehl and Tolstoy*, 2003) (Figure 3.6). Several volcanic type earthquake swarms were recorded within the EPR study area (*Fox et al.*, 2001). All swarms include a relatively small number of events, are generally of short duration, and originate from segments with relatively fast spreading rates of 125 mm/yr. On the other hand the Cocos-Nazca spreading center has persistent activity along the spreading center, similar to medium and slow spreading ridges in the northeast Pacific and Atlantic (*Fox et al.*, 2001) (Figure 3.6). Substantial seismicity is recorded from the Galapagos Islands and the spreading center to the northeast. There is a significant decrease in seismicity east of 95° on the Cocos-Nazca spreading center corresponding to an apparent increase in magma supply (*Fox et al.*, 2001) (Figure 3.6). One sequence on the Cocos-Nazca spreading center included more events, was longer in duration and originated from a spreading center at a significantly slower spreading rate of 45 mm/yr closer to those documented from the northeast Pacific (*Fox et al.*, 2001). The northeast Pacific ridge formed by the Explorer Ridge in the north, the JdFR and the Gorda Ridge in the south (Figure 3.7) shows substantial seismicity along the Explorer and Gorda Ridges and along the fracture zones that delimit them. The JdFR shows a significant decrease in seismicity apparently due to an increase in the magma supply of the JdFR (Figure 3.7). The seismicity present in the JdFR seems to be grouped in volcanic type clusters of earthquakes.

The MAR presents a persistent seismic activity along almost all of its spreading center. Seismicity recorded by the MAR hydrophone array between 15°N and 35°N (Figure 3.8), shows an uneven distribution, with sections that are seismically inactive and sections that show continuous seismic activity (*Smith et al.*, 2003). There are eleven clear, seismically active sections (Figure 3.9) (*Smith et al.*, 2003), two of which correspond to regions nearby the Kane and Atlantis transform faults. The other nine seismically active areas correspond to segments (Figure 3.9). The major transform faults associated with the Oceanographer, Hayes, Kane, Atlantis, and Fifteen-Twenty FZs show differing amounts of seismic activity during the four years of the hydro-acoustic monitoring (Figure 3.9). The Kane and Atlantis transform faults were constantly active. In contrast, the Fifteen-Twenty, Hayes, and Oceanographer transforms showed little seismic activity. The lack of AuH recorded seismicity along some of the transforms suggests that the seismic "deficit" as observed in seismological catalogs may not be accounted for by a high number of smaller-magnitude earthquakes. Instead, the lack of seismicity may indicate that aseismic slip occurs (*Smith et al.*, 2003). Also the AuH arrays also recorded a band of seismicity $\sim 70\text{km}$ west of the axis between $\sim 11.9^\circ\text{N}$ and $\sim 14.2^\circ\text{N}$ (*Escartin et al.*, 2003b) associated with exten-

sion directions consistent with the accommodation of the North-America and South American relative plate motion (*Escartin et al.*, 2003b).

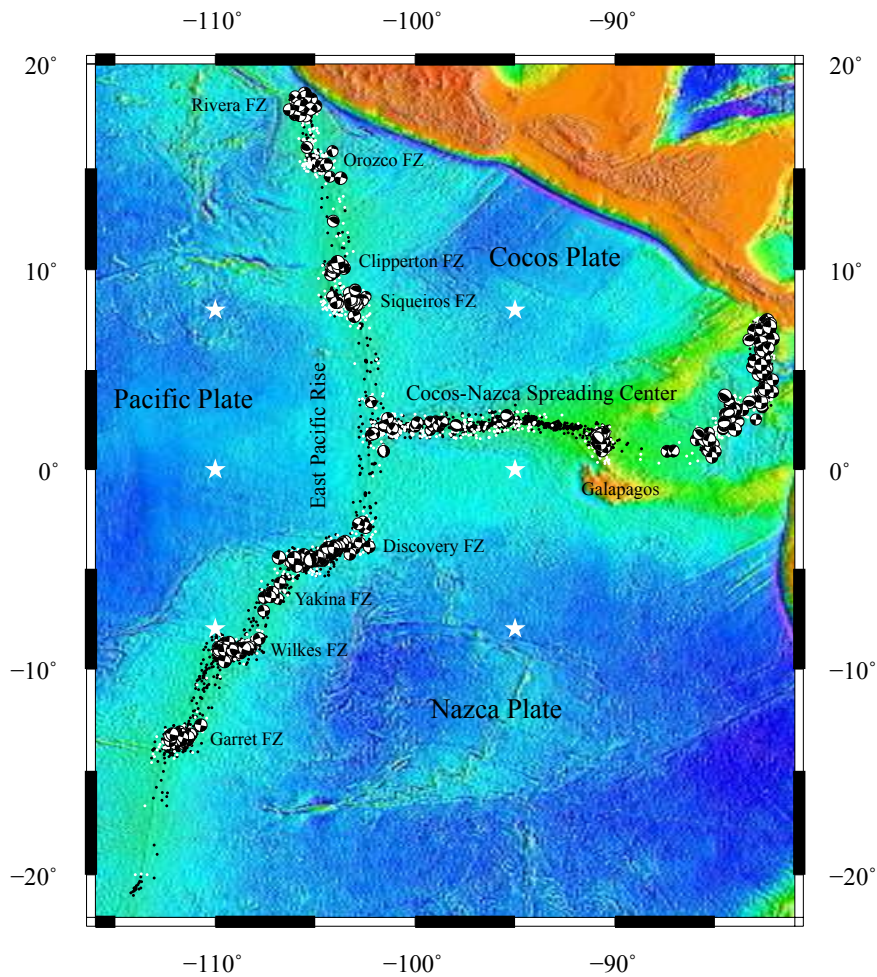


Figure 3.6: East Pacific Rise and Cocos-Nazca spreading center map. Black dots are AuH array detected events on a 6 years survey. White circles are ISC catalog earthquakes since 1964. Focal mechanisms obtained from the ISC catalog.

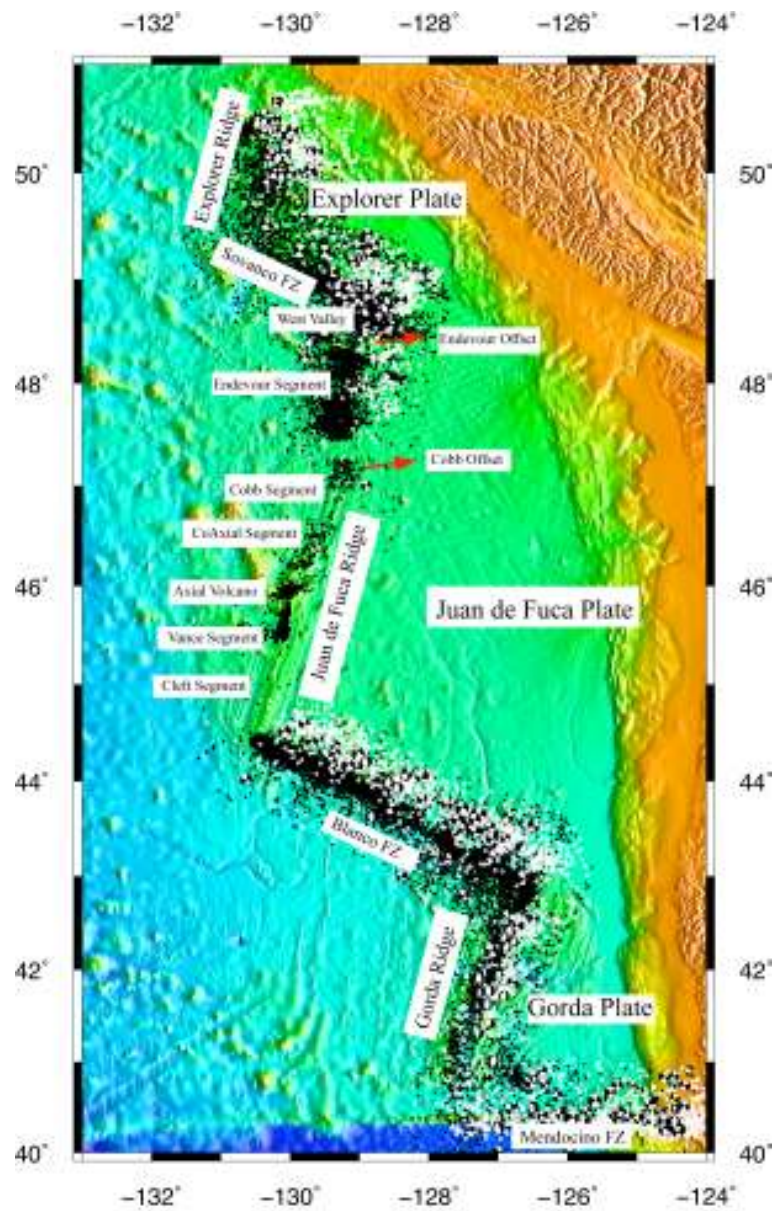


Figure 3.7: Northeast Pacific Rise map. Black dots are SOSUS array detected events on a 17 years survey. White circles are ISC catalog earthquakes since 1964. Focal mechanisms obtained from the ISC catalog.

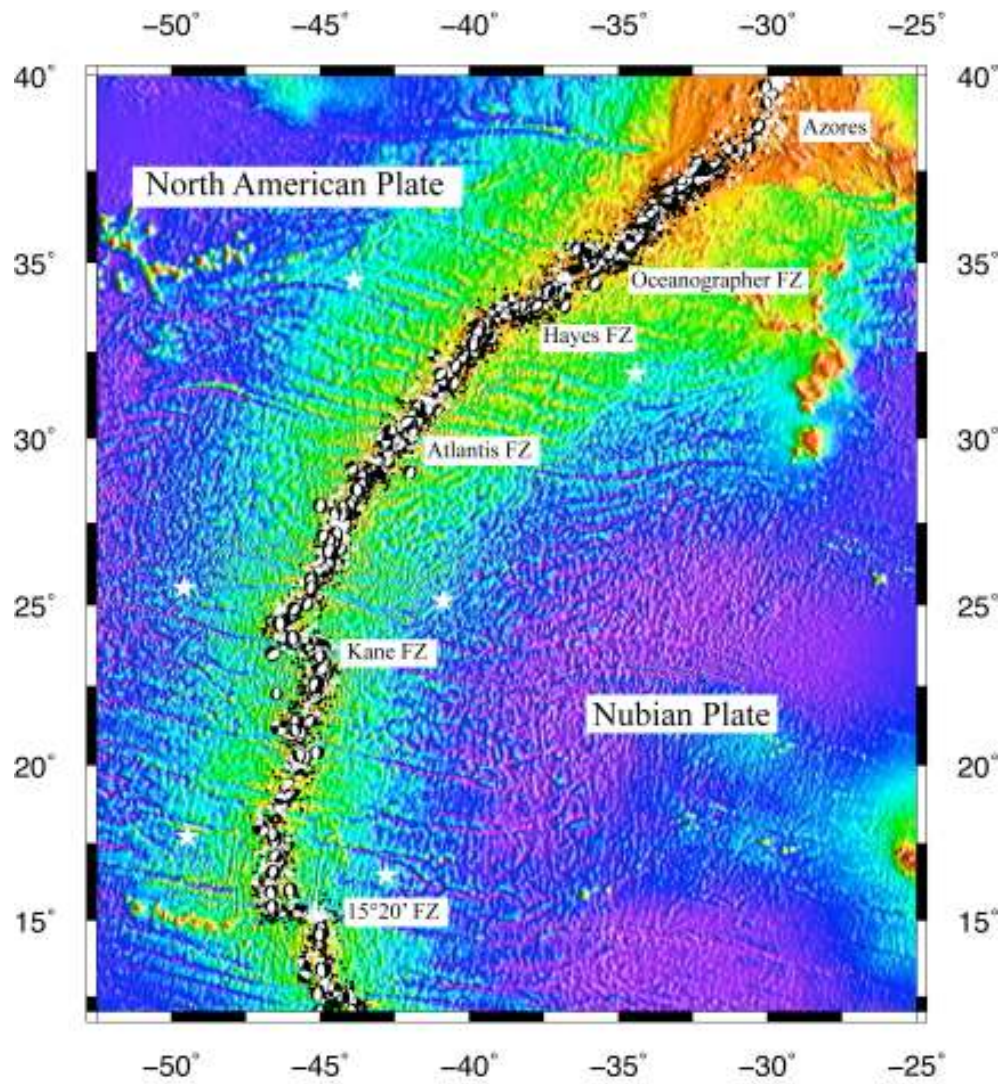


Figure 3.8: Mid Atlantic Ridge map. Black dots are AuH array detected events on a 6 years survey. White circles are ISC catalog earthquakes since 1964. Focal mechanisms obtained from the ISC catalog. White stars are AuH positions.

Figure 3.9: Plot of distance along axis versus number of events for teleseismic and hydrophone source locations after *Smith et al. (2003)*. Darker gray lines are FZs. Teleseismically events are shown as larger circles. Seismic stripes are marked with black lines and labeled with the number of the segment within which they occurred. Seismic gaps are marked by gray lines and labeled with segment numbers.

3.5 Land based arrays and OBS arrays

AuH distributions complement the poor magnitude and spatial covering of the international land based seismic networks for most parts of the world's oceans. It provides long term and more precise event locations and can be seen as a way to complement the still shorter autonomy of seismic seafloor experiments. Nevertheless, the special characteristics of *T*-phases oblige any interpretation made using AuH data to be done while keeping in mind the differences from more classical seismic data.

3.5.1 Teleseismic data

At the slow-spreading MAR the largest magnitude earthquakes (with a sufficient size to be detected by land-based seismic stations) are associated with the axis. A seismic moment deficiency has been observed teleseismically along oceanic transform faults (*Engeln et al.*, 1986; *Abercrombie and Ekström*, 2001). Other zones are seismically inactive, and might correspond either to areas where deformation is accommodated through low magnitude seismicity (lower than the detection limit of the land-based array), or to areas where deformation occurs aseismically, or to quiescent areas in which stress is accumulated and not released (*Behn et al.*, 2002b). The larger earthquakes occur preferentially in areas with a deeper median valley (*Huang and Solomon*, 1988), and are likely to be tectonic in origin. *Bergman and Solomon* (1990) concluded that volcanic earthquakes on the MAR probably fall below the magnitude threshold for teleseismic detection using global seismic networks. They observed a number of teleseismic swarms on the MAR, and determined that they were due to tectonic extension. However the results of these studies have been limited in their capacity to provide a representative account of general seismicity at the MAR, because they do not include the lower magnitude tectonic and volcanic events. Despite the fact that the pattern of seismically active/inactive areas observed in the AuH data can be recognized in the longer term teleseismic record, it is not as clearly defined. This lack of definition may be due to the lower number of events (Figure 3.9), or to the much larger error ellipses associated with teleseismic locations. The similarities suggest that the patterns of seismicity along the axis can be persistent at timescales of one year to several decades (*Smith et al.*, 2003).

3.5.2 OBS data

Micro earthquake studies help constrain the interpretation of AuH recorded events patterns due to the more detailed view of the seismicity distribution given by ocean bottom seismometers. Unfortunately these experiments are not concurrent in time with the AuH experiments and are conducted on a limited number of MAR sites. Five OBS experiments were conducted on four different segments on the MAR spanning across 20 years. Experiments were conducted on segments 15 (22.23°N - 22.67°N), 24 (25.92°N - 26.25°N), 32 (28.84°N - 29.41°N) and 45 (34.50°N - 35.27°N) (*Smith et al.*, 2003).

Microearthquake distribution seem to be quite consistent along these segments. Predominantly, earthquakes occur at segment extremities, generally linked to inside corners, and/or segment centers (*Barclay et al.*, 2001; *de Martin et al.*, 2007; *Kong et al.*, 1992; *Wolfe et al.*, 1995). Segment 15 revealed numerous microearthquakes recorded extending from the northern end of the segment to near the center (*Toomey et al.*, 1985, 1988). Seismic distribution plots with bathymetry, reveal that much of the seismic activity has a strong tectonic signature (*Barclay et al.*, 2001; *de Martin et al.*, 2007; *Kong et al.*, 1992; *Toomey et al.*, 1985, 1988; *Wolfe et al.*, 1995) suggesting that spreading has been mainly accommodated by faulting during the last few tens of millions of years on these segments. AuH recorded earthquake distribution are generally consistent with the OBS recorded ones (*Smith et al.*, 2003). Differences between the two kinds of distribution seem to be explained by the magnitude level of the microearthquakes and the detection threshold of the AuH arrays. In some of the cases AuH seismic distributions also seem to be shifted when they are close to shallow topography (*Smith et al.*, 2003). For the segment 15, AuH data revealed that the entire length of the segment was active during the years of monitoring (*Smith et al.*, 2003).

3.6 Conclusions

EPR distribution of seismicity shows almost all of its seismicity being concentrated on the fracture zones, where seismological catalogs reveal strike slip tectonic activity, and with scarce seismicity along segments being focused on volcanic type swarms. This clearly differentiates from its neighbor Cocos-Nazca spreading center and its Atlantic counterpart. These oceanic ridges present high levels of seismicity all along its spreading segments, where seismological catalogues reveal high levels of normal faulting tectonic activity, and generally fracture zones are much less active. Differences in ridge seismicity are, like their morphology and rheology, a direct effect of the oceanic crust and upper mantle regional thermal regimes. AuH arrays are

very good tools to monitor these remote regions of the ocean due to the specific characteristics of T-phase propagation in the oceans. They can complement both the teleseismic networks and the OBS experiments. AuH recorded seismicity allows the scientific community to have a clearer picture of the dynamic processes occurring in the monitored regions.

Chapter 4

MAR AuH seismicity analysis

4.1 Introduction

Historically, there have been few observations of earthquake sequences along middle oceanic ridges. This is due to the limited spatial coverage provided by the global seismic networks. PMEL's regional autonomous underwater hydrophone (AuH) arrays therefore offer an improvement in the detection capabilities of seismicity, making it possible to characterize the temporal and spatial earthquake patterns in remote oceanic areas. Hydrophone earthquake source locations are derived from distinct T -wave arrivals recorded by the AuH arrays (Fox *et al.*, 2001). These source locations represent the region where T -wave energy is radiated into the water column from seismic phases. This energy is characterized by a Source Level (Dziak, 2001; Fox *et al.*, 2001). Despite the low propagation angles that should result from the large density contrast between seafloor and water column, T -phase conversion and propagation in the SOFAR channel is made possible through high incidence angle conversion mechanisms, such as multiple reflections (Talandier and Okal, 1998), scattering from the seafloor (Yang and Forsyth, 2003) or mode coupling (Balanche *et al.*, 2009; Park *et al.*, 2001). These conversion mechanisms illustrate the complexity surrounding T -phase excitation, making it difficult to directly estimate the magnitude, hypocenter and the physical parameters of the earthquake (Williams *et al.*, 2006). Despite these complexities, hydroacoustically derived epicenters lower the detection threshold along the Mid Atlantic Ridge (MAR) by ~ 1.5 magnitude units relative to land-based seismic networks (Dziak *et al.*, 2004b). Furthermore, Bohnenstiehl and Tolstoy (2003) and Pan and Dziewonski (2005) demonstrate that earthquakes recorded by four or more AuHs have highly accurate source locations within the arrays and can therefore be used for detailed studies of the low level seismicity.

In early 1999 PMEL laboratory deployed six AuHs in the MAR between $\sim 16^\circ\text{N}$ to $\sim 34^\circ\text{N}$

(*Smith et al.*, 2002) to improve the monitoring of the MAR seismicity, which provide information as far south as the Walvis Ridge (*Haxel and Dziak*, 2005). The deployment lasted until mid 2005. The CNRS "Domaines Oceaniques" laboratory deployed another AuH array in the MAR, in the region north of the Azores between $\sim 40^\circ\text{N}$ to $\sim 50^\circ\text{N}$ monitoring the seismicity as far north as the Reykjanes Ridge (*Goslin et al.*, 2005). The duration of the deployment was 15 months, ending in mid 2003. Later, within the context of the MoMAR project, a third AuH array was deployed south of the Azores. The deployment began in mid 2005 and ended in mid 2008. The nine years of AuH deployment along the MAR provided a comprehensive dataset covering most of the northern MAR, permitting researchers to observe major seismic crises (*Bohnenstiehl et al.*, 2002; *Dziak et al.*, 2004a; *Goslin et al.*, 2005; *Haxel and Dziak*, 2005), and to better understand the spatial distribution of seismicity in the MAR (*Escartin et al.*, 2003b, 2008; *Smith et al.*, 2003, 2006; *Williams et al.*, 2006).

In this research study, a long wavelength comparative study of hydroacoustic versus teleseismic based datasets was made in the MAR from $\sim 12^\circ\text{N}$ to $\sim 52^\circ\text{N}$. To be able to evaluate variations in seismicity across space and time, recorded in different sectors of the MAR, and to interpret those variations, the detection thresholds needs to be taken into account. Detection thresholds may be dependent on the distance between the events and the array, topographic blockage or illumination due to the specific nature of the T -phases (*Dziak*, 2001; *Fox et al.*, 2001; *Williams et al.*, 2006) and instrument failure during the acquisition period. A Principal Component technique (*Goltz*, 2001) was used to analyze the spatial and temporal variations from the mean rate of AuH recorded seismicity and its influence in the overall seismicity. The results were interpreted in conjunction with high resolution bathymetric grids between $\sim 35^\circ\text{N}$ to $\sim 46.5^\circ\text{N}$, and with land based seismic catalogues, to see how these variations are affected by higher order magnitude seismicity.

4.2 AuH array error field

Expected errors in latitude, longitude, and origin time for the entire field of observations can be predicted for different array geometries and number of hydrophones (*Fox et al.*, 2001). The standard error represents T -phase source resolution and repeatability. It is possible that location biases might still be present if the assumptions used in the sound speed propagation modeling are incorrect. This is particularly true outside of the array. Further caution is required for interpreting hydro-acoustically derived T wave source locations. The location of the water-borne T wave represents the region where the seismic energy has been converted from the oceanic

crust or sediments into the overlying water column. Depending on the regional relief and depth of the hypocenter, this location may not directly overlie the hypocenter and therefore does not necessarily represent an epicenter. This topographic steering effect is most pronounced when the earthquake originates outside of the array and within a large topographic feature. For earthquakes generated within the array, topographic steering effects should generally be distributed around the true epicenter, introducing a larger location error but reducing the bias effect. The importance of these topographic effects for deep-oceanic earthquakes continues to be an area of active research (*de Groot-Hedlin and Orcutt, 1999; Talandier and Okal, 1998; Okal and Talandier, 1997; Williams et al., 2006*). For the present, it must be considered qualitatively to enable adequate interpretation of hydrophone derived *T*-wave source locations.

Four geometry simulations for the Northern Atlantic AuH arrays are presented (Figures 4.1, 4.2, 4.3 and 4.4). These plots show the predicted error field for the origin time, longitude and latitude, when *T*-phase source locations are derived from all hydrophones. Predicted error fields are presented as contours of standard error. They indicate that location errors can reach up to two kilometers inside the arrays and are larger outside. The predicted error values systematically increase outside the array formation, as distance between the array and the event increase, so does the uncertainty in location range. The error field outside the arrays is also highly distorted, with very large errors in latitude along an axis running N-S and large errors in longitude running E-W through the center of the arrays. The large asymmetries in the external error field are due to the array geometry. Essentially, sensors that are in alignment (for example, along lines of longitude) do not provide additional information for events that are external to the array along these lines, making the determination of the parameter more difficult.

The simulation for the array in Figure 4.4 reveals higher location errors inside the array between four and six kilometers. The increase in the predicted error for this array implies a poorer array configuration, possibly due to the asymmetric position of the western hydrophone related to the remaining array. The number of hydrophones deployed is also a factor, as a higher number reduces the rate at which the predicted error values increase outside the arrays. This is easily observed comparing the error field for the arrays in Figures 4.1, 4.2 and 4.3.

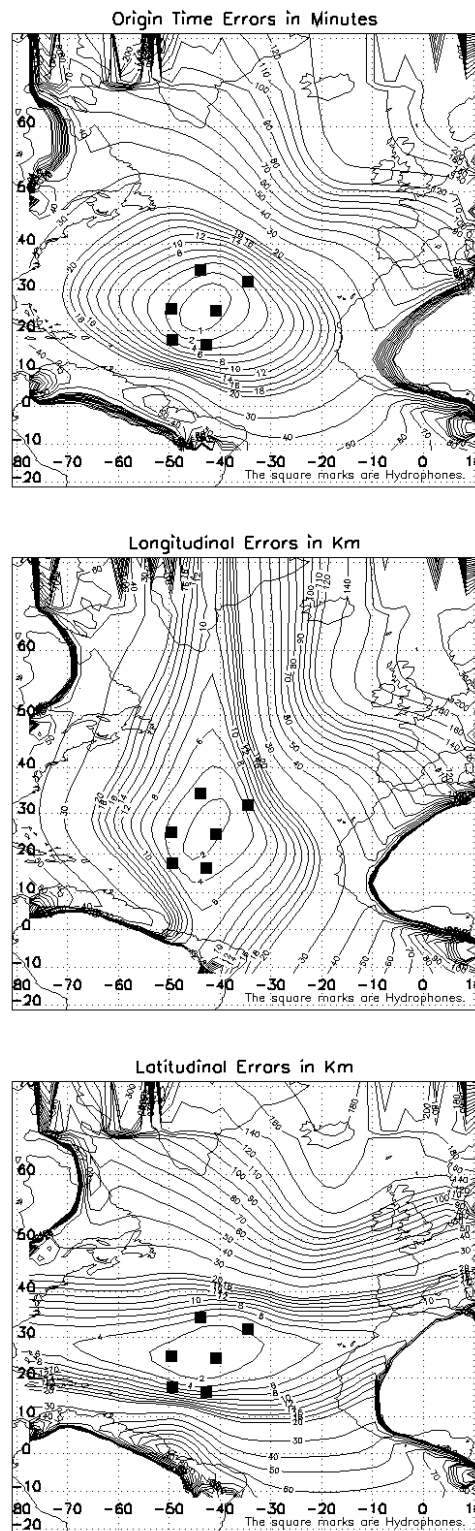


Figure 4.1: Predicted error fields represented as contours for the northern Atlantic Ocean, south of the Azores array, based on a calibrated Monte Carlos simulation: Predicted error in origin time (in seconds); Predicted error in longitude (in kilometers); Predicted error in latitude (in kilometers) (courtesy of Andy Lau (2008)). Squares represent hydrophones.

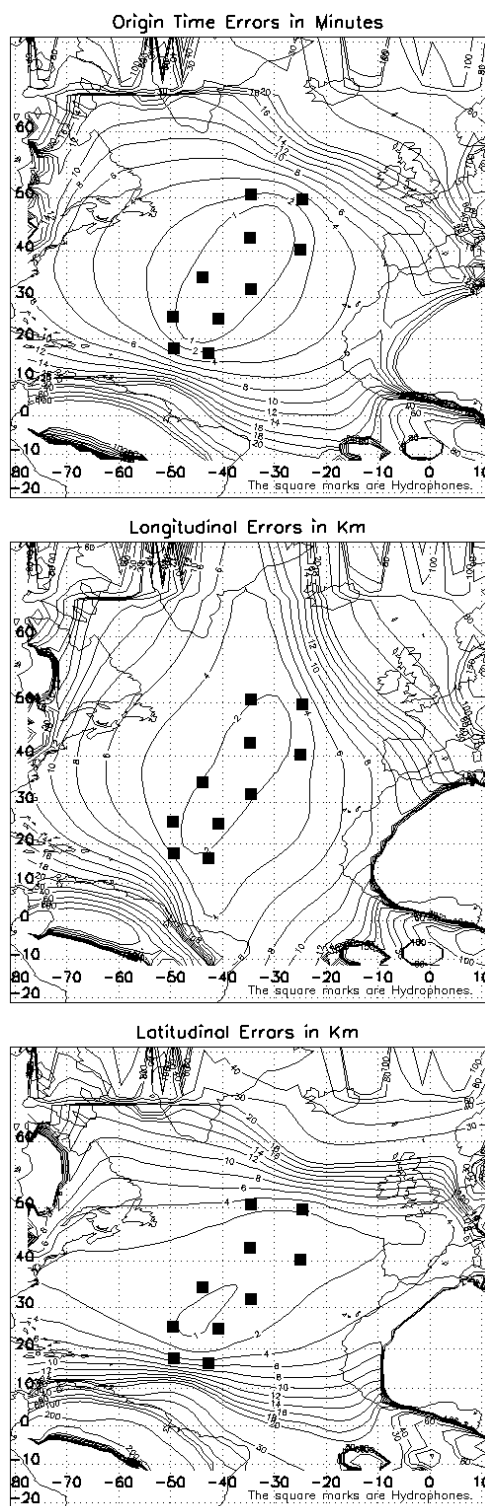


Figure 4.2: Predicted error fields represented as contours for the northern Atlantic Ocean, south of the Azores array + north Azores array (SIRENA), based on a calibrated Monte Carlo simulation: Predicted error in origin time (in seconds); Predicted error in longitude (in kilometers); Predicted error in latitude (in kilometers) (courtesy of Andy Lau (2008)). Squares represent hydrophones.

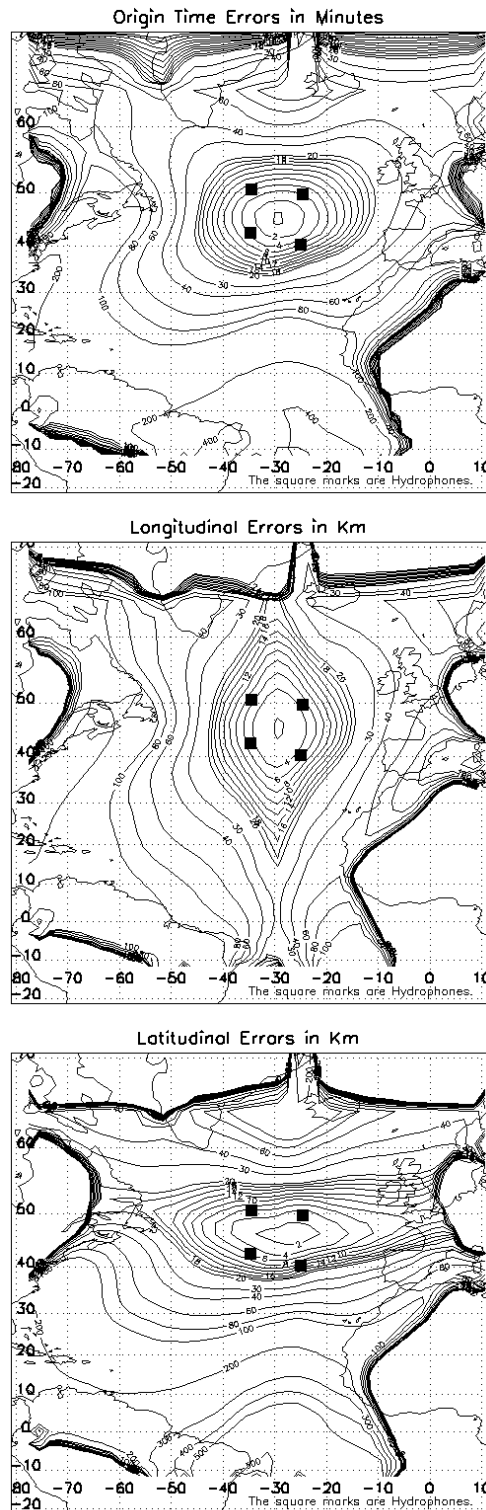


Figure 4.3: Predicted error fields represented as contours for the northern Atlantic Ocean, north of the Azores (SIRENA) array, based on a calibrated Monte Carlo simulation: Predicted error in origin time (in seconds); Predicted error in longitude (in kilometers); Predicted error in latitude (in kilometers) (courtesy of Andy Lau (2008)). Squares represent hydrophones.

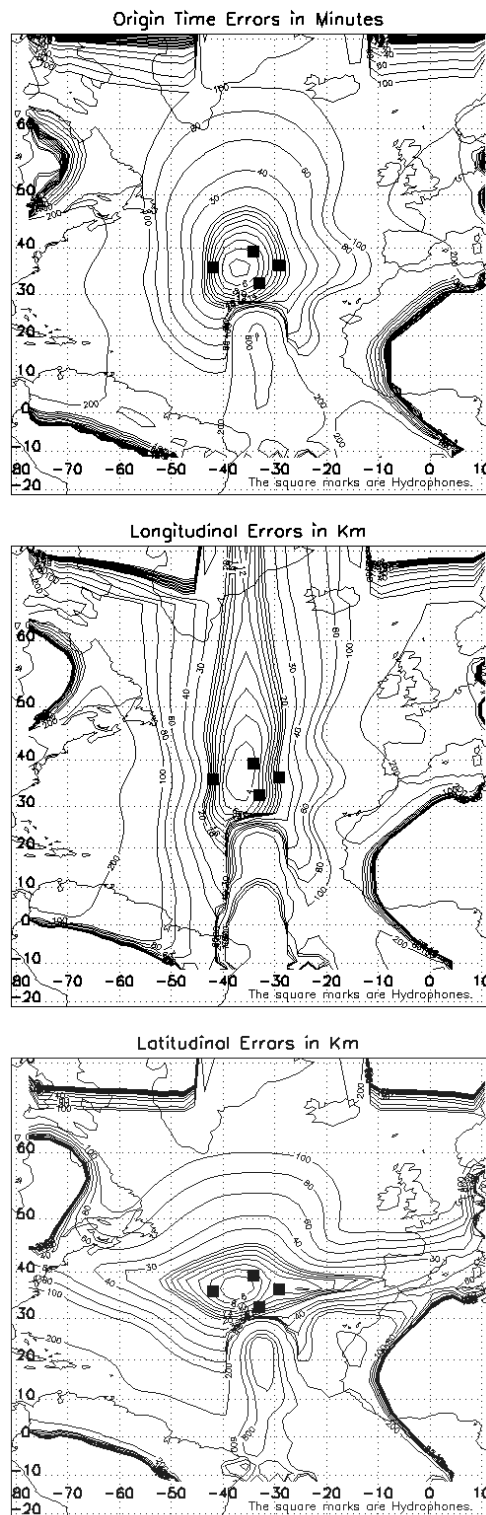


Figure 4.4: Predicted error fields represented as contours for the northern Atlantic Ocean, Azores plateau (MARCHE) array, based on a calibrated Monte Carlos simulation: Predicted error in origin time (in seconds); Predicted error in longitude (in kilometers); Predicted error in latitude (in kilometers) (courtesy of Andy Lau (2008)). Squares represent hydrophones.

4.3 MAR AuH Data

In total from February 1999 until August 2007 nearly 15000 events were located in the northern part of the MAR. They occurred in a region delimited by the Marathon Fracture Zone near 12°N, the Charlie Gibbs Fracture zone near 54°N and a cross section region delimited by the magnetic anomaly 3A (5.69 Myr).

4.3.1 Time Distance Plots

An examination of the error fields from the simulations enabled a region to be chosen for the AuH catalogue that extends from 12°N to 54°N. Along this broad region the MAR is the boundary between the tectonic plates of South America (SA) and Nubia (NU) until it reaches 14°N, the region suspected as the location of the North America (NA) - SA - NU triple junction (*Escartin et al.*, 2003b). North of the 14.3°N triple junction (14.3°N TJ), the MAR divides the NA and NU plates until it reaches the Azores triple junction (ATJ) (*Luis et al.*, 1994), where Nubia, NA and the Eurasia (EA) tectonic plates meet. North of the Azores Triple Junction, the MAR borders the NA and the EA tectonic plates. Great-arc distances were then computed between the events locations and an origin defined at the Azores triple-junction. The tectonic rotation poles between the different plates were used as centers of the great arcs. Three rotation poles were used (*Sella et al.*, 2002): the EA - NA rotation pole for great arcs north of the ATJ (38.9°N); the NA - NU rotation pole for great arcs between 14.3°N and 38.9°N; and the Nubia - SA rotation pole for great arcs south of the 14.3°N. For these southern events the great arc distances of the events were summed to the great arc between the two triple junctions. The equations below were the ones used to compute great-arc distances from the earthquake to the triple junction (Figure 4.5) :

$$d(km) = 111.19 \times \arccos(\Delta - \delta) \quad (4.1)$$

$$\Delta - \delta = \sin \lambda_p (\sin \lambda_t - \sin \lambda) + \cos \lambda_p (\cos \lambda_t \cos(\phi_t - \phi_p) - \cos \lambda \cos(\phi - \phi_p)) \quad (4.2)$$

This expression was then used to convert the latitude/longitude of all events in the AuH catalog into a distance from the ATJ (Figure 4.6). The conversion of the latitude/longitude pair into great arc distances was also conducted for events recorded by land based stations in the same region of the MAR, between 1964 to the end of 2008. The ISC web site was used to retrieve this data. A land-based catalog was created, carefully avoiding those earthquakes recorded by local

seismic networks place on the Azores islands. This meant that only events recorded by the ISC, IDC and NEIC agencies were used (Figure 4.7).

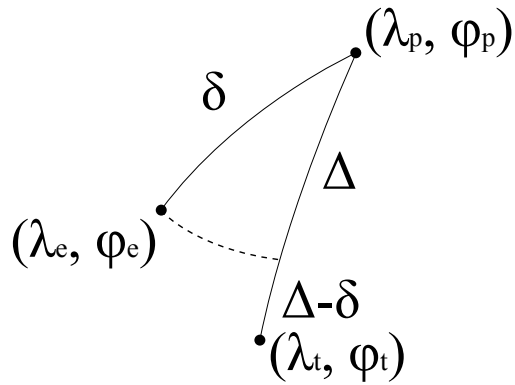


Figure 4.5: Great arc distance. Δ is the great arc distance between the pole with latitude λ_p and longitude ϕ_p and the triple junction with latitude λ_t and longitude ϕ_t . δ is the great arc distance between the pole and the event with latitude λ_e and longitude ϕ_e . $\Delta - \delta$ is the great arc distance between the event and the triple junction.

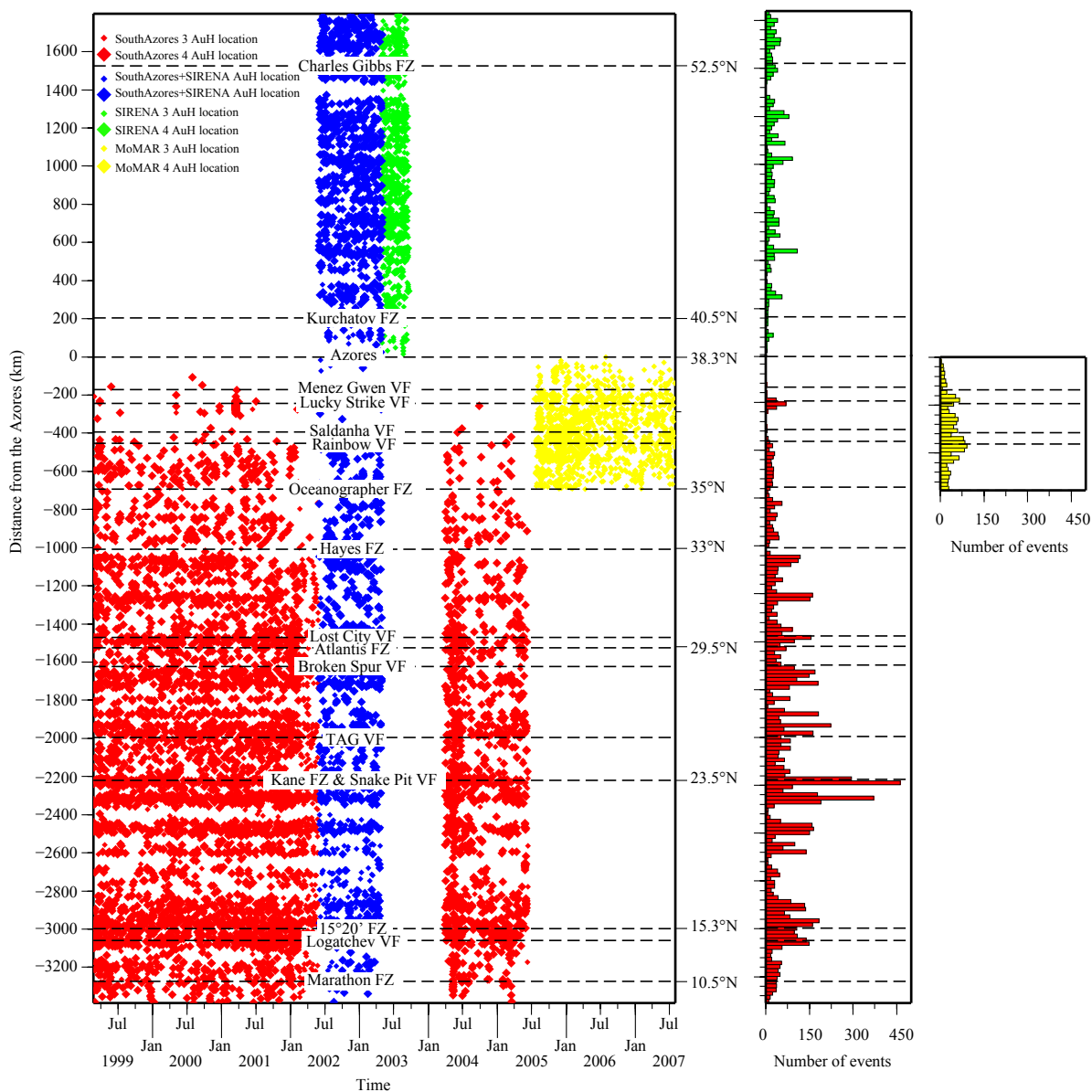


Figure 4.6: Time Distance plot of all AuH recorded seismicity for the MAR. Histograms are separated by MAR AuH seismicity recorded south of the Azores, MAR AuH seismicity recorded north of the Azores and MoMAR AuH array recorded seismicity. The gap occurred between May 2003 to May 2004, south of the Azores, is the result of AuH technical problems along that deployment. Histogram bins of 20 km.

Distance from Azores – time distribution of events

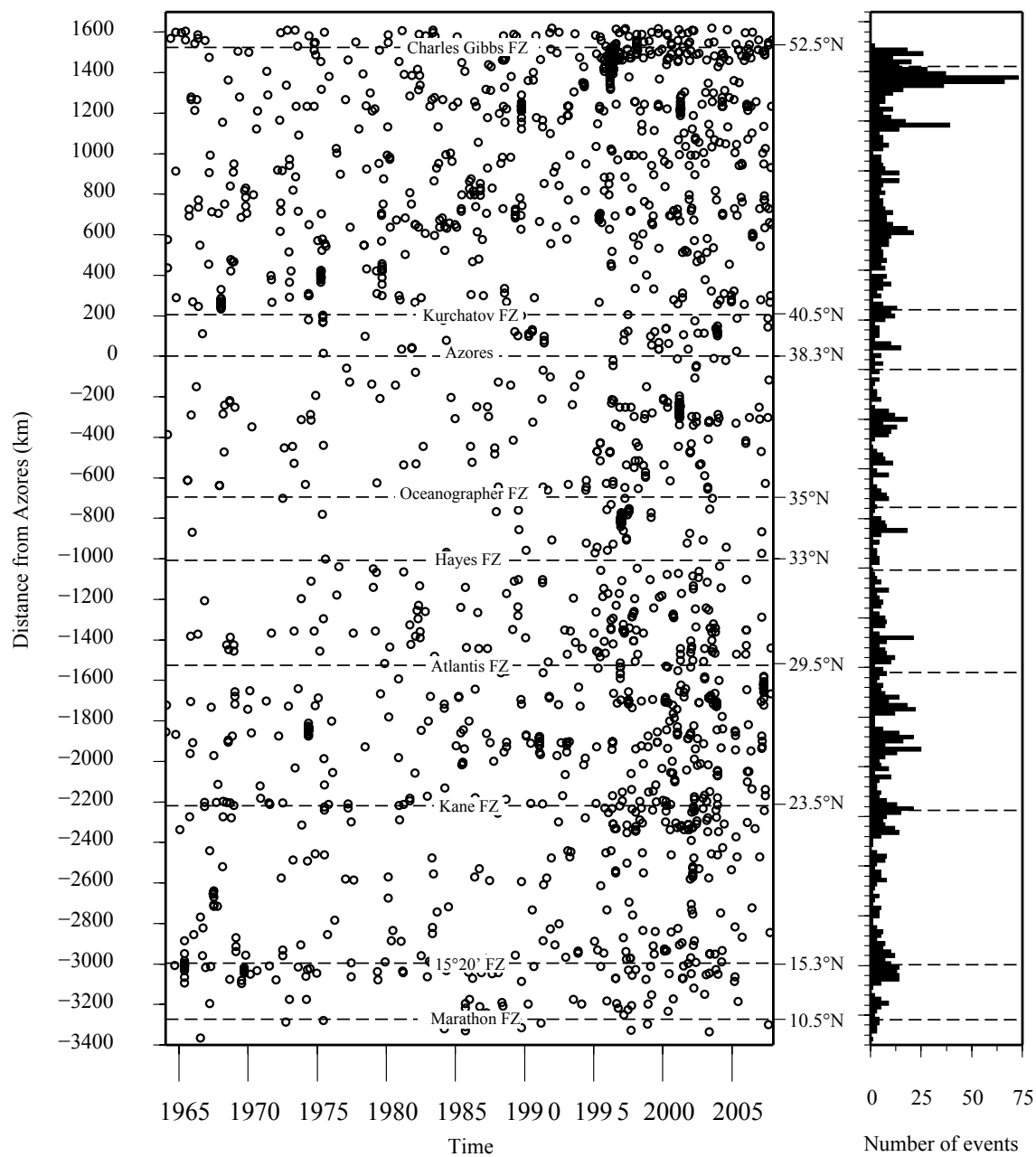


Figure 4.7: Time Distance plot of all Teleseismic recorded seismicity for the MAR from 1964 - the present and its histogram. Histogram bins of 20 km.

4.3.2 Detection thresholds analysis

To evaluate the detection threshold of the land based catalog, the Gutenberg-Richter Law (*Gutenberg and Richter, 1944*) was used:

$$\log(n) = a + bM_c \quad (4.3)$$

The magnitude of completeness M_c is the minimum magnitude for which we consider that the catalog is complete. n is the number of events with magnitude bigger than the magnitude of completeness M_c . b is representative of the size-frequency relationship and a is dependent from the total number of events. To resolve the equation, the entire magnitude range maximum likelihood method was used (*Woessner and Wiemer, 2005*). Uncertainties in M_c and b were estimated using a bootstrap approach (*Schorlemmer et al., 2003*). The analysis of the time variation of M_c shows that from 1964 until the beginning of the 1990s, M_c varies between 3.8 to 4. Following this period and up until the present, M_c became smaller with a value around 3.2.

The much higher number of events recorded by the AUH facilitates the observation of variations in the detection threshold across space and time. This can then be used as a measure of quality and homogeneity for the AuH catalogue, using the T -phase variation of the Gutenberg-Richter Law (*Bohnenstiehl et al., 2002*):

$$\log(n) = a_t + b_tSL_c \quad (4.4)$$

The AuHs record the acoustic energy of the T -phases converted at the seafloor. So SL_c , b_t and a_t are functions of the seismic phase conversion into T -phases and its propagation along the water column. The SL_c temporal and spatial variation was computed on blocks of 500 km by cruise turnover times. This resolution was chosen so that enough events were used to make the SL_c meaningful and also to illustrate how SL_c changes between turnovers (Figure 4.8).

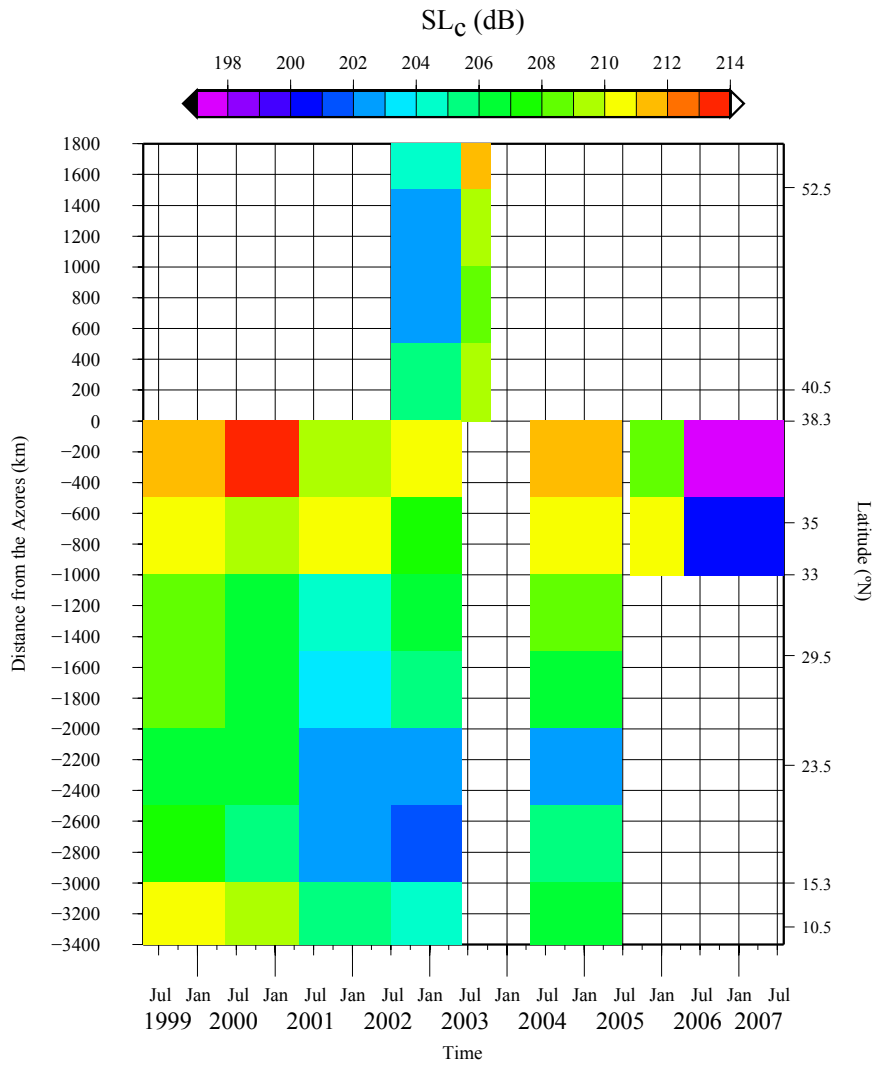


Figure 4.8: Time Distance plot of the SL_c . SL_c is the Source Level of Completeness. 500 km spatial binning. Temporal bins are array hydrophones deployment and retrievals.

4.3.3 Mean error as a function of number of stations

Time distance plots were also used to illustrate the ratio of events recorded by four or more hydrophones and the mean location error, although 100 km blocks were used instead (Figure 4.9). A measure of variability in location quality is important when using the AuH, because the ability to accurately produce locations and determine Source Levels is strongly influenced by the number of hydrophones (*Dziak, 2001; Pan and Dziawonski, 2005*). The number of hydrophones deployed/working varied during the AuH experiment in the MAR (Figure 4.10). For example in the 1999-2005 south AuH array, 6 hydrophones were moored and typically functioned as a 6-instrument array. In the 2002-2003 north Azores experiment (called SIRENA), however, 6 hydrophones were moored but only 4 were recovered and processed. In the MoMAR region the array called MARCHE consisted of 4 hydrophones that were moored and recovered in the first turnover, although only 3 were recovered in the second deployment.

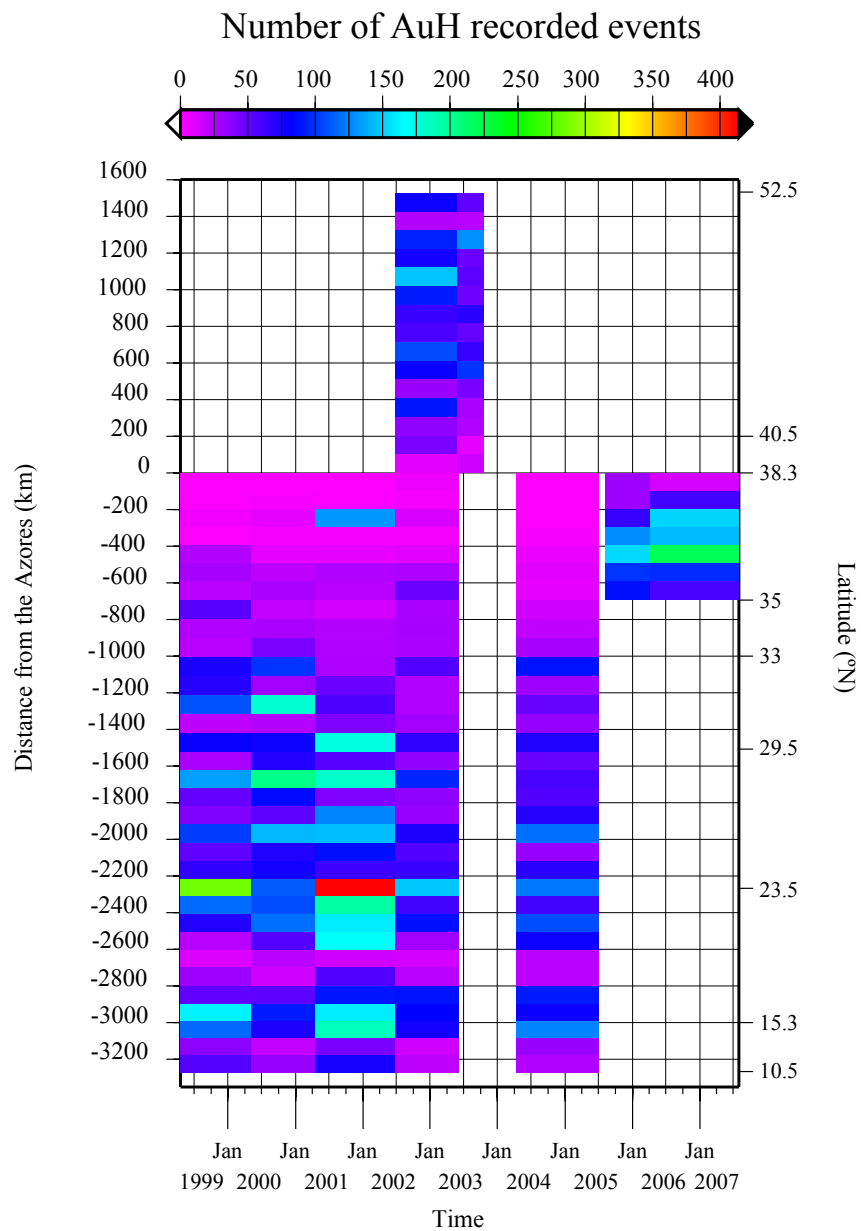


Figure 4.9: Time distance plot of the number of events in a spatial grid of 100 km along the MAR by a temporal grid of AuH array service duration.

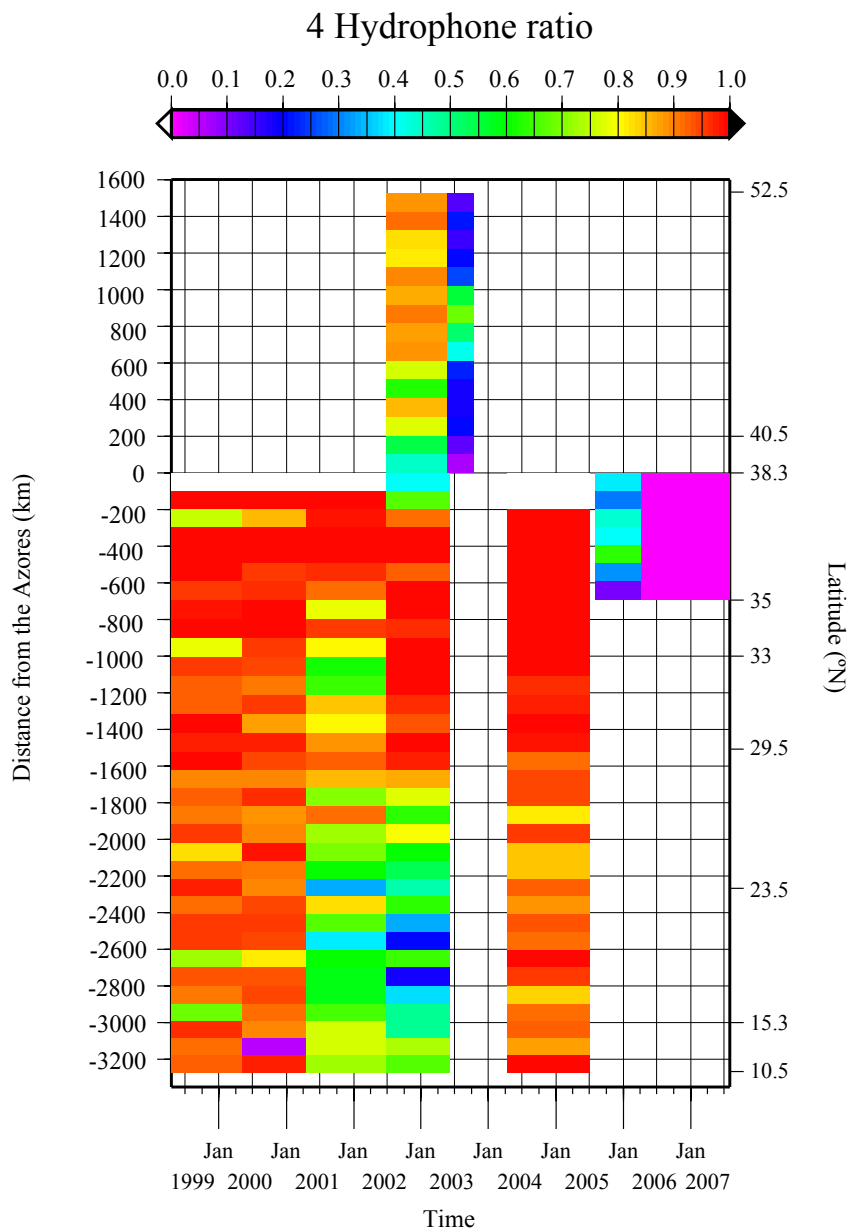


Figure 4.10: Time distance plot of the ratio of events recorded by 4 or more hydrophones in a spatial grid of 100 km along the MAR by a temporal grid of AuH array service duration.

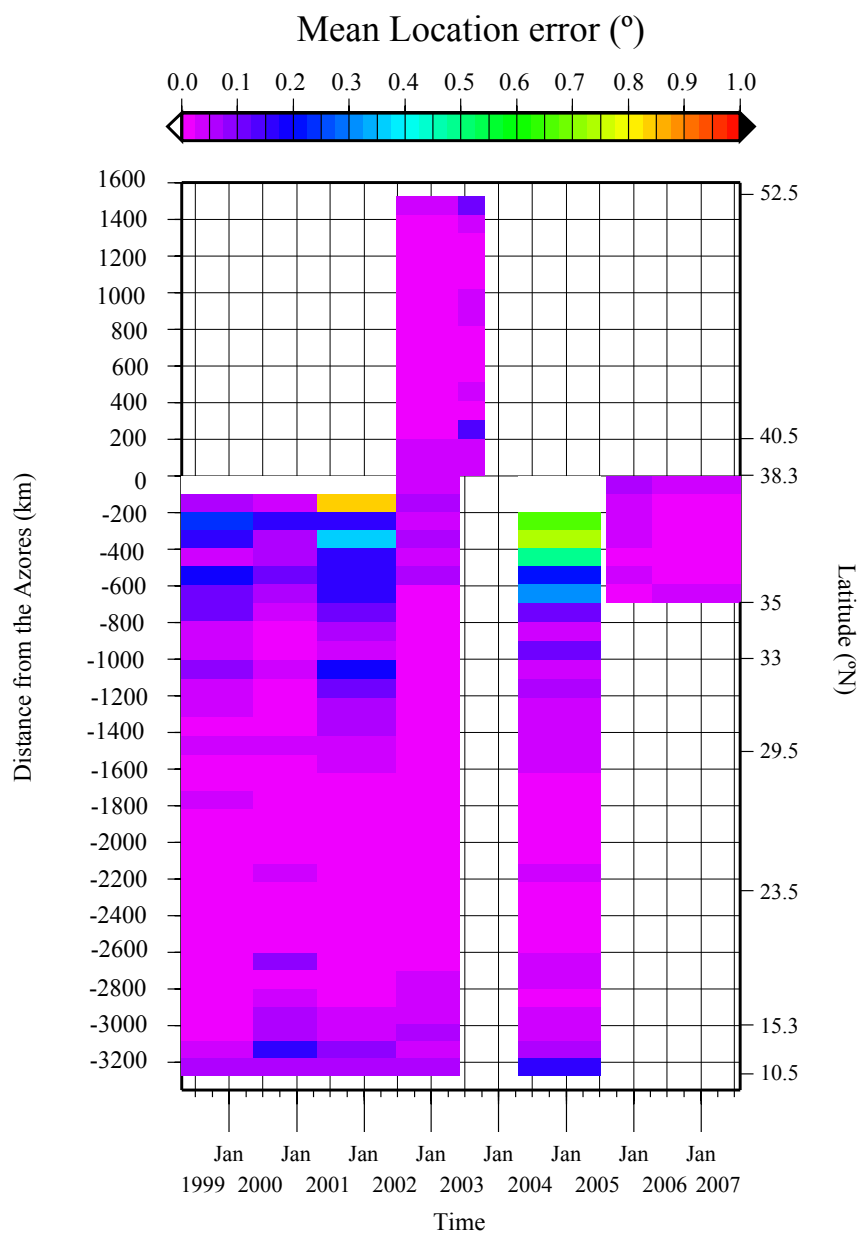


Figure 4.11: Time distance plot of the mean location error of events. Location error is based on the mean of both longitude and latitude location errors for one event. The Mean location error is then the mean of all event location errors in a spatial grid of 100 km along the MAR by a temporal grid of AuH array service duration.

4.4 Mantle Bouguer Anomaly

The Mantle Bouguer Anomaly is often used to characterize the sub-seafloor density structure and/or crustal thickness. It consists in subtracting the effects of the water crust interface and the effect of a constant thickness crustal layer below the bathymetry from the gravity anomaly (*Kuo and Forsyth, 1988*). The influence of the Azores on the MAR's MBA has already been observed and discussed by several authors (*Cannat et al., 1999; Detrick et al., 1995; Maia et al., 2007; Lin et al., 1990; Thibaud et al., 1998*). It consists of a trend of wavelength larger than 100 km, with larger positive to negative MBA values as the ridge approaches the Azores. The MBA narrower wavelength component can also be used to map local (segment scale) crustal density/thickness variations (*Detrick et al., 1995; Maia et al., 2007; Lin et al., 1990; Thibaud et al., 1998*). The Mantle Bouguer Anomaly (MBA) was then estimated along the MAR from 12°N to 54°N. The MBA was calculated using the multilayer (*Maia and Arkani-Hamed, 2002*) method, where the gravity effect of the bathymetry is estimated using constant thickness layers (Appendix A Figure 1). Crustal thickness is assumed to be 6 km and crustal and mantle densities is assumed to be 2800kg/m^3 and 3300kg/m^3 respectively (*Kuo and Forsyth, 1988*). 250 m resolution bathymetric grids of *Goslin et al. (1999)* between 40° – 45°N, *Thibaud et al. (1998)* between 15° – 40°N and *Smith et al. (2006)* between 11° – 15°N were compiled into a 1 km resolution grid and merged together with a 2 minute resolution satellite bathymetry grid (?). The final bathymetric grid was then subtracted from the marine gravity anomaly grid (*Sandwell and Smith, 1997*).

4.5 Analysis of the seismicity

The AuH arrays detected seismicity in the MAR along a range of ~ 5000 km. In this region, the MAR exhibits major features, such as the Fracture Zones and the Azores plateau. Smaller features are also found at segment scale, dependent of the type of spreading, volcanic activity and hydrothermal circulation. All of these features influence seismicity rates at different scales and at different earthquake magnitudes. At larger scale, the Azores hot spot should be the major regional influence in the MAR seismicity, as it is also the major influence in the Mantle Bouguer Anomaly and in the broad depth variation. Other major influences that can affect seismicity rates are the variability in ridge spreading rate across the ~ 5000 km MAR region bordering the four tectonic plates and the variation in the MAR's orientation (obliquity). Despite this, as was discussed earlier, AuH seismicity rates can be influenced by the AuH detection threshold variations along the MAR.

Aside from the seismic stripes and gaps described in *Smith et al.* (2003), which are associated to the modes of spreading and faulting in the MAR (*Escartin et al.*, 2008; *Smith et al.*, 2006) (Figure 4.6), there is a large seismic gap that seems to extend at least 500 km south of the Azores. This seismic gap existed only when the south Azores array was active and disappeared when the hydrophones were moved north to the MoMAR region. The large variation in seismicity rates for the regions between the Oceanographer Fracture Zone and the Azores, indicates that it is most likely that the seismic gap and the high level of seismicity were caused by different degrees of coverage in different periods of time.

The time distance plots (Figure 4.11) reveal that the south Azores array locations have higher location errors for this region, reflecting the increased difficulty for the operator to identify and associate signals so that the software can compute the locations. For the south Azores array the detection threshold SL_c is higher for the region south of the Azores. This difference can go to a maximum value of ~ 15 dB on the ~ 190 to ~ 240 dB T-phase scale range of energy. This difference can produce a dramatic outcome of many more detected events.

There is a clear connection between the completeness and the number of hydrophones in the array (Figures 4.8 and 4.11). It is obvious that there is a smaller completeness found in those regions where a higher percentage of events were recorded by only three hydrophones. This may be explained by the way the Source Level is computed by the localization software (*Dziak*, 2001; *Fox et al.*, 2001). Source Level is the mean value of all the source levels computed by each hydrophone. For example in the MoMAR array the SL_c strong variation between the two service cruises is caused by the fact that during the first deployment period the array functioned as a four hydrophone array, and that during the second deployment it was reduced to a three hydrophone array. Both hydrophone specifications and deployment location remained the same in these two cases.

Another way to evaluate broad wavelength patterns on the AuH catalog is to compare the patterns of seismicity recorded by the AuH with the seismic patterns present on land based seismic networks. To achieve this both catalogs were declustered. This meant that only the background seismicity, not connected to major seismic sequences that are limited in time, representative of a more permanent seismic regime were compared. If this is accepted as true, it is then possible to compare the different temporal recordings of the various arrays deployed in the MAR during the ~ 9 year AuH experiment and then compare them to the ~ 40 year span ISC catalog obtained for the MAR.

4.5.1 Cluster analysis

The Single Link Cluster technique of *Frohlich and Davis* (1990) and *Davis and Frohlich* (1991) was employed to identify discrete time and space clusters of seismic activity within the extensive MAR AuH and teleseismic earthquake catalogs. The process consists of linking individual events to its nearest neighbor using the metric $D = \sqrt{d^2 + bt^2}$ to form sub-groups. The d is the distance in kilometers between two events, t is the time in decimal days between two events and b is equal to 0 or 1 km/days (to include or not the temporal part). In this case the temporal part was used. This association process continues by linking each sub-group to its nearest neighbor sub-group, recursively, until the last link equals the number of events in the catalog, minus one. *Nyffenegger and Frohlich* (2000) defined the optimal D producing the best score for separating the different clusters $D_{best} = 0.8\bar{D}$, where \bar{D} is the median link of all links computed. Median links for the different AuH array configurations are represented in Table 4.1. The analysis was made for events with a Source Level bigger or equal to the completeness level and for events recorded by at least 4 hydrophones. The clusters were then dissociated from the catalog. The result is a declustered catalog that can be associated to the background seismicity.

Table 4.1: Single Link Cluster resulting D_{best} that separates clustered events from the declustered ones for different AuH array configurations.

AuH array configuration	D_{best} (km)
South Azores	10.950
South Azores + SIRENA	13.546
SIRENA	18.714
South Azores	15.948
MARCHE	13.547

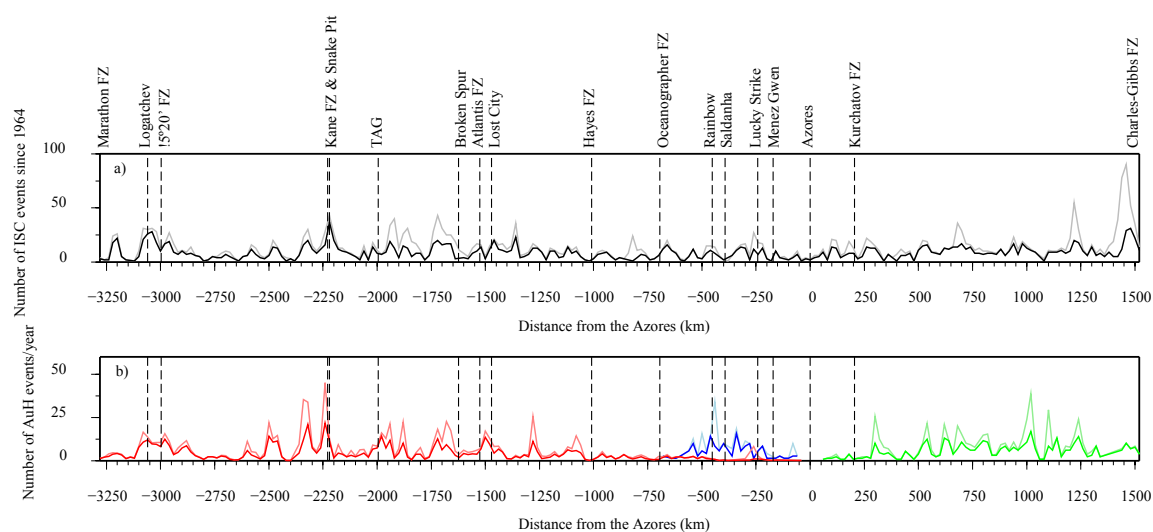


Figure 4.12: a) MAR's teleseismically recorded seismicity since 1964 profiles obtained from the ISC web site. Black profile is the declustered catalog profile. Light black profile is the full catalog. b) MAR's AuH recorded seismicity since 1999. Red profile represents the declustered South Azores AuH array catalog. Light red profile represents the full South Azores AuH array catalog. Green profile is the declustered SIRENA array catalog. Light green profile is the full SIRENA array catalogue. Blue profile represents the declustered MARCHE array catalog. Light blue profile is the full MARCHE array catalog.

Differences between the full catalogs and declustered catalogs show for the teleseismic catalog that the ridge that neighbors the Charles-Gibbs FZ accounts for a large part of its activity as seismic clusters (Figure 4.12). This is not the case for the AuH, meaning that during the almost one year period of acquisition of SIRENA no major seismic clusters were recorded. SIRENA recorded major seismic sequences on the Reykjanes Ridge north of the Charles Gibbs FZ (*Goslin et al.*, 2005) but none in the surroundings of the fracture zone. Between the Atlantis FZ and the Kane FZ the difference between the full catalog and the declustered catalog reveal a good accordance between the AuH recorded seismicity and the teleseismically recorded seismicity. Some peaks of seismically clustered activity recorded by the AuH arrays are not found in the teleseismic data. This is mostly due to the fact that seismic crises in those regions can occur below the detection threshold of land based seismometer arrays.

Visual inspection of both the AuH and teleseismically recorded seismicity declustered profiles reveal a remarkable similarity. This reveals that the continuous seismicity signature of the MAR recorded in the 40 year catalog obtained from the ISC web site, is very well represented by the much smaller time span acquisition of the AuH arrays. This implies that it is possible to infer with only a few deployments of temporally limited AuH arrays across different time periods (SIRENA array deployment lasted slightly more than one year) these continuous rates of seismic background activity on different sections of the MAR. It is also possible to observe that both the AuH and teleseismic arrays observed the same patterns of background seismic activity despite the different detection thresholds between the two (AuH arrays have a much lower detection threshold than land based arrays for these sections of the MAR).

4.5.2 Analysis of the seismicity at broad wavelength

Following on from this process, the next step was to obtain profiles along the MAR of the MBA and of the distribution of the seismicity recorded both by the AuH and the land based networks. The AuH final declustered seismicity profile is the result of the normalization of the three different arrays (by year) to obtain a distance to earthquake per year profile. MBA and seismicity profiles were then filtered using a Gaussian filter with widths varying between 100 and 300 km. The resulted profiles for 200 km are represented in Figure 4.13.

The Spearman rank correlation was used to measure the association between these three profiles, with correlation coefficient and respective correlation confidence level. Spearman's rank correlation coefficient is a type of correlation coefficient that represents the relationship between two variables that are measured on the same interval or ratio scale. The two sets of variables are ranked separately and the differences in rank, d , are calculated for each pair of variables. The

equation is:

$$r = 1 - 6 \frac{\sum_{i=1}^n d_i^2}{n^3 - n} \quad (4.5)$$

where n is the number of paired variables (*Bevington and Robinson, 2003; Press et al., 1996*). The spearman rank correlation coefficient r must be read as having low correlation for r inferior to 0.3. For r in between 0.3 and 0.5 it is considered as having a moderate correlation factor. For r equal or bigger than 0.5 the correlation between profiles is considered high.

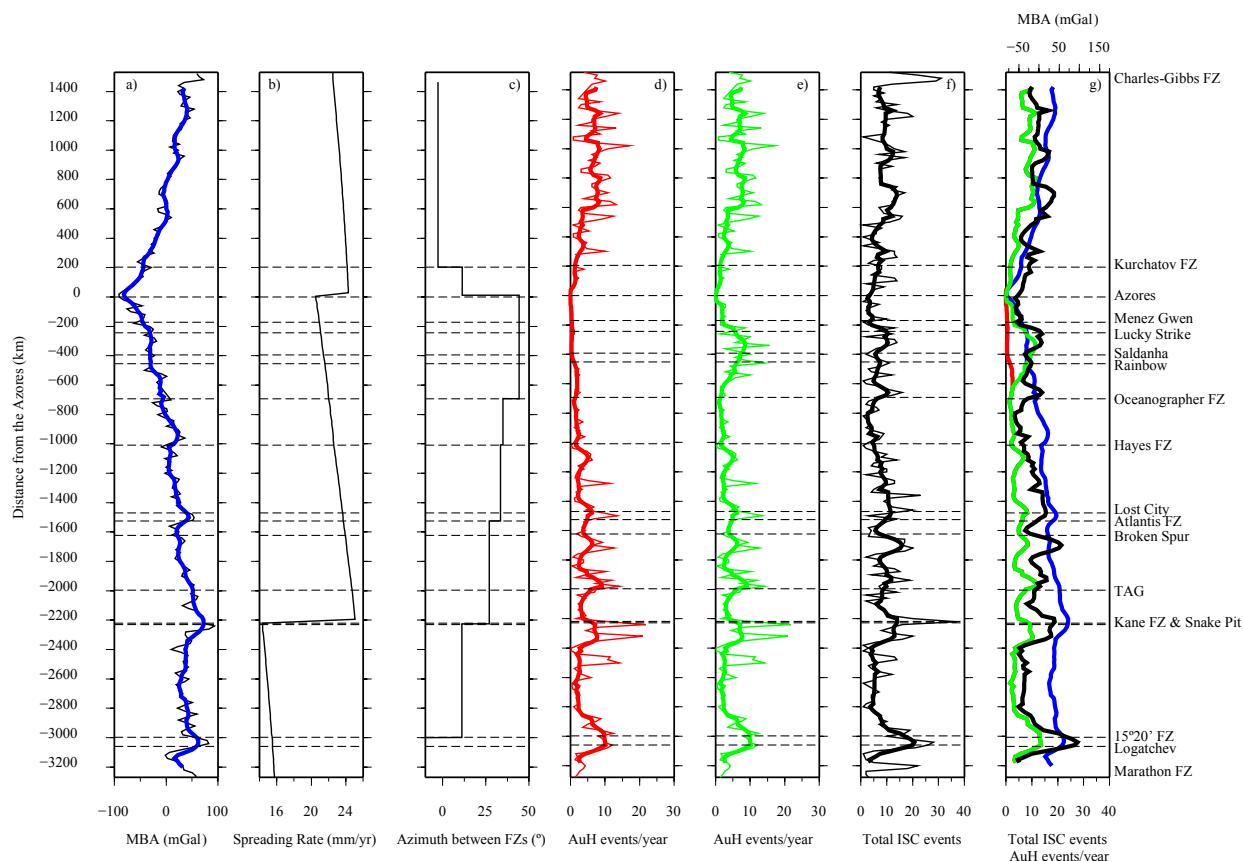


Figure 4.13: From left to right: a) Along axis MAR's MBA profile. Blue line is the MBA profile filtered with a Gaussian filter with a 200 km width. b) Along axis MAR's spreading rate following the Nuvel 1 model (*DeMets et al.*, 1990). c) Azimuth between two points at the extremities of the MAR's mega segments delimited by the Fracture Zones. d) and e) AuH recorded events per year. The differences are: e) MARCHE array data used for the region between the Oceanographer FZ and the Azores; d) used data from the South Azores array for the region between the Oceanographer FZ and the Azores. Red and green lines are the filtered profiles of the AuH seismicity using a 200 km path Gaussian filter. f) Teleseismically recorded events in the last ~ 40 years with its 200 km path Gaussian filtered profile represented by the fat black line. g) Joint representation of all the filtered profiles.

The two types of seismic catalogs both revealed that the MAR's most active regions are located around fracture zones (Figure 4.13 d, e and f). Profiles show that Charlie Gibbs FZ, Kane FZ and the 15°20'N FZ are the three most active regions in this part of the MAR. Kurchatov FZ and Atlantis FZ are also active, although Oceanographer FZ and Hayes FZ are almost seismically inactive, which has already been noticed by *Smith et al.* (2003). Generally high rates of seismicity nearby fracture zones are within the segments part of the ridge neighboring the fracture zone and mostly localized at the inside corner part of the segments. In this way the nearby fracture zone segments' inside corners are more active than its counterpart, the outside corners. But this rule doesn't apply everywhere as shown by *Smith et al.* (2003).

Table 4.2: Spearman Rank correlation between MAR's ISC and AuH declustered seismicity profiles and MBA profile for wavelengths varying from 100 to 300 km. AuH1 profile takes into account South Azores and SIRENA arrays. AuH2 profile takes into account South Azores, SIRENA and MARCHE arrays. The seismicity between the Oceanographer Fracture Zone and the Azores recorded by the MARCHE array.

Profiles	100 (km)	150 (km)	200 (km)	250 (km)	300 (km)	Level of correlation
ISC & AUH1	0.4	0.4	0.5	0.5	0.5	medium to strong
ISC & AUH2	0.6	0.7	0.7	0.7	0.7	strong
ISC & MBA	0.3	0.3	0.4	0.4	0.4	weak to medium
AUH1 & MBA	0.6	0.6	0.6	0.6	0.6	strong
AUH2 & MBA	0.4	0.4	0.4	0.4	0.4	medium

The teleseismically recorded seismicity between the Oceanographer FZ and the Azores does not show any of the dramatic variations in seismicity rates that were observed by the two AuH arrays deployed during different time periods. On top of that the AuH2 profile using data from MARCHE for the region between the Azores and the Oceanographer FZ correlates best (Table 4.2) with ISC than the AuH1 that uses the South Azores data (Figure 4.13 d, e, f and g). This can be used as an additional argument to the coverage problems that were referred above.

Table 4.3: Spearman Rank correlation between MAR's ISC and AuH declustered seismicity profiles and MBA profile for wavelengths varying from 100 to 300 km. Profiles of seismicity and MBA north of the Azores

Profiles	100 (km)	150 (km)	200 (km)	250 (km)	300 (km)	Level of correlation
ISC & AUH	0.6	0.6	0.7	0.7	0.8	strong
ISC & MBA	0.5	0.5	0.5	0.5	0.6	medium to strong
AUH & MBA	0.6	0.6	0.7	0.7	0.7	strong

Due to these coverage problems, Spearman rank analysis was conducted three times. Firstly for the profile that extends along the entirety of the MAR from Marathon FZ to the Charlie Gibbs FZ. The remaining analyses were conducted for smaller profiles that extend from Charlie Gibbs

to the Azores and from the Oceanographer FZ to the Marathon FZ, excluding the problematic region. All profile correlations have p values less than to 0.005, meaning that they are all inside the 99.95% confidence level.

The visual inspection and Spearman Rank analysis of the seismicity and MBA profiles show that MAR's seismicity levels around the Azores ($\pm 200\text{km}$) are very low both for the AuH and ISC, mimicking the same influence that the Azores hotspot has on the MBA. The influence on this region of the MAR is revealed by its morphology, that presents a very shallow and narrow axial valley (Cannat *et al.*, 1999; Detrick *et al.*, 1995; Thibaud *et al.*, 1998). This is a result of the influence the Azores has on the rheology of the nearby ridge. This then seems to provoke a clear decrease in seismicity rates. North of the Azores the correlation between seismicity rates and MBA is strong (Table 4.3) revealing that the MAR's seismicity is influenced by the processes occurring deep below in the lower crust and upper mantle and its thermal influence on the ridge's morphology and rheology. On the other hand, across the region spanning between 200 km south of the Azores until the Oceanographer FZ this correlation between seismicity and MBA is much weaker (Figure 4.13 g and Table 4.2). South of the Oceanographer FZ the correlation between the MBA and seismicity rates returns strongly (Figure 4.13 g and Table 4.4). The sector between the Oceanographer FZ and the Azores is the most oblique of the north MAR (Figure 4.13 c). The orientation of segments have a large azimuth and the overall azimuth of this sector of the ridge is also large. This creates relatively big offsets between adjacent segments Detrick *et al.* (1995); Thibaud *et al.* (1998) and can create high levels of asymmetric tectonic strain originating high levels of asymmetric spreading and be the main influence in the region's levels of seismic activity.

Table 4.4: Spearman Rank correlation between MAR's ISC and AuH declustered seismicity profiles and MBA profile for wavelengths varying from 100 to 300 km. Profiles of seismicity and MBA south of the Oceanographer Fracture Zone.

Profiles	100 (km)	150 (km)	200 (km)	250 (km)	300 (km)	Level of correlation
ISC & AUH	0.7	0.7	0.8	0.8	0.8	strong
ISC & MBA	0.5	0.5	0.5	0.5	0.5	medium to strong
AUH & MBA	0.6	0.6	0.6	0.6	0.6	strong

4.5.3 Principal Component Analysis of the MAR Seismicity

A Principal Component Analysis method was used to decompose spatio-temporal patterns and to discriminate which regions were most active along the MAR, north of the Oceanographer Fracture Zone. The method involves detecting changes from the mean rate of seismicity and

represents it in a more appropriate way, delineating areas with significant fluctuations (Goltz, 2001).

The first step was to rearrange the input data to use the variance/covariance matrix:

$$C_x = \frac{1}{n-1} \sum_{i=1}^n (x_i - u_x)(x_i - u_x)^t \quad (4.6)$$

to describe the variability of the seismicity rate around u_x , the mean vector of x , where x_i represents the set of earthquake counts for each grid cell at all times. A transformation into a new coordinate system was then made:

$$C_y = TC_xT^t \quad (4.7)$$

where the transformation matrix T is the transposed matrix of eigenvectors ε_i of C_x . C_y is then the diagonal matrix of eigenvalues λ_i of C_x . The eigenvalues of C_x are thus the variances of the transformed variables. To compute T , first one obtains the eigenvalues of C_x by solving:

$$|C_x - \lambda I| = 0 \quad (4.8)$$

where I is the identity matrix and the eigenvectors then result from:

$$(C_x - \lambda I)\varepsilon = 0 \quad (4.9)$$

This is constrained by the fact that T must be orthogonal. The transformed variables are then obtained by doing $y = Tx$. The new variables are called principal components, denoted by C_i with $i = 1, 2, \dots, n$. The time component of this analysis consists of different time period snapshots of one grid cell at different, consecutive time intervals. The resulting principal components will still give spatial information, but C_i will now show, as i increases, increasingly subtle components of temporal change.

This analysis was conducted on the complete SIRENA and MoMAR catalogs, using all events recorded by four or more AuH in the region north of the Oceanographer Fracture Zone up to the Charlie Gibbs Fracture Zone, with Source Levels equal or greater than the SL_c . The region between the Oceanographer Fracture Zone and the Charlie Gibbs Fracture Zone was chosen to make an additional complementary study of the MAR AuH seismicity, in comparison to those studies in the more southern zones (Escartin *et al.*, 2008; Smith *et al.*, 2003). Joint interpretation of seismicity and bathymetry is limited to the region south of $\sim 46.5^\circ\text{N}$ by the lack of high resolution bathymetric grids for the region to the north.

Data were organized spatially on 0.125° grids so that the spatial gridding was inferior or

equal to segment scale. In regards to the temporal organization of the data it was important to take into account that different time interval snapshots of the data would change the variance of the modes of fluctuation of the rate of seismicity. One week time snapshots were chosen because at this time scale it is possible to see the effect of the major earthquakes recorded by international land based stations (Figures 4.14 and 4.15). It appears that all teleseismic recorded earthquakes provoke fluctuations, even if some are of small amplitude on the AuH recorded seismicity. Furthermore, the relationship between magnitude and/or number of teleseismically recorded earthquakes and the fluctuations on the AuH recorded seismicity is not straightforward. Some strong fluctuations on the AuH seismicity are not related to the teleseismically recorded earthquakes. This can be justified by the fact that those fluctuations originated from earthquakes with magnitudes below the detection threshold of the land based stations. Otherwise, the lack of a straightforward relationship between the modes of fluctuation on the AuH seismicity and teleseismic earthquakes is further evidence of the complexity of the seismicity patterns and fault mechanics on the MAR. In addition, the mean Source Level generally doesn't seem to noticeably increase when linked with a fluctuation created by a teleseismically recorded earthquake.

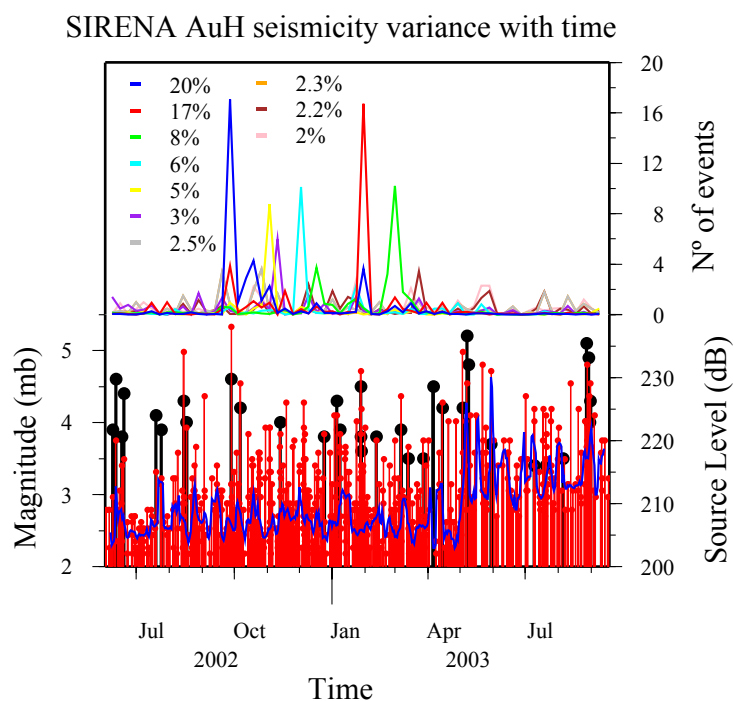


Figure 4.14: SIRENA AuH catalogs Principal Component modes variance with time. Colored lines and diamonds give the number of events and the places on the ridge where fluctuations from the mean level of seismicity (in percentages) occurred. Black bars represent teleseismically recorded magnitudes. Red bars represent AuH recorded Source Level. Blue line is the average Source Level variation.

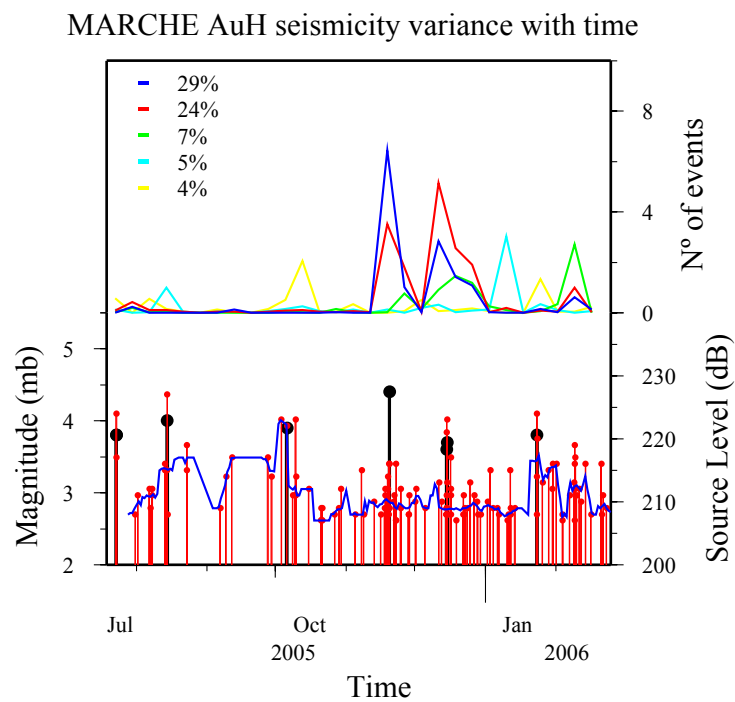


Figure 4.15: MoMAR AuH catalogs Principal Component modes variance with time. Colored lines and diamonds give the number of events and the places on the ridge where fluctuations from the mean level of seismicity (in percentages) occurred. Black bars represent teleseismically recorded magnitudes. Red bars represent AuH recorded Source Level. Blue line is the average Source Level variation.

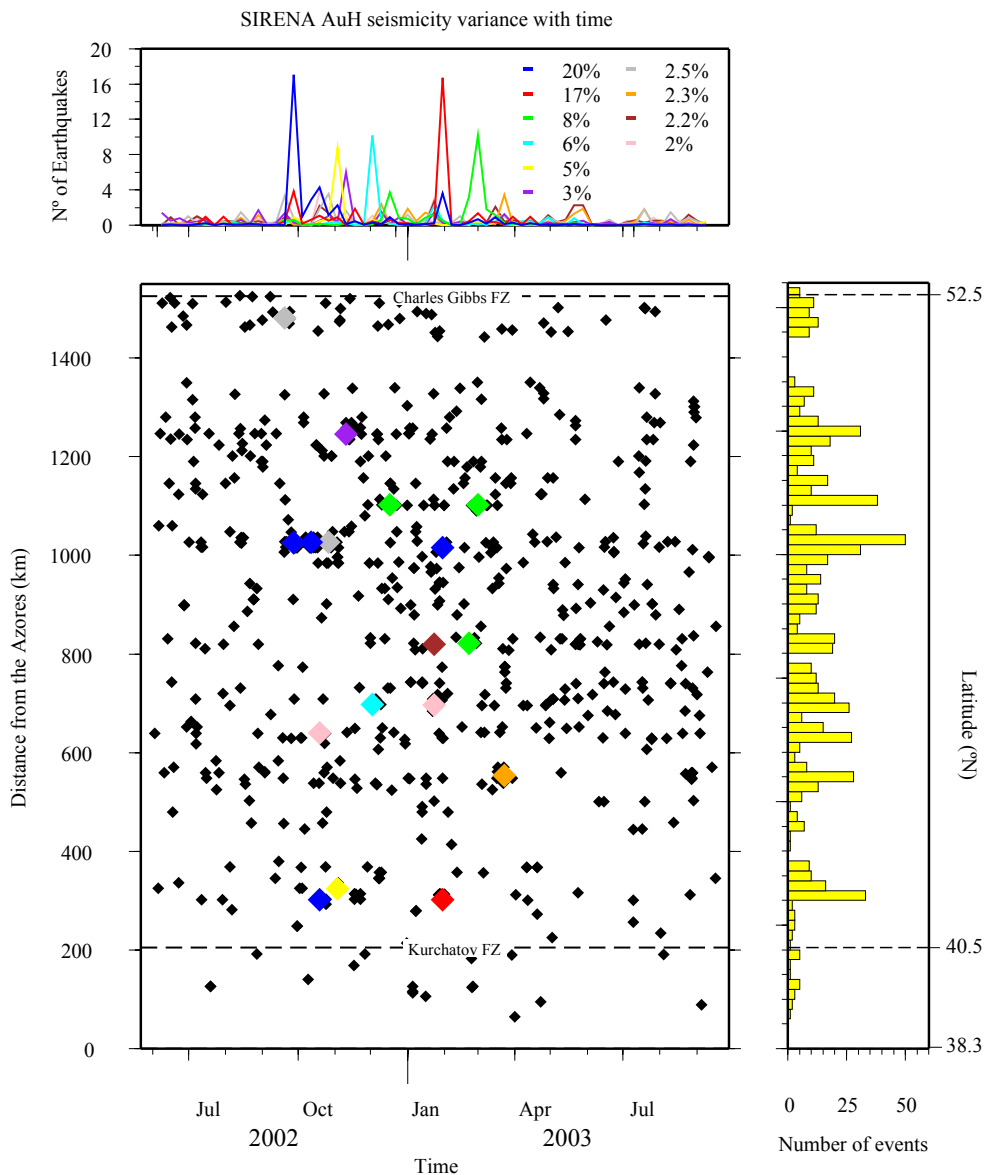


Figure 4.16: Time distance plot of the AuH SIRENA array catalog with its Principal Component analysis. Different modes with different variances are represented by different lines (top) and diamonds (bottom) representing the time and distances from the Azores fluctuations. Histogram (right) bin of 200 km.

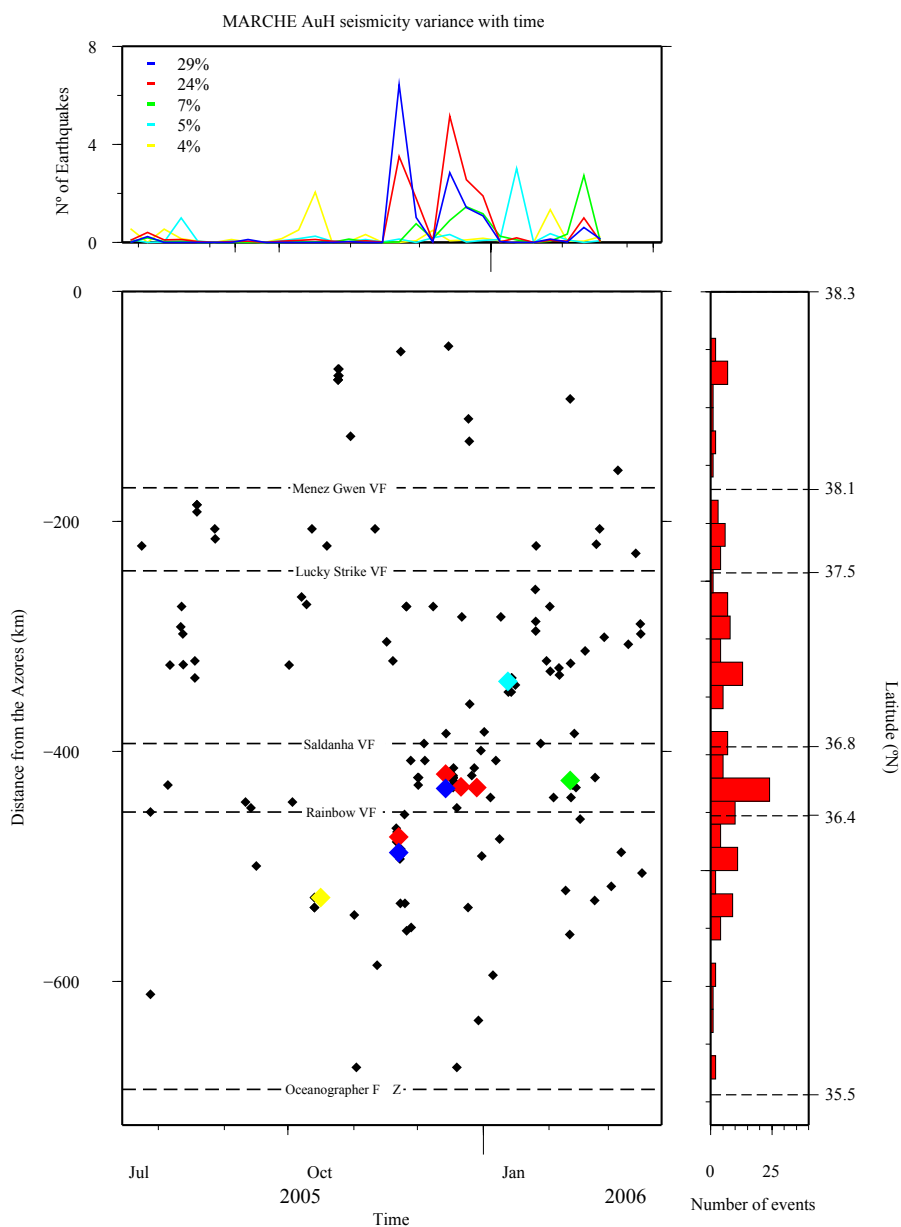


Figure 4.17: Time distance plot of the AuH MARCHE array catalog with its Principal Component analysis. Different modes with different variances are represented by different lines (top) and diamonds (bottom) representing the time and distance of from the Azores fluctuations. Histogram (right) bin of 200 km.

The most active area in the MoMAR region is the sector near $\sim 36.5^\circ\text{N}$ north of the Rainbow vent field (Desbruyeres et al., 2001), where the majority of the seismicity is associated with seismic swarms linked to normal fault teleseismically recorded earthquakes (Figure 4.17 and 4.18) on a segment that shows a strong asymmetric morphology. North of the Azores the area near $\sim 47.6^\circ\text{N}$ ($\sim 1050\text{km}$) spans a high level of seismic activity across the AuH acquisition period (Figure 4.16). Five other areas have high levels of activity. The sections $\sim 41.625^\circ\text{N}$ (~ 300), $\sim 43.75^\circ\text{N}$ (~ 600), $\sim 44.5^\circ\text{N}$ (~ 700) and $\sim 49^\circ\text{N}$ (~ 1300) (Figure 4.16). The areas $\sim 43.75^\circ\text{N}$ and $\sim 44.5^\circ\text{N}$ have a near continuous level of seismic activity that took place during the AuH acquisition. The area $\sim 41.625^\circ\text{N}$ shows a more clustered type of seismicity. The areas with near continuous seismicity also had seismic cluster activity. For these regions seismic cluster represent nearly half of all activity and, in fact, the most active sections of this part of the MAR are the sections where seismic cluster occurs (Figure 4.16). The near continuous type of seismic activity mimics the spatio-temporal stripe distributions observed south of the Oceanographer Fracture Zone (Smith et al., 2003), which were later linked to detachment faults (Escartin et al., 2008).

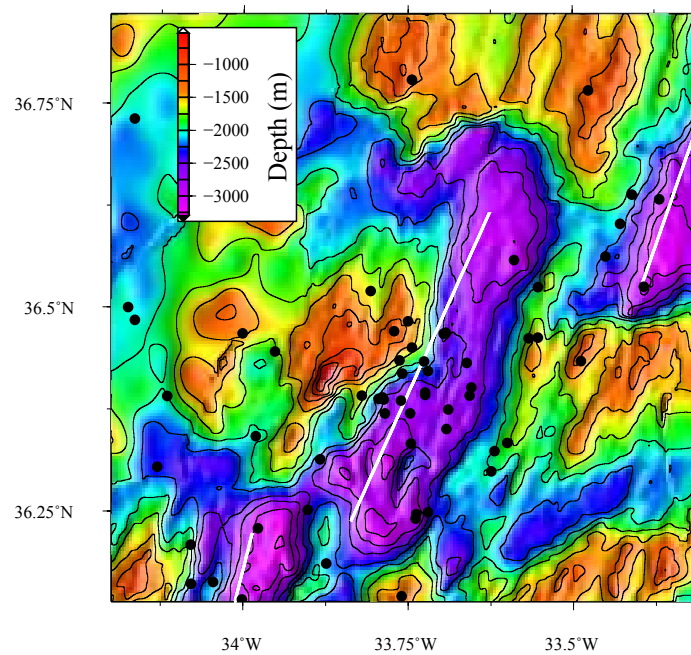


Figure 4.18: Bathymetric plot of the south Azores part of the MAR segment that goes from 36.250°N to 36.750°N. Black dots represent AuH seismicity recorded by the MARCHE array with at least 4 hydrophones and white segments represent MAR's segmentation according to *Thibaud et al. (1998)*. *Thibaud et al. (1998)* define this segment PO6 as in a intermediate to cold state with a wide and deep axial valley.

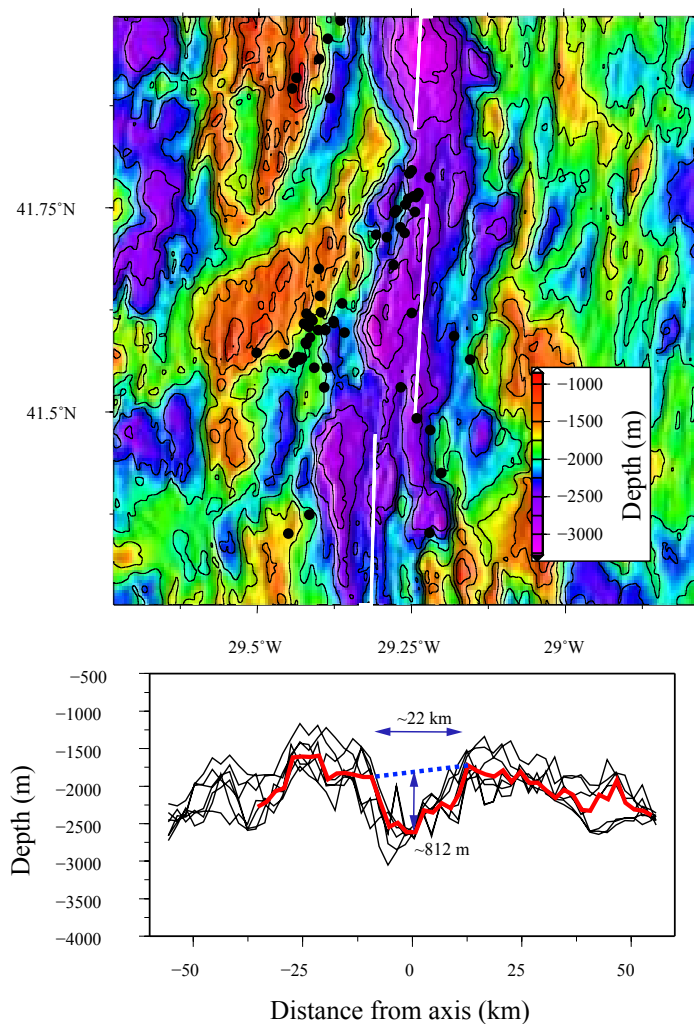


Figure 4.19: Bathymetric plot of the north Azores part of the MAR segment that goes from 41.496°N to 41.756°N. Black dots represent AuH seismicity recorded by the SIRENA array with at least 4 hydrophones and white segments represent MAR's segmentation according to *Maia et al.* (2007) (top). It is one of the most active segments of this part of the MAR. Consecutive 0.05° apart across segment profiles (bottom). Red profile is the mean across segment profile obtained from all the profiles.

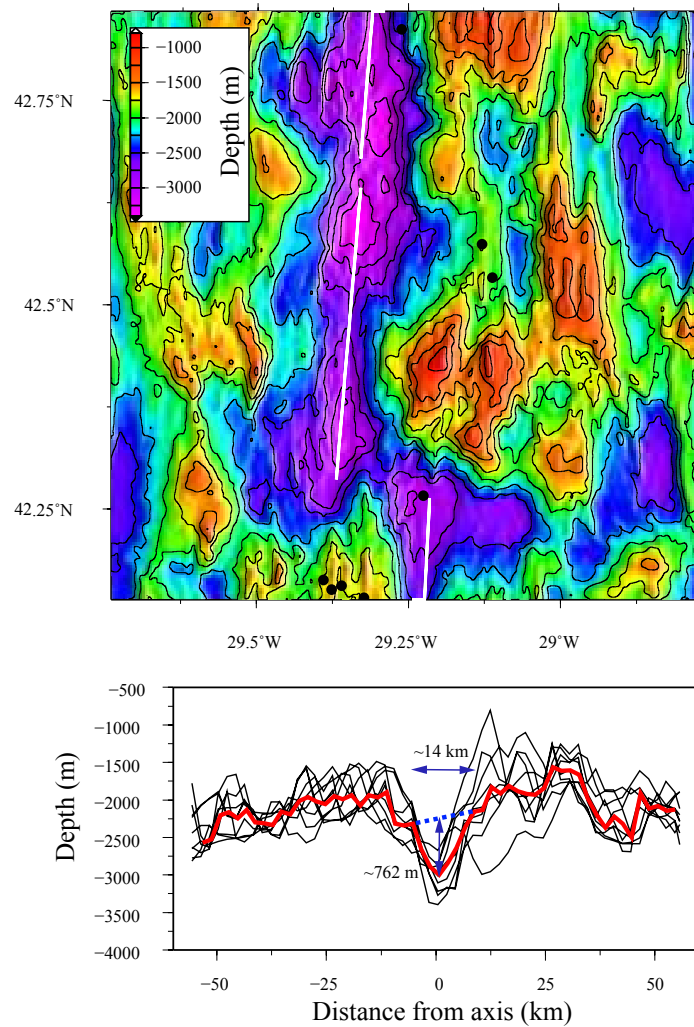


Figure 4.20: Bathymetric plot of the north Azores part of the MAR segment that goes from 42.287°N to 42.644°N . Black dots represent AuH seismicity recorded by the SIRENA array with at least 4 hydrophones and white segments represent MAR's segmentation according to *Maia et al.* (2007) (top). It is one of the most active segments of this part of the MAR. Consecutive 0.05° apart across segment profiles (bottom). Red profile is the mean across segment profile obtained from all the profiles.

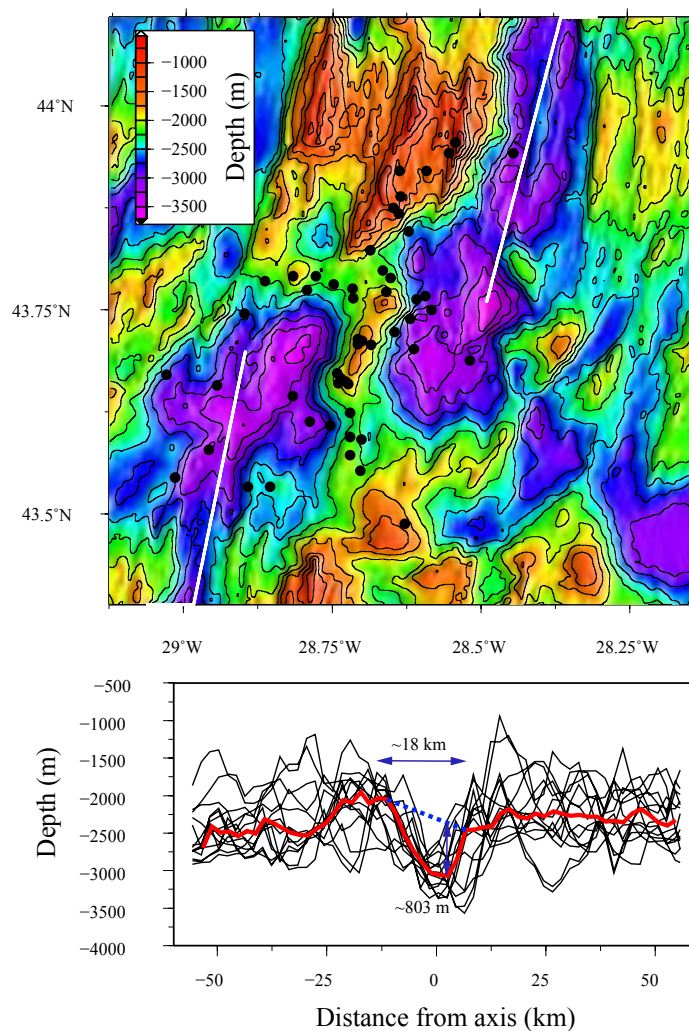


Figure 4.21: Bathymetric plot of the north Azores part of the MAR segment that goes from 43.106°N to 43.701°N . Black dots represent AuH seismicity recorded by the SIRENA array with at least 4 hydrophones and white segments represent MAR's segmentation according to *Maia et al.* (2007) (top). It is one of the most active segments of this part of the MAR. Consecutive 0.05° apart across segment profiles (bottom). Red profile is the mean across segment profile obtained from all the profiles.

Figure 4.16 also shown seismic gaps along the MAR. The one located $\sim 51.5^{\circ}\text{N}$ ($\sim 1400\text{km}$) is a major seismic gap. Unfortunately there is no high resolution bathymetry for this part of the MAR. Other major seismic gaps occur at $\sim 48^{\circ}\text{N}$ ($\sim 1100\text{km}$), $\sim 45.875^{\circ}\text{N}$ ($\sim 850\text{km}$), $\sim 44^{\circ}\text{N}$ ($\sim 600\text{km}$) and $\sim 42.5^{\circ}\text{N}$ ($\sim 400\text{km}$). Inspection of the bathymetry for the seismically active sections and for the seismic gap sections reveal that though there are distinct ridge and axial valley morphologies for active and inactive sections, in all cases they occurred on segments with well defined axial valleys associated to intermediate to cold thermal regime (*Cannat et al.*, 1999; *Thibaud et al.*, 1998). Figures 4.19, 4.21, and 4.22 show three active sections of the MAR associated with segments with a wider and deeper axial valley. Seismicity is normally recorded at segment extremities and/or at segment flanks showing strong asymmetric morphologies. The seismic gaps represented on Figures 4.20, 4.23, and 4.24 occurred on segments with axial valleys that were narrower than those for active sections. These differences in axial valley dimensions are related to the thermal structure of the crust. This is confirmed by the correlation between the MBA and the AuH and teleseismic seismicity discussed in section 4.5.2. Axial valley morphology also suggests more symmetric valleys associated to a more symmetric type of accretion. Special focus is needed on the MAR's segment that spans from $\sim 43.75^{\circ}\text{N}$ to $\sim 44.25^{\circ}\text{N}$ with its southern part which is very active due to its proximity to a ridge offset with a strong asymmetric morphology and its northern part which consists of almost no activity and is associated to a more symmetric type of morphology. All of this occurs within the same segment.

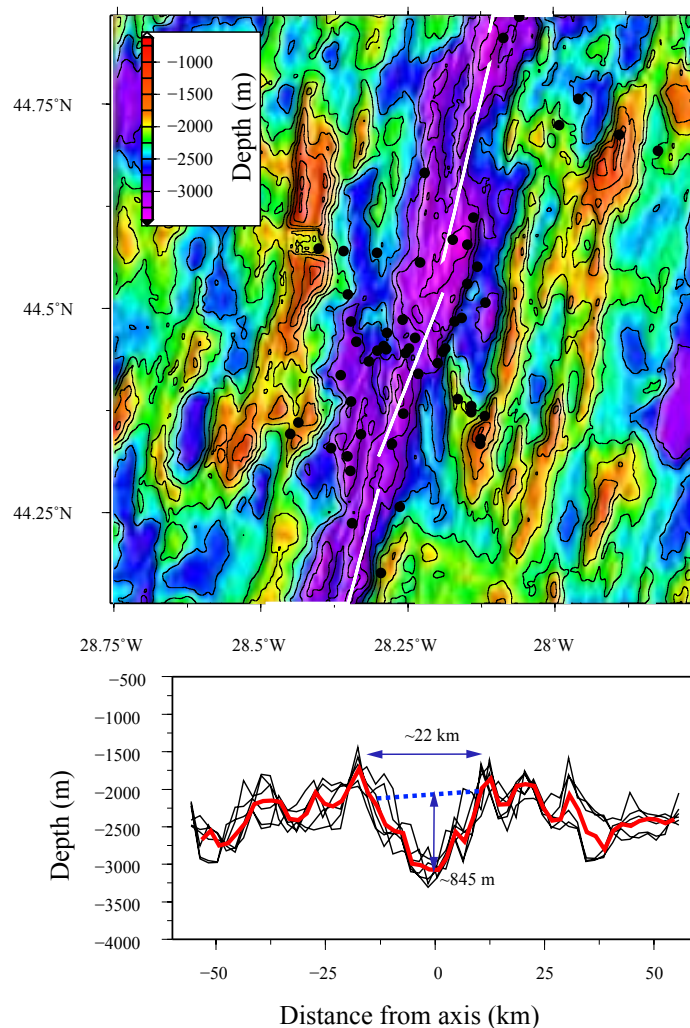


Figure 4.22: Bathymetric plot of the north Azores part of the MAR segment that goes from 43.760°N to 44.280°N . Black dots represent AuH seismicity recorded by the SIRENA array with at least 4 hydrophones and white segments represent MAR's segmentation according to *Maia et al.* (2007) (top). It is one of the most active segments of this part of the MAR. Consecutive 0.05° apart across segment profiles (bottom). Red profile is the mean across segment profile obtained from all the profiles.

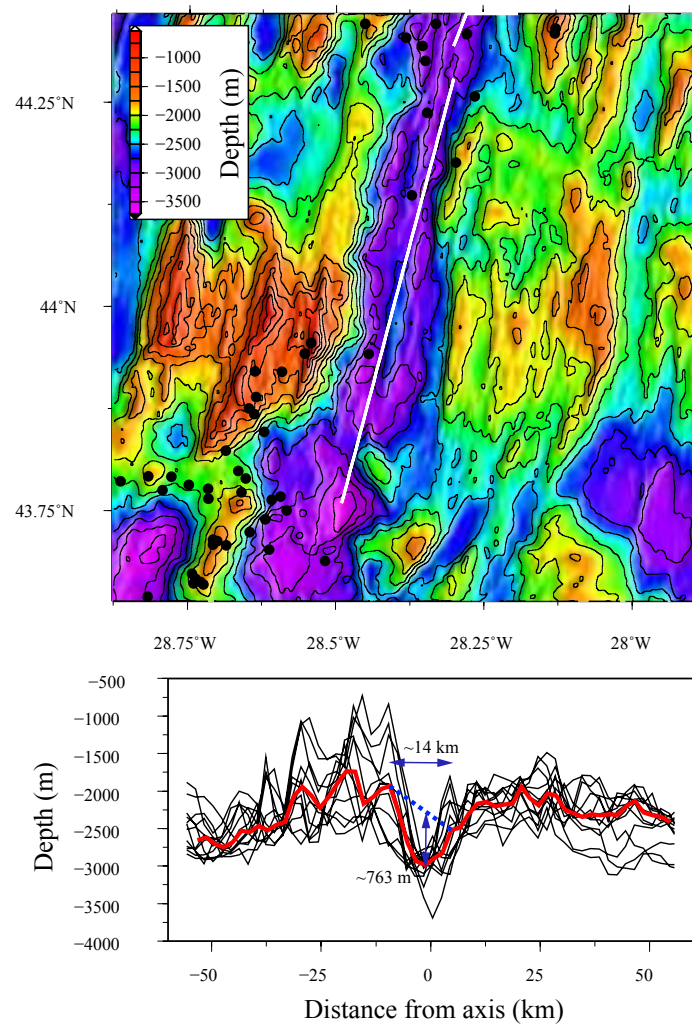


Figure 4.23: Bathymetric plot of the north Azores part of the MAR segment that goes from 44.320°N to 44.520°N . Black dots represent AuH seismicity recorded by the SIRENA array with at least 4 hydrophones and white segments represent MAR's segmentation according to *Maia et al.* (2007) (top). It is one of the most active segments of this part of the MAR. Consecutive 0.05° apart across segment profiles (bottom). Red profile is the mean across segment profile obtained from all the profiles.

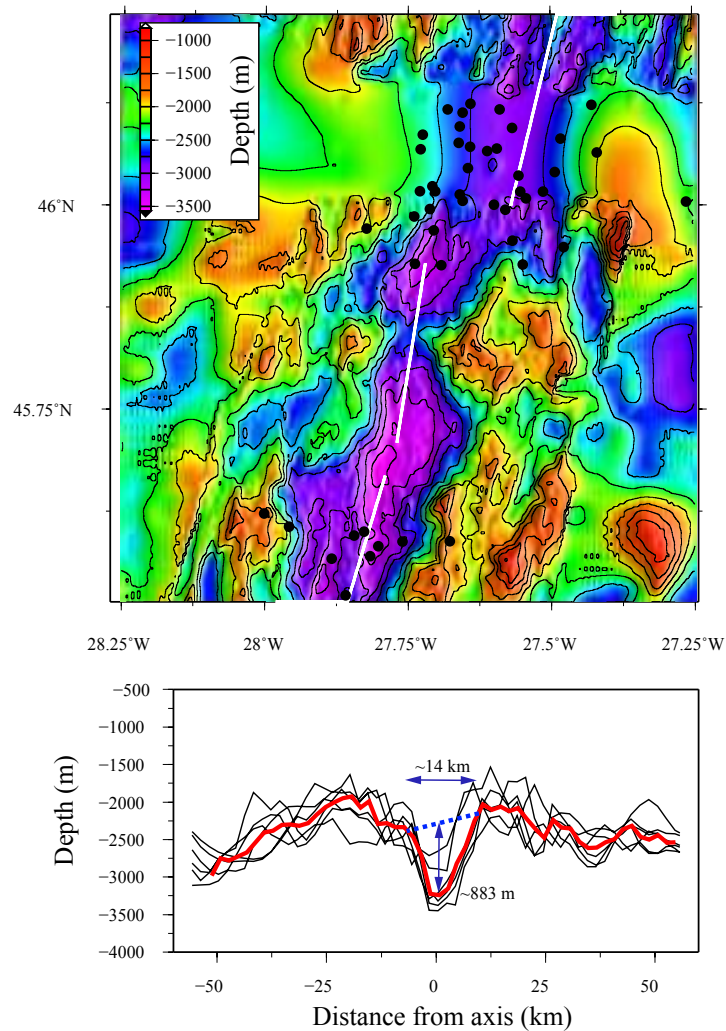


Figure 4.24: Bathymetric plot of the north Azores part of the MAR segment that goes from 45.710°N to 45.930°N . Black dots represent AuH seismicity recorded by the SIRENA array with at least 4 hydrophones and white segments represent MAR's segmentation according to *Maia et al.* (2007) (top). It is one of the most active segments of this part of the MAR. Consecutive 0.05° apart across segment profiles (bottom). Red profile is the mean across segment profile obtained from all the profiles.

4.6 Conclusions

The major assets of AuH arrays are: i) their relatively small error fields in locations, in comparison to the teleseismically localized earthquakes for remote parts of the oceans, and; ii) their capability to estimate - prior to deployment - the error field of those arrays. The predicted error fields of each configuration of AuH array that had been used since the beginning of 1999 until the present were produced, revealing how important the number of instruments and the geometry of the array are to the quality of the error fields. Error fields can vary between 2 to 8 km inside the arrays and increase very quickly for regions outside the array geometry.

Another major advantage, in comparison with teleseismically recorded earthquakes, is the lower detection threshold that AuH arrays have. A size frequency analysis of the AuH catalogs deployed in the MAR revealed that the Source Level of Completeness can vary in a range of ~ 15 dB in a region of the MAR delimited by the Marathon and Charlie Gibbs Fracture zones. A region spanning more than 5000 km. This difference in SL_c can have a dramatic influence on the numbers of recorded earthquakes. This seems to be particularly true in the region between the Oceanographer Fracture Zone and the Azores, where, for the period up until 2005 there was a deficiency in the number of earthquakes recorded. This deficiency was no more for the period between 2005 and 2007.

The visual inspection and correlation analysis of broad wavelength profiles of MAR's seismicity reveal a strong correlation between declustered catalogs of the AuH recorded seismicity and the teleseismically recorded seismicity. Revealing that temporally limited seismic monitoring experiments on the MAR can reveal the background seismicity patterns observed on more than 40 year of teleseismic observation. The joint analysis of the long wavelengths of the AuH and ISC seismicity distributions reveals low levels of seismicity for a distance as far a 200 km from the Azores that can be linked to the influence of the "hotspot". For long wavelengths the value of the MBA correlates very well with seismicity, all along the MAR, except on the region that goes from the region 200k south of the Azores until the Oceanographer FZ. This correlation suggests that seismicity along the MAR is influenced by the thermal state variation of the crust inferred from the MBA. The sector between the Azores and the Oceanographer FZ shows that a strong ridge obliquity can also have a large influence on the MAR's seismicity rates.

The principal component analysis reveals that for short time period snapshots, medium to large magnitude earthquakes recorded by land based stations have a complex relationship with AuH recorded seismicity. It also shows that the most active areas of the northern Azores region of the MAR are the sectors where the AuH recorded the major limited in time seismic crisis. It was also revealed for this region of the MAR that seismic active sectors and seismic inactive sectors

occur on different segment morphologies. With seismic sectors occurring on segments with a more asymmetrical morphology and relatively wider and deeper axial valley than the aseismic sectors.

Chapter 5

Analysis of MAR AuH seismic clusters

5.1 Introduction

Hydroacoustically derived source locations were used to identify earthquake sequences on the MAR. These sequences were plotted in high-resolution bathymetry and MBA grids, first, to identify the ridge structures that are able to cause this kind of seismic activity and, second, to correlate the primary influence in terms of thermal regime and/or fault regime in the sequence's earthquake occurrence decay rate. Before the earthquake occurrence decay rate analysis, size-frequency analysis of each sequence was made and all sequence events smaller than the completeness were eliminated. Size-frequency analysis of each sequence was estimated and compared with its source location and transmission loss estimates.

5.2 Catalog cluster identification using Single Link Cluster analysis

The method used to identify the cluster was the Single Link Cluster analysis, described in Chapter 4. In this analysis only events located by four or more hydrophones were incorporated. The Single Link Cluster technique was used as a filter that discards all declustered events. Regions along the ridge where clusters of earthquakes occurred were identified. Next, the clustered earthquakes were separated by region from the main catalog and time series for each discrete seismic sequence were developed after close visual inspection.

5.3 Mainshock-aftershock sequences

Middle to large magnitude earthquakes generally produce aftershocks that are clustered in space and time around the mainshock and are generally referred as aftershock sequences. Analysis of the sequences was done using the Modified Omori Law (MOL) (*Kisslinger and Jones, 1991; Utsu et al., 1995*), and the *Bohnenstiehl et al. (2002)* size-frequency relationship for T -phases based in the Gutenberg-Richter Law (GRL). The MOL states that a mainshock at $t = 0$ triggers an aftershock that in turn triggers its own aftershocks and so on till the stresses are relieved from the focal area.

5.3.1 Modified Omori Law

In a seismic sequence a mainshock triggers aftershocks with an occurrence rate that decreases with time according to:

$$n = \frac{K}{(c + t)^p} \quad (5.1)$$

Where n is the cumulated number of earthquakes having occurred at time t after the mainshock, K is a constant that reflects the total number of events within the sequence and the size of the main-shock, c reflects the rate of activity within the earliest part of the earthquake sequence, t is the time and p is the aftershock rate decay. This formulation gives the characteristic MOL and suggests an interpretation of the aftershock decay rate of the fault in terms of changes in strain.

The aftershock rate decay clearly reflects the process of relaxing strain concentrations produced by the main fault rupture (*Scholz, 1990*). Several authors have suggested that regions with higher crustal temperatures have a higher likelihood of being subjected to more rapid strain release, and thus inducing p -values greater than 1 (*Kisslinger and Jones, 1991; Kisslinger, 1996; Rabinowitz and Steinberg, 1998; Klein et al., 2006*). A general state-variable constitutive formula for the occurrence rate of earthquakes with changes in the lithospheric strain properties was proposed by *Dieterich (1994)*.

The *Ogata and Shimazaki (1984)* method was used to fit the MOL and a bootstrap approach was used to estimate errors in the MOL parameters (*Wiemer, 2001; Wiemer et al., 2002*). This method allows the characterization of sequences that contain secondary aftershocks - following a major aftershock - that would change the rate at which the strain is released. It consists of fitting the seismic sequences by comparing four models. In the first model the p , c and K are calculated for only one sequence. In the second model, two sequences are considered where p and c are the

same in the two sequences and only K changes. In the third model, two sequences are considered where p is the same in the two sequences and where c and K change from one sequence to the other. In the fourth model, two sequences are considered and p , c , and K are different in the two sequences. The model that best fits the data was chosen following the Akaike Information Criterion (AIC):

$$AIC = (-2)\{\max \log(L)\} + 2k \quad (5.2)$$

Where L is the likelihood function and k is the number of free parameters (Akaike, 1973; Ogata, 1983). The AIC it is not a measure of the goodness of fit of the chosen model, it is the parameter used to choose the best model. So the Kolmogorov-Smirnov test was used (*Marsaglia et al.*, 2003; *Massey*, 1951; *Miller*, 1956; *Wiemer*, 2001) to obtain a statistical goodness of fit between the model and the data. Using this test all MOL fitting was made considering a 95% confidence level (Tables 1 and 2 of Appendix 2). The Kolmogorov-Smirnov goodness of fit test statistic is defined as:

$$KS_{stat} = \max |F_n(x) - F(x)| \quad (5.3)$$

Where $F_n(x)$ and $F(x)$ are the cumulative distributions of the data and model distribution tested. KS_{stat} varies between 0 and 1 is a function of the difference between the data and the model and depends of the number of samples in the distribution. The MOL parameters can be biased if we assume the starting time of the sequence $T_{min} = 0$, due to the difficulty in detecting aftershocks in the first moments of the sequence, resulting from the mainshock coda duration and/or complex nature of the aftershocks (*Nyffenegger and Frohlich*, 1998; *Ogata*, 1983). To avoid this, T_{min} was found to best fit the data in the period $[T_{min}, T_{max}]$.

5.3.2 Size-frequency relationship

To determine reliable MOL parameters, events in the sequence were restricted to those larger than the Source Level of Completeness. This was achieved by using the Gutenberg-Richter Law as modified by *Bohnenstiehl et al.* (2002) which states that the cumulative distribution of earthquakes vs. Source Level is given by:

$$\log(N) = a_t + b_t SL_c \quad (5.4)$$

Where N is the number of earthquakes, a_t is a constant dependent on the total number of

events, b_t is a constant representative of the size-frequency relationship and SL_c is the event Source Level of Completeness. To resolve the size frequency relationship, the entire magnitude range maximum likelihood method was used (Aki, 1965; Ogata and Katsura, 1993; Utsu, 1965; Woessner and Wiemer, 2005). A measure of quality for the b_t and SL_c in each sequence was obtained through a bootstrap method (Schorlemmer et al., 2003). The completeness is a measure of quality and homogeneity for a catalog and can be used to illustrate the temporal variations due to improvements or failures in the sensors or environmental changes surrounding the array. Several studies have related the more orthodox b -values to physical properties such as stress components, material homogeneity and pore pressure (Shaw, 1995; Scholz, 1990; Warren and Latham, 1970). More recently, high b -value anomalies were proposed to indicate near field proximity to active magma chambers (Wiemer and Wyss, 2002; Wyss et al., 2001a,b) and to show a dependency with the strain regime of the fault mechanism (Schorlemmer et al., 2005).

In this size-frequency relationship variation of the Gutenberg Richter Law, AuH Source Levels were used instead of the traditional magnitudes. The Source Levels scale range from around ~ 190 to ~ 240 dB, that differs greatly from the magnitude scales used by seismologists. This difference is also reflected in the values of b_t . Thus both the completeness SL_c and b_t depend on the energy liberated by the earthquake for the conversion process of the seismic phases into T -phases and for the propagation path to the sensors.

Once the Single Link Cluster analysis was completed, only sequences chosen with more than 40 events were retained, to ensure that SL_c and the b_t were meaningful (Wiemer and Wyss, 2002). For the MOL calculations, only events with Source Levels bigger than the SL_c were taken into account, as the p -value is independent of the earthquake magnitude only when the size of the events are bigger than SL_c (Utsu et al., 1995). Using these parameters, it is possible to compare p -values from sequences detected by different arrays and different regions of the MAR (Figure 5.1). Following the discussion above, the SL_c , b_t and p -value estimates will be used to characterize the earthquake clusters.

5.4 Miami Parabolic Equation model

To better interpret SL_c and b_t a transmission loss study was made using the Monterey Miami Parabolic Equation (MMPE) model. The objective was to better account for the propagation loss in evaluating the variations in SL_c and b_t , in terms of propagation of the acoustic wave energy from the source to the AuH. In the early 1990's, a numerical code known as the University of Miami Parabolic Equation (UMPE) Model was documented and made available to the gen-

eral research community. This model uses the split-step Fourier (SSF) technique to resolve the parabolic equation (Smith, 2001), and had been adapted from previous versions developed by Fred Tappert at the University of Miami. A subsequent version, known as the Monterey-Miami Parabolic Equation (MMPE) Model, was developed in the mid-1990's that was more streamlined and user friendly (Smith, 2001). This code was thoroughly tested against several existing scenarios, such as for deep water columns and extensive propagation paths (Chapp *et al.*, 2005), in layered waveguide situations (Smith *et al.*, 1993) and with low frequency sources (Berchok *et al.*, 2006; Chapp *et al.*, 2005). The reason for choosing the MMPE model from the numerous existing models was that it has a relatively short period of computation and is capable of producing very effective results for simulations with deep water columns and extensive propagation paths. The model also permits to the researcher to define the physical properties of the sea-floor in the model, producing much more realistic simulations when there is bathymetric interference in the acoustic wave guide.

5.5 Previous analyses of seismic sequences along the MAR

There have been several prior studies of MAR hydroacoustic seismicity. In a detailed analysis, Bohnenstiehl *et al.* (2002) identified two distinct spreading center earthquake sequences along the MAR. The first mainshock-aftershock sequence occurred on April 1999 at 24°25'N, the NEIC network registered four shocks, the main one being a normal 5.9 Mw fault event. The AuH array recorded more than 160 aftershocks occurring within a radius of 15-20 km of the main shock with a spatial distribution that lies parallel to the rift valley and bounding walls. The SL_c end of the sequence was estimated at 208 dB with a b_t -value of 0.08, and the best fit for the p -value was 1.6 in the period of 33 days. The second sequence occurred along the third segment, north of the 15°20' Fracture Zone, on February 2000 (Bohnenstiehl *et al.*, 2002). The NEIC network recorded three events with the main event a 5.6 Mw normal faulting earthquake. The AuH recorded more than 40 events in 12 days, separated into two smaller sequences distributed along the structural trend of the axis, and the SL_c was estimated at 207 dB with a b_t -value of 0.09. The two sequences were fit together with a p -value 2.2. A swarm was identified as having magmatic origin (Dziak *et al.*, 2004a). A cluster of 147 earthquakes recorded by the AuH was located within the Lucky Strike segment of the MAR on March 2001. In addition to the seismicity, the authors also identified a broadband tremor-like signal occurring near the beginning of the sequence. The NEIC registered the main shock as 5.0 Mw normal fault earthquake and 32 aftershocks with magnitudes ranging from 3.6 mb to 5.0 mb. Goslin *et al.* (2005) identified

5 earthquake sequences along the Reykjanes Ridge. The first sequence consists of 304 events recorded by the SIRENA AuH array on October 2002 with a p -value 1.0. This sequence was initiated by a 5.6 Mw normal fault event with 15 aftershocks registered by land-based stations. On January 2003, the AUH recorded 31 events in a second seismic sequence. The third sequence happened on February 2003 with a 4.4 mb earthquake followed by three teleseismically recorded events with larger magnitudes. The AuH record consists of 257 earthquakes for this sequence. In July of 2003, two sequences were recorded by the AuH array. The first sequence had 182 events and the second recorded 35 events. The last four sequences had rates of activity more consistent with a magmatic-triggered mechanism.

5.6 Mantle Bouguer anomaly inversion and MAR segmentation

Gravity anomalies over slow spreading ridges often exhibit circular mantle Bouguer anomaly (MBA) lows (bull's-eyes) centered over each segment center, and large along-axis MBA gradients (Kuo and Forsyth, 1988; Lin *et al.*, 1990; Lin and Phipps Morgan, 1992). These features have been interpreted in terms of crustal thickness and/or density variations with thicker less dense crust beneath the middle of the segment and thinner more dense crust to the distal ends (Lin *et al.*, 1990). This variation of the crust density/depth can influence the location of seismic swarms. Along the MAR, MBA generally increases from the center towards segment ends (Detrick *et al.*, 1995; Maia *et al.*, 2007; Thibaud *et al.*, 1998), indicating greater crustal thickness at the segment center. The origin of these variations is mainly connected to the presence of lower density rocks at the segment center and directly dependent on the thermal structure of the crust. The ΔMBA (Lin *et al.*, 1990), the along axis variation of depth (Thibaud *et al.*, 1998) and the axial valley width and depth (Cannat *et al.*, 1999; Thibaud *et al.*, 1998) concepts can be used as proxies for each segment thermal regime. But the concept of the axial valley dimensions seem to be the one more closely connected to the mechanical properties of each sections crust (Cannat *et al.*, 1999). In this way the axial valley depth and width will be used as the concept to evaluate the thermal state of the studied sequence's segments (Figure 5.2). To interpret the spatial distribution of the seismic sequences along the MAR segmentation, the segmentations of Thibaud *et al.* (1998) was used between $15^\circ - 40^\circ\text{N}$, Maia *et al.* (2007) between $40^\circ - 45^\circ\text{N}$ and Smith *et al.* (2008) between $12^\circ - 15^\circ\text{N}$.

5.7 Mid-Atlantic Ridge seismic sequences

In total 10 new hydroacoustically derived seismic sequences were identified and analyzed using the methodology referred above and interpreted together with the two sequences reported in *Bohnenstiehl et al. (2002)* and the one reported in *Dziak et al. (2004a)* (Appendix C). For the thirteen sequences, the previously described methodology was used to obtain size-frequency relationships (Table 5.3) and to fit the MOLs (Table 5.4). Two of the sequences need to be viewed as special cases. The first is the sequence recorded on March 2001 *Dziak et al. (2004a)* that was located well outside the South Azores array. The second, the sequence recorded on February 2007, was only recorded in its entirety by 3 hydrophones during the second deployment of the MARCHE array.

Table 5.1: Sequences, number of events, mean sequence localizations, T -phase excitation mean depth, mean earthquake distance to the segment axis. Mean axial valley width and mean axial valley depth.

Date	Events	Longitude ($^{\circ}$)	Latitude ($^{\circ}$)	$\overline{D_{th}}$ (m)	\overline{D} (km)	Mean axial valley width (km)	Mean axial valley depth (m)
1999 04 06	165	-46.335 ± 0.030	24.364 ± 0.049	-2808 ± 518	12.7 ± 3.4	22	1561
2000 02 18	54	-46.578 ± 0.056	16.553 ± 0.094	-3638 ± 423	5.0 ± 3.5	22	1392
2000 10 05	126	-40.850 ± 0.070	31.605 ± 0.055	-3121 ± 372	5.8 ± 3.9	17	653
2001 01 12	45	-44.672 ± 0.061	26.450 ± 0.081	-3442 ± 333	5.3 ± 4.9	22	1051
2001 02 28	96	-43.397 ± 0.049	28.981 ± 0.039	-2683 ± 248	13.4 ± 3.3	12	632
2001 03 16	125	-32.285 ± 0.089	37.375 ± 0.148	-2295 ± 500	7.5 ± 5.7	24	735
2001 07 13	64	-43.340 ± 0.039	28.644 ± 0.047	-2629 ± 265	18.9 ± 4.6	26	1141
2001 11 12	53	-45.049 ± 0.042	22.218 ± 0.053	-3803 ± 404	7.0 ± 3.9	21	811
2001 12 13	59	-44.306 ± 0.044	26.899 ± 0.080	-2748 ± 280	18.2 ± 4.6	18	1015
2002 03 24	198	-46.361 ± 0.030	24.319 ± 0.033	-2756 ± 452	12.2 ± 2.8	22	1561
2003 08 27	42	-28.740 ± 0.090	43.784 ± 0.065	-2172 ± 496	13.4 ± 3.7	18	803
2004 04 16	54	-39.356 ± 0.029	32.827 ± 0.048	-1986 ± 277	29.4 ± 4.8	16	821
2007 02 13	77	-33.942 ± 0.151	36.085 ± 0.076	-2002 ± 462	10.6 ± 6.5	16	699

In order to have an estimate of the spatial location of each sequence with respect to the ridge morphology, the mean position from the earthquake locations, the mean depth of the seismic to T -phase conversion locations, and the distance from the sequence mean position to the closest segment axis were calculated (Table 5.1).

Using the ISC web site seismic catalog, the events recorded by the land-based stations were identified for each seismic sequence as well as existing focal mechanism information. ISC web site based information from NEIC, ISC and IDC agencies were used for the hypocentral locations. ISC based information from HRVRD, NEIC and ZUR-RMT agencies were used for the focal mechanisms. Earthquake locations were based on the agency that used more stations for the relocations (*Engen et al., 2003*). When referring to magnitudes, priority goes first to M_w , second to M_s and third to m_b (*Bohnenstiehl et al., 2002*).

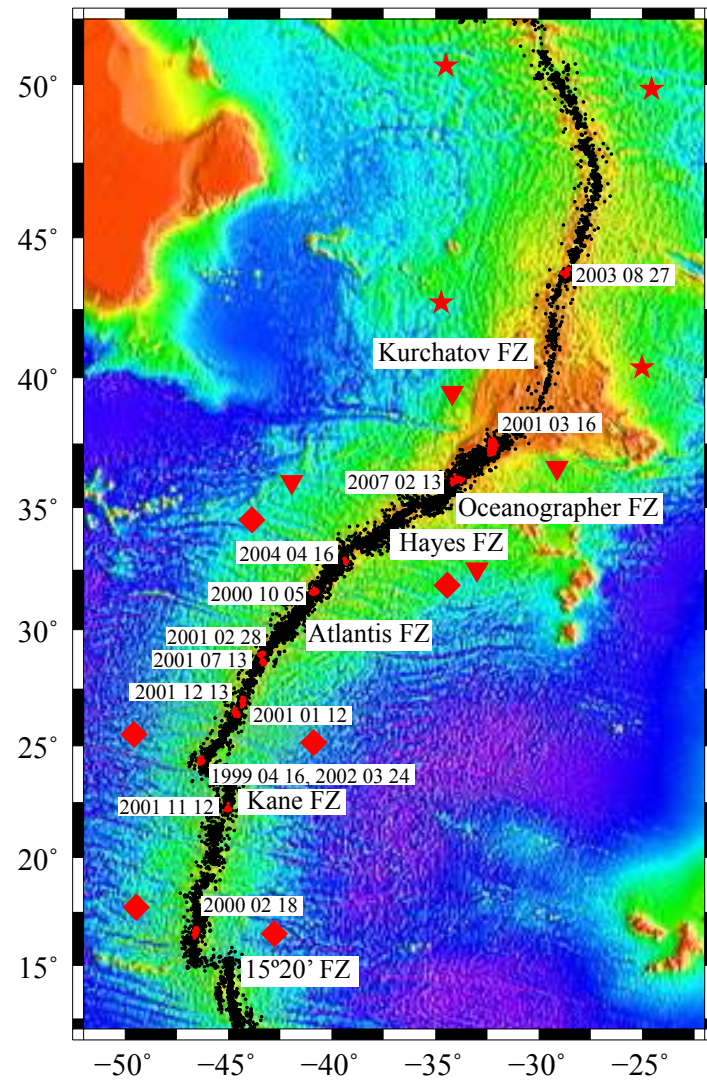


Figure 5.1: MAR AuH recorded seismicity. Red circle clusters represent the identified sequences. Red diamonds the South Azores AuHs. Red Inverted triangles show the locations of the MARCHE AuHs. Red stars show the locations of the SIRENA AuHs

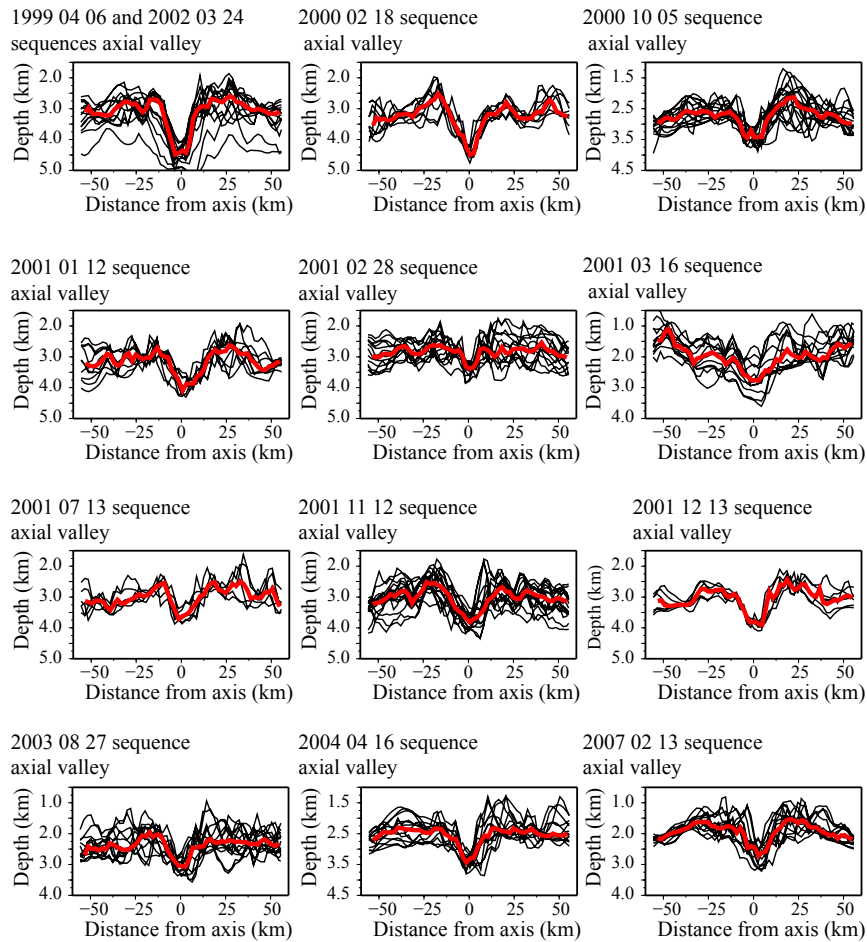


Figure 5.2: Axial valley across axis profiles taken each 5 km for segments where seismic sequences occurred. Red line is the stack of all profiles.

Detected sequences occurred across the entire range of morphological features on the MAR. Sequences were recorded inside the axial valley as the sequence that occurred on October 2000 (Figure 5.3), or as was the case for the sequence in December 2001 when they were recorded on segment flanks (Figure 5.4). The sequence recorded on April 2003 indicates that the ridge lithosphere can be broken by active faulting, up to distances as great as 30km from the ridge axis (Table 5.1). The majority of the sequences, 9 in 13 occurred in parts of the MAR where spreading occurs in an asymmetrical mode and associated with detachment faulting (Figures 5.13, 5.3 and 5.4) (Escartin *et al.*, 2008). The other four sequences occurred on abyssal hill faulting regions associated with symmetrical spreading (Figure 5.5). Figure 5.1 clearly indicates that most of the sequences were recorded between the Hayes and Kane Fracture Zones. This is not an artifact in the data that could be explained by the AuH having increased sensitivity in this region compared

to other areas, as will be shown later when size frequency is discussed.

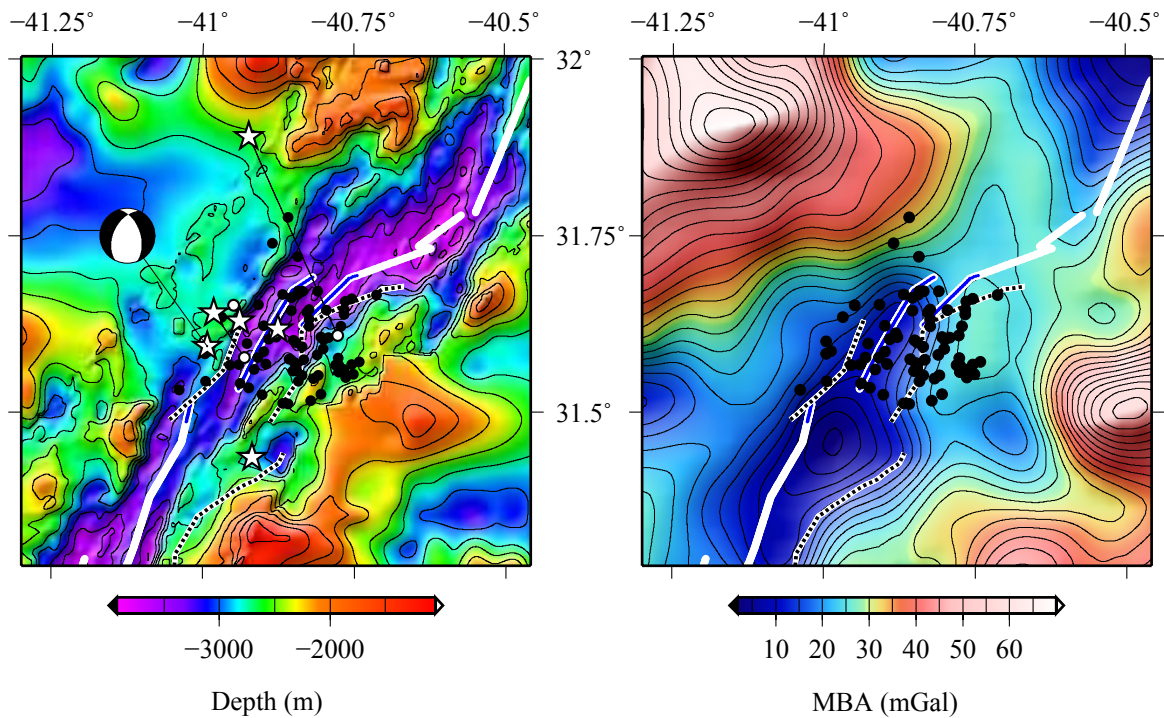


Figure 5.3: Seismic sequence that started on the 5th October 2000. Black circles are AuH recorded earthquakes. White stars are land based detected earthquakes. White segments are the MAR segments (*Thibaud et al.*, 1998). Red segments represents symmetric accretion, blue segments represents asymmetric accretion, red dashed curves are ridgeward initiation of detachment and black dashed curves are ridgeward initiation of abyssal hills as defined by *Escartin et al.* (2008).

The seismic sequences were recorded on segments with relatively wide (12 - 26 km) and deep (632-1561 m) axial valleys (Figure 5.2 and Table 5.1). Despite some considered differences between segment's axial valley dimensions, all segments suggest a to be in intermediate to cold thermal state (*Thibaud et al.*, 1998). MBA grid plots of the sequences show that in all cases, sequences occurred on colder parts of the gravimetric segmentation (Figures 5.3, 5.4 and 5.5). All sequences occurred in areas more than half way between the segment center and ends with bigger positive MBA values (relative to the segment).

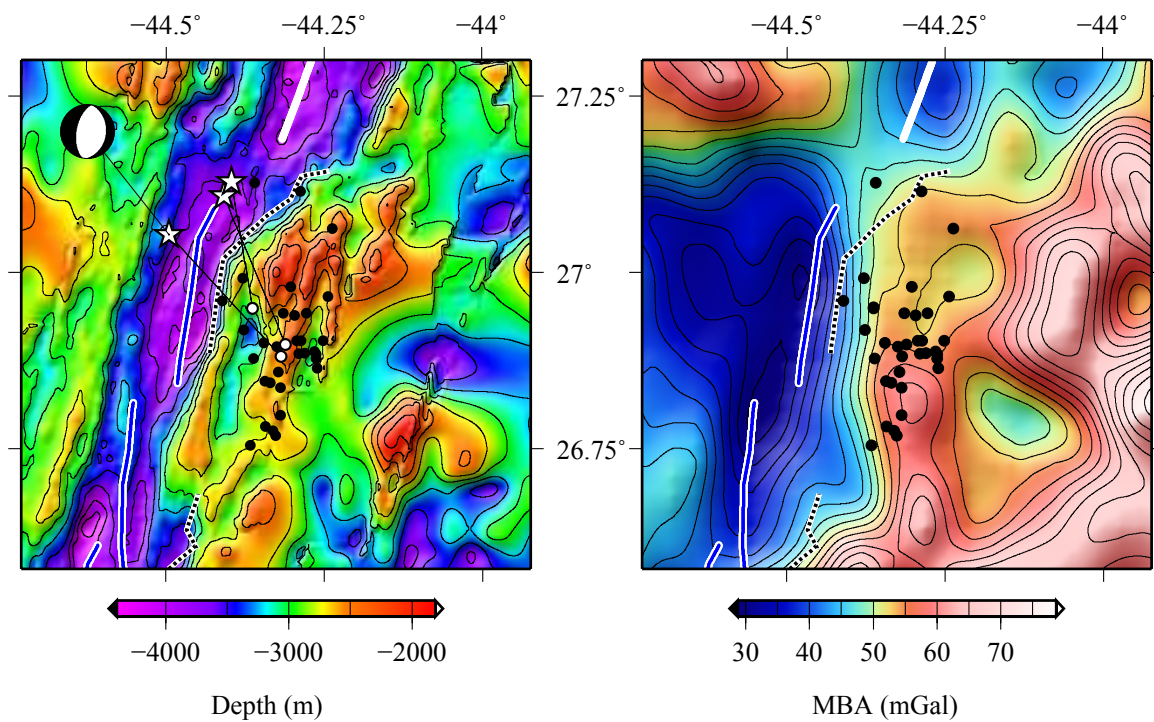


Figure 5.4: Seismic sequence that started on the 13th December 2001. Black circles are AuH recorded earthquakes. White stars are land based detected earthquakes. White segments are the MAR segments (*Thibaud et al.*, 1998). Red segments represents symmetric accretion, blue segments represents asymmetric accretion, red dashed curves are ridgeward initiation of detachment and black dashed curves are ridgeward initiation of abyssal hills as defined by *Escartin et al.* (2008).

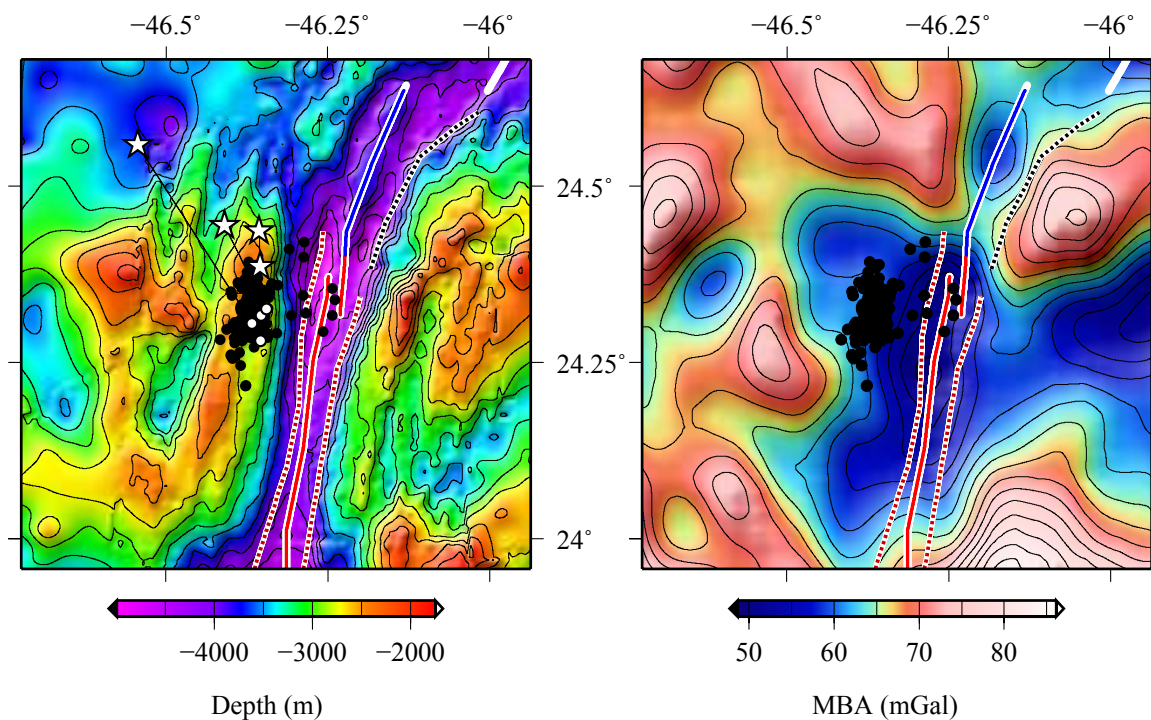


Figure 5.5: Seismic sequence that started on the 24th March 2002. Black circles are AuH recorded earthquakes. White stars are land based detected earthquakes. White segments are the MAR segments (*Thibaud et al.*, 1998). Red segments represents symmetric accretion, blue segments represents asymmetric accretion, red dashed curves are ridgeward initiation of detachment and black dashed curves are ridgeward initiation of abyssal hills as defined by *Escartin et al.* (2008).

5.8 Transmission Loss analyses

The MMPE model was used to quantify the Transmission Loss between the mean sequence location and each of the hydrophone locations in the array that recorded the seismic sequence. To run the MMPE models it was required to define the seafloor bathymetry and the physical properties of the two layers below the seafloor. The shallower layer was defined as being made of sediments with a density of $2.3g/cm^3$, a compression wave velocity of 1650 m/s, a compression attenuation of 0.1 dB/m/kHz, a shear wave velocity of 990 m/s and a shear attenuation of 0.04 dB/m/kHz (*Leurer, 2004*). The sediment layer was defined as being non-existent in the first 50km cross axis ridge and then to linearly increase until reaching 200 m thick at a distance of 250 km from the ridge axis. The sediment layer thickness is set to 200 m for distances bigger than 250 km. The deeper layer was defined as being made of basalt with a density of $2.6g/cm^3$, a compression wave velocity of 5000 m/s, a compression attenuation of 0.25 dB/m/kHz, a shear wave velocity of 3300 m/s, and a shear attenuation of 0.1 dB/m/kHz (*Tompkins and Christensen, 2001*). The oceanic sound speed profiles used in the model were calculated from temperature, salinity and pressure profiles from World Ocean Atlas 2005 (WOA05) (*Antonov et al., 2006; Locarnini et al., 2006*). Figures 5.6 and 5.7 are examples of the MMPE model transmission loss model. The sources for each simulation based its location and depth on the mean depth of source conversion and the mean location for each sequence (Table 5.1). The frequency range for the sources for each simulation was 0-60 Hz.

Table 5.2: Mean distance between the seismic sequence mean localization and the hydrophone localization, the mean Transmission Loss at the hydrophone in the 0 to 60 Hz frequency range and the difference between the MMPE Transmission Loss and the equations 2.6 and 2.7 computed Transmission Loss.

Date	\overline{Dst} (km)	TL (0-60Hz) (dB)	δTL (dB)
1999 04 06	874 ± 393	98	7
2000 02 18	1167 ± 756	107	12
2000 10 05	1049 ± 568	109	16
2001 01 12	862 ± 331	101	8
2001 02 28	921 ± 389	99	8
2001 03 16	1784 ± 827	105	12
2001 07 13	910 ± 376	97	6
2001 11 12	891 ± 426	103	9
2001 12 13	867 ± 332	97	6
2002 03 24	875 ± 395	97	6
2003 08 27	651 ± 189	95	7
2004 04 16	1147 ± 658	100	10
2007 02 13	483 ± 161	96	10

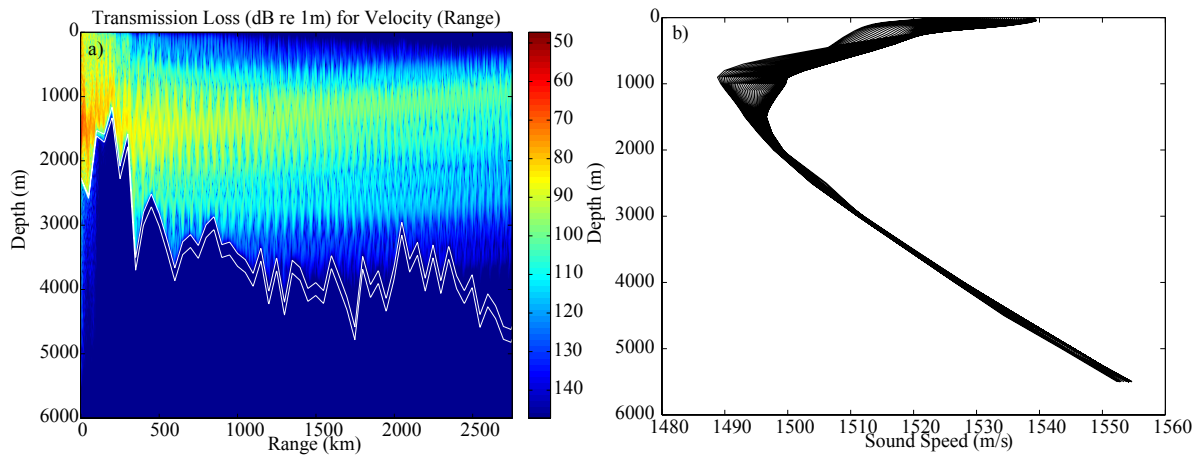


Figure 5.6: a) MMPE transmission loss modeling from a source located at the mean localization of the 3rd March 2001 sequence on the Lucky Strike segment to the farthest AuH located at 17.72°N, 42.78°W. Upper white line is the boundary between the water column and sediment layer, Lower white line is the boundary between the sediment layer and the rock layer. b) Sound speed profiles used on the MMPE modeling. Sound speed profiles taken each 25 km interval from the source to the hydrophone position.

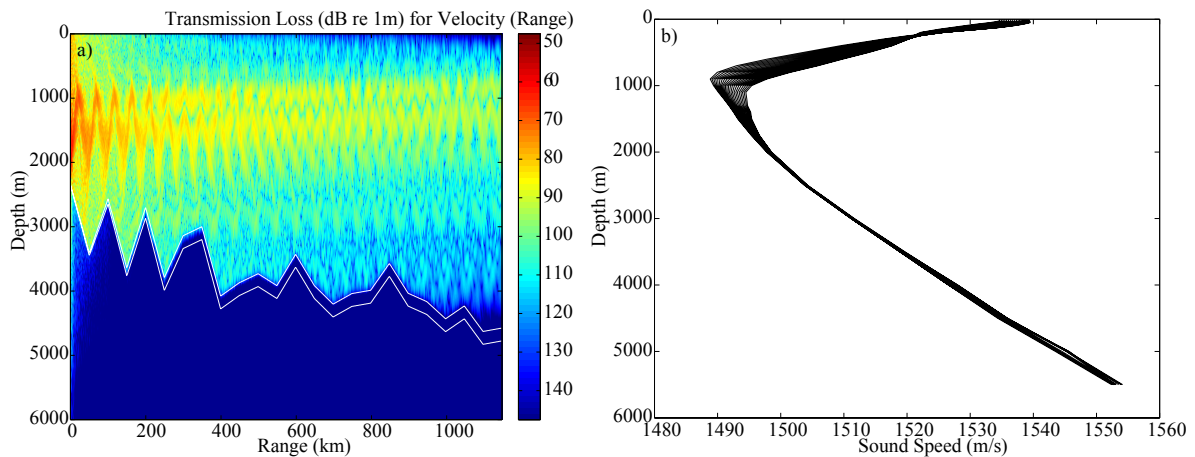


Figure 5.7: a) MMPE transmission loss modeling from a source located at the mean localization of the 13th December 2001 sequence on the Lucky Strike segment to the farthest AuH located at 17.72°N, 42.78°W. Upper white line is the boundary between the water column and sediment layer, Lower white line is the boundary between the sediment layer and the rock layer. b) Sound speed profiles used on the MMPE modeling. Sound speed profiles taken each 25 km interval from the source to the hydrophone position.

The parabolic equation model seems to simulate transmission loss of T-phases better than ray trace models. Ray trace attenuation models suggest that energy from below the critical depth and energy coupled into the water column in the valley floor should not be able to propagate in the SOFAR channel (*Williams et al.*, 2006). The MMPE is able to simulate the transmission loss of a source localized well below the SOFAR channel and its propagation all along the water column. It also simulates better the interaction of this acoustics phase with the surrounding bathymetry. Acoustic phases are clearly attenuated when they go through bathymetric obstacles but are not completely blocked as is the case in the ray model used by *Williams et al.* (2006).

The *T*-phase processing software compensates transmission losses using the equations 2.6 and 2.7 from Chapter 2. It works in the following way: if the distance of the localized event from the hydrophone is less than 5000 m its compensation is considered to be solely spherical, if its distance is bigger than 5000 m, its compensation is considered to be spherical for the first 5000 m and then cylindrical for the remaining distance (*TK Andy Lau, personal communication*). This compensation does not take into account the bathymetric effects in the acoustic guided wave, nor the compressional attenuation. Furthermore, following this simplistic theoretical consideration, where only geometrical spreading is the sole influence on transmission loss, equations 2.6 and 2.7 from Chapter 2 were computed for all sequences and compared to the values obtained by the MMPE model. This methodology was used to examine whether bathymetric effects play a major role in the measure of the sound energy recorded by the AuH. The Source Level of an earthquake is defined as the mean value of all recording AuH source levels in a frequency range that goes from ~ 0 Hz to ~ 60 Hz (*Dziak et al.*, 1997; *Dziak*, 2001; *Fox et al.*, 2001). MMPE was then used to compute transmission loss for each recording AuH position (depth and distance from the source) in the 0-60Hz frequency range and then it was averaged (Figure 5.8).

As expected, the mean depth of the sequence's earthquakes and the mean distance between the sequence location and the AuH play an important role in the transmission loss of the source level that reaches the AuH. Further, swarms that occurred on the axial valley seafloor and that were bounded by the valley walls were found to have greater transmission losses. The greatest differences between the MMPE computed transmission loss and the equations 2.6 and 2.7 transmission loss values (Table 5.2) occurred on three swarms that had a large number of earthquakes recorded on the axial valley floor. This shows that bathymetric interference also plays an important role on the energy that arrives at the AuH. The question that this poses is: Does the fact that the *T*-phase processing software does not take into account losses due to bathymetric effects affect the detection threshold of the AuH arrays? This question will be considered in the following section.

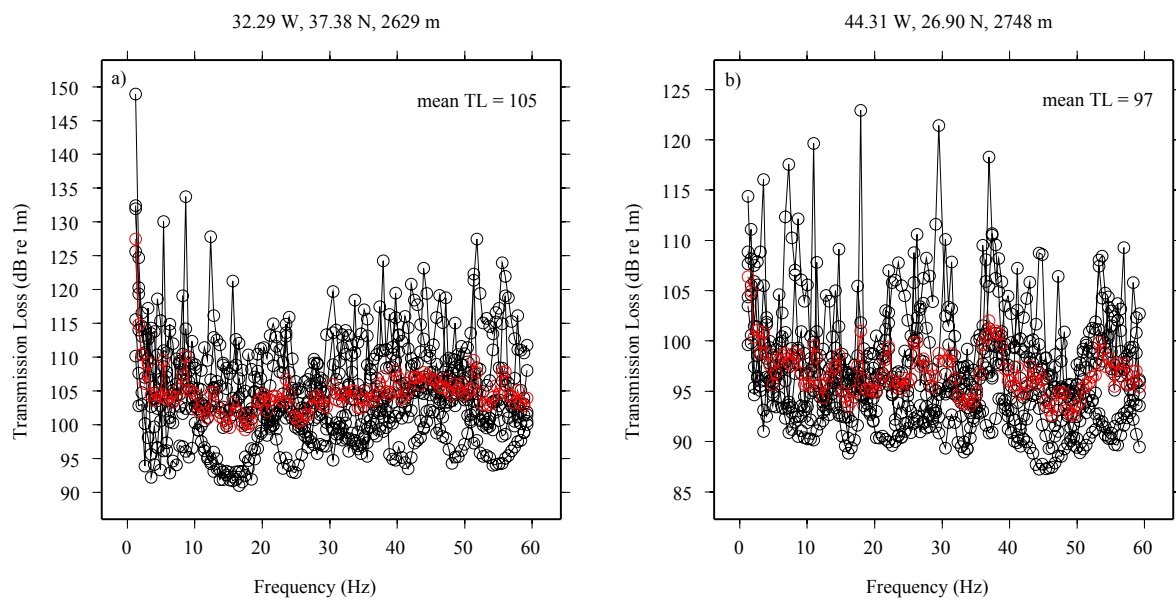


Figure 5.8: Transmission loss on the 0-60Hz frequency range at the 17N AuH. a) from a source located on the 3rd March 2001 sequence. b) from a source located on the 13th December 2001 sequence. Red circles are the mean transmission loss of all hydrophones for each frequency in the range 0-60 Hz.

5.9 Size Frequency analyses

The entire suite of earthquake clusters with 40 or more events went through a size-frequency analysis. For each sequence its SL_c , and b_t -value (Table 5.3) (Figure 5.10) were obtained. Seismic sequences recorded on October 2000, January 2001, and November 2001 had most of their events located inside the axial valley at depths well below the bathymetry highs of the axial valley walls (Figure 5.9a). This shows that T -phase conversion occurs as frequently in the deep seafloor as in shallower regions. It also appears that SL_c does not depend on the location of the swarms inside the ridge axial valley, where the propagation path interacts strongly with bathymetry, or within shallower regions where the path of propagation is clearer. The fact that 8 sequences were recorded between the Hayes and Kane fracture zones is not directly connected to the detection threshold, because the SL_c for those sequences are not systematically smaller than the detection threshold of the sequences recorded in other regions.

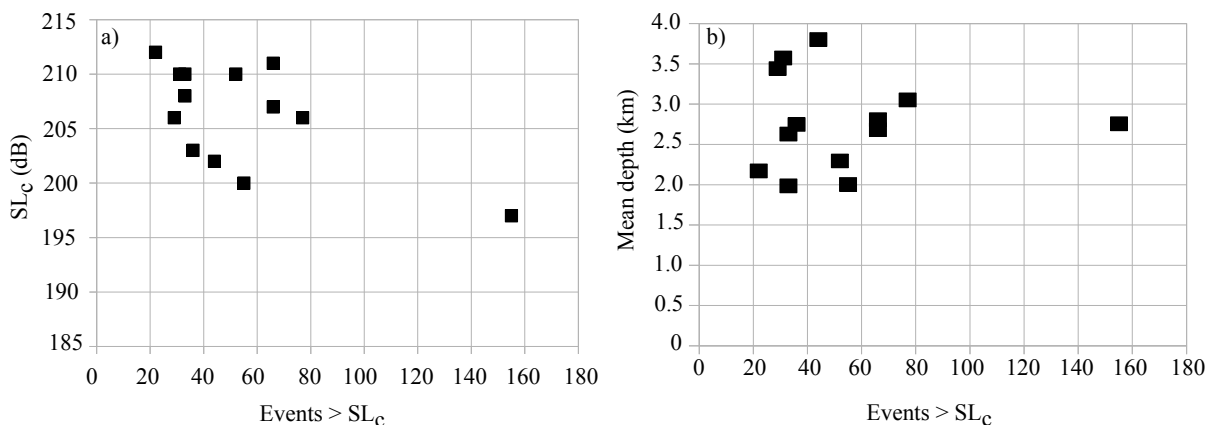


Figure 5.9: Relationships between the number of events with source level greater than the SL_c with the mean depth at which the sequence occurred (a) and the Source Level of Completeness (SL_c).

The numbers of events in the sequences with a Source Level bigger than the SL_c used for the MOL fits does not have a clear dependence on the SL_c (Figure 5.9b). This implies that the number of events recorded by the AuH for each sequence is above all a result of the fault mechanics and/or of the seismic phases to T -phase conversion.

It is possible to use b_t -value analyses of the sequences to provide an idea of the source level distribution of earthquakes. A sequence with a large b_t -value has a majority of earthquakes with low source levels, while a sequence with a small b_t -value has a majority of earthquakes with high source levels. 10 of the 13 sequences have b_t -values in between 0.07 and 0.10. The sequence

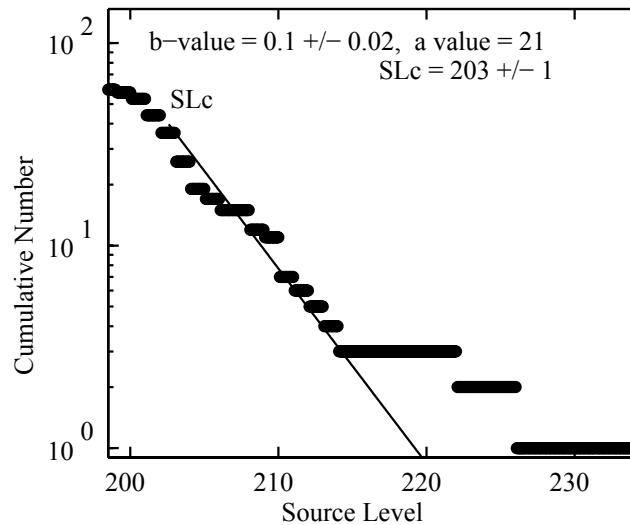


Figure 5.10: Size frequency relationship from the 13th December 2001 sequence.

recorded on March 2004 at a distance of 30 km from the ridge axis had a relatively small b_t -value of 0.05. The b_t -value shows that this sequence had higher source levels than the rest of the other sequences. This seems to coincide with the fact that this was the sequence that occurred farthest from the ridge axis and therefore probably at a colder lithosphere regional setting prone to producing stronger earthquakes. The sequence recorded on January 2001 had a b_t -value of 0.12 suggesting that it occurred in a weaker lithosphere that would produce a majority of low source level earthquakes. The sequence occurred very close to the ridge axis on a part of the ridge where spreading is considered to be asymmetrical and where detachment faulting is common (Figure 5.13). The sequence recorded on March 2001 also has a large b_t -value of 0.14. It occurred all along the Lucky Strike segment (Figure 16 of Appendix 3). This sequence was also well recorded by land based networks due to a large number of medium to large magnitude earthquakes. These observations seem to contradict the b_t -value and the hypothesis of warmer and weaker lithosphere producing a majority of low level earthquakes.

Generally, events occurring at the beginning of the sequences have higher Source Levels and are directly linked to the mainshock and to stronger events. The three exceptions to this are the January 2001 sequence and the February 2001 sequence, where land based networks did not record any event, and the March 2001 sequence where the Source Levels linked to the magnitude of the earthquakes recorded by the land based networks were low (Figure 5.11). The consistently higher regional SL_c obtained in Chapter 4 that occurred close to the Azores can

Table 5.3: Seismic sequence dates and size-frequency relationship parameters.

Date	SL_c (dB)	b_t	a_t	events $\geq SL_c$	\overline{SL} (dB)
1999 04 06	211 ± 2	0.09 ± 0.02	21	66	216
2000 02 18	210 ± 5	0.07 ± 0.02	17	31	216
2000 10 05	206 ± 1	0.07 ± 0.00	16	49	212
2001 01 12	206 ± 1	0.12 ± 0.05	27	29	210
2001 03 16	210 ± 2	0.14 ± 0.00	32	66	212
2001 02 28	207 ± 2	0.09 ± 0.02	20	52	213
2001 07 13	208 ± 2	0.09 ± 0.00	20	33	213
2001 11 12	202 ± 1	0.07 ± 0.01	15	44	208
2001 12 13	203 ± 1	0.10 ± 0.02	21	36	207
2002 03 24	197 ± 2	0.08 ± 0.01	17	155	202
2003 08 27	212 ± 4	0.08 ± 0.05	19	22	217
2004 04 16	210 ± 2	0.05 ± 0.00	12	33	219
2007 02 13	200 ± 2	0.09 ± 0.02	19	55	205

be seen as an indicator of a relatively deficient detection threshold of the South Azores Array for this region. Although the sequence SL_c and the mean Transmission Loss calculated for this zone are relatively high, they are not extreme in comparison with other sequences from other regions (Tables 5.2 and 5.3). This and the anomalously high b_t -value again indicate that there is some kind of T -phase conversion or propagation issues for this sequence, perhaps caused by the sequence location on a shallower region on the middle of the Azores Plateau.

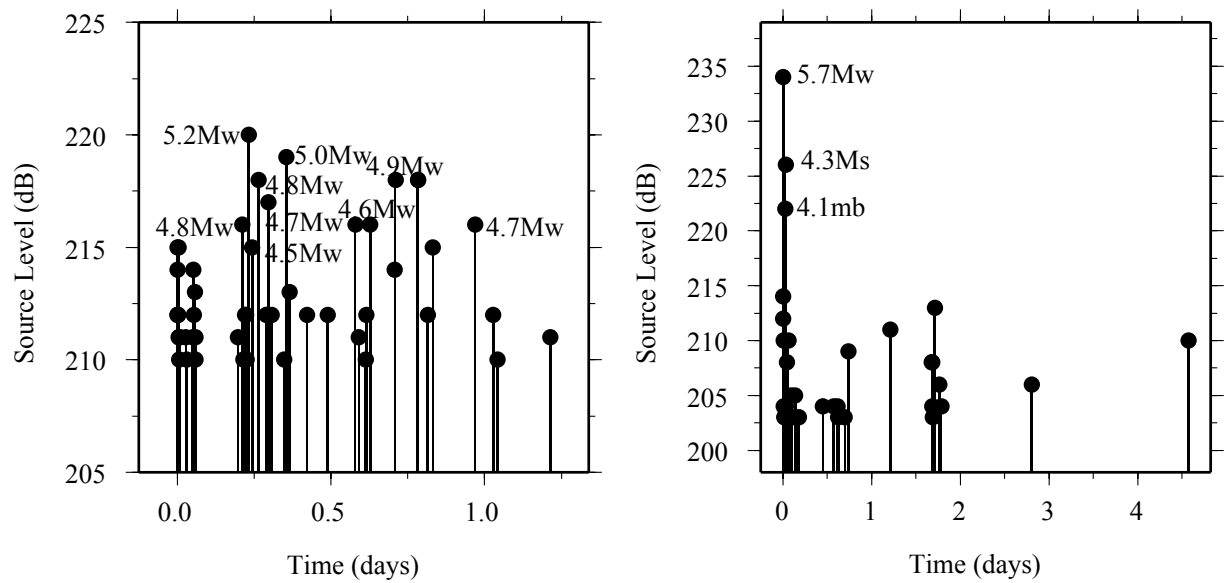


Figure 5.11: a) Source Level distribution across time of the 3rd March 2001 sequence. b) Source Level distribution across time of the 13th December 2001 sequence.

5.10 MOL analysis

From the thirteen identified seismic sequences, only 9 sequences have sufficiently good fits to be interpreted. This means that only sequences with goodness of fit $K S_{stat}$ values smaller than those tabulated for the 95% confidence level were interpreted (*Miller, 1956*) (Table 5.4, Tables 1 and 2 of Appendix B). Table 5.4 and Figure 5.12 show that 4 seismic sequences have extremely high p -values (> 2) and are of short duration. Other studies conducted on MAR seismic sequences suggested that large p -values can be due to hypocentral high temperatures normally found in the ridge median valley (*Bohnenstiehl et al., 2002*) and that short duration sequences may involve the migration of hydrothermal fluids that will reduce the strength of fault zones (*Goslin et al., 2005*). A recent study quantified and identified the modes of accretion in the MAR south of the Oceanographer Fracture Zone until the Marathon Fracture Zone (*Escartin et al., 2008*). The plot of the sequences with the modes of accretion proposed by (*Escartin et al., 2008*) (Figure 5.13) show that the sequences occurring in regions with asymmetrical spreading and associated detachment faulting have much higher p -values than those recorded in regions of symmetrical spreading abyssal hill faulting (Figures 5.12 and 5.13). An exception to this is the sequence recorded on April 2004, although this sequence occurred 30 km away from the axial ridge far from the active zone defined by (*Escartin et al., 2008*).

Table 5.4: Seismic sequences Modified Omori Law fitting parameters.

Date	Tmin (days)	Tmax (days)	Sec.Af. (days)	p1	c1	K1	p2	c2	K2	AIC	K-S _{stat}	K-S _{stat} (95%)
1999 04 06	0.001	11.890	-	1.7 ± 0.3	0.24 ± 0.15	18.1 ± 7.3	-	-	-	-288	0.108	0.164
2000 02 18	0.019	6.733	3.946	2.7 ± 0.1	1.51 ± 0.28	78.6 ± 19.7	-	-	18.3 ± 9.5	-37	0.182	0.238
2000 10 05	0.003	1.762	-	2.7 ± 0.6	0.30 ± 0.12	10.0 ± 4.3	-	-	-	-236	0.189	0.218
2001 01 12	0.021	3.837	-	2.7 ± 0.4	0.38 ± 0.15	10.0 ± 9.3	-	-	-	-98	0.125	0.246
2001 02 28	0.005	20.503	-	1.1 ± 0.3	0.67 ± 0.78	20.2 ± 15.3	-	-	-	-80	0.062	0.164
2001 03 16	0.001	1.214	-	0.9 ± 0.8	0.01 ± 0.46	10.0 ± 21.4	-	-	-	-161	0.129	0.238
2001 07 13	0.003	2.431	1.690	2.3 ± 0.6	1.15 ± 0.59	48.0 ± 26.5	-	-	48.7 ± 23.3	-112	0.188	0.231
2001 11 12	0.002	2.793	-	2.7 ± 0.4	0.32 ± 0.06	10.0 ± 1.8	-	-	-	-202	0.242	0.201
2001 12 13	0.001	1.785	-	0.8 ± 0.6	0.01 ± 0.37	10.0 ± 14.2	-	-	-	-167	0.286	0.227
2002 03 24	0.003	22.319	-	1.2 ± 0.1	0.05 ± 0.04	24.9 ± 3.9	-	-	-	-749	0.058	0.109
2003 08 27	0.002	17.584	-	1.5 ± 0.3	0.51 ± 0.70	10.1 ± 8.6	-	-	-	9	0.350	0.281
2004 04 16	0.001	12.776	-	1.4 ± 0.4	0.24 ± 0.33	10.0 ± 14.6	-	-	-	-35	0.125	0.231
2007 02 13	0.040	4.898	-	0.8 ± 0.6	0.01 ± 0.51	10.6 ± 18.9	-	-	-	-133	0.278	0.180

The dependence of the p -value on the type of accretion can be explained by the fact that tectonic strain can vary independently of its position along the length of the segment due to asymmetry in accretion (*Allerton et al., 2000; Escartin et al., 1999, 2008; Searle et al., 1998a*). Fault strength can - to a large extent - depend on the effect of hydrothermal activity that in turn influences the yield strength of the lithosphere and its effective elastic thickness (*Escartin and Lin, 1998; Lavier and Buck, 2002; Phipps Morgan and Chen, 1993*). In addition to this, serpentinite substantially lowers fracture and frictional strength in comparison to unaltered peridotite and gabbro. Serpentinite also has a nearly non dilatant style of brittle deformation that may confine

fluids to further weaken faults (*Cann et al.*, 1997; *Escartin et al.*, 1997, 2003a). This evidence suggest that detachment faults are characterized by a very efficient localization of the deformation, caused by the presence of weak minerals and fluids along the fault zone. This localization can further reduce the effective pressure and hence the strength of the fault, making them capable of triggering earthquake sequences that have faster strain decay and shorter durations (Figure 5.14).

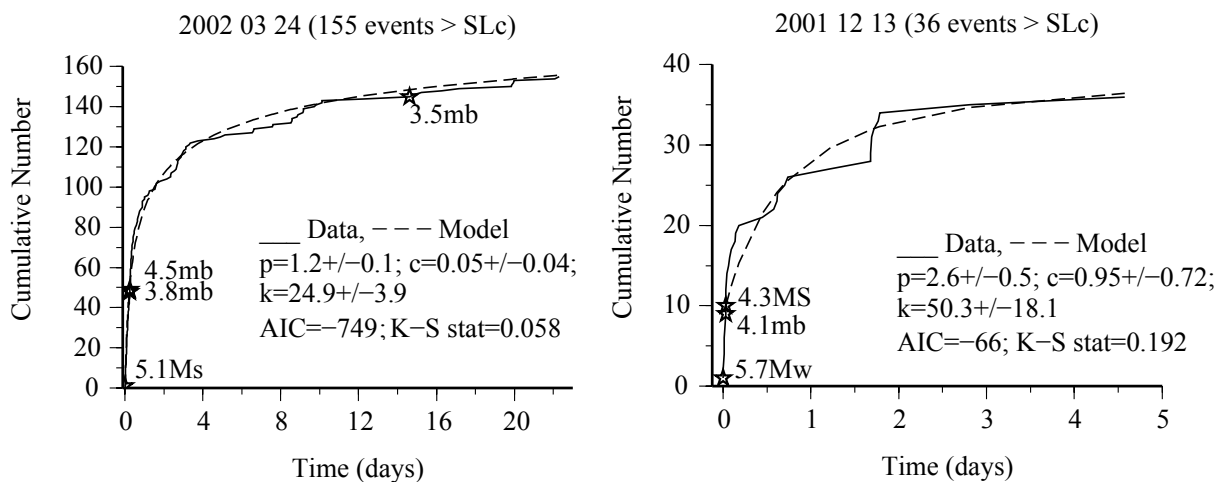


Figure 5.12: a) MOL fit of the 24th March 2002 sequence. b) MOL fit of the 13th December 2001 sequence.

5.11 Conclusions

The cluster analysis of the seismicity on the MAR was carried out with with the objective of adding further data to existing work on cluster analysis and of emphasizing seismic sequence analysis, using MOL and size-frequency principles, in order to better constrain the modes of faulting and the detection threshold issues from different regions of the MAR. Seismic sequences occur on segments with well developed axial valleys reinforcing the idea that these segments are in a relatively cold thermal state. Seismic sequences can be detected inside the axial valley or on the flanks until distances as far as ~ 30 km off axis.

Size frequency analysis and transmission loss analysis suggest that T -phase based earthquake energy source level are more strongly dependent on the conversion of the seismic waves into

acoustic waves than on the interaction of the propagated wave with the surrounding bathymetry. This dependence is not restrictive though, because as shown, the number of events detected for each sequence does not depend entirely on the detection threshold SL_c and can be representative of the faulting mechanisms. This permits T -phase detected earthquake mainshock aftershock sequences to be used on number rate decay with MOL analysis.

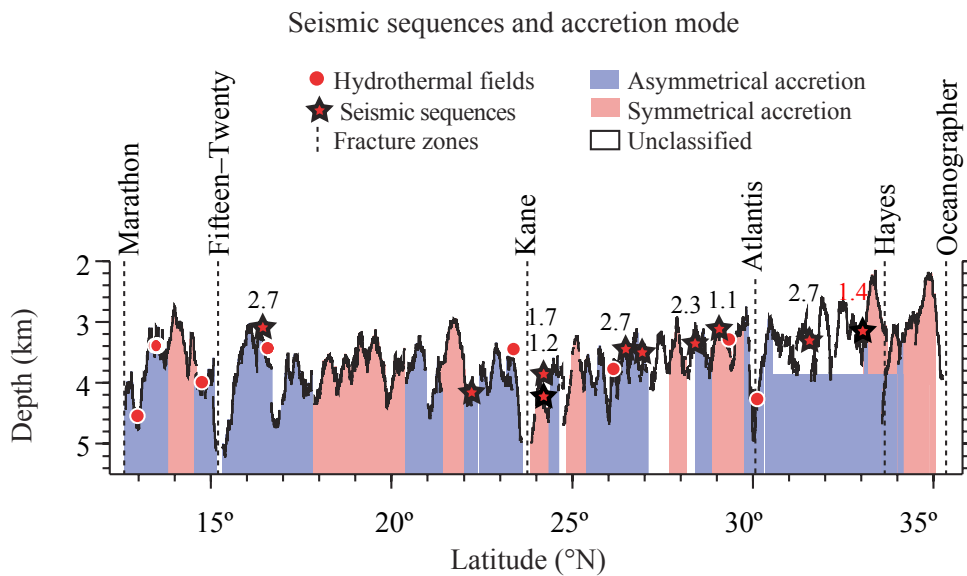


Figure 5.13: Modified figure from *Escartin et al. (2008)* with sequences emplacements and respective p -values (numbers) of the sequences. It is clear that sequences recorded on detachment faulting regions have higher p -values than the ones recorded on the abyssal hill faulting regions. The red square p -values is from the sequence that was recorded at an 30 km distance from the ridge.

The locations of the sequences were also analyzed regarding the segmentation and the MBA of the MAR. They all occurred on relatively cold segments with well defined axial valleys. This clearly shows that all the sequences are associated with higher MBA areas of the segments, suggesting that seismic sequences are more prone to occur in regions of the MAR with a denser and thinner type of crust. The crust thermal regime does not seem to be the major influence in the earthquake decay rate and the rheological strength of the fault region. The resulting p -values seems to be more dependent on the type of faulting occurring in the region and seems to suggest that high anomaly p -values are generally associated to detachment faulting created by asym-

metric accretion on the MAR and that smaller p -values are associated with normal abyssal hill type of faulting associated with more symmetric type of accretion. Such dependence may result from the presence of serpentine along the detachment faults that substantially lowers fracture and frictional strength of the lithosphere.

The transmission loss model still do not do a good job in describing T -phase generation and propagation. Nonetheless, geologic patterns are evident in the T -phase locations and character, and thus provide insight into processes acting at this slow-spreading ridge.

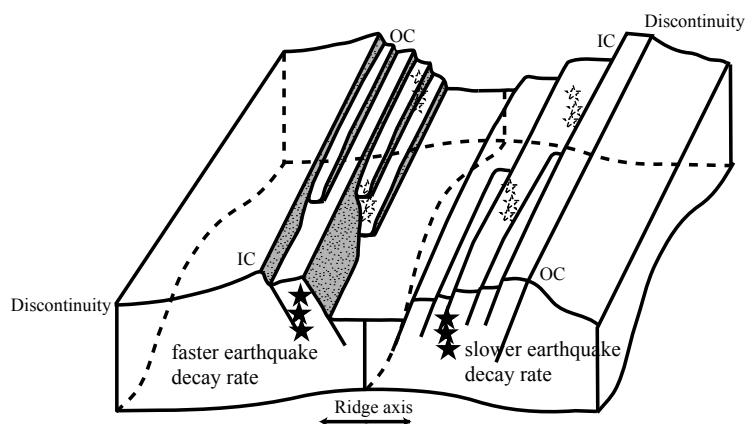


Figure 5.14: Sketch of the generic modes of faulting on one generic MAR segment related to fault strength and earthquake decay rate of seismic sequences. Detachment faults associated to a asymmetrical mode of spreading have a faster decay rate. Abyssal hill faulting associated to o asymmetrical mode of spreading have a slower decay rate of earthquakes. Stars represent seismic sequences.

Chapter 6

General Conclusions

AuH arrays prove to be an excellent tool for monitoring remote oceanic regions, due to the specific characteristics of T -phase propagation in the oceans. The AuH arrays can complement both the existing teleseismic land based networks and the OBS experiments. This work and the dissertation have focused on the eight years of data obtained during several deployments of AuH arrays on the Mid Atlantic Ridge to improve our understanding of the dynamic processes occurring along this active spreading center.

In comparison to the teleseismic record of seismicity for this oceanic region, the implementation of the AuH system, with its ensuing smaller location error confidence ellipses and lower detection thresholds, reveals what a good asset these arrays are for low magnitude seismicity studies. Furthermore, localization errors can be estimated before the arrays are deployed, which provides an indication of the precision of the earthquake locations prior to deployment. Of course, as was noted, it must not be forgotten that error confidence ellipses are strongly dependent on the number of instruments, the sound speed model of the water column and the geometry of the array.

Quantifying the AuH Source Level of earthquake energy has by certain pitfalls, which must also be considered. Instead of a measure of energy released by an earthquake (as in the case of more orthodox magnitudes) the AuHs measure the energy that is converted from seismic phases into sound at the sea-seafloor interface. Essentially this means that it does not provide a direct estimate of the earthquake's energy. With this in mind, size vs. frequency analyses of the AuH arrays deployed on the MAR revealed that the SL_c can vary in a range of ~ 15 dB, across a region of the MAR that spans more than 5000 km and which is delimited by the Marathon and Charlie Gibbs Fracture zones. This difference in SL_c can have a dramatic influence in the region between the Oceanographer Fracture Zone and the Azores. Once again, caution is required in interpreting

these results. As was indicated in the size-frequency analysis of the seismic sequences, lower or higher SL_c does not necessarily imply a smaller or greater number of recorded earthquakes. Size frequency analysis and transmission loss analysis suggest that T -phase based earthquake energy Source Levels are more strongly dependent on the conversion of seismic waves into acoustic waves than on the interaction of the propagated wave with the surrounding bathymetry.

The joint analysis of the ISC seismicity catalog and AuH catalog revealed that time limited seismic monitoring experiments on the MAR show the same background seismicity patterns observed across more than 40 years of teleseismic observation.

One of the open questions about the MAR's seismicity was: could the upper mantle and crust thermal regime bear an influence on the along-ridge distribution of the seismicity? In other words, could a slow spreading ridge have its levels of seismicity reduced as it gets over a warmer upper mantle and crust. The longer wavelengths of the MBA, with lower negatives MBA in the vicinity of the Azores, clearly hint towards an influence of the plume on the axial crustal temperature-dependent parameters. After careful consideration of the AuH detection thresholds along the MAR, the joint analysis of the long wavelengths of the AuH and ISC seismicity distributions reveals low levels of seismicity for a distance as far as 200 km from the Azores. This is a strong evidence that the presence of the Azores as a "hotspot" can truly influence the MAR's seismicity. Seismicity rates and MBA correlate very well all along the MAR, except for the region spanning from 200km south of the Azores to the Oceanographer FZ. This suggests that the crust thermal state can influence MAR's rates of seismicity. The sector between the Azores and the Oceanographer FZ shows that a strong ridge obliquity may have a large influence on the MAR's seismicity rates.

AuH seismicity revealed that medium to large magnitude earthquakes recorded by land based stations liaison with the AuH seismicity records is not strait-forward. It also shows that the most active areas in the northern sector of the Azores MAR are those where the major seismic crises recorded by the AuH occur. Furthermore, it revealed that in this sector of the MAR the seismic active sectors and seismic inactive sectors occur on very different segment morphologies. Seismic sectors typically occurred on segments with a more asymmetrical morphology and relatively wider and deeper axial valley than the aseismic sectors.

Ten new AuH-recorded seismic swarms were identified on the MAR. Seismic sequences were recorded on "cold" segments with wide and deep axial valleys. Seismic sequences were detected by the AuH arrays within the axial valley or on the flanks as far as ~ 30 km off-axis. The locations of the sequences were also analyzed with respect of the topography and MBA segmentation patterns of the MAR. This analysis shows that all the sequences were recorded

within regions where faulting (*Escartin et al.*, 2008) occurs and are associated with higher MBA areas of the segments. This suggests that seismic sequences are more prone to occur in parts of the segment with a denser and thinner type of crust.

The local crust thermal regime and the resulting rheological strength of the fault region, does not seem to bear the major influence in the earthquake decay rate. The resulting p -values seems to be more dependent on the type of faulting occurring in the region where the swarm occurred. High anomaly p -values would be generally associated to detachment faulting created by asymmetric accretion on the MAR, while smaller p -values linked to normal abyssal hill type of faulting is associated with more symmetric type of accretion. High p -values may result from the presence of serpentine along the detachment faults faults that substantially lowers fracture and frictional strength of the lithosphere.

In a final summary, the objectives of this work were: to present the autonomous hydrophone technology and its use to achieve the acoustic monitoring of distant parts of the ocean. To show the advantages and drawbacks of this technique with respect to other methods of seismic surveillance in remote parts of the oceans and to present convincing arguments that the advantages largely outweigh the drawbacks. Finally to use these inherent advantages presented by the AuH system in seismicity studies to add more to the existing knowledge of the dynamics and mechanics of the Mid Atlantic Ridge.

Bibliography

- Abercrombie, R. E., and G. Ekström (2001), Earthquake slip on oceanic transform faults., *Nature*, 410, 74–77, doi:10.1038/35065064.
- Aki, K. (1965), Maximum likelihood estimate of b in the formula $\log n = a - bM$ and its confidence limits., *Bulletin of the Earthquake Research Institute*, 43, 237–239.
- Allerton, S., J. Escartin, and R. C. Searle (2000), Extremely asymmetric magmatic accretion of oceanic crust at the ends of slow-spreading ridge-segments., *Geology*, 28(2), 179–182.
- Antonov, J. I., R. A. Locarnini, T. P. Boyer, A. V. Mishonov, and H. E. Garcia (2006), *World Ocean Atlas 2005, Volume 2: Salinity.*, 182 pp., NOAA Atlas NESDIS 62, U.S. Government Printing Office, Washington, D.C.
- Balanche, A., C. Guennou, J. Goslin, and C. Mazoyer (2009), Generation of hydroacoustic signals by oceanic subseafloor earthquakes: A mechanical model, *Geophysical Journal International*, 177(2), 476–480.
- Barclay, A. H., D. R. Toomey, and S. C. Solomon (2001), Microearthquake characteristics and crustal VP /VS structure at the Mid-Atlantic Ridge, 35 ° N., *Journal of Geophysical Research*, 106(B2), 2017–2034.
- Bazin, S., H. van Avendonk, H. A. J., J. A. Orcutt, J. P. Canales, and R. S. Detrick (1998), Crustal structure of the flanks of the East Pacific Rise: Implications for overlapping spreading centers., *Geophysical Research Letters*, 25(12), 2213–2216.
- Behn, M., J. Lin, and M. T. Zuber (2002a), Mechanisms of normal fault development at mid-ocean ridges., *Journal of Geophysical Research*, 107(B4), 10.1029/2001JB000,503, doi:10.1029/2001JB000503.
- Behn, M. D., and G. Ito (2008), Magmatic and tectonic extension at mid-ocean ridges: 1. controls on fault characteristics, *Geochem. Geophys. Geosyst.*, 9.

- Behn, M. D., J. Lin, and M. T. Zuber (2002b), A continuum mechanics model for normal faulting using a strain-rate softening rheology: implications for thermal and rheological controls on continental and oceanic rifting., *Earth and Planetary Science Letters*, 202(3-4), 725–740.
- Berchok, C. L., D. L. Bradley, and T. B. Gabrielson (2006), St. Lawrence blue whale vocalizations revisited: Characterization of calls detected from 1998 to 2001, *The Journal of the Acoustical Society of America*, 120(4), 2340–2354 doi:10.1121/1.2335,676.
- Bergman, E. A., and S. C. Solomon (1990), Earthquake swarms on the Mid-Atlantic Ridge: Products of magmatism or extensional tectonics?, *Journal of Geophysical Research*, 95(B4), 4943–4965.
- Bevington, P., and K. D. Robinson (2003), *Data Reduction and Error Analysis for the Physical Sciences (3rd Edition)*., 320 pp., McGraw-Hill, New York.
- Bohnenstiehl, D. R., and S. M. Carbotte (2001), Faulting patterns near 19°30'S on the East Pacific Rise: Fault formation and growth at a superfast spreading center., *Geochemistry Geophysics Geosystems*, 2, 2001GC000,156, doi:2001GC000156.
- Bohnenstiehl, D. R., and M. C. Kleinrock (1999), Faulting and fault scaling on the median valley floor of the Trans-Atlantic Geotraverse (TAG) segment, 26°N on the Mid-Atlantic Ridge., *Journal of Geophysical Research*, 104(B12), 29,351–29,364.
- Bohnenstiehl, D. R., and M. Tolstoy (2003), Comparison of teleseismic- and hydroacoustic-derived earthquake locations along the north-central Mid-Atlantic Ridge and equatorial East-Pacific Rise., *Seismological Research Letters*, 74(6), 790–801.
- Bohnenstiehl, D. R., M. Tolstoy, R. P. Dziak, C. G. Fox, and D. K. Smith (2002), Aftershock sequences in the mid-ocean ridge environment: An analysis using hydroacoustic data., *Tectonophysics*, 354, 49–70.
- Bohnenstiehl, D. R., M. Tolstoy, D. K. Smith, C. G. Fox, and R. P. Dziak (2003), Time-clustering behavior of spreading-center seismicity between 15° and 35°N on the Mid-Atlantic Ridge: Observations from hydroacoustic monitoring., *Physics of the Earth and Planetary Interiors*, 138, 147–161, doi:10.1016/S0031-9201(03)00113-4.
- Bohnenstiehl, D. R., R. P. Dziak, M. Tolstoy, C. G. Fox, and M. Fowler (2004), Temporal and spatial history of the 1999-2000 Endeavour Segment seismic series, Juan de Fuca Ridge., *Geochemistry Geophysics Geosystems*, 5(9), Q09,003, doi:10.1029/2004GC000735.

- Buck, W. R. (1988), Flexural rotation of normal faults., *Tectonophysics*, 7(5), 959–973.
- Buck, W. R. (2001), Accretional curvature of lithosphere at magmatic spreading centers and the flexural support of axial highs., *Journal of Geophysical Research*, 106(B3), 3953–3960.
- Buck, W. R., and A. N. B. Poliakov (1998), Abyssal hills formed by stretching oceanic lithosphere., *Nature*, 392, 272–275.
- Butler, R., and C. Lomnitz (2002), Coupled seismoacoustic modes on the seafloor., *Geophysical Research Letters*, 29(10), 1418, doi:10.1029/2002GL014722.
- Canales, J. P., J. J. Danobeitia, R. S. Detrick, E. E. E. Hooft, B. Rafael, and D. F. Naar (1997), Variations in axial morphology along the Galápagos spreading center and the influence of the Galápagos hotspot., *Journal of Geophysical Research*, 102(B12), 27,341–27,354.
- Canales, J. P., R. S. Detrick, S. Bazin, A. J. Harding, and J. A. Orcutt (1998), Off-axis crustal thickness across and along the East Pacific Rise within the MELT area., *Science*, 280, 1218–1221.
- Canales, J. P., R. S. Detrick, J. Lin, J. A. Collins, and D. R. Toomey (2000), Crustal and upper mantle seismic structure beneath the rift mountains and across a non-transform offset at the Mid-Atlantic Ridge (35°N)., *Journal of Geophysical Research*, 105(B2), 2699–2719.
- Cann, J. R., D. K. Blackman, D. K. Smith, E. McAllister, B. Janssen, S. Mello, E. Avgarinos, A. R. Pascoe, and J. Escartin (1997), Corrugated slip surfaces formed at ridge-transform intersections on the Mid Atlantic Ridge., *Nature*, 385, 329–332.
- Cannat, M. (1993), Emplacement of mantle rocks in the seafloor at mid-ocean ridges., *Journal of Geophysical Research*, 98, 4163–4172.
- Cannat, M., A. Briais, C. Deplus, J. Escartín, J. Georgen, J. Lin, S. Mercouriev, C. Meyzen, M. Muller, G. Pouliquen, A. Rabain, and P. Silva (1999), Mid-Atlantic Ridge-Azores hotspot interactions: along-axis migration of a hotspot-derived event of enhanced magmatism 10 to 4 Ma ago., *Earth and Planetary Science Letters*, 173(3), 257–269.
- Carbotte, S. M., and K. C. Macdonald (1994), Comparison of seafloor tectonic fabric at intermediate, fast, and super fast spreading ridges: Influence of spreading rate, plate motions, and ridge segmentation on fault patterns., *Journal of Geophysical Research*, 99(B7), 13,609–13,631.

- Carbotte, S. M., W. B. F. Ryan, W. Jin, M.-H. Cormier, E. Bergmanis, J. Sinton, and S. White (2002), Magmatic subsidence of the east pacific rise (EPR) at 18°14'S revealed through fault restoration of ridge crest bathymetry., *Geochemistry Geophysics Geosystems*, 3(1), 10.1029/2002GC000,337, doi:10.1029/2002GC000337.
- Chapp, E., D. R. Bohnenstiehl, and M. Tolstoy (2005), Sound-channel observations of ice-generated tremor in the Indian Ocean., *Geochemistry Geophysics Geosystems*, 6(doi:10.1029/2004GC000889).
- Chen, Y., and W. J. Morgan (1990a), A non linear rheology model for mid-ocean ridge axis topography., *Journal of Geophysical Research*, 95, 17,583–17,604.
- Chen, Y., and W. J. Morgan (1990b), Rift valley/no rift valley transition at mid-ocean ridges., *Journal of Geophysical Research*, 95, 17,571–17,581.
- Cowie, P. A., and C. H. Scholz (1992), Displacement-length scaling relationship for faults: Data synthesis and discussion., *Journal of Structural Geology*, 14, 1149–1156.
- Cowie, P. A., C. H. Scholz, M. Edwards, and A. Malinverno (1993), Fault strain and seismic coupling on mid-ocean ridges., *Journal of Geophysical Research*, 98, 17,911–17,920.
- Davis, S. D., and C. Frohlich (1991), Single-link cluster analysis, synthetic earthquake catalogues, and aftershock identification., *Geophysical Journal International*, 104(2), 289–306, doi:10.1111/j.1365-246X.1991.tb02512.x.
- de Groot-Hedlin, C. D., and J. A. Orcutt (1999), Synthesis of earthquake generated T-waves., *Geophysical Research Letters*, 26(9), 1227–1230.
- de Groot-Hedlin, C. D., and J. A. Orcutt (2001), Excitation of T-phases by seafloor scattering., *Journal of the Acoustical Society of America*, 109(5), 1–11, doi:10.1121/1.1361057.
- de Martin, B. J., R. A. Sohn, J. P. Canales, and S. E. Humphris (2007), Kinematics and geometry of active detachment faulting beneath the Trans-Atlantic Geotraverse (TAG) hydrothermal field on the Mid-Atlantic Ridge., *Geology*, 35(8), 711–714, doi:10.1130/G23718A.1.
- DeMets, C., R. G. Gordon, D. F. Argus, and S. Stein (1990), Current plate motions., *Geophysical Journal International*, 101(2), 425–478.

- Detrick, R. S., J. C. Mutter, P. Buhl, and I. I. Kim (1990), No evidence from multichannel reflection data for a crustal magma chamber in the MARK area on the Mid-Atlantic Ridge., *Nature*, 347, 61–64, doi:10.1038/347061a0.
- Detrick, R. S., H. D. Needham, and V. Renard (1995), Gravity anomalies and crustal thickness variations along the Mid-Atlantic Ridge between 33°N and 40°N., *Journal of Geophysical Research*, 100(B3), 3767–3787.
- Dick, H. J. B., J. H. Natland, J. C. Alt, W. Bach, D. Bideau, J. S. Gee, S. Haggas, J. G. H. Hertogen, G. Hirth, P. M. Holm, B. Ildefonse, G. J. Iturrino, B. E. John, D. S. Kelley, E. Kikawa, A. Kingdon, P. J. LeRoux, J. Maeda, P. S. Meyer, D. J. Miller, H. R. Naslund, Y. Niu, P. T. Robinson, J. Snow, R. A. Stephen, P. W. Trimby, H.-U. Worm, and A. Yoshinobu (2000), A long in situ section of the lower ocean crust: results of ODP Leg 176 drilling at the Southwest Indian Ridge., *Earth and Planetary Science Letters*, 179(1), 31–51, doi:10.1016/S0012-821X(00)00102-3.
- Dick, H. J. B., M. A. Tivey, and B. E. Tucholke (2008), Plutonic foundation of a slow-spreading ridge segment: Oceanic core complex at Kane Megamullion, 23°30'N, 45°20'W., *Geochemistry Geophysics Geosystems*, 9(5), Q05,014, doi:10.1029/2007GC001645.
- Dieterich, J. (1994), A constitutive law for rate of earthquake production and its application to earthquake clustering., *Journal of Geophysical Research*, 99(B9), 2601–2618.
- Dziak, R. P. (2001), Empirical relationship of T-wave energy and fault parameters of northeast Pacific Ocean earthquakes., *Geophysical Research Letters*, 28(13), 2537–2540.
- Dziak, R. P. (2006), Explorer deformation zone: Evidence of a large shear zone and reorganization of the Pacific-Juan de Fuca-North American triple junction., *Geology*, 34(3), 213–216, doi:10.1130/G22164.1.
- Dziak, R. P., and C. G. Fox (1999a), Long-term seismicity and ground deformation at Axial Volcano, Juan de Fuca Ridge., *Geophysical Research Letters*, 26(24), 3641–3644.
- Dziak, R. P., and C. G. Fox (1999b), The January 1998 earthquake swarm at Axial Volcano, Juan de Fuca Ridge: Hydroacoustic evidence of a seafloor volcanic activity., *Geophysical Research Letters*, 26(23), 3429–3432.

- Dziak, R. P., C. G. Fox, and A. E. Schreiner (1995), The June-July 1993 seismo-acoustic event at Co-Axial segment, Juan de Fuca Ridge: Evidence for a lateral dike injection., *Geophysical Research Letters*, 22(2), 135–138.
- Dziak, R. P., C. G. Fox, H. Matsumoto, and A. E. Schreiner (1997), The April 1992 Cape Mendocino earthquake sequence: seismo-acoustic analysis utilizing fixed hydrophone arrays., *Marine Geophysical Researches*, 19, 137–162.
- Dziak, R. P., C. G. Fox, R. W. Embley, J. L. Nabelek, J. Braunmiller, and R. A. Koski (2000), Recent tectonics of the Blanco Ridge, eastern Blanco transform fault zone., *Marine Geophysical Researches*, 21, 423–450.
- Dziak, R. P., W. W. Chadwick Jr., C. G. Fox, and R. W. Embley (2003), Hydrothermal temperature changes at the southern Juan de Fuca Ridge associated with Mw 6.2 Blanco Transform earthquake., *Geology*, 31(2), 119–122, doi:10.1130/0091-7613(2003)031.
- Dziak, R. P., D. K. Smith, D. R. Bohnenstiehl, C. G. Fox, D. Desbruyeres, H. Matsumoto, M. Tolstoy, and D. J. Fornari (2004a), Evidence of a recent magma dike intrusion at the slow spreading Lucky Strike segment, Mid-Atlantic Ridge., *Journal of Geophysical Research*, 109(B12102), 10.1029/2004JB003141, doi:10.1029/2004JB003141.
- Dziak, R. P., D. R. Bohnenstiehl, H. Matsumoto, C. G. Fox, D. K. Smith, M. Tolstoy, T.-K. Lau, J. H. Haxel, and M. J. Fowler (2004b), P- and T-wave detection thresholds, Pn velocity estimate, and detection of lower mantle and core P-waves on ocean sound-channel hydrophones at the Mid-Atlantic Ridge., *Bulletin of the Seismological Society of America*, 94(2), 665–677, doi:10.1785/0120030156.
- Engeln, J. F., D. A. Wiens, and S. Stein (1986), Mechanisms and depths of Atlantic transform earthquakes., *Journal of Geophysical Research*, 91, 548–577, doi:10.1029/JB091iB01p00548.
- Engen, O., O. Eldholm, and H. Bungum (2003), The Arctic plate boundary., *Journal of Geophysical Research*, 108(B2), 2075, doi:10.1029/2002JB001809.
- Escartin, J., and M. Cannat (1999), Ultramafic exposures and the gravity signature of the lithosphere near the Fifteen-Twenty Fracture Zone (Mid-Atlantic Ridge, 14°-16.5°N)., *Earth and Planetary Science Letters*, 171, 411–424.
- Escartin, J., and J. Lin (1995), Ridge offsets, normal faulting, and gravity anomalies of slow spreading ridges., *Journal of Geophysical Research*, 100(B4), 6163–6177.

- Escartin, J., and J. Lin (1998), Tectonic modification of axial crustal structure: Evidence from spectral analyses of residual gravity and bathymetry of the Mid-Atlantic Ridge flanks., *Earth and Planetary Science Letters*, 154, 279–293.
- Escartin, J., G. Hirth, and B. Evans (1997), Effects of serpentinization on the lithospheric strength and the style of normal faulting at slow-spreading ridges., *Earth and Planetary Science Letters*, 151, 181–189.
- Escartin, J., P. A. Cowie, R. C. Searle, S. Allerton, N. C. Mitchell, C. J. MacLeod, and P. A. Sloomweg (1999), Quantifying tectonic strain and magmatic accretion at a slow-spreading ridge segment, Mid-Atlantic Ridge, 29°N., *Journal of Geophysical Research*, 104, 10,421–10,437.
- Escartin, J., C. Mével, C. J. MacLeod, and A. M. McCaig (2003a), Constraints on deformation conditions and the origin of oceanic detachments: The Mid-Atlantic Ridge core complex at 15°45'N., *Geochemistry Geophysics Geosystems*, 4(8), 1067, doi:10.1029/2002GC000472.
- Escartin, J., D. K. Smith, and M. Cannat (2003b), Parallel bands of seismicity at the Mid-Atlantic Ridge, 12–14°N., *Geophysical Research Letters*, 30(12), 1620, doi:10.1029/2003GL017226.
- Escartin, J., D. K. Smith, J. Cann, H. Schouten, C. H. Langmuir, and S. Escrig (2008), Central role of detachment faults in accretion of slow-spreading oceanic lithosphere, *Nature*, 455(7214), 790–794.
- Fox, C. G., and R. P. Dziak (1998), Hydroacoustic detection of volcanic activity on the Gorda Ridge, February–March 1996., *Deep-Sea Research II*, 45, 2513–2530.
- Fox, C. G., W. E. Radford, R. P. Dziak, T.-K. Lau, H. Matsumoto, and A. E. Schreiner (1995), Acoustic detection of a seafloor spreading episode on the Juan de Fuca Ridge using military hydrophone arrays., *Geophysical Research Letters*, 22(2), 131–134.
- Fox, C. G., H. Matsumoto, and A. L. Tai-Kwan (2001), Monitoring Pacific Ocean seismicity from an autonomous hydrophone array., *Journal of Geophysical Research*, 106(B3), 4183–4206.
- Fox, J. (1984), *Linear statistical models and related methods with applications to social research.*, 449 pp., Wiley, New York.
- Fox, P. J., N. R. Grindlay, and K. C. MacDonald (1991), The Mid-Atlantic Ridge (31°S 34°30'S): Temporal and spatial variations of accretionary processes., *Marine Geophysical Researches*, 13(1), 1–20, doi:10.1007/BF02428193.

- Frohlich, C., and S. D. Davis (1990), Single-link cluster analysis as a method to evaluate spatial and temporal properties of earthquake catalogues., *Geophysical Journal International*, 100(1), 19–32, doi:10.1111/j.1365-246X.1990.tb04564.x.
- Fujiwara, T., J. Lin, T. Matsumoto, P. B. Kelemen, B. E. Tucholke, and J. F. Casey (2003), Crustal evolution of the Mid-Atlantic Ridge near Fifteen-Twenty Fracture Zone in the last 5 Ma., *Geochemistry Geophysics Geosystems*, 4, 1024, doi:10.1029/2002GC000364.
- Gac, S., J. Dymant, C. Tisseau, and J. Goslin (2003), Axial magnetic anomalies over slow-spreading ridge segments: insights from numerical 3-D thermal and physical modelling, *Geophysical Journal International*, 154(3), 618–632.
- Gac, S., C. Tisseau, J. Dymant, and J. Goslin (2006), Modelling the thermal evolution of slow-spreading ridge segments and their off-axis geophysical signature, *Geophysical Journal International*, 164(doi:10.1111/j.1365-246X.2005.02844.x), 341–358(18).
- Goltz, C. (2001), Decomposing spatio-temporal seismicity patterns, *Natural Hazards and Earth System Science*, 1(1/2), 83–92.
- Goslin, J., M. Benoit, D. Blanhard, M. Bohn, L. Dosso, S. Dreher, P. Gente, R. Gloaguen, M. Maia, J.-P. Oldra, M. Ravilly, and J.-L. Thirot (1999), Extent of Azores plume influence on the Mid-Atlantic Ridge north of the hotspot., *Geology*, 27(11), 991–994, doi:10.1130/0091-7613(1999)027<0991:EOAPIO>2.3.CO;2.
- Goslin, J., N. Lourenço, R. P. Dziak, D. R. Bohnenstiehl, J. Haxel, and J. Luis (2005), Long-term seismicity of the Reykjanes Ridge (North Atlantic) recorded by a regional hydrophone array., *Geophysical Journal International*, 162, 516–524, doi:10.1111/j.1365-246X.2005.02678.x.
- Grandin, R., A. Socquet, R. Binet, Y. Klinger, E. Jacques, J. B. de Chabalier, G. C. P. King, C. Lasserre, S. Tait, P. Tapponnier, A. Delorme, and P. Pinzuti (2009), September 2005 manda hararo-dabbahu rifting event, afar (ethiopia): Constraints provided by geodetic data, *J. Geophys. Res.*, 114.
- Grindlay, N. R., P. J. Fox, and K. C. MacDonald (1991), Second-order ridge axis discontinuities in the south Atlantic: Morphology, structure, and evolution., *Marine Geophysical Researches*, 13(1), 21–49, doi:10.1007/BF02428194.

- Grindlay, N. R., P. J. Fox, and P. R. Vogt (1992), Morphology and tectonics of the Mid-Atlantic Ridge (25°-27°30'S) from sea beam and magnetic data., *Journal of Geophysical Research*, 97(B5), 6983–7010.
- Gutenberg, B., and C. Richter (1944), Frequency of earthquakes in California., *Bulletin of the Seismological Society of America*, 34(4), 185–188.
- Haxel, J. H., and R. P. Dziak (2005), Evidence of explosive seafloor volcanic activity from the Walvis Ridge, South Atlantic Ocean., *Geophysical Research Letters*, 32, L13,609, doi:10.1029/2005GL023205.
- Helfrich, G., S. I. N. Heleno, B. Faria, and J. F. B. D. Fonseca (2006), Hydroacoustic detection of volcanic ocean-island earthquakes., *Geophysical Journal International*, 167, 1529–1536, doi:10.1111/j.1365-246X.2006.03228.x.
- Hooft, E. E. E., R. S. Detrick, D. R. Toomey, J. A. Collins, and J. Lin (2000), Crustal thickness and structure along three contrasting spreading segments of the Mid-Atlantic Ridge, 33.5°-35°N., *Journal of Geophysical Research*, 105(B4), 8205–8226.
- Huang, P. Y., and S. C. Solomon (1988), Centroid depths of mid-ocean ridge earthquakes: Dependence on spreading rate., *Journal of Geophysical Research*, 93, 13,445–13,477.
- Jaroslow, G. E., G. Hirth, and H. J. B. Dick (1996), Abyssal peridotite mylonites: Implications for grain-size sensitive flow and strain localization in the oceanic lithosphere., *Tectonophysics*, 256(1-4), 17–37.
- Karson, J. A., G. Thompson, S. E. Humphris, J. M. Edmond, W. B. Bryan, J. R. Brown, A. T. Winters, R. A. Pockalny, J. R. Casey, G. Klinkhammer, M. R. Palmer, R. J. Kinzler, and M. M. Sulanowska (1987), Along-axis variations in seafloor spreading in the MARK area., *Nature*, 328, 681–685.
- Kibblewhite, A. C., and L. D. Hampton (1980), A review of deep ocean sound attenuation data at very low frequencies., *Journal of the Acoustical Society of America*, 67(1), 147–157, doi:10.1121/1.384473.
- Kinsler, L. E., A. R. Frey, A. B. Coppens, and J. V. Sanders (1982), *Fundamentals of Acoustics*., 480 pp., Wiley, New York.
- Kisslinger, C. (1996), Aftershocks and fault-zone properties., *Advances in geophysics*, 38, 1–36.

- Kisslinger, C., and L. M. Jones (1991), Properties of aftershock sequences in southern California., *Journal of Geophysical Research*, 96(B7), 11,947–11,958.
- Klein, F. W., T. Wright, and J. Nakata (2006), Aftershock decay, productivity, and stress rates in Hawaii: Indicators of temperature and stress from magma sources., *Journal of Geophysical Research*, 111(B7), B07,307, doi:10.1029/2005JB003949.
- Kong, L. S. L., S. C. Solomon, and G. M. Purdy (1992), Microearthquake characteristics of a mid-ocean ridge along-axis high., *Journal of Geophysical Research*, 97(B2), 1659–1685.
- Kuo, B.-Y., and D. W. Forsyth (1988), Gravity anomalies of the ridge-transform system in the South Atlantic between 31 and 34.5°S: Upwelling centers and variations in crustal thickness., *Marine Geophysical Researches*, 10(3-4), 205–232, doi:10.1007/BF00310065.
- Lavier, L. L., and W. R. Buck (2002), Half graben versus large-offset low-angle normal fault: Importance of keeping cool during normal faulting., *Journal of Geophysical Research*, 107(B6), 2122, doi:10.1029/2001JB000513.
- Lavier, L. L., W. R. Buck, and A. N. B. Poliakov (1999), Self-consistent rolling-hinge model for the evolution of large-offset low-angle normal faults., *Geology*, 27(12), 1127–1130.
- Leurer, K. C. (2004), Compressional- and shear-wave velocities and attenuation in deep-sea sediment during laboratory compaction., *The Journal of the Acoustical Society of America*, 116(4), 2023–2030, doi:10.1121/1.1782932.
- Lin, J., and E. M. Parmentier (1989), Mechanisms of lithospheric extension at mid-ocean ridges., *Geophysical Journal*, 96, 1–22.
- Lin, J., and J. Phipps Morgan (1992), The spreading rate dependence of three-dimensional mid-ocean ridge gravity structure., *Geophysical Research Letters*, 19(1), 13–16.
- Lin, J., G. M. Purdy, H. Schouten, J.-C. Sempéré, and C. Zervas (1990), Evidence from gravity data for focused magmatic accretion along the Mid-Atlantic Ridge., *Nature*, 344, 627–632, doi:10.1038/344627a0.
- Locarnini, R. A., A. V. Mishonov, J. I. Antonov, T. P. Boyer, and H. E. Garcia (2006), *World Ocean Atlas 2005, Volume 1: Temperature.*, 182 pp., NOAA Atlas NESDIS 61, U.S. Government Printing Office, Washington, D.C.

- Luis, F. J., J. M. Miranda, A. Galdeano, P. Patriat, J. C. Rossignol, and L. A. Mendes Victor (1994), The Açores Triple Junction evolution since 10 Ma from an aeromagnetic survey of the Mid-Atlantic Ridge., *Earth and Planetary Science Letters*, 125, 439–459.
- Macdonald, K. C. (1998), *Faulting and Magmatism at Mid-Ocean Ridges*, vol. 106, chap. Linkages between faulting, volcanism, hydrothermal activity and segmentation on fast spreading centers., pp. 27–58, Geophysical Monograph, American Geophysical Union, Washington, D.C.
- Macdonald, K. C., D. S. Scheirer, and S. M. Carbotte (1991), Mid-ocean ridges: Discontinuities, segments and giant cracks., *Science*, 253, 986–994.
- MacLeod, C. J., J. Escartin, D. Banerji, G. J. Banks, M. Gleeson, D. B. Irving, R. M. Lilly, A. M. McCaig, Y. Niu, S. Allerton, and D. K. Smith (2002), Direct geological evidence for oceanic detachment faulting: The Mid-Atlantic Ridge, 15°45'N., *Geology*, 30(10), 879–882.
- Magde, L. S., and D. W. Sparks (1997), Three-dimensional mantle upwelling, melt generation, and melt migration beneath segment slow spreading ridges., *Journal of Geophysical Research*, 102(B9), 20,571–20,583.
- Magde, L. S., D. W. Sparks, and R. S. Detrick (1997), The relationship between buoyant mantle flow, melt migration, and gravity bull's eyes at the Mid-Atlantic Ridge between 33°N and 35°N., *Earth and Planetary Science Letters*, 148(1-2), 59–67, doi:10.1016/S0012-821X(97)00039-3.
- Maia, M., and J. Arkani-Hamed (2002), The support mechanism of the young Foundation Seamounts inferred from bathymetry and gravity., *Geophysical Journal International*, 149(1), 190–210, doi:10.1046/j.1365-246X.2002.01635.x.
- Maia, M., J. Goslin, and P. Gente (2007), Evolution of the accretion processes along the Mid-Atlantic Ridge north of the Azores since 5.5 Ma: An insight into the interactions between the ridge and the plume., *Geochemistry Geophysics Geosystems*, 8(3), Q03,013, doi:10.1029/2006GC001318.
- Marsaglia, G., W. W. Tsang, and J. Wang (2003), Evaluating Kolmogorov's Distribution., *Journal of Statistical Software*, 8(18).
- Massey, F. J. (1951), The Kolmogorov-Smirnov test for goodness of fit, *Journal of the American Statistical Association*, 46(253), 68–78.

- Miller, L. H. (1956), Table of percentage points of Kolmogorov Statistics., *Journal of the American Statistical Association*, 51(273), 111–121.
- Nyffenegger, P., and C. Frohlich (1998), Recommendations for determining p-values for aftershock sequences and catalogs., *Bulletin of the Seismological Society of America*, 88(5), 1144–1154.
- Nyffenegger, P., and C. Frohlich (2000), Aftershock occurrence rate decay properties for intermediate and deep earthquake sequences., *Geophysical Research Letters*, 27(8), 1215–1218.
- Odom, R. I. (1986), A coupled mode examination of irregular waveguides including the continuum spectrum., *Geophysical Journal of the Royal Astronomical Society*, 86(2), 425–453, doi:10.1111/j.1365-246X.1986.tb03836.x.
- Ogata, Y. (1983), Estimation of the parameters in the modified Omori formula for aftershock frequencies by the maximum likelihood procedure., *Journal of Physics of the Earth*, 31(2), 115–124.
- Ogata, Y., and K. Katsura (1993), Analysis of temporal and spatial heterogeneity of magnitude frequency distribution inferred from earthquake catalogues., *Geophysical Journal International*, 113, 727–738, doi:10.1111/j.1365-246X.1993.tb04663.x.
- Ogata, Y., and K. Shimazaki (1984), Transition from aftershock to normal activity: The 1965 Rat Islands earthquake aftershock sequence., *Bulletin of the Seismological Society of America*, 74(5), 1757–1765.
- Okal, E. A., and J. Talandier (1997), T waves from the great 1994 Bolivian deep earthquake in relation to channeling of S wave energy up the slab., *Journal of Geophysical Research*, 102(B12), 27,421–27,437.
- Pan, J., and M. Dziewonski (2005), Comparison of mid-oceanic earthquake epicentral differences of travel time, centroid locations, and those determined by autonomous underwater hydrophone arrays., *Journal of Geophysical Research*, 110, B07,302, doi:10.1029/2003JB002785.
- Park, M., and R. I. Odom (1999), Propagators and Feynman diagrams for laterally heterogeneous elastic media., *Geophysical Journal International*, 160, 289–301, doi:10.1111/j.1365-246X.2004.02469.x.

- Park, M., R. I. Odom, and D. J. Soukup (2001), Modal scattering: a key to understanding oceanic T-waves., *Geophysical Research Letters*, 28(17), 3401–3404.
- Pekeris, C. L. (1948), Theory of propagation of explosive sound in shallow water., *Geol. Soc. Am. Memoir*, 27.
- Phipps Morgan, J., and Y. J. Chen (1993), Dependence of ridge-axis morphology on magma supply and spreading rate., *Nature*, 364, 706–708.
- Press, W. H., S. A. Teukolsky, W. T. Vetterling, and B. P. Flannery (1996), *Numerical Recipes in Fortran 90*, Cambridge University Press, Cambridge, U. K.
- Rabinowitz, N., and D. M. Steinberg (1998), Aftershock decay of three recent strong earthquakes in the Levant ., *Bulletin of the Seismological Society of America*, 88(6), 1580–1587.
- Ranero, C. R., and T. J. Reston (1999), Detachment faulting at ocean core complexes., *Geology*, 27(11), 983–986.
- Richardson, W. J., C. R. J. Greene, M. C. J., and D. H. Thomson (1995), *Marine Mammals and Noise.*, 576 pp., Academic Press, San Diego, CA.
- Ross, D. (1976), *Mechanics of Underwater Noise.*, 375 pp., Pergamon Press.
- Sandwell, D. T., and W. H. F. Smith (1997), Marine gravity anomaly from GEOSAT and ERS1 satellite altimetry., *Journal of Geophysical Research*, 102(B5), 10,039–10,054.
- Scholz, H. (1990), *The Mechanics of Earthquakes and Faulting.*, 439 pp., Cambridge University Press, Cambridge, U. K.
- Schorlemmer, D., G. Neri, S. Wiemer, and A. Mostaccio (2003), Stability and significance tests for b-value anomalies: Example from the Tyrrhenian Sea., *Geophysical Research Letters*, 30(16), 1835, doi:10.1029/2003GL017335.
- Schorlemmer, D., S. Wiemer, and M. Wyss (2005), Variations in earthquake-size distribution across different stress regimes., *Nature*, 437, doi:10.1038/nature04,094.
- Schouten, H., K. D. Klitgord, and J. A. Whitehead (1985), Segmentation of mid-ocean ridges., *Nature*, 317, 225–229, doi:10.1038/317225a0.

- Schreiner, A. E., C. G. Fox, and R. P. Dziak (1995), Spectra and magnitudes of T-waves from the 1993 earthquake swarm on the Juan de Fuca Ridge., *Geophysical Research Letters*, 22(2), 139–142.
- Searle, R. C., and J. Escartin (2004), *The rheology and morphology of oceanic lithosphere and mid-ocean ridges.*, vol. 148, pp. 63–93, Geophysical Monograph, American Geophysical Union, Washington, DC.
- Searle, R. C., J. A. Keeton, R. B. Owens, R. S. White, R. Mecklenburgh, B. Parsons, and S. M. Lee (1998a), The Reykjanes Ridge: structure and tectonics of a hot-spot-influenced, slow-spreading ridge, from multibeam bathymetry, gravity and magnetic investigations., *Earth and Planetary Science Letters*, 160(3-4), 463–478, doi:10.1016/S0012-821X(98)00104-6.
- Searle, R. C., P. A. Cowie, N. C. Mitchell, S. Allerton, C. J. MacLeod, J. Escartin, S. M. Russell, P. A. Slooteg, and T. Tanaka (1998b), Fault structure and detailed evolution of a slow spreading ridge segment: the Mid-Atlantic Ridge at 29°N., *Earth and Planetary Science Letters*, 154, 167–183.
- Searle, R. C., M. Cannat, K. Fujioka, C. Mevel, H. Fujimoto, A. Bralee, and L. Parson (2003), The FUJI Dome: A large detachment fault near 64°E on the very slow-spreading southwest Indian Ridge., *Geochemistry Geophysics Geosystems*, 4(8), 9105, doi:10.1029/2003GC000519.
- Sella, G. F., T. H. Dixon, and A. Mao (2002), REVEL: A model for recent plate velocities from space geodesy., *Journal of Geophysical Research*, 107(B4), 2081, doi:10.1029/2000JB000033.
- Sempéré, J.-C., P. Blondel, A. Briais, T. Fujiwara, L. Géli, N. Isezaki, J. E. Pariso, L. Parson, P. Patriat, and C. Rommevaux (1995), The Mid-Atlantic Ridge between 29°N and 31°30'N in the last 10 Ma., *Earth and Planetary Science Letters*, 130(1-4), 45–55, doi:10.1016/0012-821X(94)00259-2.
- Severinghaus, J. P., and K. C. MacDonald (1988), High inside corners at ridge-transform intersections., *Marine Geophysical Researches*, 9, 353–367.
- Shaw, B. E. (1995), Frictional weakening and slip complexity in earthquake faults., *Journal of Geophysical Research*, 100.
- Shaw, P. R. (1992), Ridge segmentation, faulting and crustal thickness in the Atlantic ocean., *Nature*, 358, 490–493.

- Shaw, W. J., and J. Lin (1996), Models of ocean ridge lithospheric deformation: Dependence on crustal thickness, spreading rate, and segmentation., *Journal of Geophysical Research*, *101*(B8), 17,977–17,993.
- Shurbet, D. H., and M. Ewing (1957), T-phases at Bermuda and transformation of elastic waves., *Bulletin of the Seismological Society of America*, *47*(3), 251–262.
- Sinton, J. M., and R. S. Detrick (1992), Mid-ocean ridge magma chambers, *Journal of Geophysical Research*, *97*(B1), 197–216.
- Slack, P. D., C. G. Fox, and R. P. Dziak (1999), P wave detection thresholds, Pn velocity estimates, and T-wave location uncertainty from oceanic hydrophones., *Journal of Geophysical Research*, *104*(B6), 13,061–13,072.
- Smith, D. K., M. Tolstoy, C. G. Fox, B. D. R., H. Matsumoto, and M. J. Fowler (2002), Hydroacoustic monitoring of seismicity at the slow-spreading Mid-Atlantic Ridge., *Geophysical Research Letters*, *29*(11), 10.1029/2001GL013,912, doi:10.1029/2001GL013912.
- Smith, D. K., J. Escartin, M. Cannat, M. Tolstoy, C. G. Fox, D. R. Bohnenstiehl, and S. Bazin (2003), Spatial and temporal distribution of seismicity along the northern Mid-Atlantic Ridge (15°–35°N)., *Journal of Geophysical Research*, *108*(B3), 2167, doi:10.1029/2002JB001964.
- Smith, D. K., J. R. Cann, and J. Escartin (2006), Widespread active detachment faulting and core complex formation near 13°N on the Mid-Atlantic Ridge., *Nature*, *442*(7101), 440–443, doi:10.1038/nature04950.
- Smith, D. K., J. Escartin, H. Schouten, and J. R. Cann (2008), Fault rotation and core complex formation: Significant processes in seafloor formation at slow-spreading mid-ocean ridges (Mid-Atlantic Ridge, 13°–15°N)., *Geochemistry Geophysics Geosystems*, *9*(03), Q03,003, doi:10.1029/2007GC001699.
- Smith, K. B. (2001), Convergence, stability, and variability of shallow water acoustic predictions using a split-step Fourier parabolic equation model., *Journal of Computational Acoustics*, *9*(1), 243–285.
- Smith, K. B., G. L. D'Spain, and W. S. Hodgkiss (1993), Modeling acoustic particle velocity in range-dependent environments with a parabolic equation code., *The Journal of the Acoustical Society of America*, *94*(3), 1885–1885 doi:10.1121/1.407,541.

- Sparks, D. W., and E. M. Parmentier (1991), Melt extraction from the mantle beneath spreading centers., *Earth and Planetary Science Letters*, 105(4), 368–377, doi:10.1016/0012-821X(91)90178-K.
- Talandier, J., and E. A. Okal (1998), On the mechanism of conversion of seismic waves to and from T waves in the vicinity of island shores., *Bulletin of the Seismological Society of America*, 88, 621–632.
- Tapponnier, P., and J. Francheteau (1978), Necking of the lithosphere and the mechanics of slowly accreting plate boundaries., *Journal of Geophysical Research*, 83, 3955–3970.
- Teague, W. J., M. J. Carron, and P. J. Hogan (1990), A comparison between the Generalized Digital Environmental Model and Levitus climatologies., *Journal of Geophysical Research*, 95, 7167–7183.
- Thibaud, R., P. Gente, and M. Maia (1998), A systematic analysis of the Mid-Atlantic Ridge morphology and gravity between 15°N and 40°N: Constraints of the thermal structure., *Journal of Geophysical Research*, 103(B10), 24,223–24,243.
- Tompkins, M. J., and N. I. Christensen (2001), Ultrasonic P- and S-wave attenuation in oceanic basalt., *Geophysical Journal International*, 145(1), 172–186, doi:10.1046/j.0956-540x.2001.01354.x.
- Toomey, D. R., S. C. Solomon, G. M. Purdy, and M. H. Murray (1985), Microearthquakes beneath the median valley of the Mid-Atlantic Ridge near 23°N: Hypocenters and focal mechanisms., *Journal of Geophysical Research*, 90(B7), 5443–5458, doi:10.1029/JB090iB07p05443.
- Toomey, D. R., S. C. Solomon, and G. M. Purdy (1988), Microearthquakes beneath the median valley of the Mid-Atlantic Ridge near 23°N: Tomography and tectonics., *Journal of Geophysical Research*, 93(B8), 9093–9112.
- Tucholke, B., J. Lin, and M. Kleinrock (1998), Megamullions and mullion structure defining oceanic metamorphic core complexes on the Mid-Atlantic Ridge., *Journal of Geophysical Research*, 103(B5), 9857–9866.
- Tucholke, B. E., and J. Lin (1994), A geological model for the structure of ridge segments in slow spreading ocean crust., *Journal of Geophysical Research*, 99, 11,937–11,958.

- Tucholke, B. E., J. Lin, M. C. Kleinrock, M. A. Tivey, B. Reed, Thomas, J. Goff, and G. E. Jaroslow (1997), Segmentation and crustal structure of the western Mid-Atlantic Ridge flank, 25°25'N-27°10'N and 0-29 m.y., *Journal of Geophysical Research*, 102(B5), 10,203–10,223.
- Tucholke, B. E., K. Fujioka, T. Ishihara, G. Hirth, and M. Kinoshita (2001), Submersible study of an oceanic megamullion in the central North Atlantic., *Journal of Geophysical Research*, 106, 16,145–16,161.
- Urick, R. J. (1983), *Principles of Underwater Sound. 3rd Edition*, 423 pp., McGraw-Hill, New York.
- Utsu, T. (1965), A method for determining the value of b in a formula $\log n = a - bM$ showing the magnitude-frequency relation for earthquakes., *Geophysical Bulletin of the Hokkaido University*, 13, 99–103.
- Utsu, T., Y. Ogata, and R. S. Matsu'ura (1995), The centenary of the Omori formula for a decay law of aftershock activity., *Journal of Physics of the Earth*, 43, 1–33.
- Warren, N. W., and G. V. Latham (1970), An experimental study of thermally induced microfracturing and its relation to volcanic seismicity., *Journal of Geophysical Research*, 75.
- Wiemer, S. (2001), A software package to analyze seismicity: ZMAP., *Seismological Research Letters*, 72(2), 374–383.
- Wiemer, S., and M. Wyss (2002), Mapping spatial variability of the frequency-magnitude distribution of earthquakes., *Advances in geophysics*, 45, 259–302.
- Wiemer, S., M. Gerstenberger, and E. Hauksson (2002), Properties of the Aftershock Sequence of the 1999 Mw 7.1 Hector Mine Earthquake: Implications for Aftershock Hazard, *Bulletin of the Seismological Society of America*, 92(4), 1227–1240, doi:10.1785/0120000914.
- Williams, C. M., R. A. Stephen, and D. K. Smith (2006), Hydroacoustic events located at the intersection of the Atlantis (30°N) and Kane (23°40'N) transform faults with the Mid-Atlantic Ridge., *Geochemistry Geophysics Geosystems*, 7(6), Q06,015, doi:10.1029/2005GC001127.
- Woessner, J., and S. Wiemer (2005), Assessing the quality of earthquake catalogues: Estimating the magnitude of completeness and its uncertainty., *Bulletin of the Seismological Society of America*, 95(2), 684–698, doi:10.1785/0120040007.

- Wolfe, C. J., G. M. Purdy, D. R. Toomey, and S. C. Solomon (1995), Microearthquake characteristics and crustal velocity structure at 29°N on the Mid-Atlantic Ridge: The architecture of a slowspreading segment., *Journal of Geophysical Research*, 100(B12), 24,449–24,472, doi: 10.1029/95JB02399.
- Wright, T. J., C. Ebinger, J. Biggs, A. Ayele, G. Yirgu, D. Keir, and A. Stork (2006), Magma-maintained rift segmentation at continental rupture in the 2005 afar dyking episode, *Nature*, 442(7100), 291–294, doi:10.1038/nature04978.
- Wyss, M., F. Klein, K. Nagamine, and S. Wiemer (2001a), Anomalously high b-values in the south flank of Kilauea volcano, Hawaii: evidence for the distribution of magma below Kilauea's east rift zone., *Journal of Volcanology and Geothermal Research*, 106(1-2), 23 – 37.
- Wyss, M., A. Hasegawa, and J. Nakajima (2001b), Source and path of magma for volcanoes in the subduction zone of northeastern Japan., *Geophysical Research Letters*, 28(9), 1819–1822.
- Yang, Y., and D. W. Forsyth (2003), Improving epicentral and magnitude estimation of earthquakes from T-phases by considering the excitation function., *Bulletin of the Seismological Society of America*, 93, 2106–2122.

Appendices

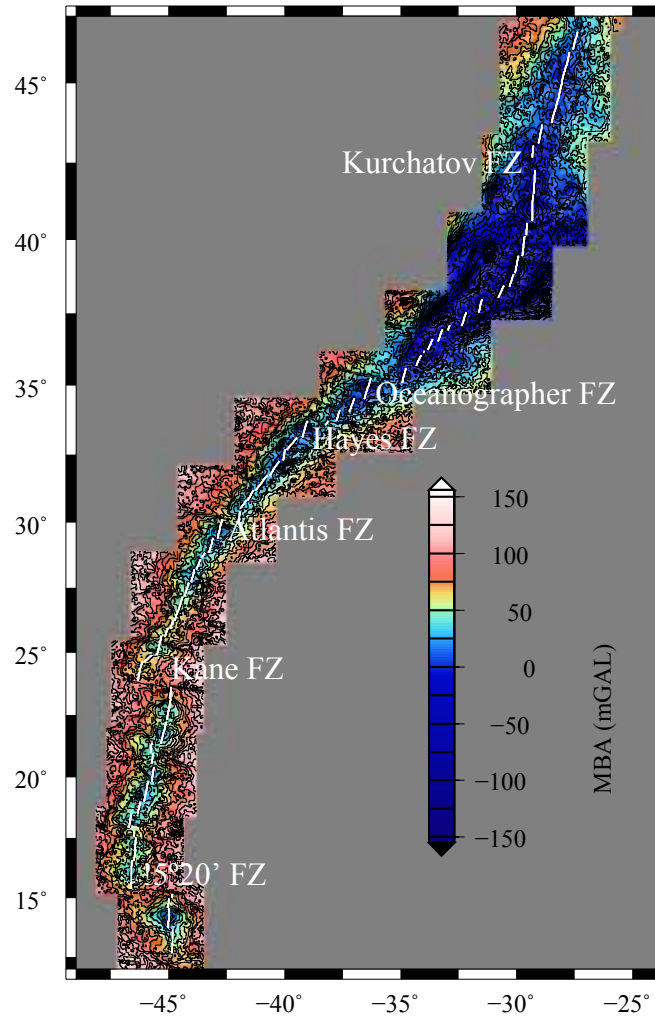
A Figure of the MBA

Figure 1: MAR's Mantle Bouguer Anomaly. White segments represent MAR's segmentation. MAR Segmentation following *Maia et al.* (2007), *Smith et al.* (2008) and *Thibaud et al.* (1998).

B Kolmogorov-Smirnov tables

Table 1: Kolmogorov-Smirnov test confidence table part 1.

n	80%	90%	95%	98%	99%
1	0.90000	0.95000	0.97500	0.99000	0.99500
2	0.68377	0.77639	0.84189	0.90000	0.92929
3	0.56481	0.63604	0.70760	0.78456	0.82900
4	0.49265	0.56522	0.62394	0.68887	0.73424
5	0.44698	0.50945	0.56328	0.62718	0.66853
6	0.41037	0.46799	0.51926	0.57741	0.61661
7	0.38148	0.43607	0.48342	0.53844	0.57581
8	0.35831	0.40962	0.45427	0.50654	0.54179
9	0.33910	0.38746	0.43001	0.47960	0.51332
10	0.32260	0.36866	0.40925	0.45662	0.48893
11	0.30829	0.35242	0.39122	0.43670	0.46770
12	0.29577	0.33815	0.37543	0.41918	0.44905
13	0.28470	0.32549	0.36143	0.40362	0.43247
14	0.27481	0.31417	0.34890	0.38970	0.41762
15	0.26588	0.30397	0.33760	0.37713	0.40420
16	0.25778	0.29472	0.32733	0.36571	0.39201
17	0.25039	0.28627	0.31796	0.35528	0.38086
18	0.24360	0.27851	0.30936	0.34569	0.37062
19	0.23735	0.27136	0.30143	0.33685	0.36117
20	0.23156	0.26473	0.29408	0.32866	0.35241
21	0.22617	0.25858	0.28724	0.32104	0.34427
22	0.22115	0.25283	0.28087	0.31394	0.33666
23	0.21645	0.24746	0.27490	0.30728	0.32954
24	0.21205	0.24242	0.26931	0.30104	0.32286
25	0.20790	0.23768	0.26404	0.29516	0.31657
26	0.20399	0.23320	0.25907	0.28962	0.31064
27	0.20030	0.22898	0.25438	0.28438	0.30502
28	0.19680	0.22497	0.24993	0.27942	0.29971
29	0.19348	0.22117	0.24571	0.27471	0.29466
30	0.19032	0.21756	0.24170	0.27023	0.28987
31	0.18732	0.21412	0.23788	0.26596	0.28530
32	0.18445	0.21085	0.23424	0.26189	0.28094
33	0.18171	0.20771	0.23076	0.25801	0.27677
34	0.17909	0.20472	0.22743	0.25429	0.27279
35	0.17659	0.20185	0.22425	0.25073	0.26897
36	0.17418	0.19910	0.22119	0.24732	0.26532
37	0.17188	0.19646	0.21826	0.24404	0.26180
38	0.16966	0.19392	0.21544	0.24089	0.25843
39	0.16753	0.19148	0.21273	0.23786	0.25518
40	0.16547	0.18913	0.21012	0.23494	0.25205

Table 2: Kolmogorov-Smirnov test confidence table part 2.

n	80%	90%	95%	98%	99%
41	0.16349	0.18687	0.20760	0.23213	0.24904
42	0.16158	0.18468	0.20517	0.22941	0.24613
43	0.15974	0.18257	0.20283	0.22679	0.24332
44	0.15796	0.18053	0.20056	0.22426	0.24060
45	0.15623	0.17856	0.19837	0.22181	0.23798
46	0.15457	0.17665	0.19625	0.21944	0.23544
47	0.15295	0.17481	0.19420	0.21715	0.23298
48	0.15139	0.17302	0.19221	0.21493	0.23059
49	0.14987	0.17128	0.19028	0.21277	0.22828
50	0.14840	0.16959	0.18841	0.21068	0.22604
51	0.14697	0.16796	0.18659	0.20864	0.22386
52	0.14558	0.16637	0.18482	0.20667	0.22174
53	0.14423	0.16483	0.18311	0.20475	0.21968
54	0.14292	0.16332	0.18144	0.20289	0.21768
55	0.14164	0.16186	0.17981	0.20107	0.21574
56	0.14040	0.16044	0.17823	0.19930	0.21384
57	0.13919	0.15906	0.17669	0.19758	0.21199
58	0.13801	0.15771	0.17519	0.19590	0.21019
59	0.13686	0.15639	0.17373	0.19427	0.20844
60	0.13573	0.15511	0.17231	0.19267	0.20673
65	0.13052	0.14913	0.16567	0.18525	0.19877
70	0.12586	0.14381	0.15975	0.17863	0.19167
75	0.12167	0.13901	0.15442	0.17268	0.18528
80	0.11787	0.13467	0.14960	0.16728	0.17949
85	0.11442	0.13072	0.14520	0.16236	0.17421
90	0.11125	0.12709	0.14117	0.15786	0.16938
95	0.10833	0.12375	0.13746	0.15371	0.16493
100	0.10563	0.12067	0.13403	0.14987	0.16081
$n > 100$	$1.073/\sqrt{n}$	$1.223/\sqrt{n}$	$1.358/\sqrt{n}$	$1.518/\sqrt{n}$	$1.629/\sqrt{n}$

C Figures of the seismic sequences

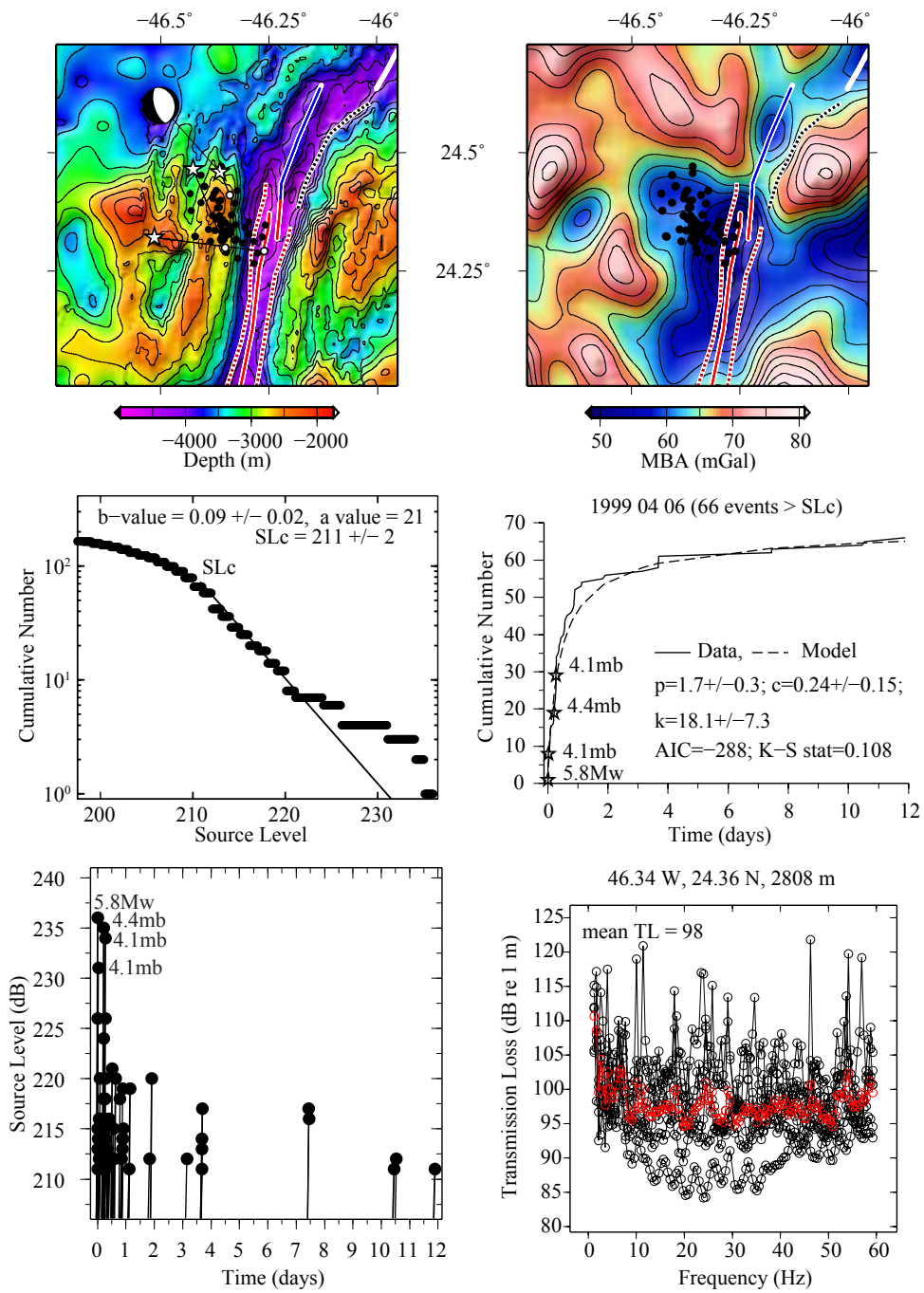


Figure 2: 1999 04 06 seismic sequence

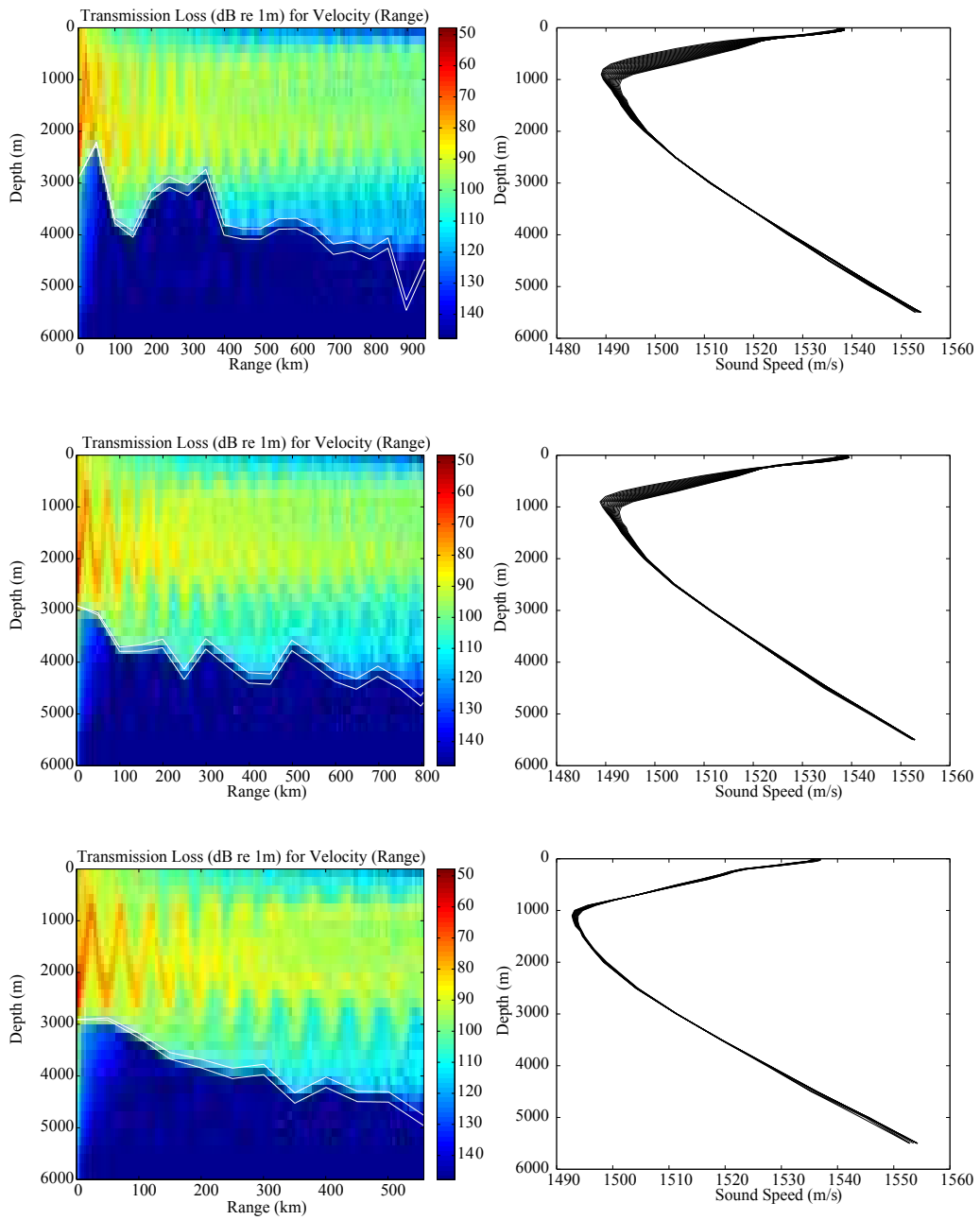


Figure 3: 1999 04 06 seismic sequence

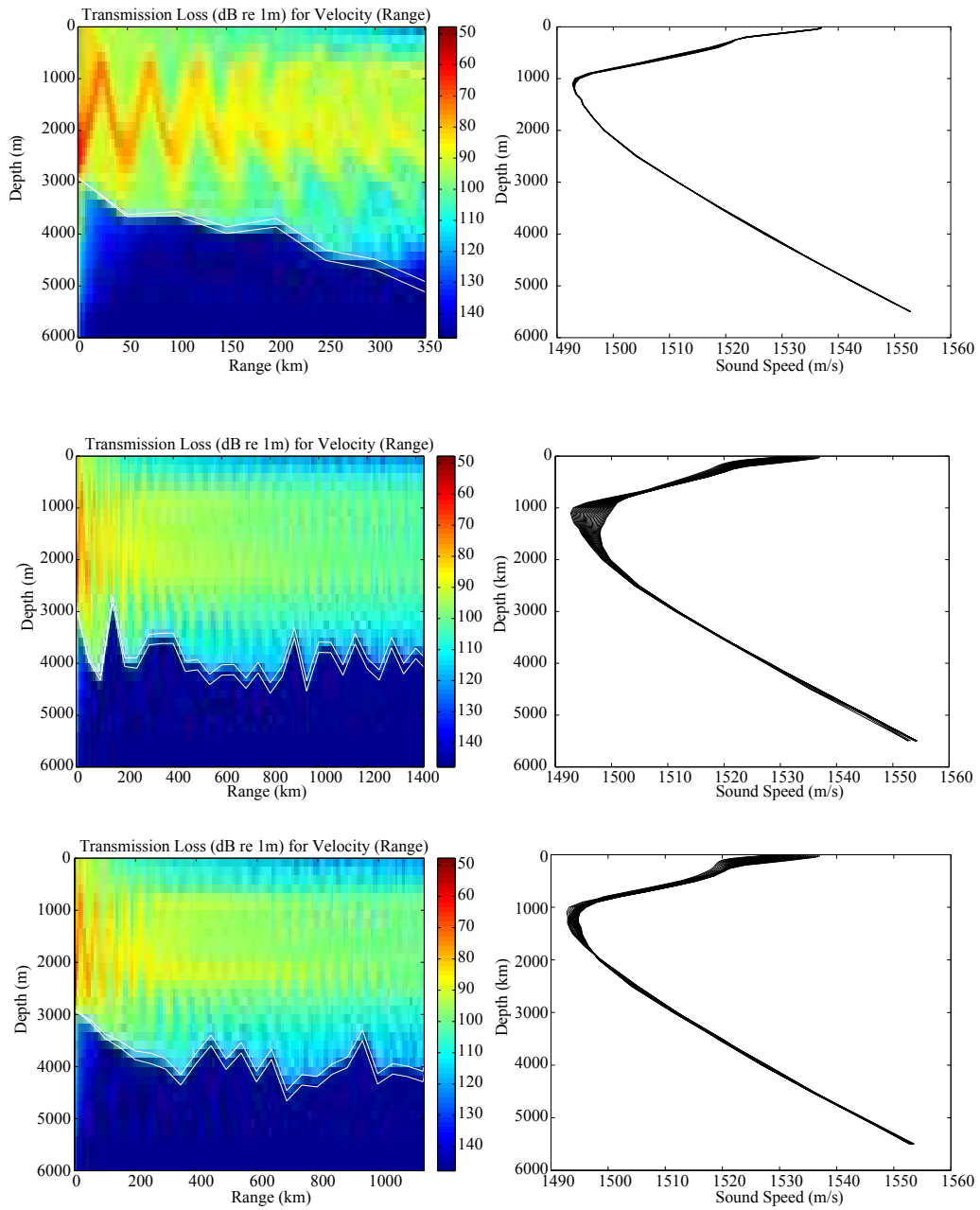


Figure 4: 1999 04 06 seismic sequence

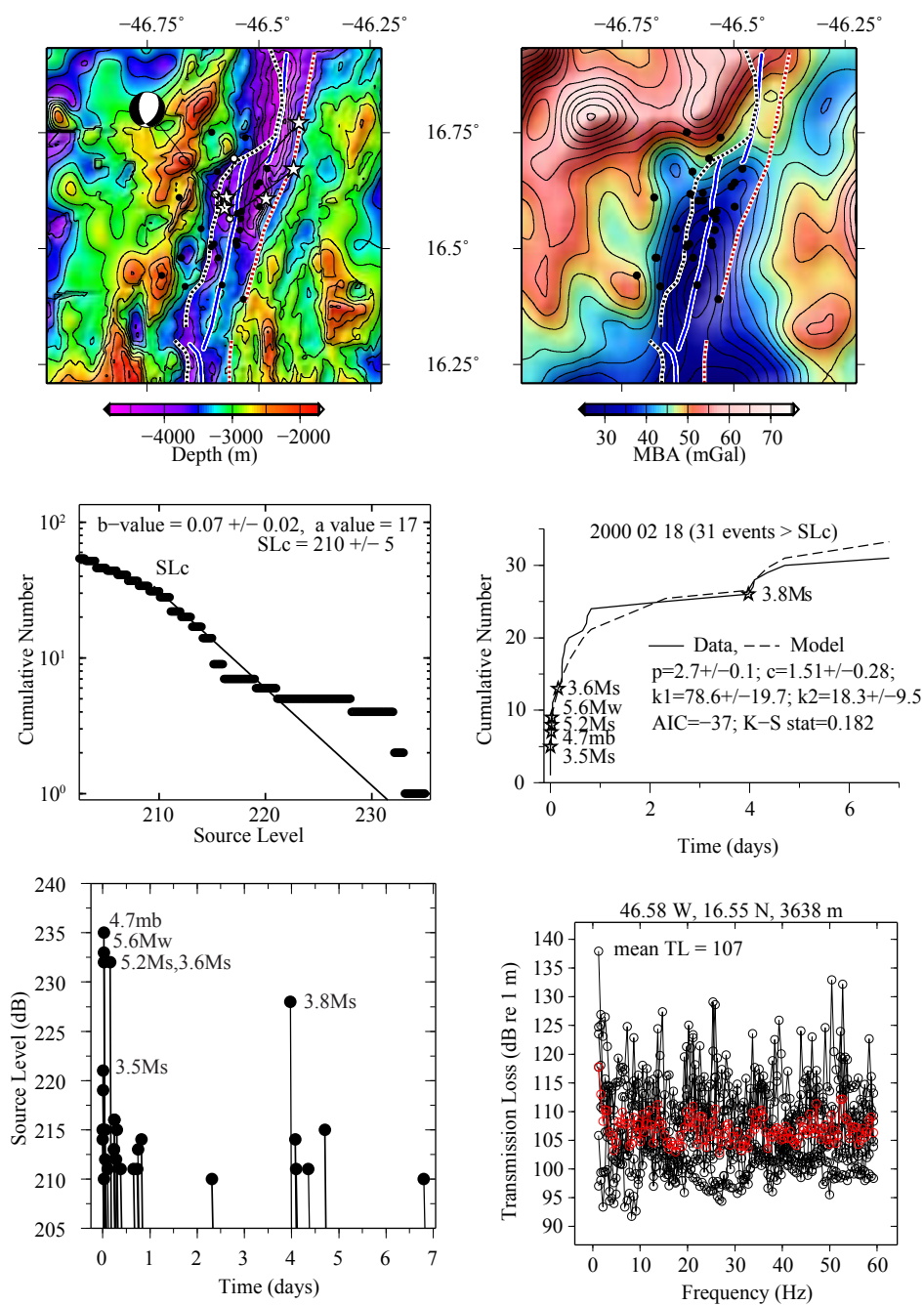


Figure 5: 2000 02 18 seismic sequence

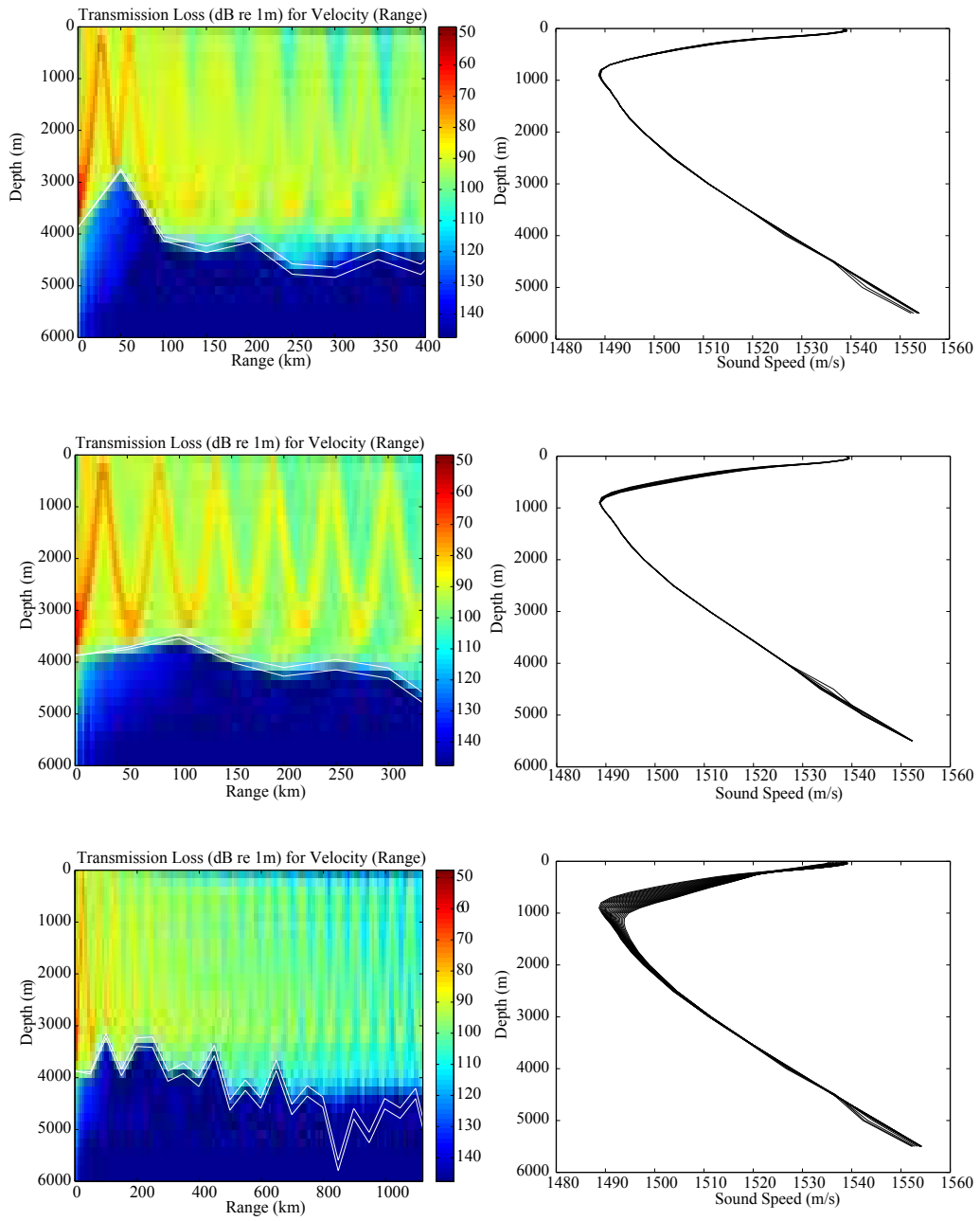


Figure 6: 2000 02 18 seismic sequence

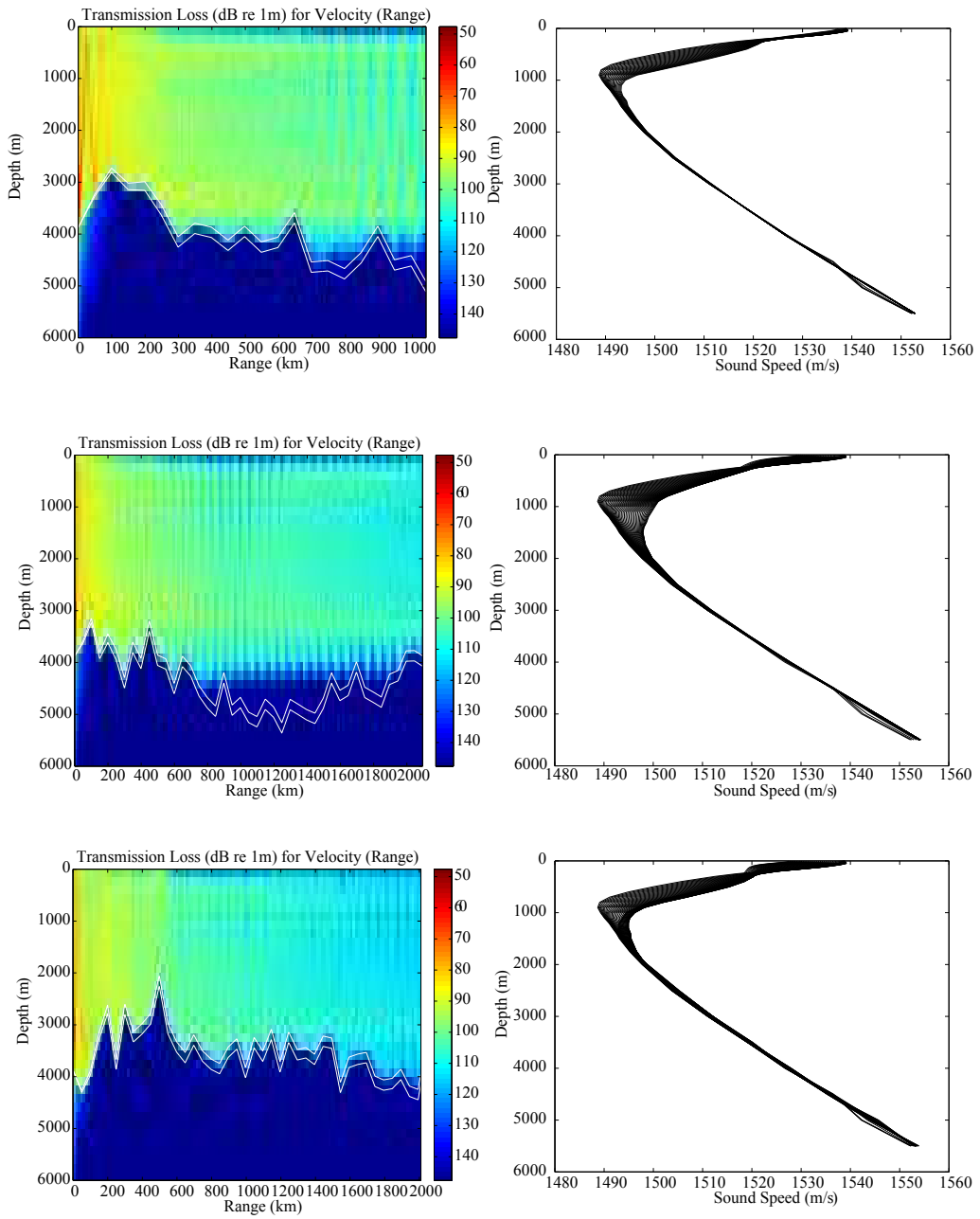


Figure 7: 2000 02 18 seismic sequence

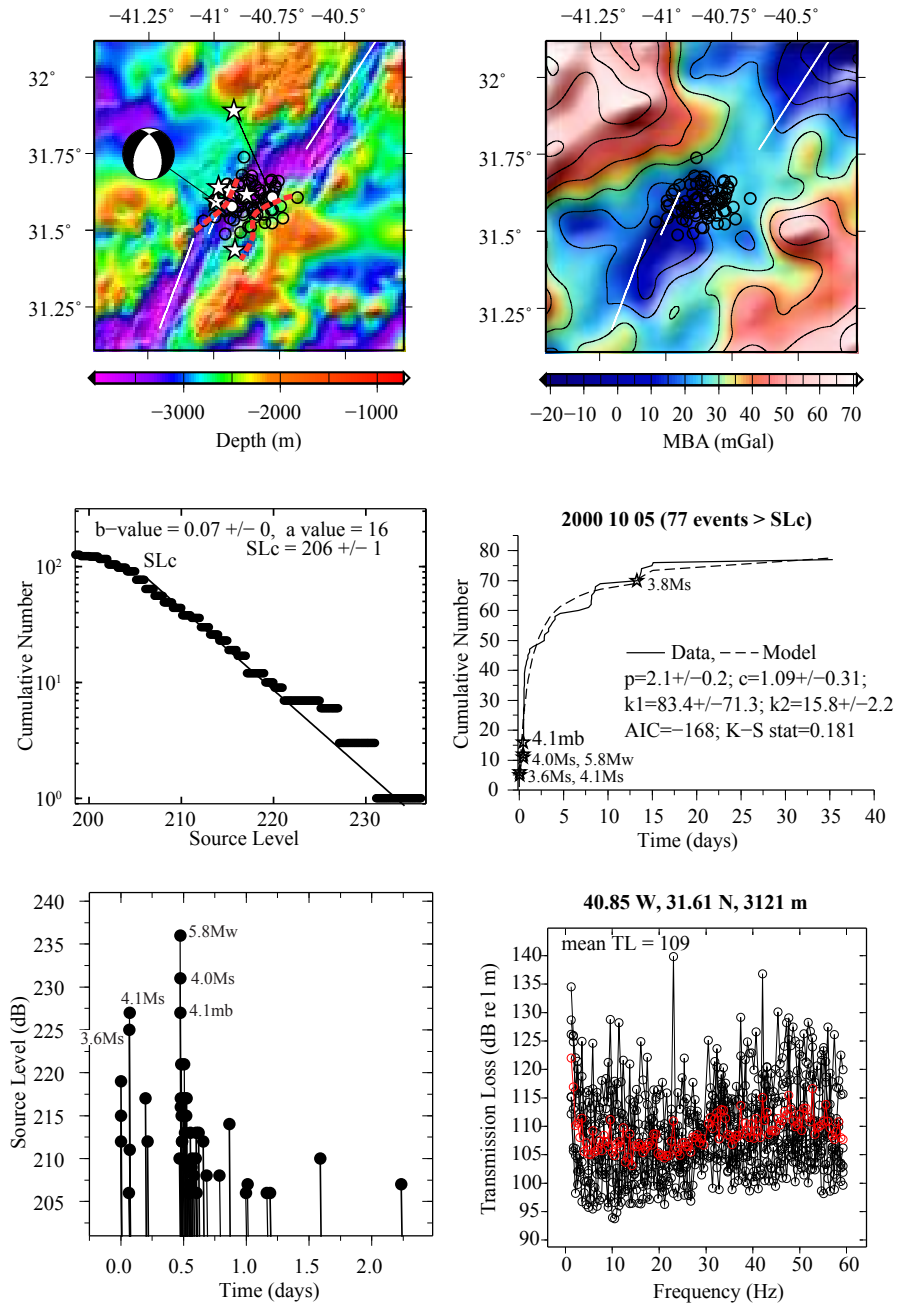


Figure 8: 2000 10 05 seismic sequence

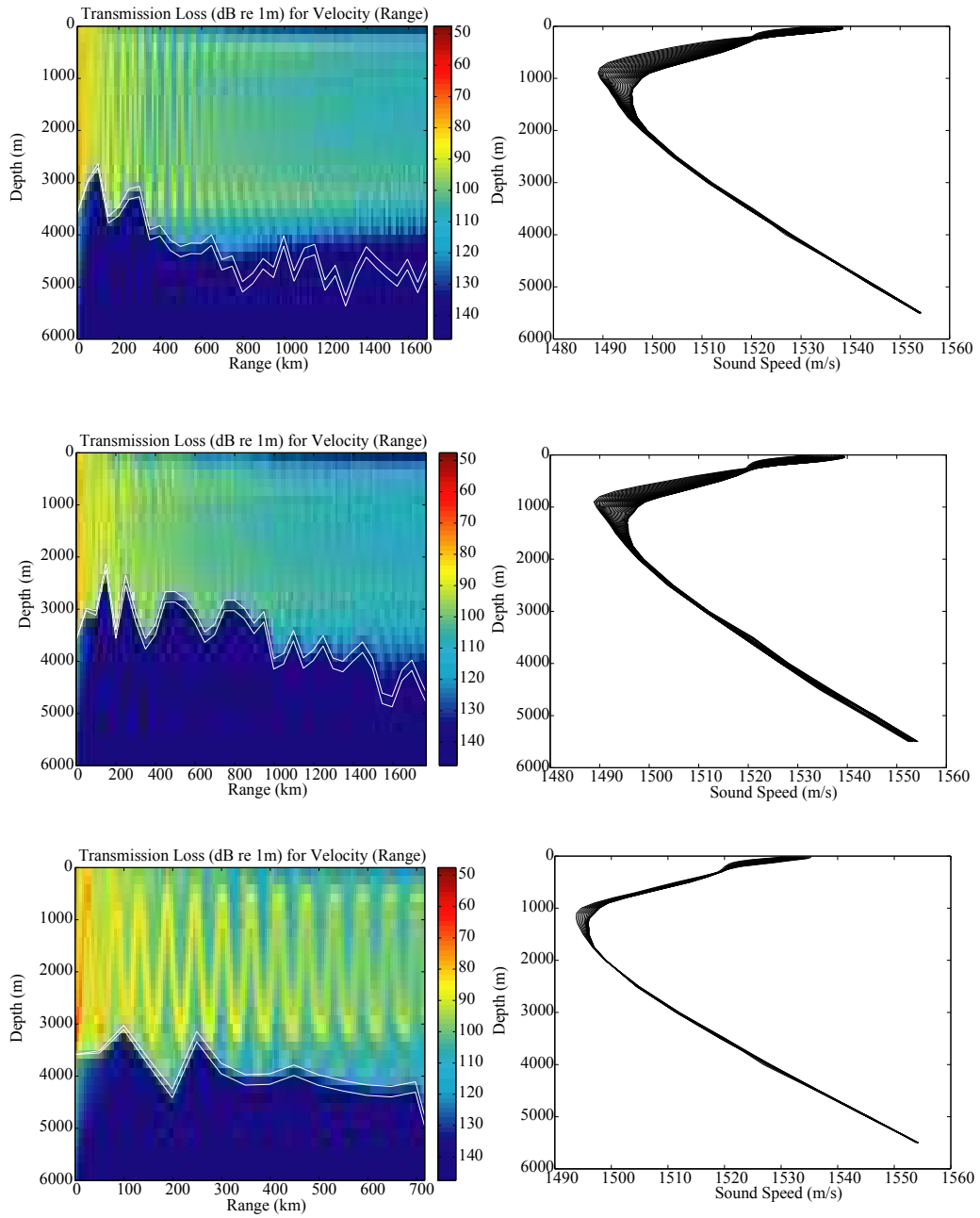


Figure 9: 2000 10 05 seismic sequence

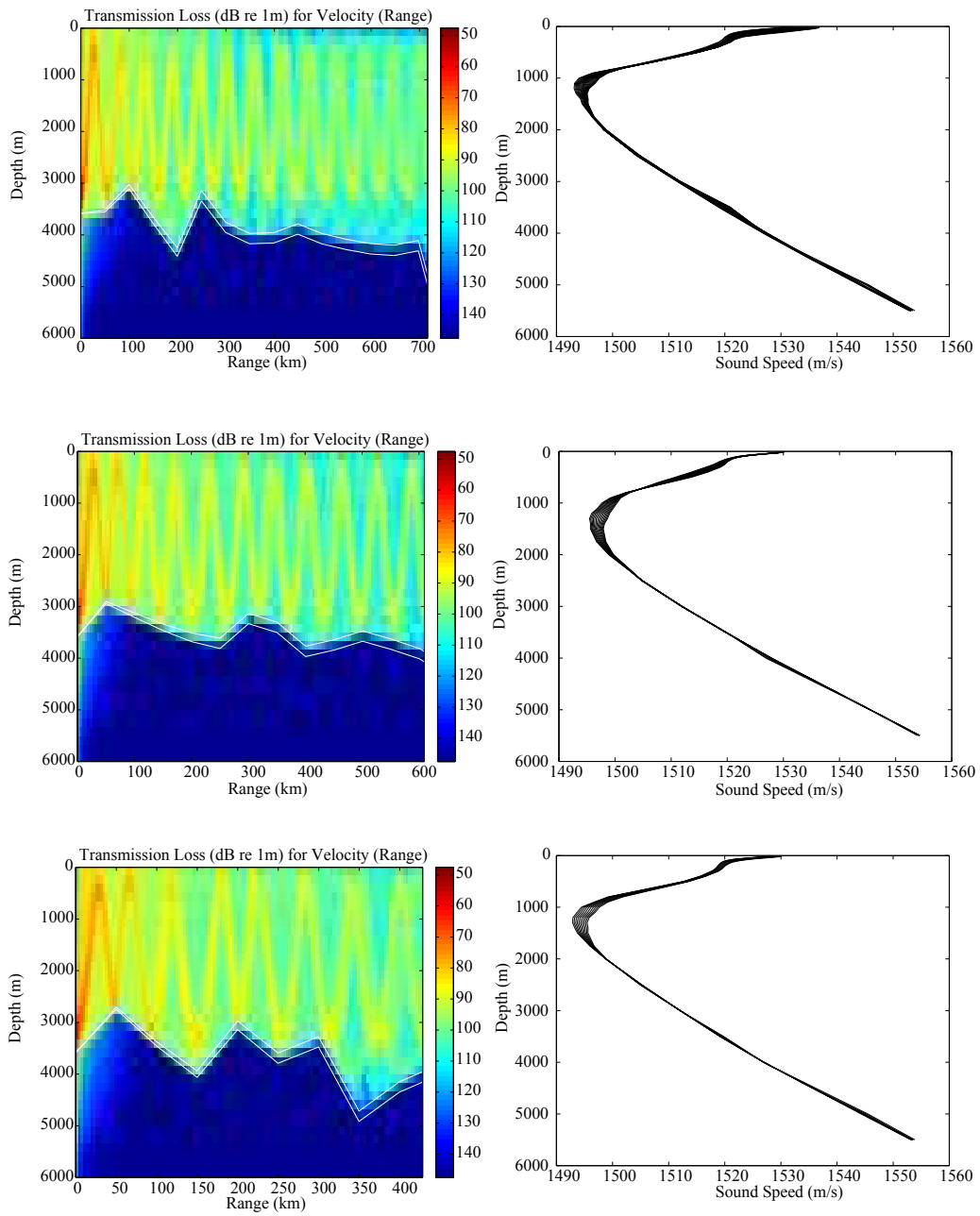


Figure 10: 2000 10 05 seismic sequence

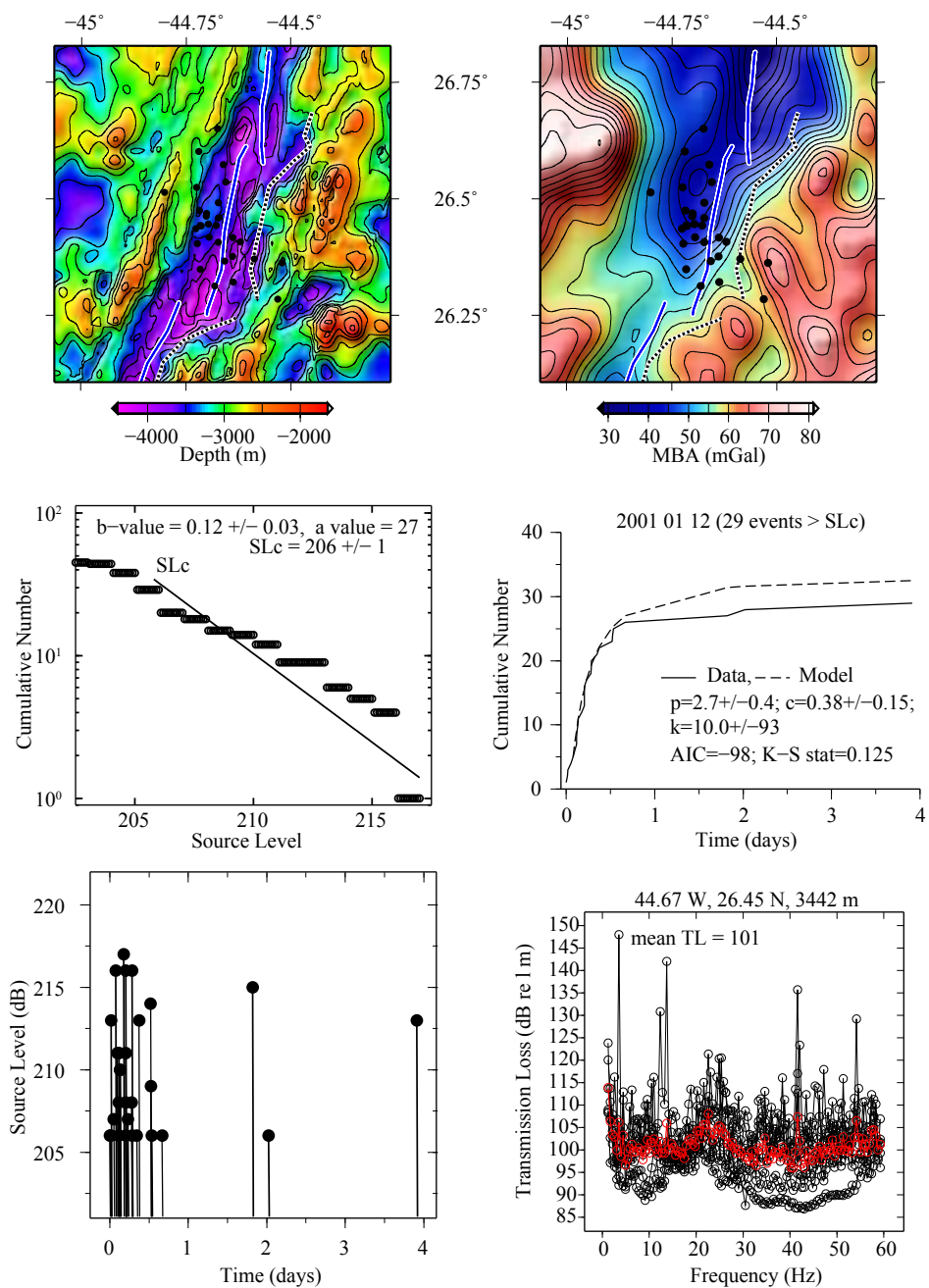


Figure 11: 2001 01 12 seismic sequence

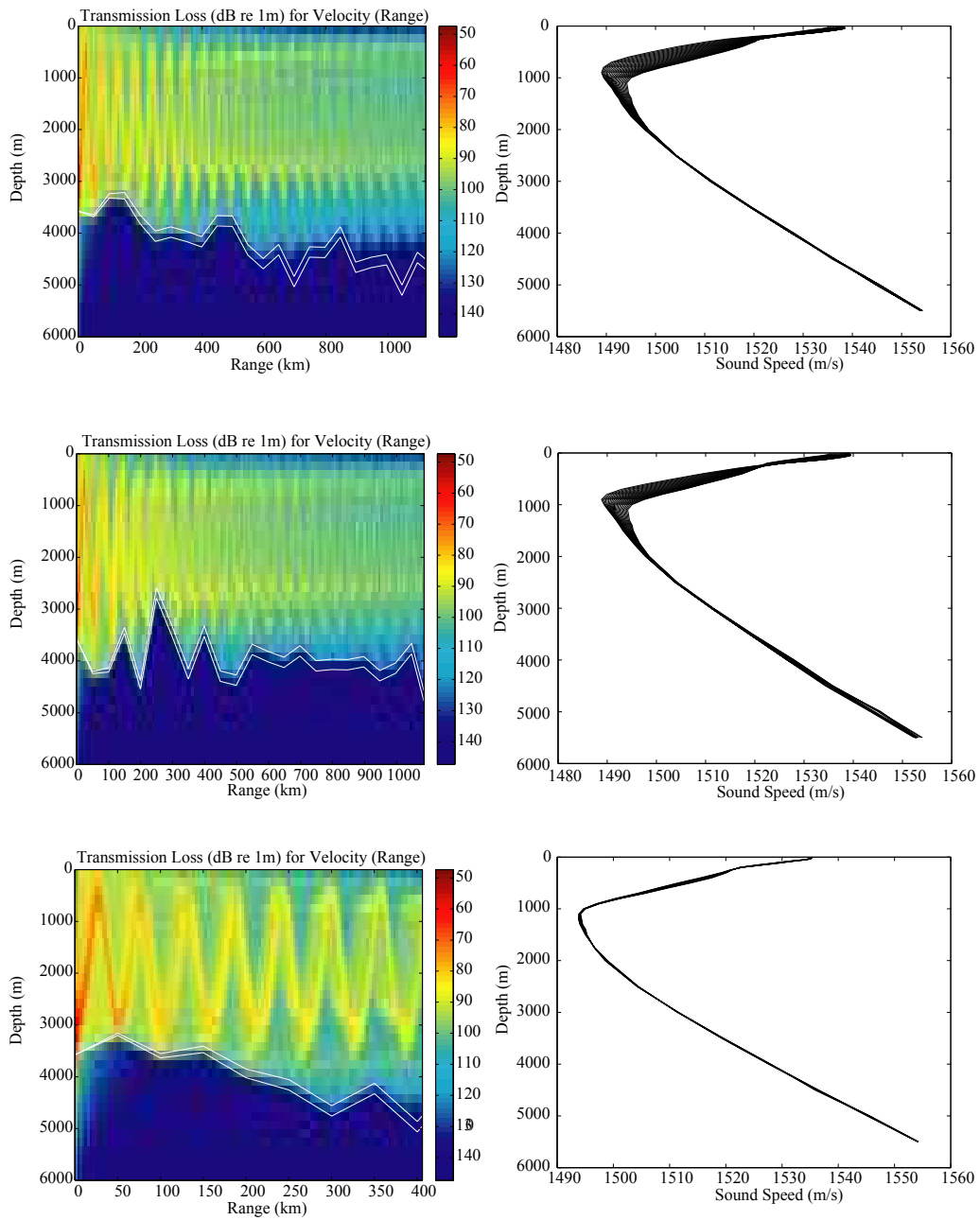


Figure 12: 2001 01 12 seismic sequence

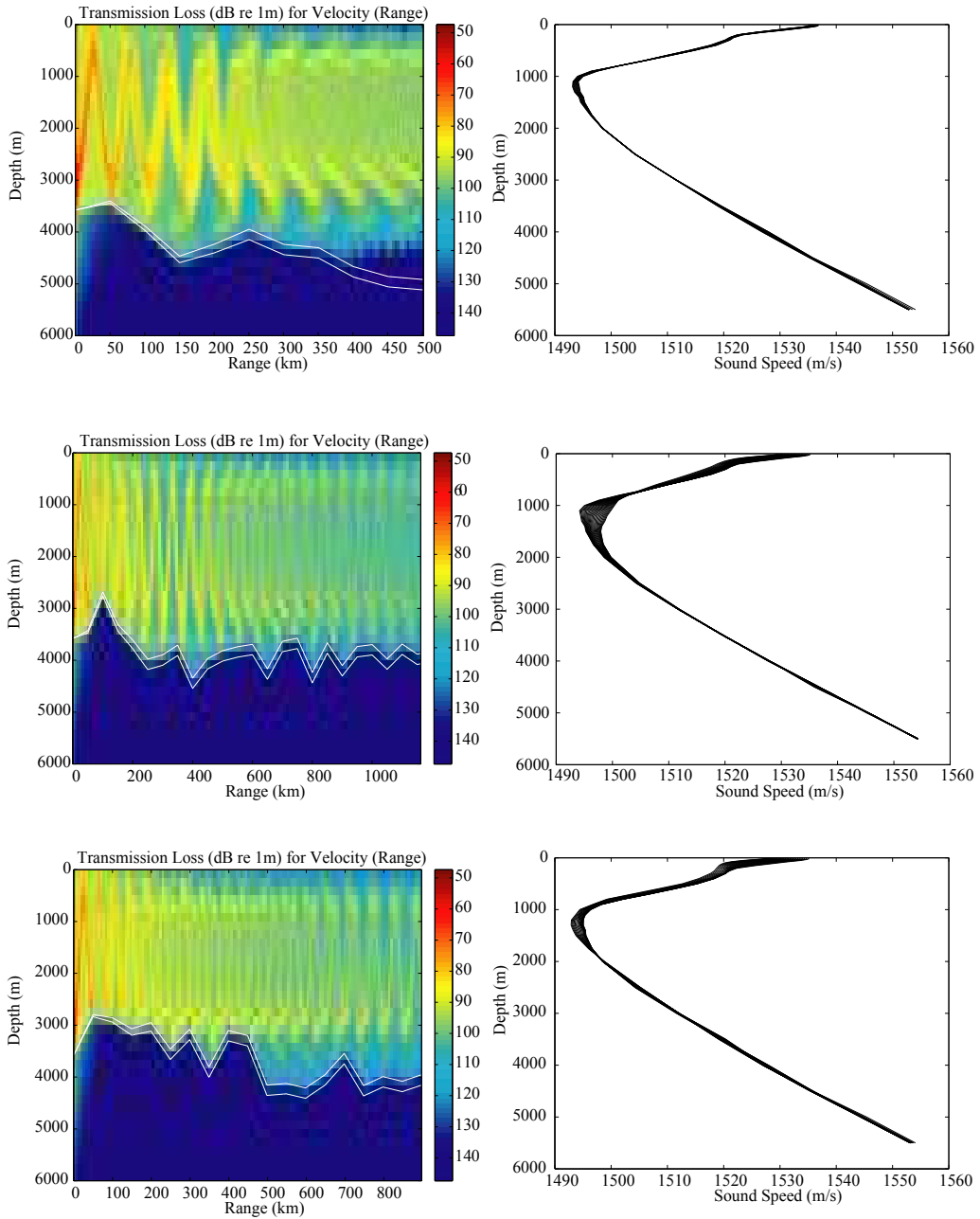


Figure 13: 2001 01 12 seismic sequence

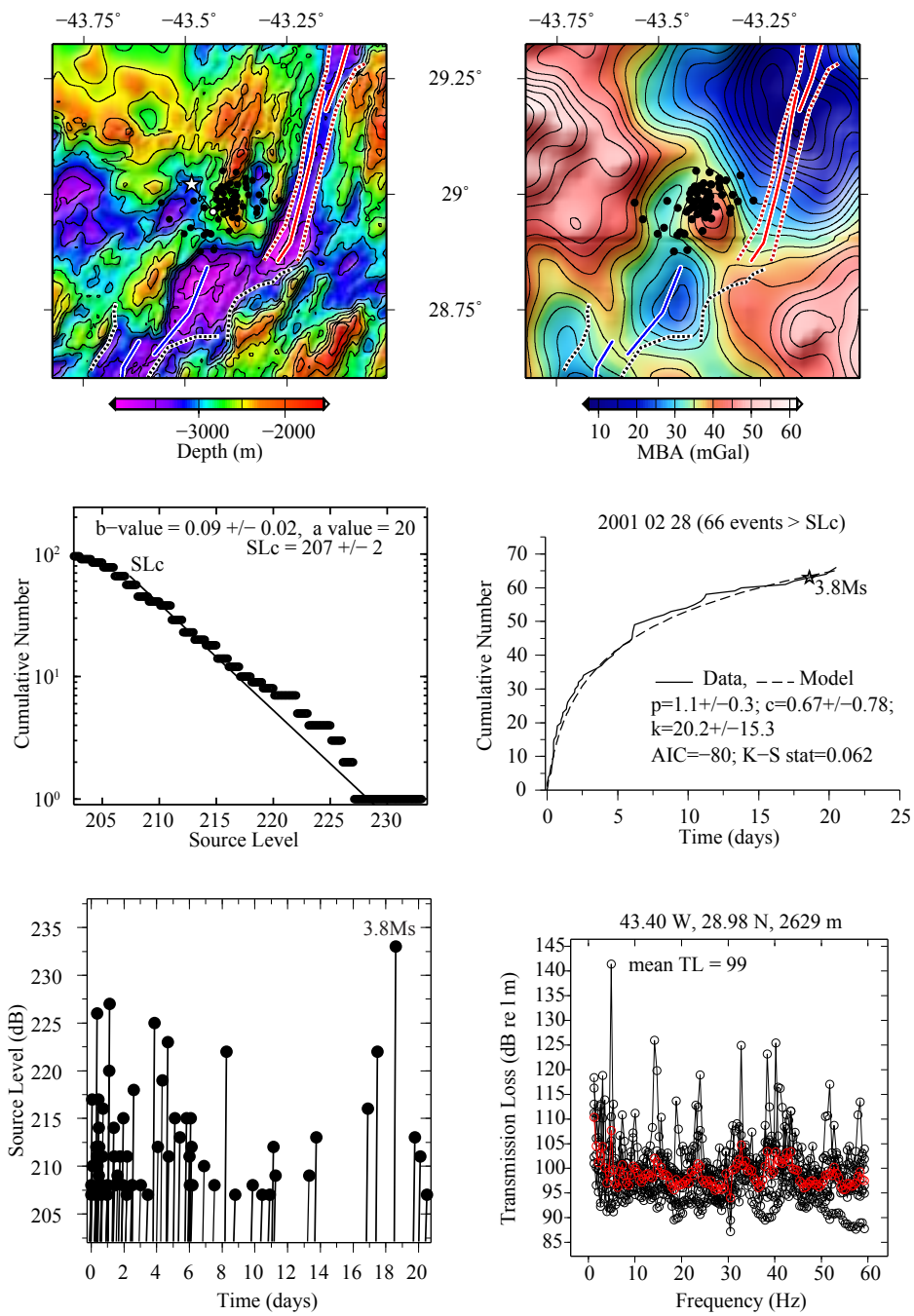


Figure 14: 2001 02 28 seismic sequence

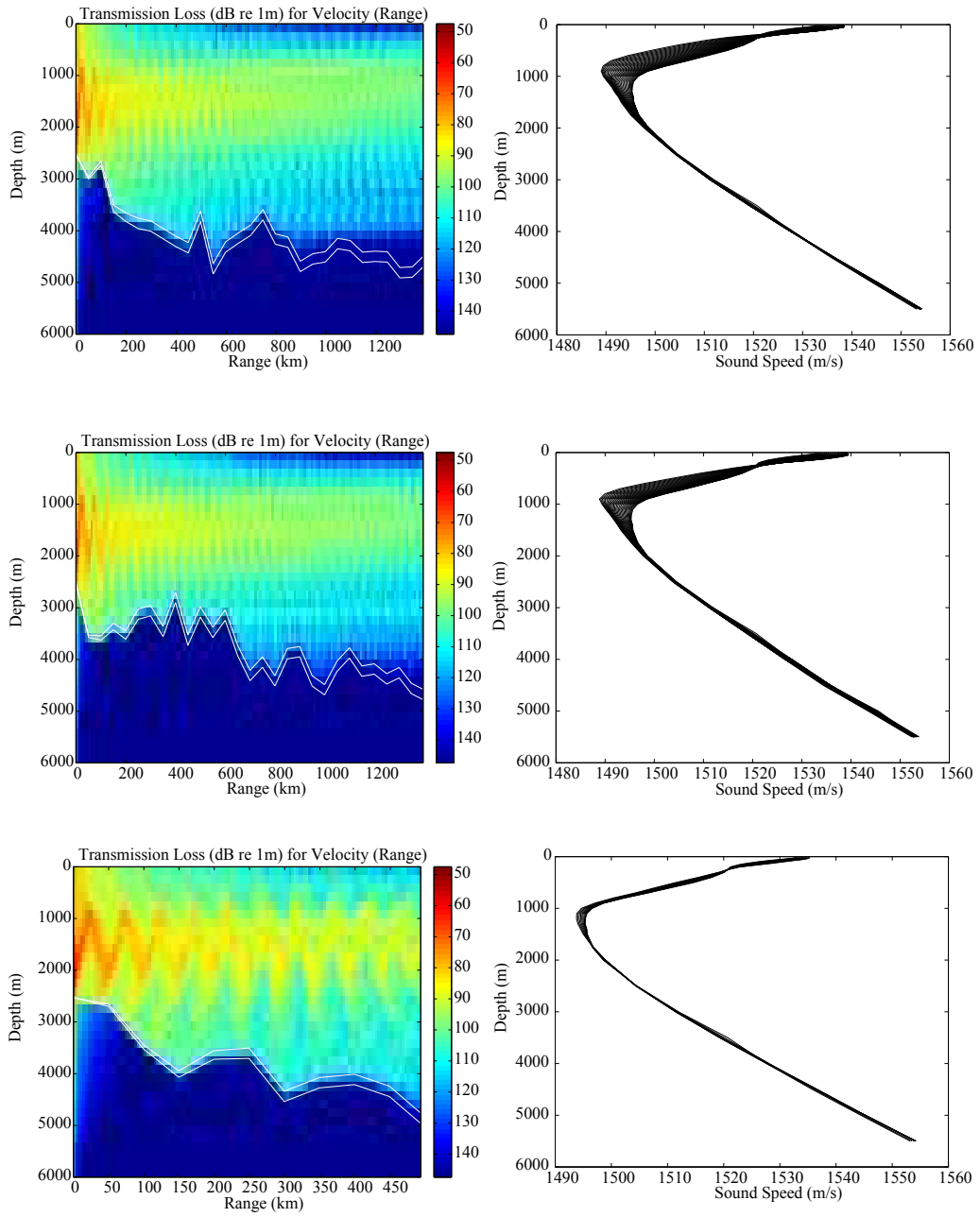


Figure 15: 2001 02 28 seismic sequence

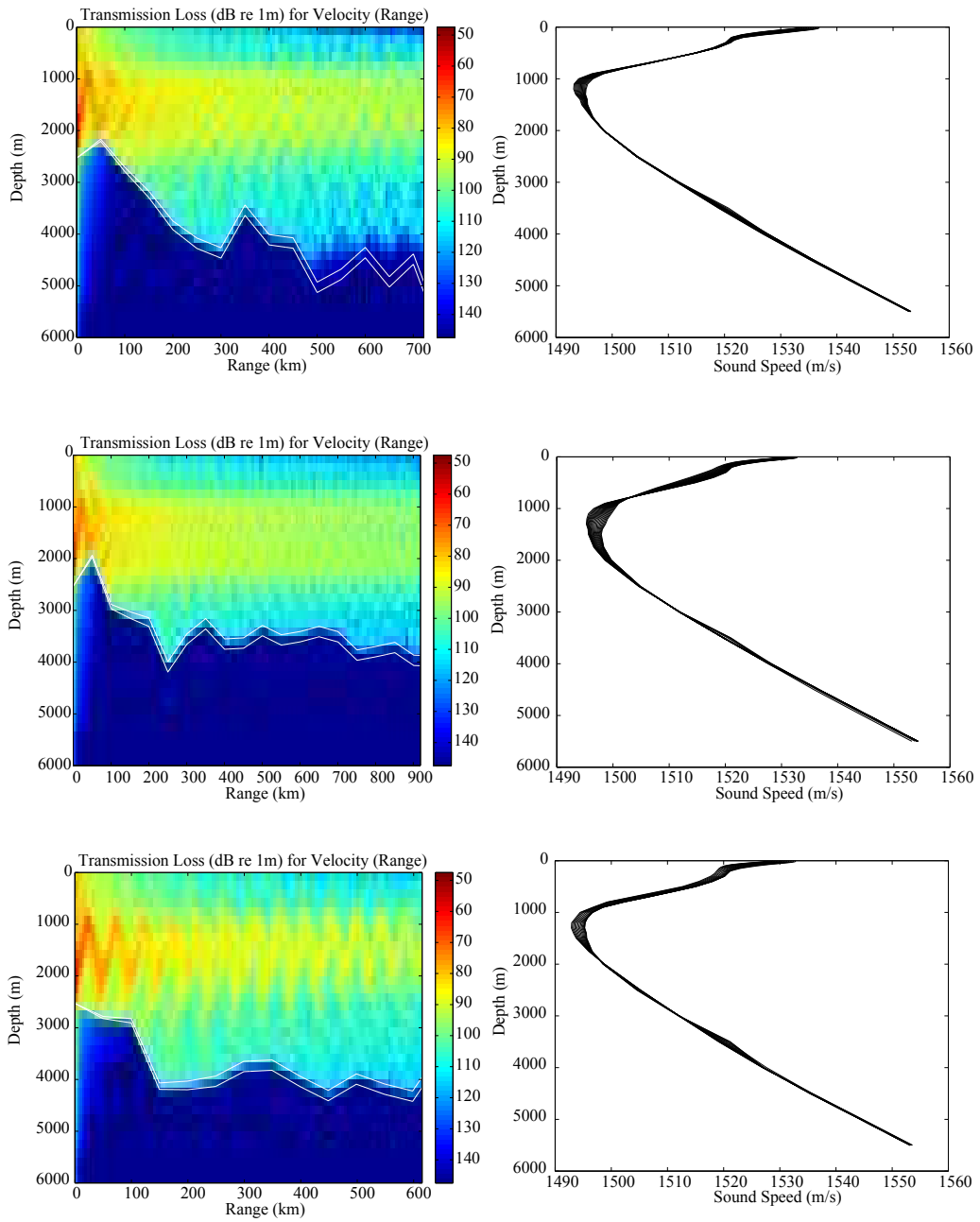


Figure 16: 2001 02 28 seismic sequence

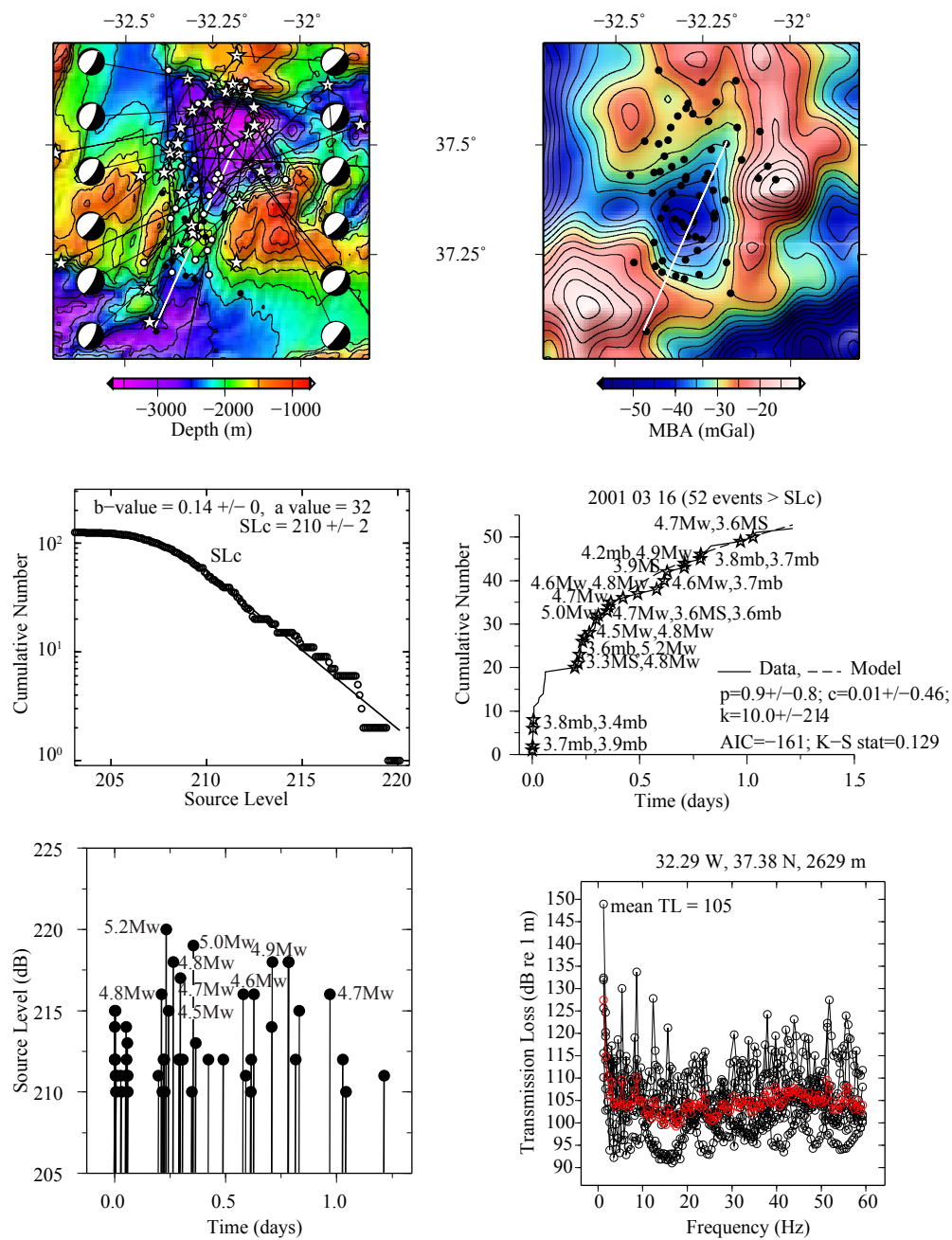


Figure 17: 2001 03 16 seismic sequence

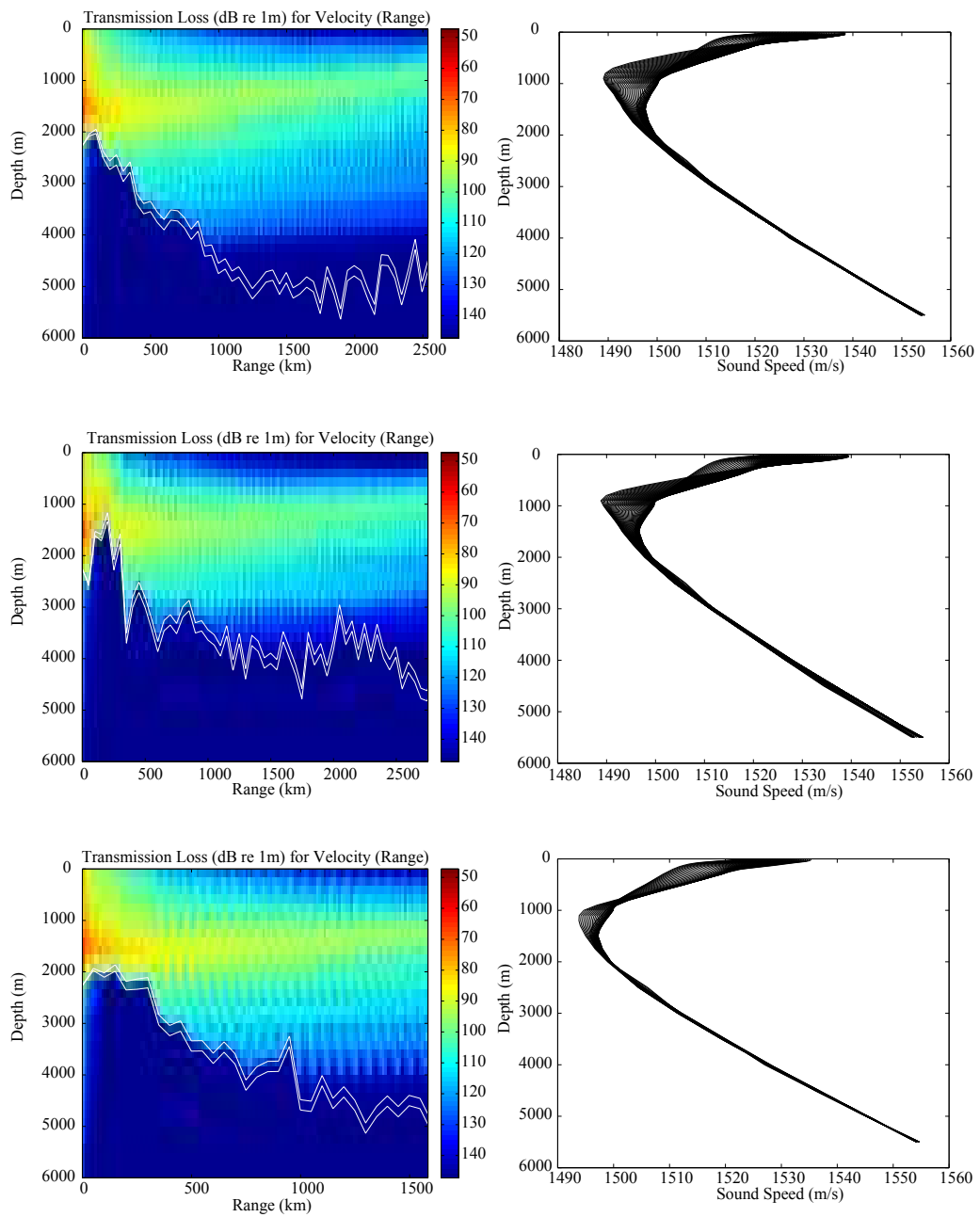


Figure 18: 2001 03 16 seismic sequence

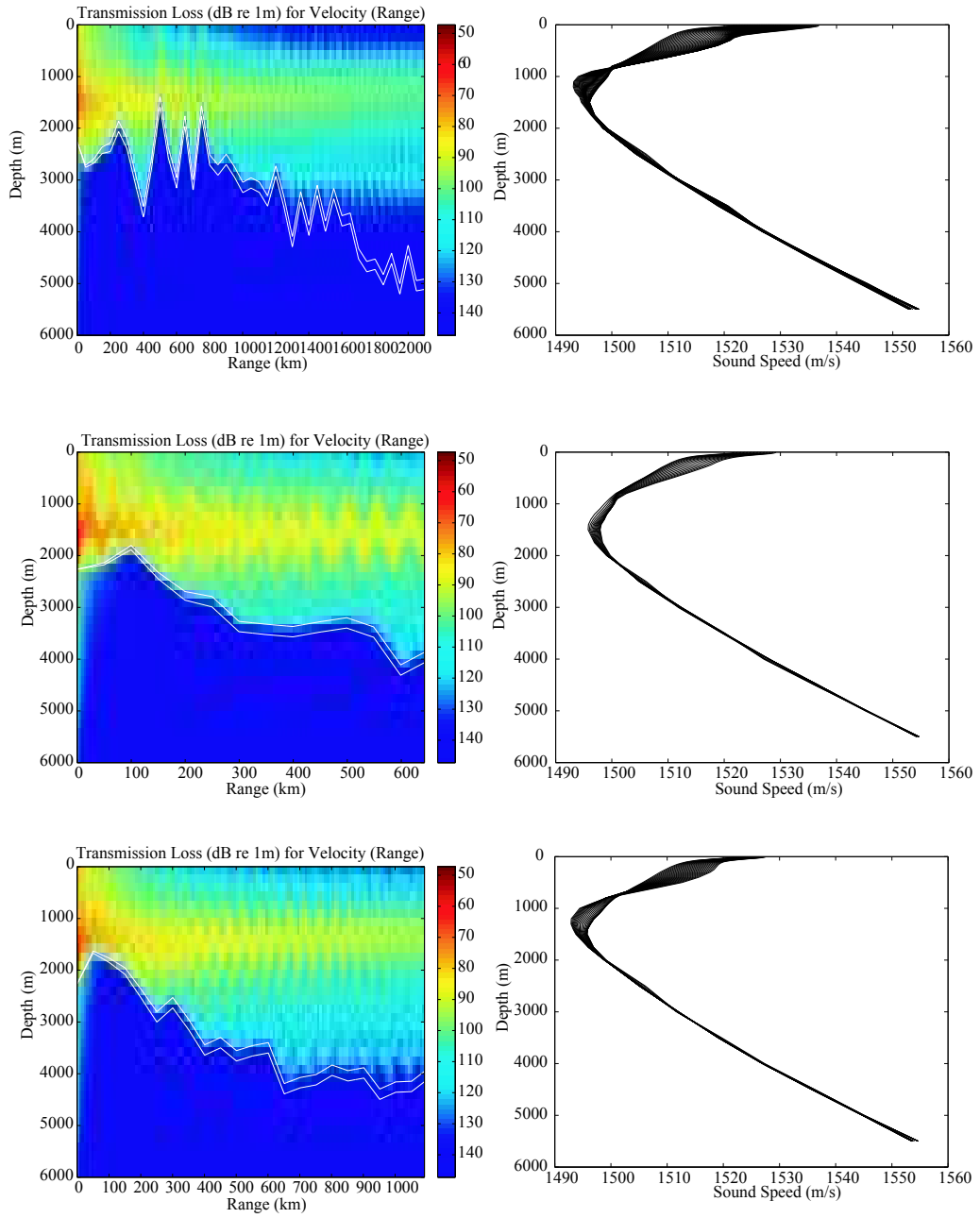


Figure 19: 2001 03 16 seismic sequence

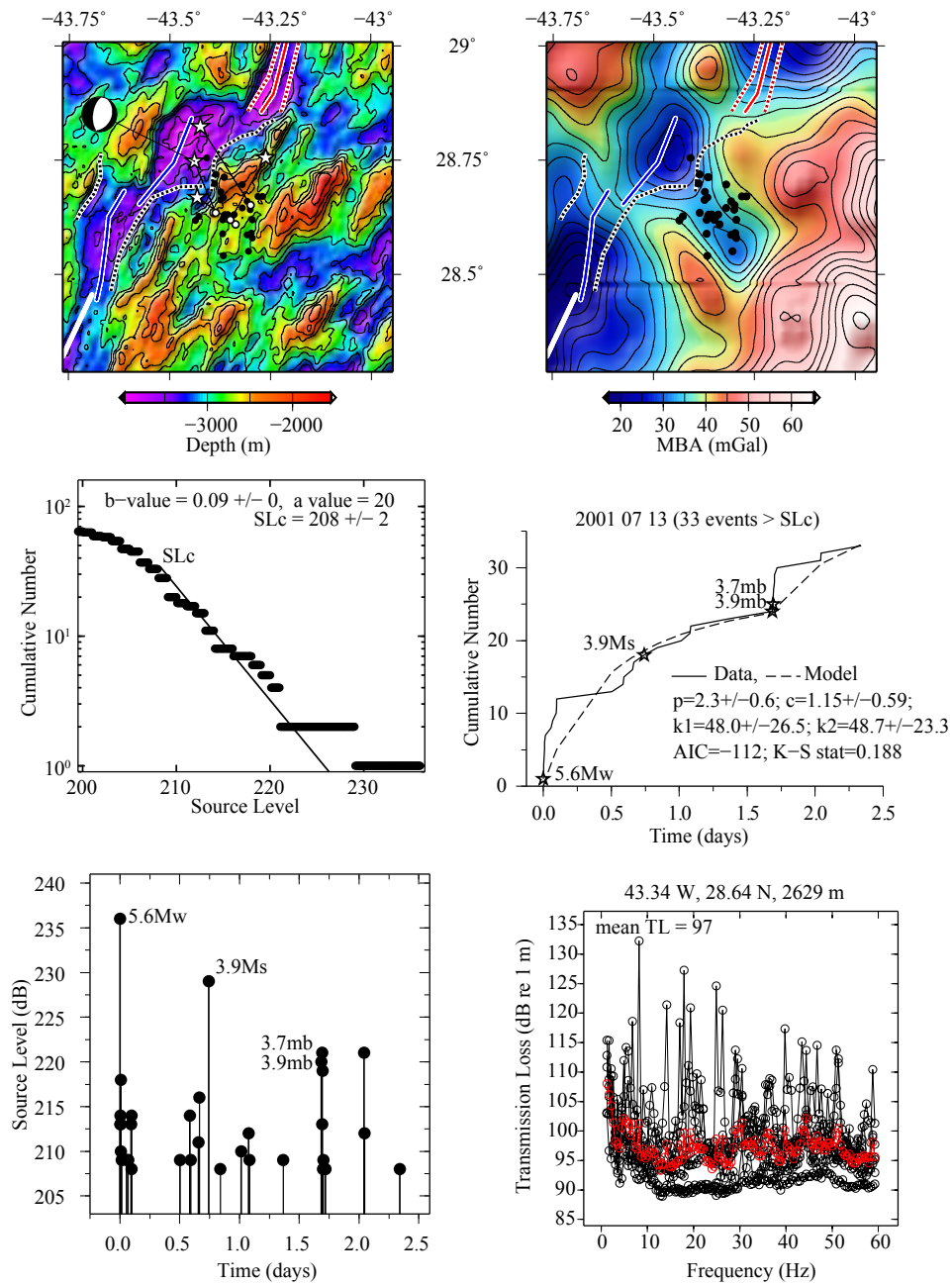


Figure 20: 2001 07 13 seismic sequence

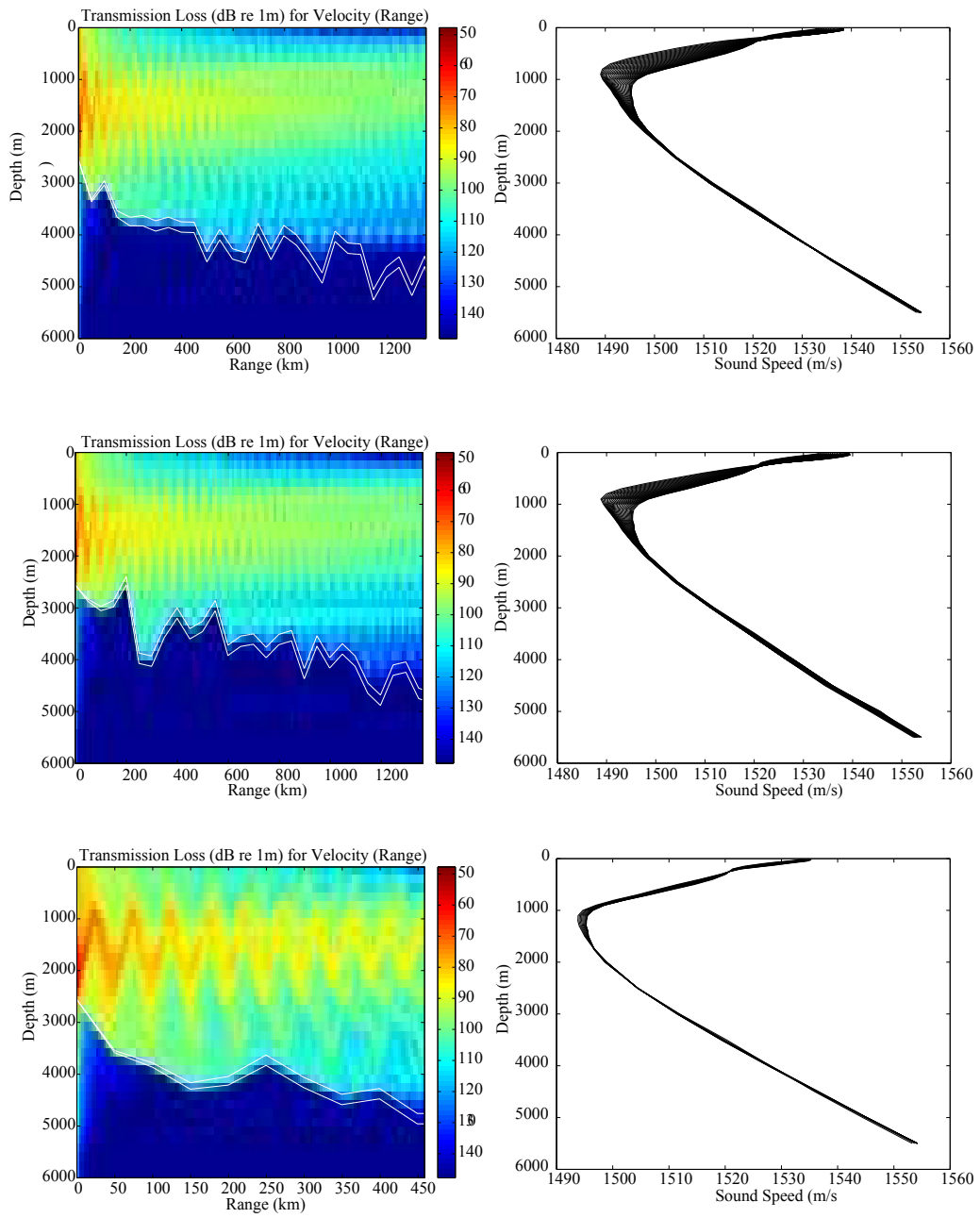


Figure 21: 2001 07 13 seismic sequence

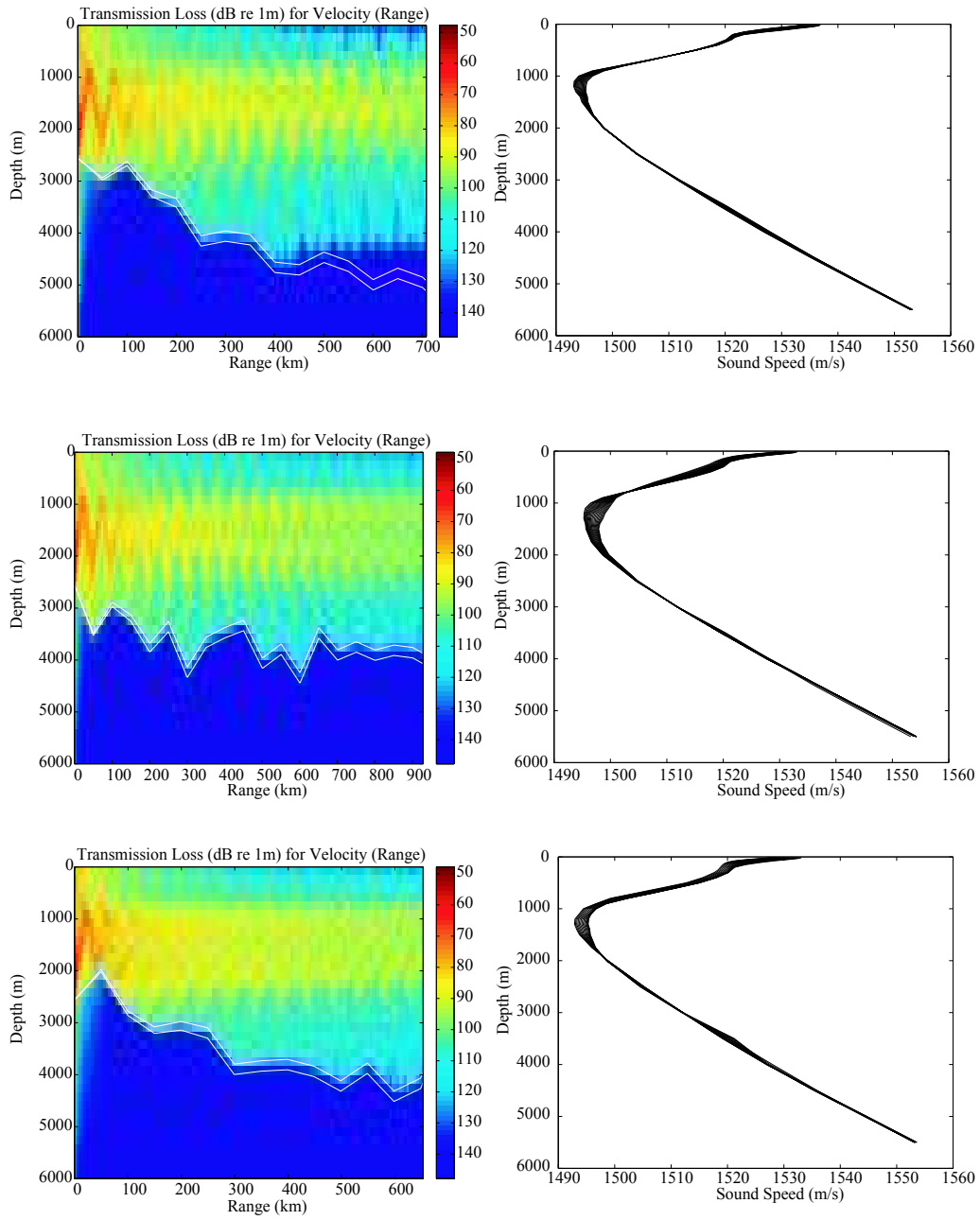


Figure 22: 2001 07 13 seismic sequence

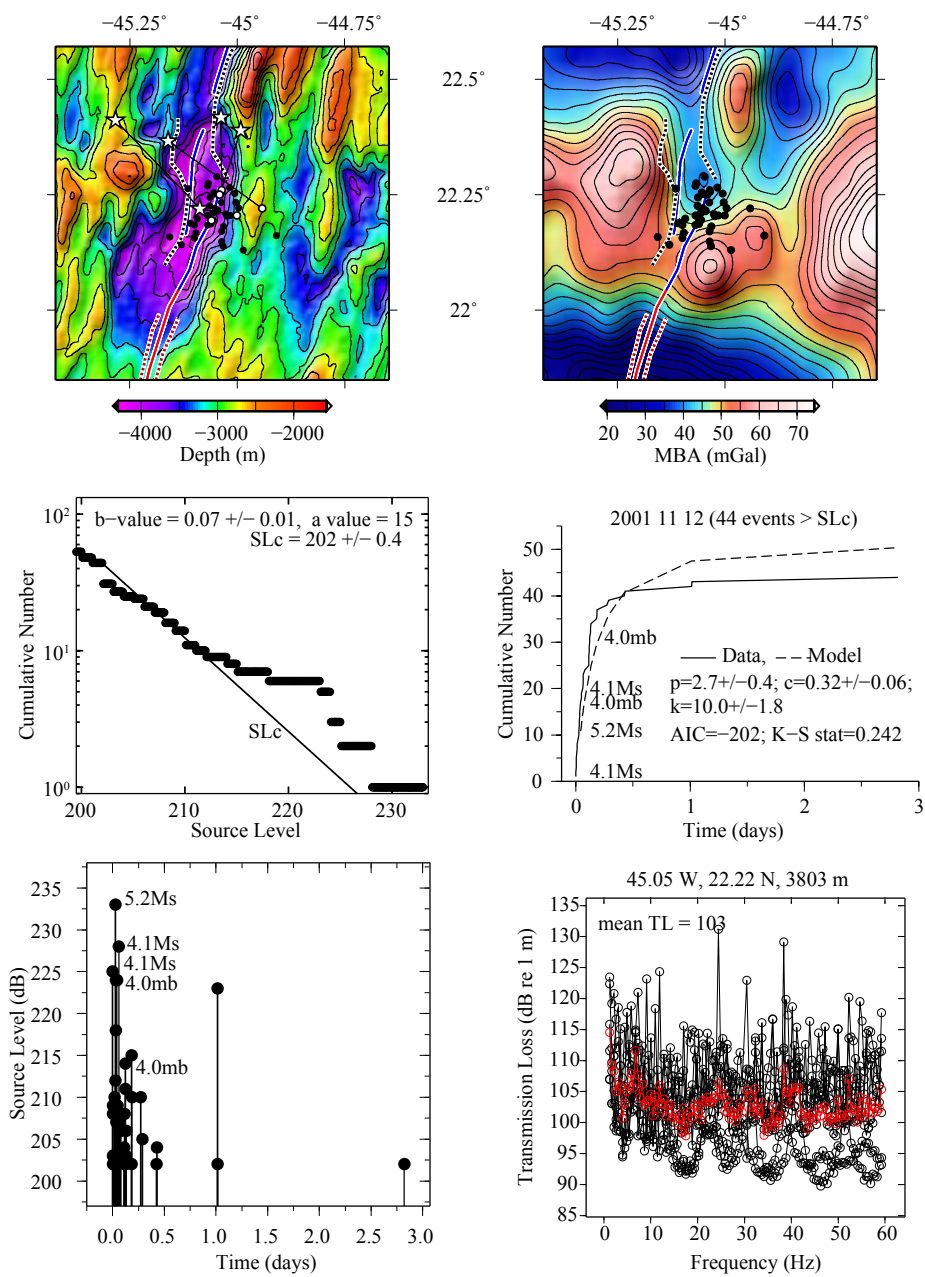


Figure 23: 2001 11 12 seismic sequence

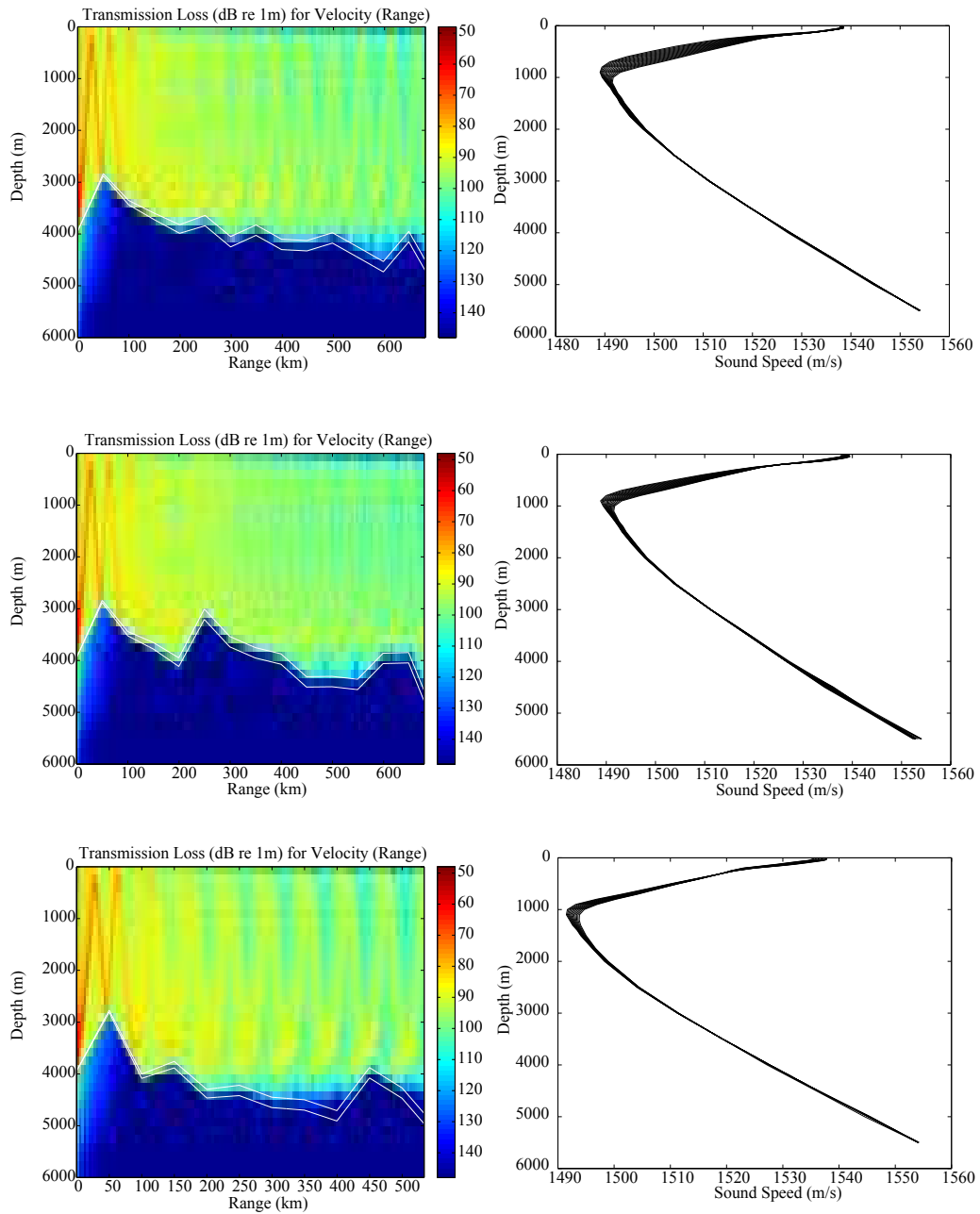


Figure 24: 2001 11 12 seismic sequence

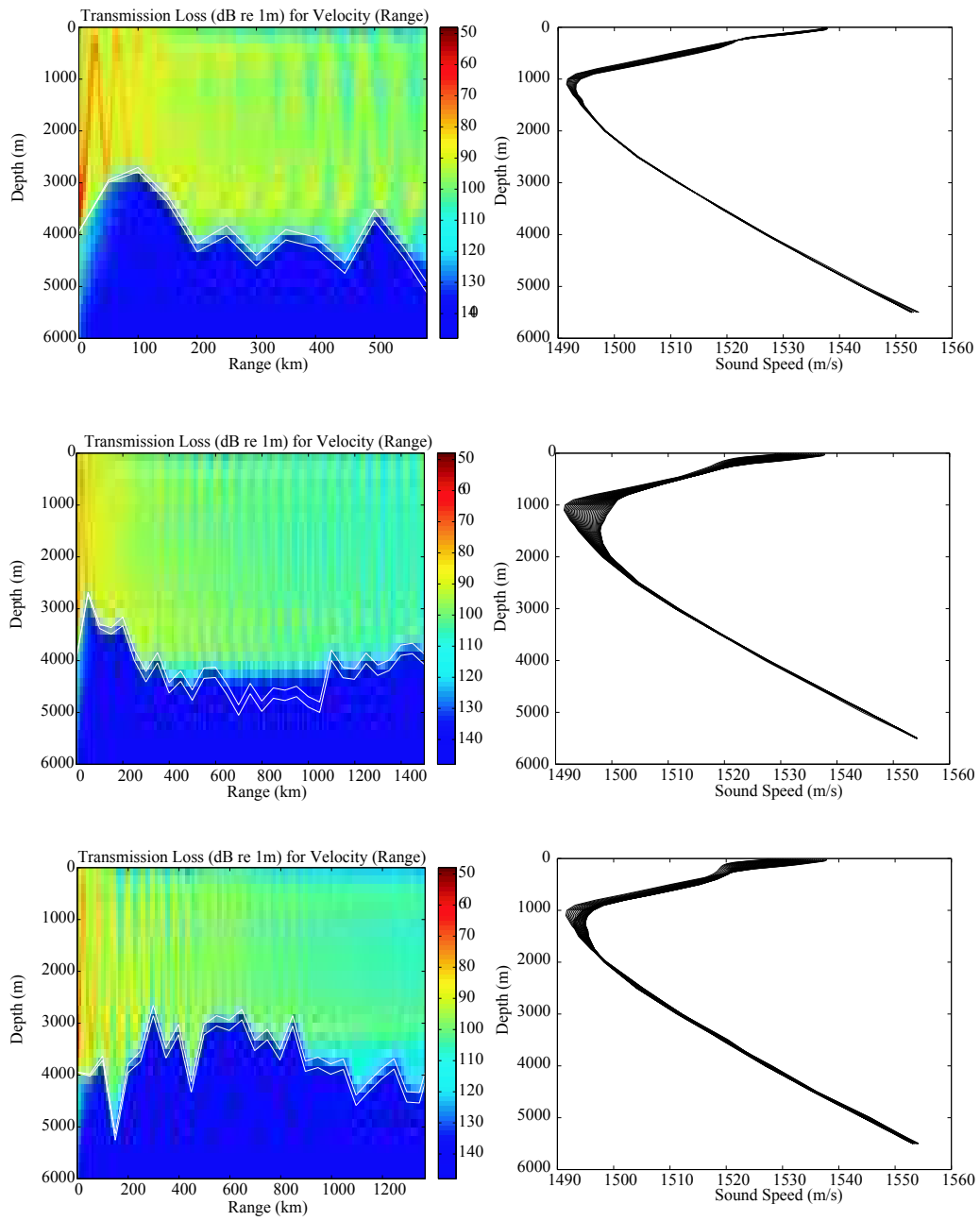


Figure 25: 2001 11 12 seismic sequence

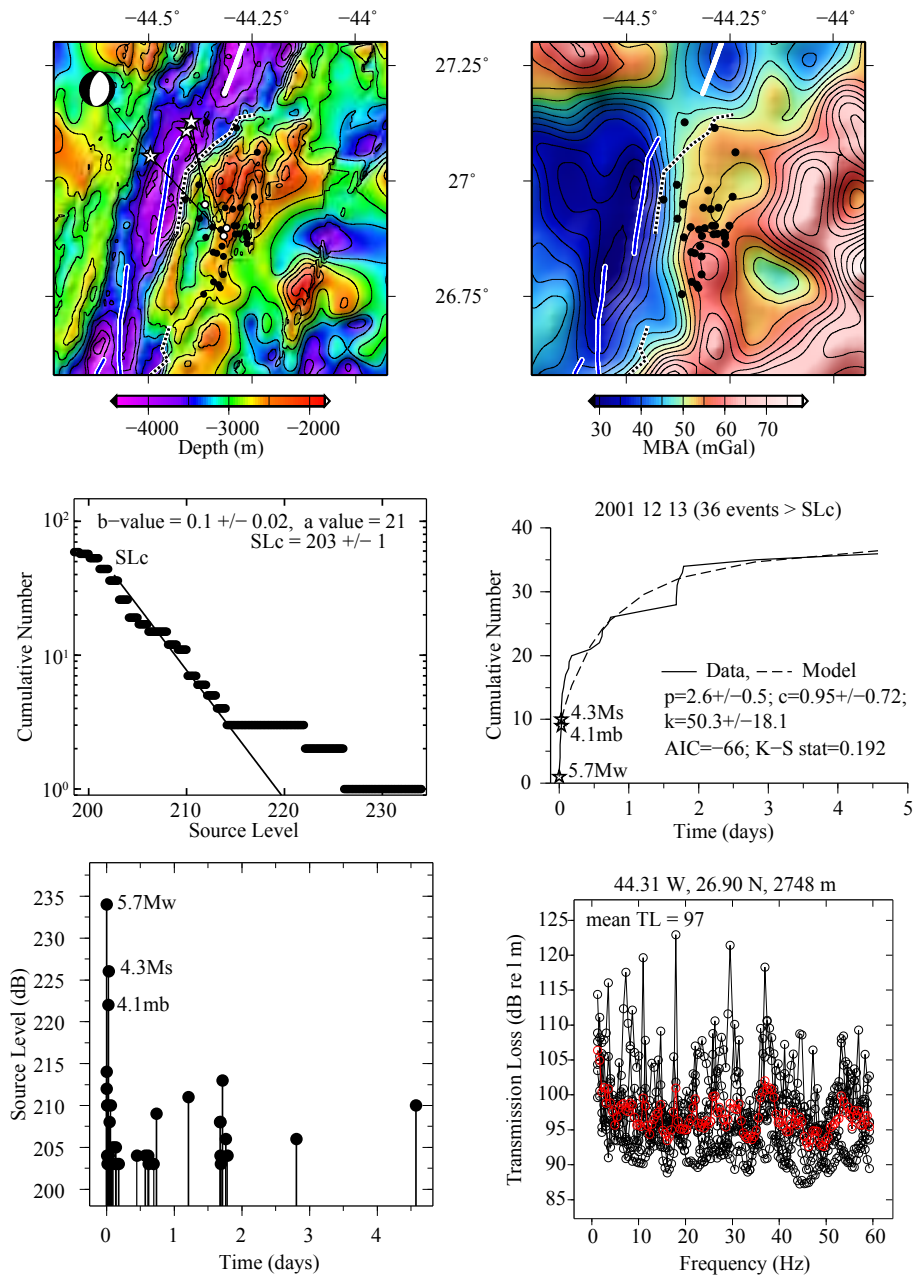


Figure 26: 2001 12 13 seismic sequence

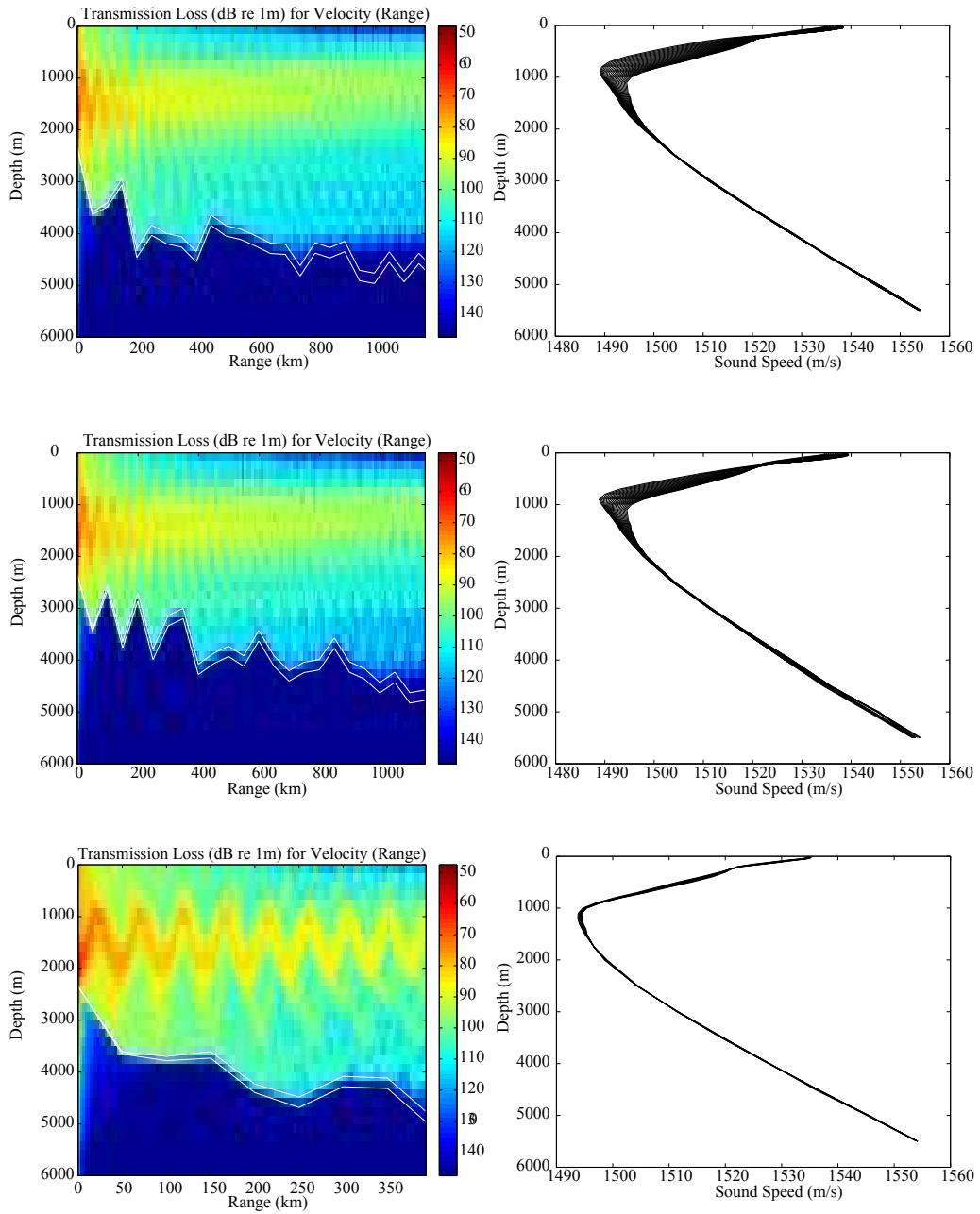


Figure 27: 2001 12 13 seismic sequence

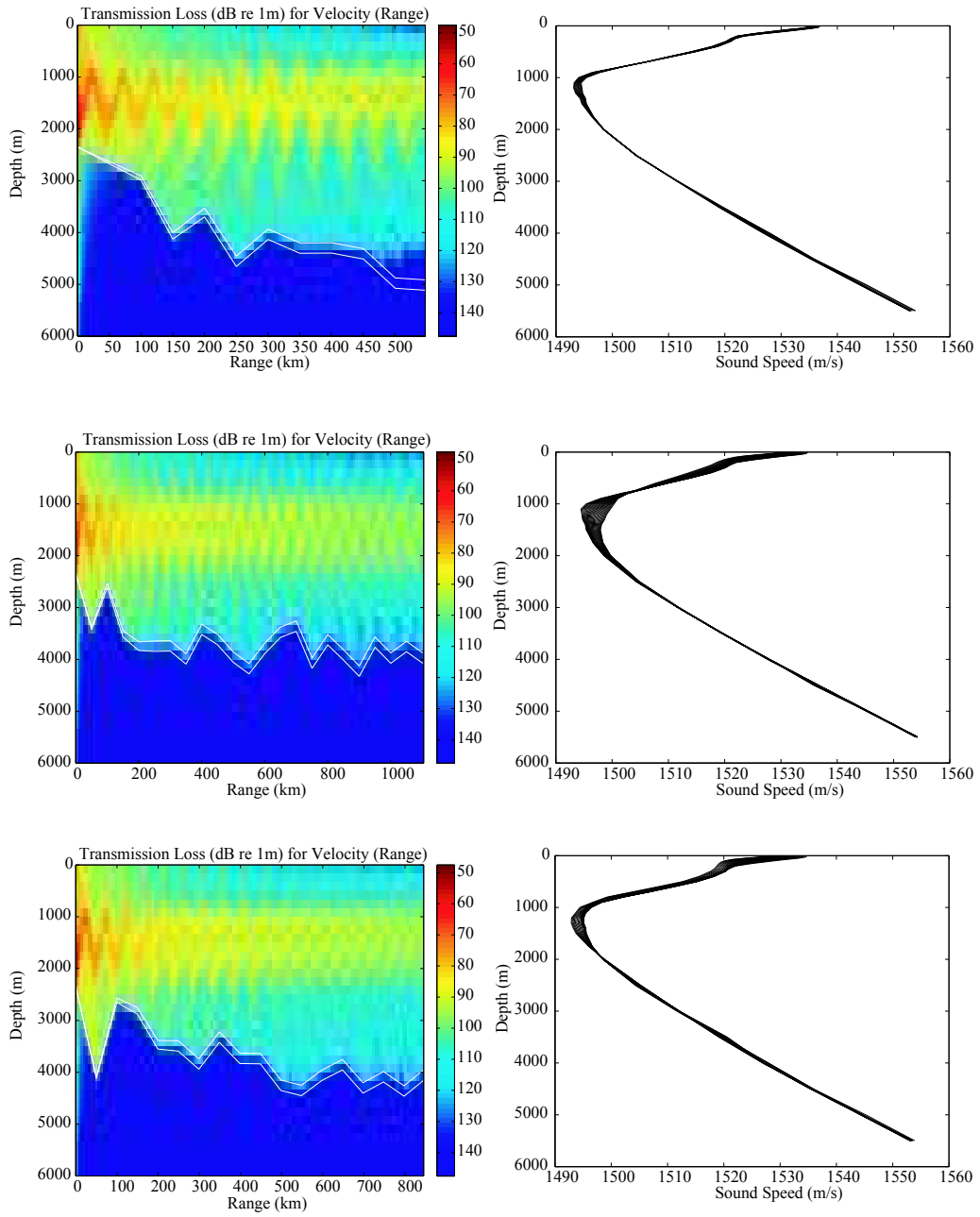


Figure 28: 2001 12 13 seismic sequence

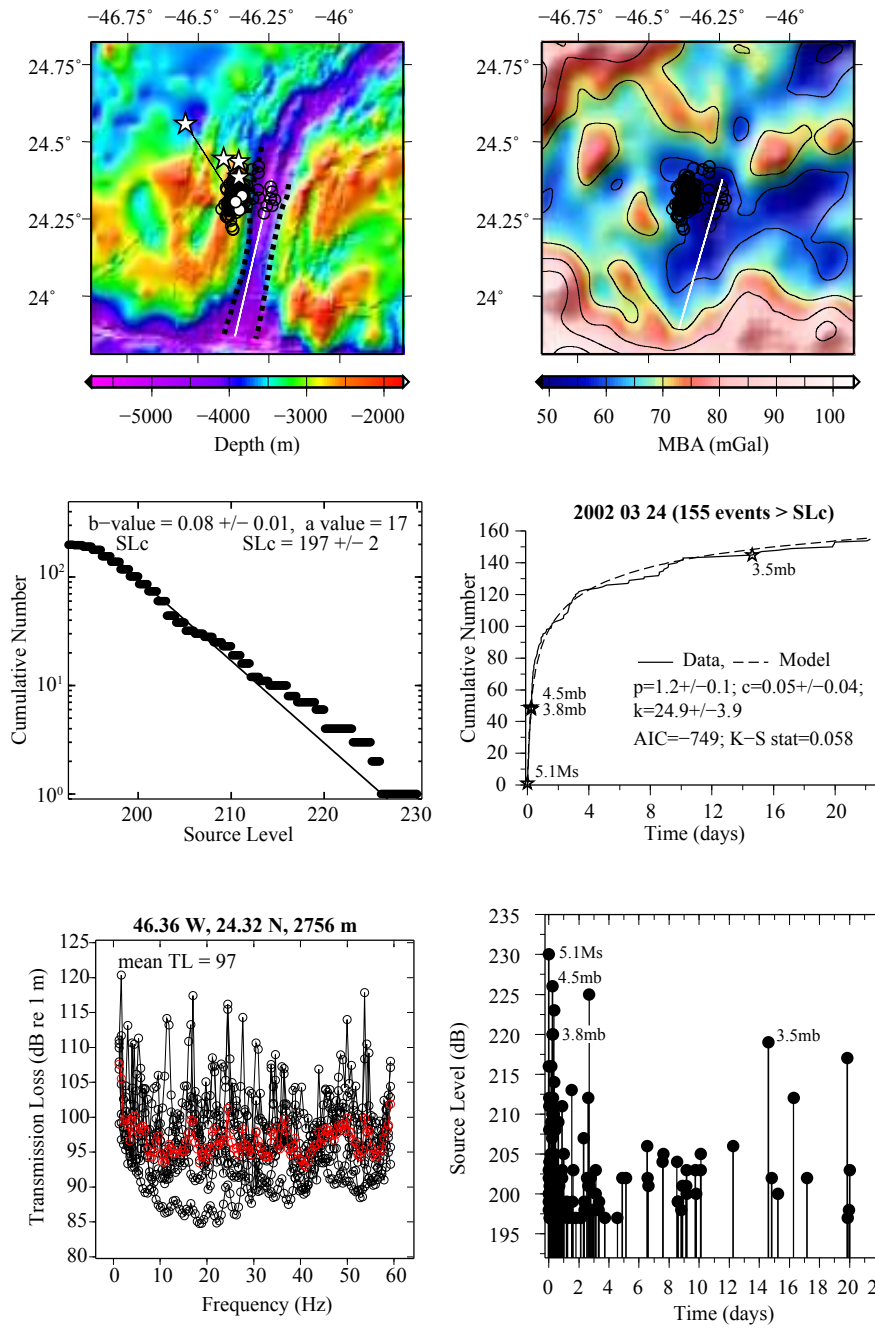


Figure 29: 2002 03 24 seismic sequence

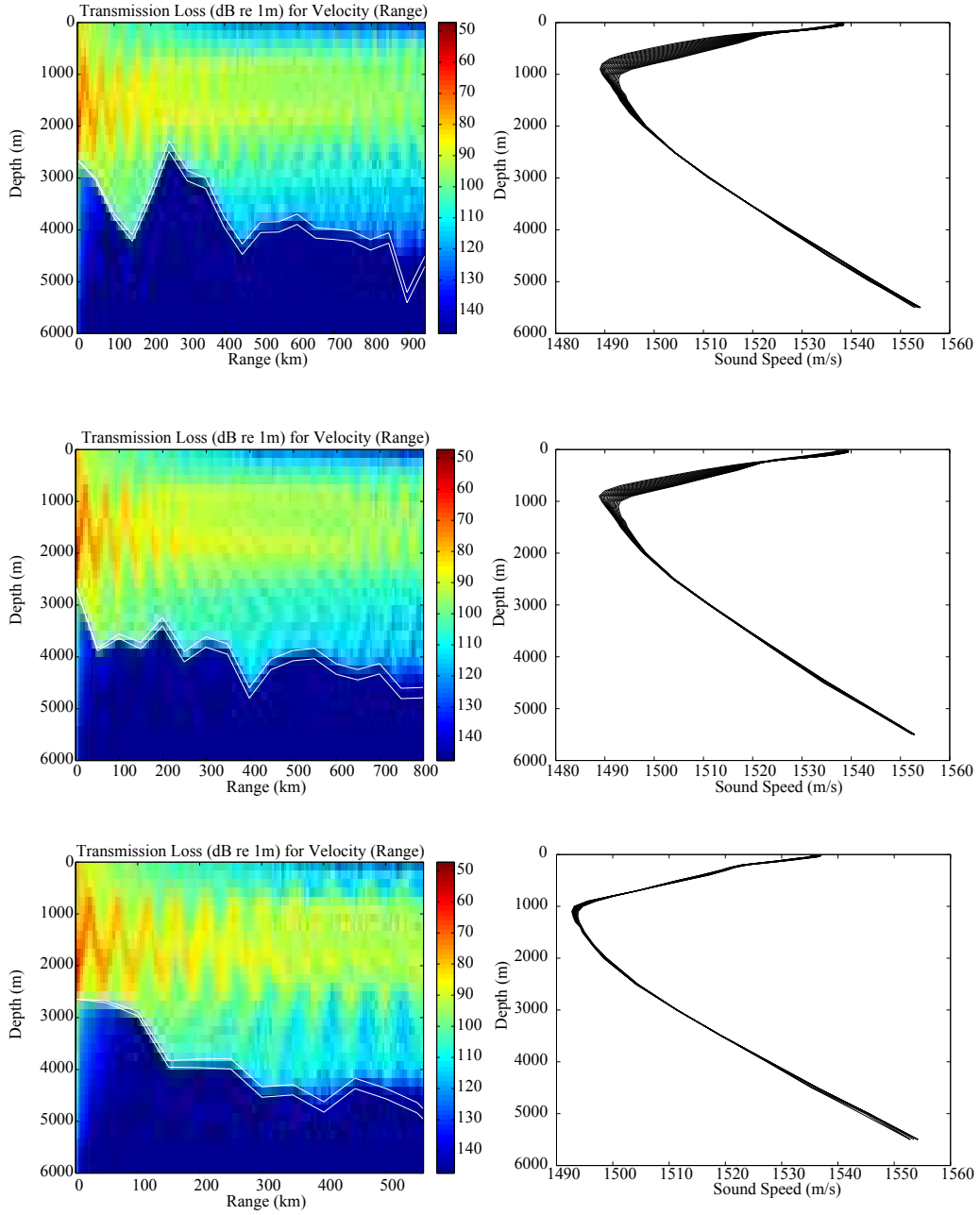


Figure 30: 2002 03 24 seismic sequence

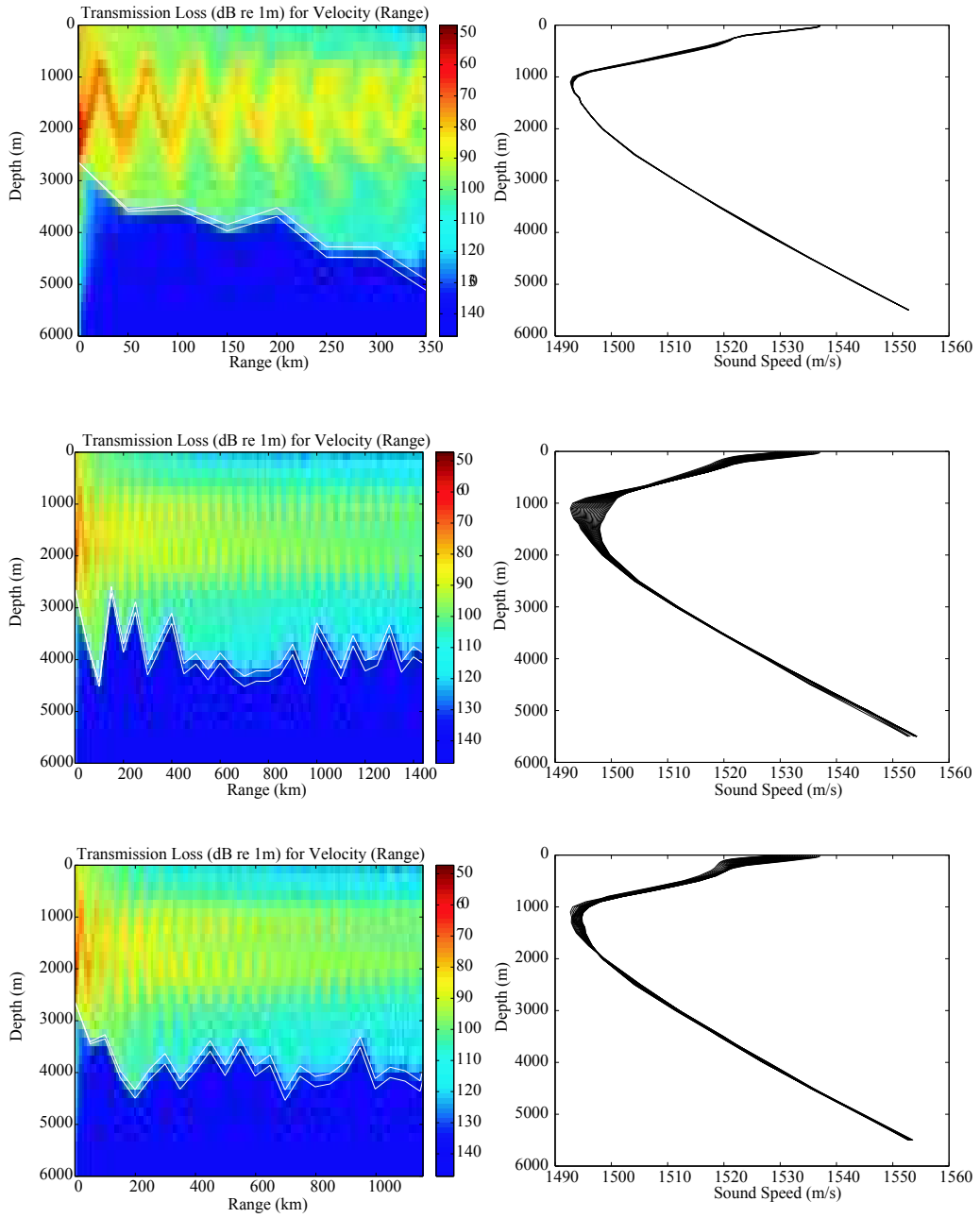


Figure 31: 2002 03 24 seismic sequence

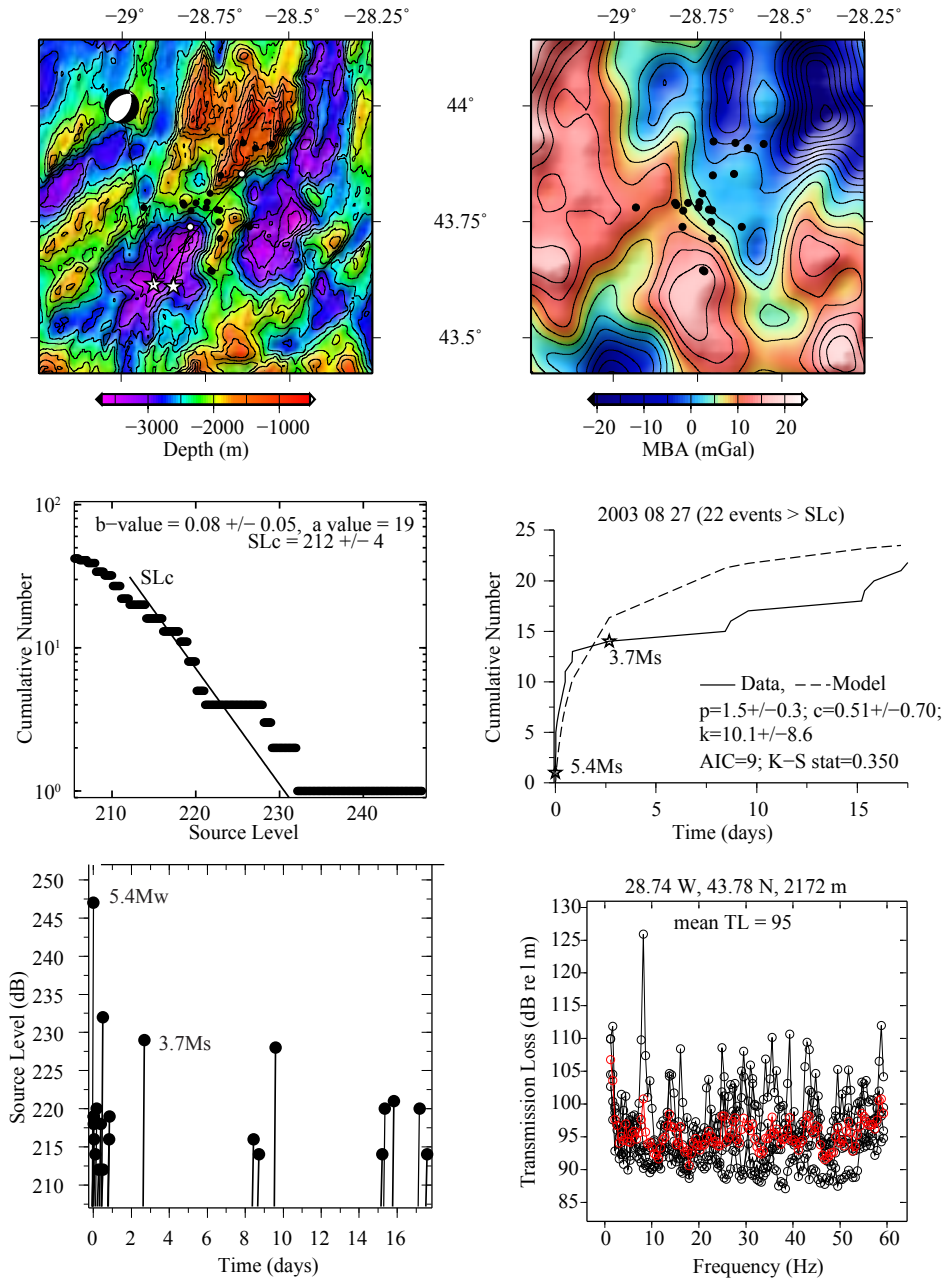


Figure 32: 2003 08 27 seismic sequence

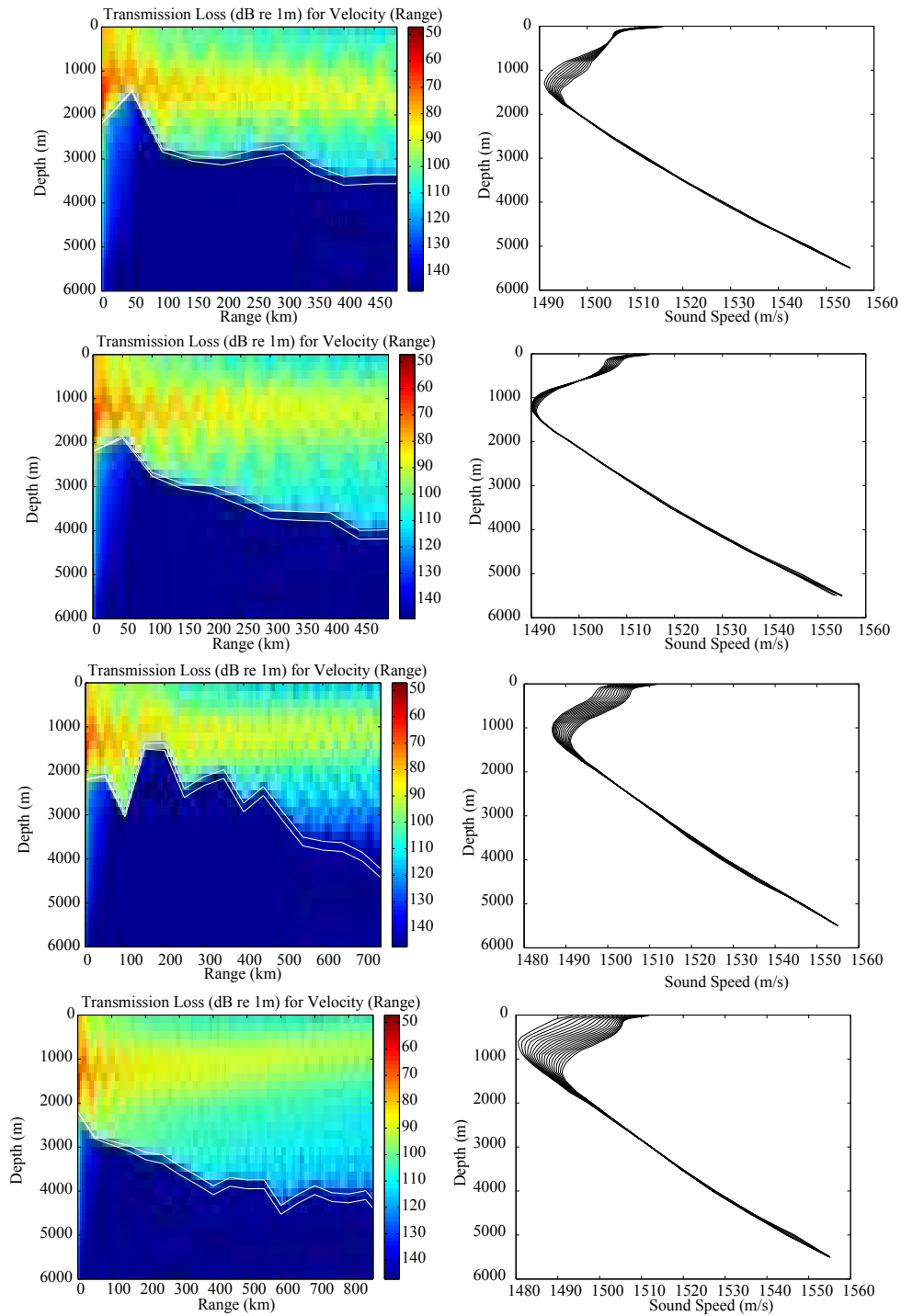


Figure 33: 2003 08 27 seismic sequence

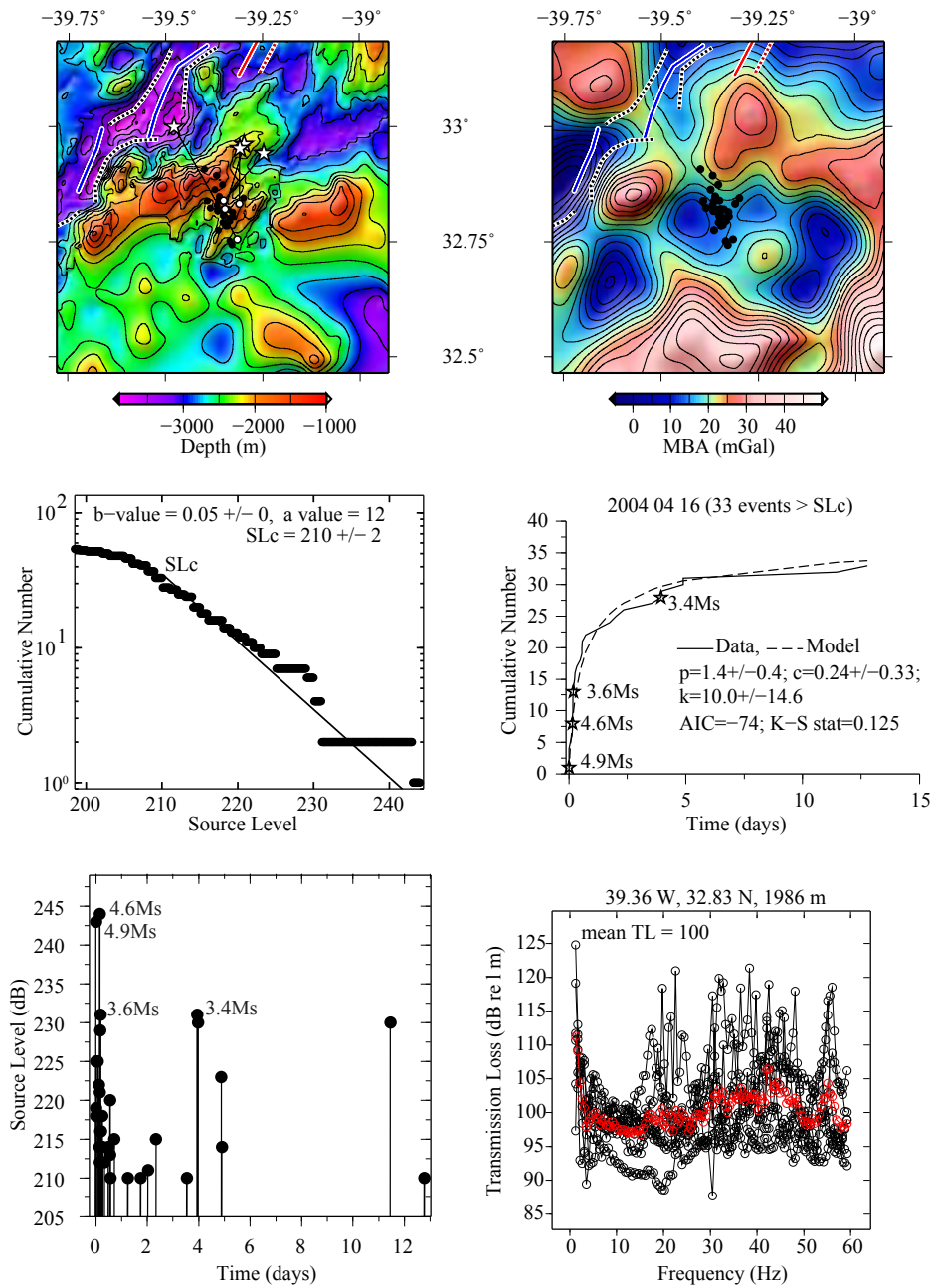


Figure 34: 2004 04 16 seismic sequence

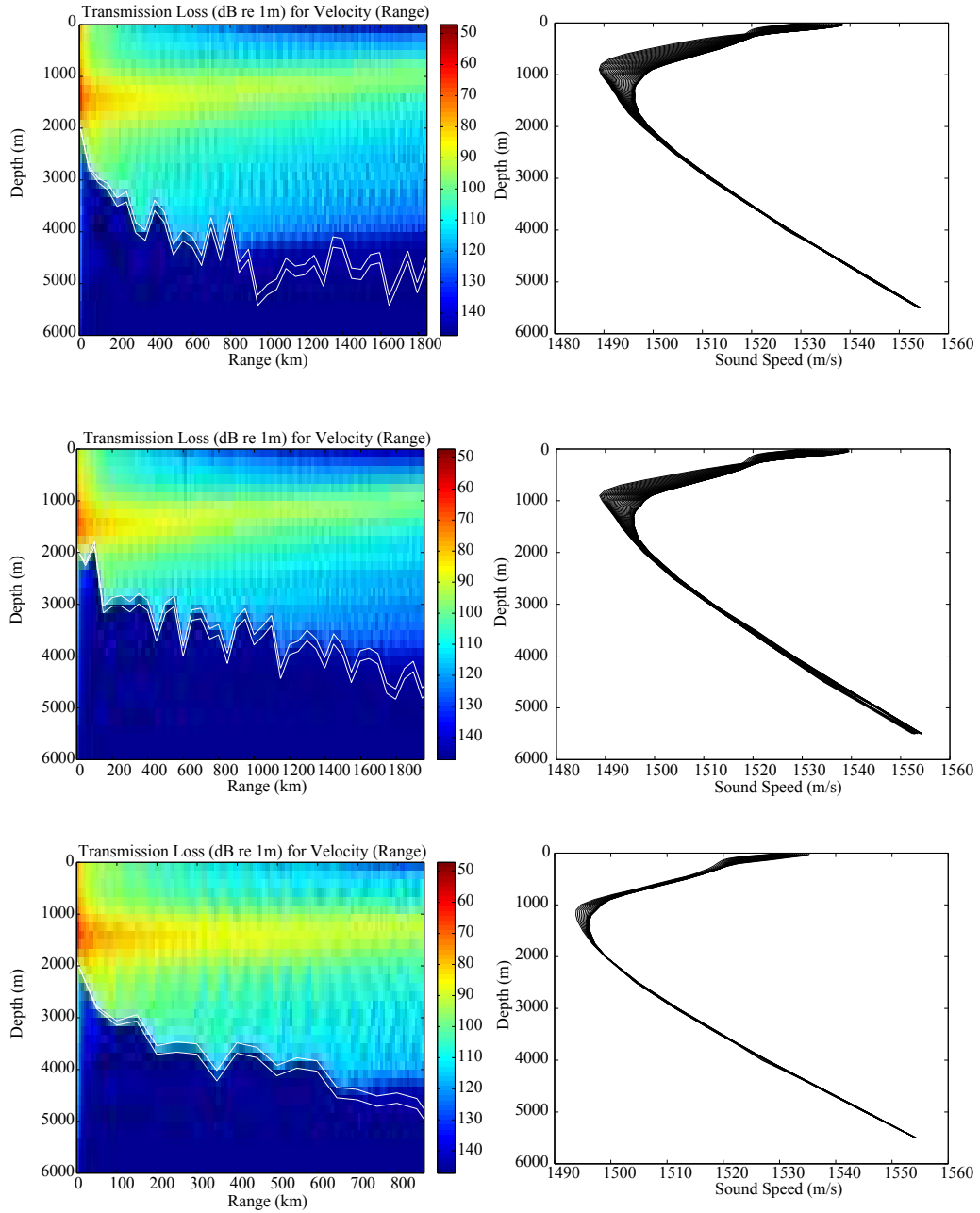


Figure 35: 2004 04 16 seismic sequence

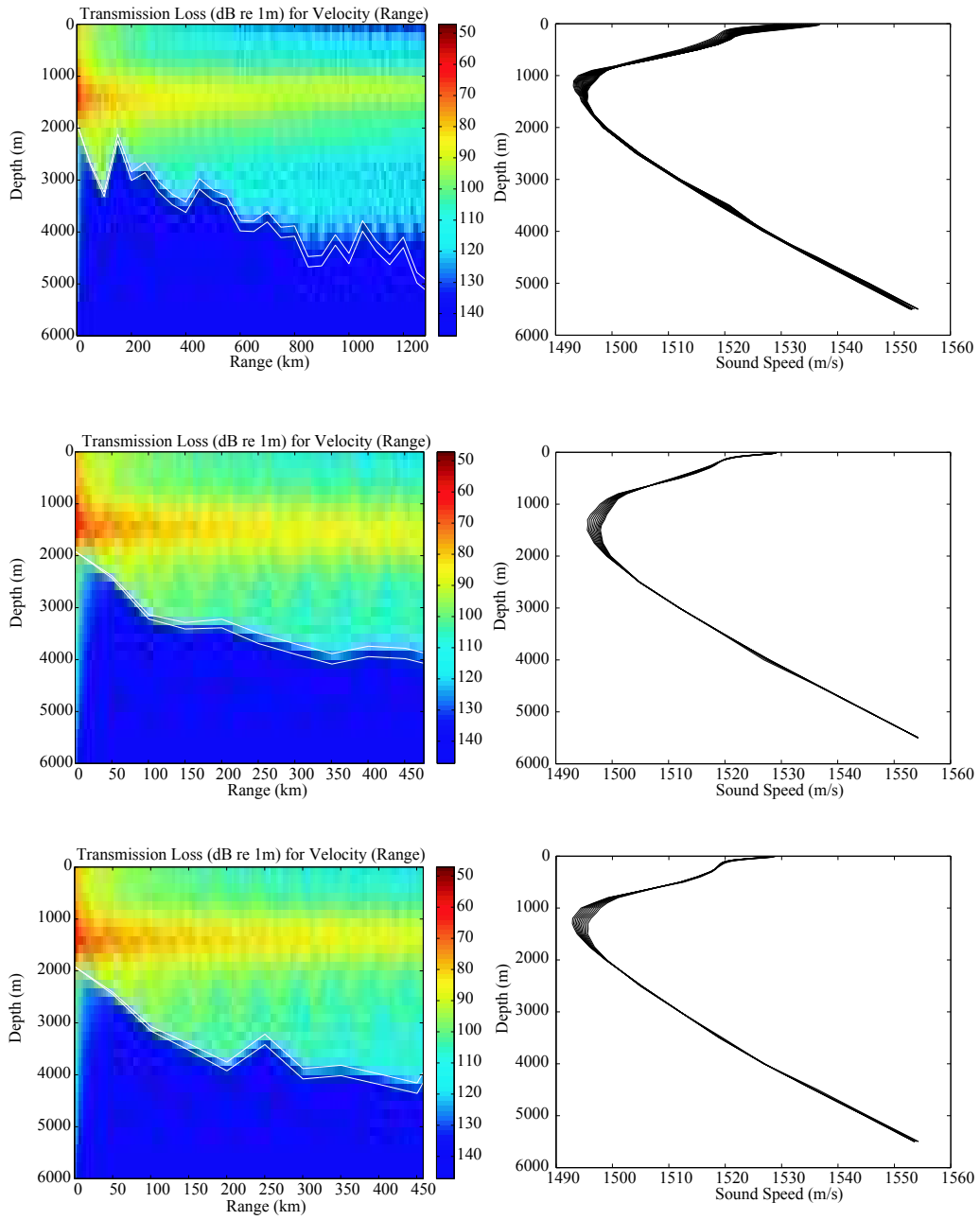


Figure 36: 2004 04 16 seismic sequence

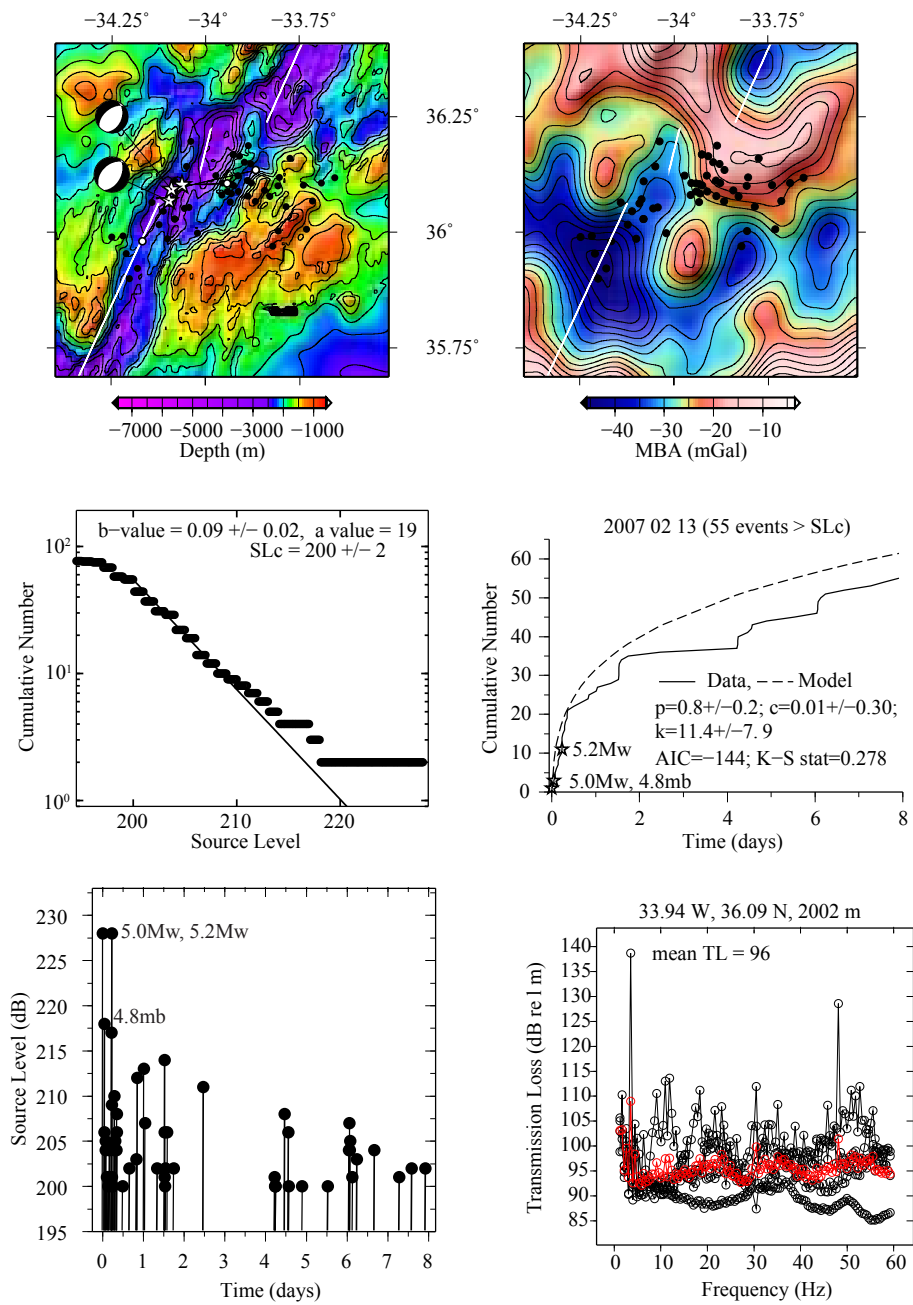


Figure 37: 2007 04 16 seismic sequence

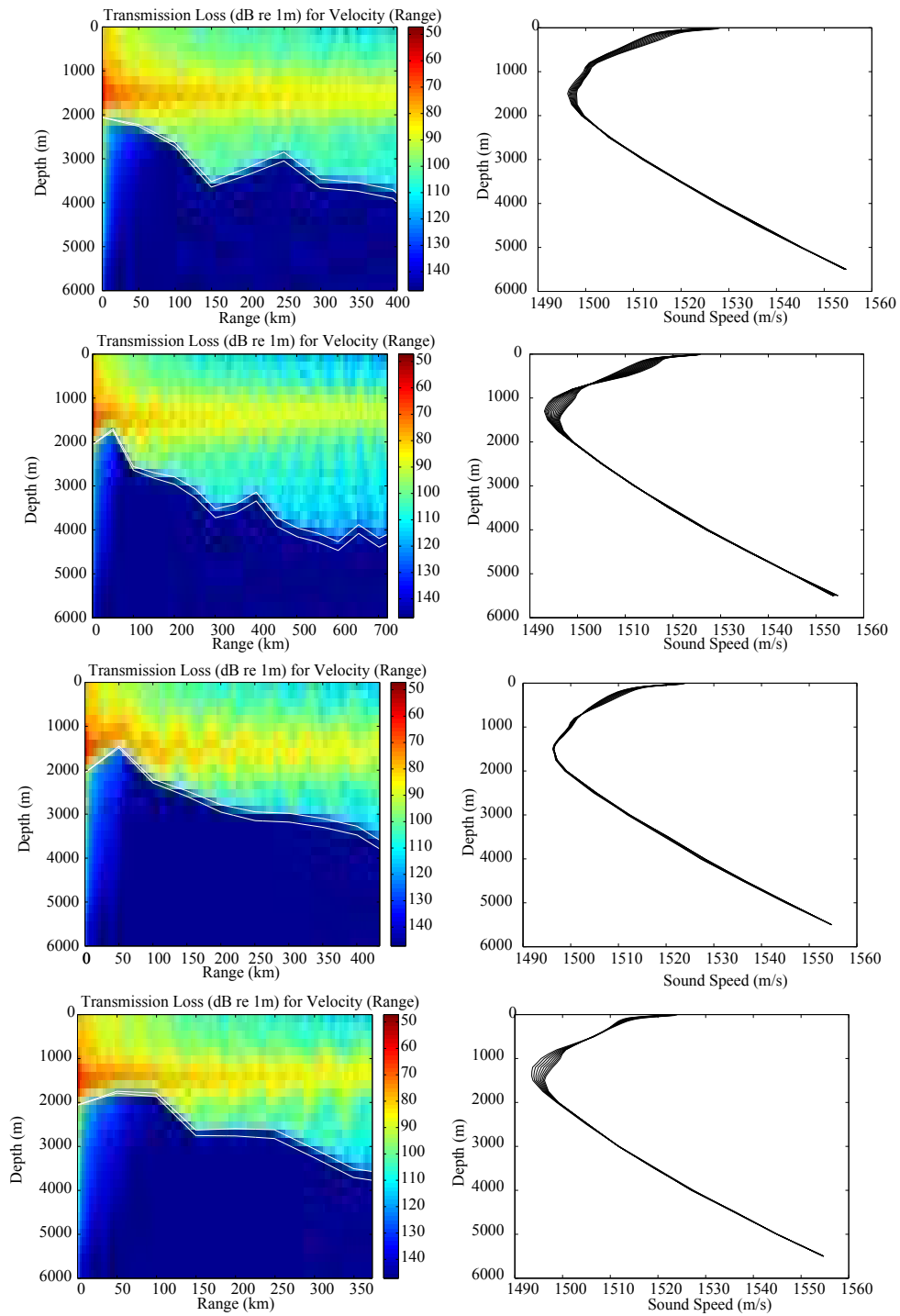


Figure 38: 2007 04 16 seismic sequence

List of Tables

2.1	AuH arrays on the MAR	26
4.1	Single Link Cluster resulting D_{best} that separates clustered events from the declustered ones for different AuH array configurations.	68
4.2	Spearman Rank correlation between MAR's ISC and AuH declustered seismicity profiles and MBA profile for wavelengths varying from 100 to 300 km. AuH1 profile takes into account South Azores and SIRENA arrays. AuH2 profile takes into account South Azores, SIRENA and MARCHE arrays. The seismicity between the Oceanographer Fracture Zone and the Azores recorded by the MARCHE array.	73
4.3	Spearman Rank correlation between MAR's ISC and AuH declustered seismicity profiles and MBA profile for wavelengths varying from 100 to 300 km. Profiles of seismicity and MBA north of the Azores	73
4.4	Spearman Rank correlation between MAR's ISC and AuH declustered seismicity profiles and MBA profile for wavelengths varying from 100 to 300 km. Profiles of seismicity and MBA south of the Oceanographer Fracture Zone.	74
5.1	Sequences, number of events, mean sequence localizations, T -phase excitation mean depth, mean earthquake distance to the segment axis. Mean axial valley width and mean axial valley depth.	99
5.2	Mean distance between the seismic sequence mean localization and the hydrophone localization, the mean Transmission Loss at the hydrophone in the 0 to 60 Hz frequency range and the difference between the MMPE Transmission Loss and the equations 2.6 and 2.7 computed Transmission Loss.	105
5.3	Seismic sequence dates and size-frequency relationship parameters.	111
5.4	Seismic sequences Modified Omori Law fitting parameters.	113

1	Kolmogorov-Smirnov test confidence table part 1.	142
2	Kolmogorov-Smirnov test confidence table part 2.	143

List of Figures

2.1	Typical deep-sea sound speed profiles. (a) Profile showing layer structure of the sound speed in the water due to temperature variations (b) Average sound speed profiles in different seasons in a area halfway between Newfoundland and Great Britain (modified from <i>Urick</i> (1983)).	6
2.2	Ray diagram for sound transmission and sound speed profile at right from a source on the deep ocean sound channel axis (e.g. SOFAR channel) (modified from <i>Richardson et al.</i> (1995)).	7
2.3	<i>P</i> -, <i>S</i> - and <i>T</i> -phases recorded by the three components of a seismometer.	10
2.4	P - T and S - T conversions in presence of a gently sloping beach. (a) and (b) show rays departing the focus at 1° and 10° incidence angles respectively. Each requires several reverberations to penetrate the SOFAR channel, and when combined in (c), this results in a wavetrain of longer duration. (d) shows similar characteristics for the S - T conversion for an 9° incidence angle (from (<i>Talandier and Okal</i> , 1998)).	11
2.5	(a) First overtone solution of 5 Hz, computed by <i>Park et al.</i> (2001) for a 2.25 km deep ocean featuring a SOFAR channel; is the eigenfunction of the horizontal displacement, that of the vertical displacement. Note that the mode does not penetrate the solid earth. (b) Same as (a) for the 32nd overtone mode plotted using a different vertical scale. Note that energy is present both in the liquid and solid, but the larger phase velocity expresses the inefficient lateral propagation of the energy in the liquid layer (adapted from <i>Park et al.</i> (2001)).	12

- 2.6 (a) Initial excitation, at $f = 5$ Hz, of the various overtone modes of a flat layered structure by a double-couple source located at 9 km depth (the 2.25 km deep ocean layer, is shown in a darker tone). Note that only overtones of order 18-55 are substantially excited. In particular the lower overtones corresponding to propagation in the water column are not. (b) Mode excitation by sea bottom scattering. Note that the energy of the higher modes in (a) has been converted into the lower overtones (of order less than 20), propagating in the SOFAR channel (from *Park et al. (2001)*). 13
- 2.7 T-phase time series waveform and respective 0-50 Hz spectrogram. 15
- 2.8 Hydrophone registered Atlantic Ocean ambient sounds. a) Blue whale calls. b) Air guns signal. c) Ship signal. 16
- 2.9 a) Current configuration of the Model 3 autonomous hydrophone. (b) Mooring diagram. 17
- 2.10 T-phase analysis software. The display shows the time series and corresponding frequency spectra for several earthquakes side by side. Time stamps are shown along the time series data. The diagram shows several minutes of hydrophone time series data sampled at 128 Hz. The frequency spectra range from 0 to 50 Hz and were estimated from consecutive 1-s windows of the time series data. 21
- 2.11 MAR seismicity recorded by AuH arrays. Blue stars represent hydrophones from the south Azores array, white stars represent hydrophones from the MARCHE array and red stars represent hydrophones from the SIRENA array. 27
- 3.1 Along axis variation of crustal thickness based on seismic observations (top) and gravity modelling (bottom) after *Detrick et al. (1995)*. The gravity scale is reversed. 32
- 3.2 Along axis variation in crustal thickness and lithology after *Cannat (1993)*. Continuous white line represents the base of the lithosphere. White, sub-vertical lines represent mantle dykes. 33
- 3.3 Block model of varying fault style along a spreading ridge segment after *Searle and Escartin (2004)*. 36
- 3.4 Shaded bathymetry of the detachment at $15^{\circ}45'N$ on the MAR after *Escartin et al. (2003a)*. The detachment is sub horizontal and gently curved in the direction of the spreading, and has bathymetric corrugations at wavelengths of ~ 1 km. The exposed fault surface is up to 12 km wide. These detachment surfaces show lineations at shorter wavelengths and fault striations at rock outcrops. . . . 38

- 3.5 Model setup used for numerical simulations of magmatic spreading at a mid-ocean ridge from *Behn and Ito (2008)*. The dike injection zone is illustrated with the thick black line. Gray region represents the portion of the model space that experiences brittle deformation, while the white region behaves viscously. Deformation is driven by applying a uniform half-spreading rate, u_s , to either side of the model space. The rate of magma injection u_{dike} is controlled by the parameter M , which is defined as the fraction of the total spreading rate accommodated by magma accretion. 40
- 3.6 East Pacific Rise and Cocos-Nazca spreading center map. Black dots are AuH array detected events on a 6 years survey. White circles are ISC catalog earthquakes since 1964. Focal mechanisms obtained from the ISC catalog. 42
- 3.7 Northeast Pacific Rise map. Black dots are SOSUS array detected events on a 17 years survey. White circles are ISC catalog earthquakes since 1964. Focal mechanisms obtained from the ISC catalog. 43
- 3.8 Mid Atlantic Ridge map. Black dots are AuH array detected events on a 6 years survey. White circles are ISC catalog earthquakes since 1964. Focal mechanisms obtained from the ISC catalog. White stars are AuH positions. 44
- 3.9 Plot of distance along axis versus number of events for teleseismic and hydrophone source locations after *Smith et al. (2003)*. Darker gray lines are FZs. Teleseismically events are shown as larger circles. Seismic stripes are marked with black lines and labeled with the number of the segment within which they occurred. Seismic gaps are marked by gray lines and labeled with segment numbers. 45
- 4.1 Predicted error fields represented as contours for the northern Atlantic Ocean, south of the Azores array, based on a calibrated Monte Carlos simulation: Predicted error in origin time (in seconds); Predicted error in longitude (in kilometers); Predicted error in latitude (in kilometers) (courtesy of Andy Lau (2008)). Squares represent hydrophones. 52
- 4.2 Predicted error fields represented as contours for the northern Atlantic Ocean, south of the Azores array + north Azores array (SIRENA), based on a calibrated Monte Carlos simulation: Predicted error in origin time (in seconds); Predicted error in longitude (in kilometers); Predicted error in latitude (in kilometers) (courtesy of Andy Lau (2008)). Squares represent hydrophones. 53

- 4.3 Predicted error fields represented as contours for the northern Atlantic Ocean, north of the Azores (SIRENA) array, based on a calibrated Monte Carlos simulation: Predicted error in origin time (in seconds); Predicted error in longitude (in kilometers); Predicted error in latitude (in kilometers) (courtesy of Andy Lau (2008)). Squares represent hydrophones. 54
- 4.4 Predicted error fields represented as contours for the northern Atlantic Ocean, Azores plateau (MARCHE) array, based on a calibrated Monte Carlos simulation: Predicted error in origin time (in seconds); Predicted error in longitude (in kilometers); Predicted error in latitude (in kilometers) (courtesy of Andy Lau (2008)). Squares represent hydrophones. 55
- 4.5 Great arc distance. Δ is the great arc distance between the pole with latitude λ_p and longitude ϕ_p and the triple junction with latitude λ_t and longitude ϕ_t . δ is the great arc distance between the pole and the event with latitude λ_e and longitude ϕ_e . $\Delta - \delta$ is the great arc distance between the event and the triple junction. . . . 57
- 4.6 Time Distance plot of all AuH recorded seismicity for the MAR. Histograms are separated by MAR AuH seismicity recorded south of the Azores, MAR AuH seismicity recorded north of the Azores and MoMAR AuH array recorded seismicity. The gap occurred between May 2003 to May 2004, south of the Azores, is the result of AuH technical problems along that deployment. Histogram bins of 20 km. 58
- 4.7 Time Distance plot of all Teleseismic recorded seismicity for the MAR from 1964 - the present and its histogram. Histogram bins of 20 km. 59
- 4.8 Time Distance plot of the SL_c . SL_c is the Source Level of Completeness. 500 km spatial binning. Temporal bins are array hydrophones deployment and retrievals. . . 61
- 4.9 Time distance plot of the number of events in a spatial grid of 100 km along the MAR by a temporal grid of AuH array service duration. 63
- 4.10 Time distance plot of the ratio of events recorded by 4 or more hydrophones in a spatial grid of 100 km along the MAR by a temporal grid of AuH array service duration. 64
- 4.11 Time distance plot of the mean location error of events. Location error is based on the mean of both longitude and latitude location errors for one event. The Mean location error is then the mean of all event location errors in a spatial grid of 100 km along the MAR by a temporal grid of AuH array service duration. . . 65

- 4.12 a) MAR’s teleseismically recorded seismicity since 1964 profiles obtained from the ISC web site. Black profile is the declustered catalog profile. Light black profile is the full catalog. b) MAR’s AuH recorded seismicity since 1999. Red profile represents the declustered South Azores AuH array catalog. Light red profile represents the full South Azores AuH array catalog. Green profile is the declustered SIRENA array catalog. Light green profile is the full SIRENA array catalogue. Blue profile represents the declustered MARCHE array catalog. Light blue profile is the full MARCHE array catalog. 69
- 4.13 From left to right: a) Along axis MAR’s MBA profile. Blue line is the MBA profile filtered with a Gaussian filter with a 200 km width. b) Along axis MAR’s spreading rate following the Nuvel 1 model (*DeMets et al.*, 1990). c) Azimuth between two points at the extremities of the MAR’s mega segments delimited by the Fracture Zones. d) and e) AuH recorded events per year. The differences are: e) MARCHE array data used for the region between the Oceanographer FZ and the Azores; d) used data from the South Azores array for the region between the Oceanographer FZ and the Azores. Red and green lines are the filtered profiles of the AuH seismicity using a 200 km path Gaussian filter. f) Teleseismically recorded events in the last ~ 40 years with its 200 km path Gaussian filtered profile represented by the fat black line. g) Joint representation of all the filtered profiles. 72
- 4.14 SIRENA AuH catalogs Principal Component modes variance with time. Colored lines and diamonds give the number of events and the places on the ridge where fluctuations from the mean level of seismicity (in percentages) occurred. Black bars represent teleseismically recorded magnitudes. Red bars represent AuH recorded Source Level. Blue line is the average Source Level variation. . . . 77
- 4.15 MoMAR AuH catalogs Principal Component modes variance with time. Colored lines and diamonds give the number of events and the places on the ridge where fluctuations from the mean level of seismicity (in percentages) occurred. Black bars represent teleseismically recorded magnitudes. Red bars represent AuH recorded Source Level. Blue line is the average Source Level variation. . . . 78
- 4.16 Time distance plot of the AuH SIRENA array catalog with its Principal Component analysis. Different modes with different variances are represented by different lines (top) and diamonds (bottom) representing the time and distances from the Azores fluctuations. Histogram (right) bin of 200 km. 79

- 4.17 Time distance plot of the AuH MARCHE array catalog with its Principal Component analysis. Different modes with different variances are represented by different lines (top) and diamonds (bottom) representing the time and distance of from the Azores fluctuations. Histogram (right) bin of 200 km. 80
- 4.18 Bathymetric plot of the south Azores part of the MAR segment that goes from 36.250°N to 36.750°N. Black dots represent AuH seismicity recorded by the MARCHE array with at least 4 hydrophones and white segments represent MAR's segmentation according to *Thibaud et al. (1998)*. *Thibaud et al. (1998)* define this segment PO6 as in a intermediate to cold state with a wide and deep axial valley. 82
- 4.19 Bathymetric plot of the north Azores part of the MAR segment that goes from 41.496°N to 41.756°N. Black dots represent AuH seismicity recorded by the SIRENA array with at least 4 hydrophones and white segments represent MAR's segmentation according to *Maia et al. (2007)* (top). It is one of the most active segments of this part of the MAR. Consecutive 0.05° apart across segment profiles (bottom). Red profile is the mean across segment profile obtained from all the profiles. 83
- 4.20 Bathymetric plot of the north Azores part of the MAR segment that goes from 42.287°N to 42.644°N. Black dots represent AuH seismicity recorded by the SIRENA array with at least 4 hydrophones and white segments represent MAR's segmentation according to *Maia et al. (2007)* (top). It is one of the most active segments of this part of the MAR. Consecutive 0.05° apart across segment profiles (bottom). Red profile is the mean across segment profile obtained from all the profiles. 84
- 4.21 Bathymetric plot of the north Azores part of the MAR segment that goes from 43.106°N to 43.701°N. Black dots represent AuH seismicity recorded by the SIRENA array with at least 4 hydrophones and white segments represent MAR's segmentation according to *Maia et al. (2007)* (top). It is one of the most active segments of this part of the MAR. Consecutive 0.05° apart across segment profiles (bottom). Red profile is the mean across segment profile obtained from all the profiles. 85

- 4.22 Bathymetric plot of the north Azores part of the MAR segment that goes from 43.760°N to 44.280°N. Black dots represent AuH seismicity recorded by the SIRENA array with at least 4 hydrophones and white segments represent MAR's segmentation according to *Maia et al. (2007)* (top). It is one of the most active segments of this part of the MAR. Consecutive 0.05° apart across segment profiles (bottom). Red profile is the mean across segment profile obtained from all the profiles. 87
- 4.23 Bathymetric plot of the north Azores part of the MAR segment that goes from 44.320°N to 44.520°N. Black dots represent AuH seismicity recorded by the SIRENA array with at least 4 hydrophones and white segments represent MAR's segmentation according to *Maia et al. (2007)* (top). It is one of the most active segments of this part of the MAR. Consecutive 0.05° apart across segment profiles (bottom). Red profile is the mean across segment profile obtained from all the profiles. 88
- 4.24 Bathymetric plot of the north Azores part of the MAR segment that goes from 45.710°N to 45.930°N. Black dots represent AuH seismicity recorded by the SIRENA array with at least 4 hydrophones and white segments represent MAR's segmentation according to *Maia et al. (2007)* (top). It is one of the most active segments of this part of the MAR. Consecutive 0.05° apart across segment profiles (bottom). Red profile is the mean across segment profile obtained from all the profiles. 89
- 5.1 MAR AuH recorded seismicity. Red circle clusters represent the identified sequences. Red diamonds the South Azores AuHs. Red Inverted triangles show the locations of the MARCHE AuHs. Red stars show the locations of the SIRENA AuHs 100
- 5.2 Axial valley across axis profiles taken each 5 km for segments where seismic sequences occurred. Red line is the stack of all profiles. 101
- 5.3 Seismic sequence that started on the 5th October 2000. Black circles are AuH recorded earthquakes. White stars are land based detected earthquakes. White segments are the MAR segments (*Thibaud et al., 1998*). Red segments represents symmetric accretion, blue segments represents asymmetric accretion, red dashed curves are ridgeward initiation of detachment and black dashed curves are ridgeward initiation of abyssal hills as defined by *Escartin et al. (2008)*. . . . 102

- 5.4 Seismic sequence that started on the 13th December 2001. Black circles are AuH recorded earthquakes. White stars are land based detected earthquakes. White segments are the MAR segments (*Thibaud et al.*, 1998). Red segments represents symmetric accretion, blue segments represents asymmetric accretion, red dashed curves are ridgeward initiation of detachment and black dashed curves are ridgeward initiation of abyssal hills as defined by *Escartin et al.* (2008). . . . 103
- 5.5 Seismic sequence that started on the 24th March 2002. Black circles are AuH recorded earthquakes. White stars are land based detected earthquakes. White segments are the MAR segments (*Thibaud et al.*, 1998). Red segments represents symmetric accretion, blue segments represents asymmetric accretion, red dashed curves are ridgeward initiation of detachment and black dashed curves are ridgeward initiation of abyssal hills as defined by *Escartin et al.* (2008). . . . 104
- 5.6 a) MMPE transmission loss modeling from a source located at the mean localization of the 3rd March 2001 sequence on the Lucky Strike segment to the farthest AuH located at 17.72°N, 42.78°W. Upper white line is the boundary between the water column and sediment layer, Lower white line is the boundary between the sediment layer and the rock layer. b) Sound speed profiles used on the MMPE modeling. Sound speed profiles taken each 25 km interval from the source to the hydrophone position. 106
- 5.7 a) MMPE transmission loss modeling from a source located at the mean localization of the 13th December 2001 sequence on the Lucky Strike segment to the farthest AuH located at 17.72°N, 42.78°W. Upper white line is the boundary between the water column and sediment layer, Lower white line is the boundary between the sediment layer and the rock layer. b) Sound speed profiles used on the MMPE modeling. Sound speed profiles taken each 25 km interval from the source to the hydrophone position. 106
- 5.8 Transmission loss on the 0-60Hz frequency range at the 17N AuH. a) from a source located on the 3rd March 2001 sequence. b) from a source located on the 13th December 2001 sequence. Red circles are the mean transmission loss of all hydrophones for each frequency in the range 0-60 Hz. 108
- 5.9 Relationships between the number of events with source level greater than the SL_c with the mean depth at which the sequence occurred (a) and the Source Level of Completeness (SL_c). 109
- 5.10 Size frequency relationship from the 13th December 2001 sequence. 110

5.11	a) Source Level distribution across time of the 3 rd March 2001 sequence. b) Source Level distribution across time of the 13 th December 2001 sequence.	112
5.12	a) MOL fit of the 24 th March 2002 sequence. b) MOL fit of the 13 th December 2001 sequence.	114
5.13	Modified figure from <i>Escartin et al.</i> (2008) with sequences emplacements and respective p -values (numbers) of the sequences. It is clear that sequences recorded on detachment faulting regions have higher p -values than the ones recorded on the abyssal hill faulting regions. The red square p -values is from the sequence that was recorded at an 30 km distance from the ridge.	115
5.14	Sketch of the generic modes of faulting on one generic MAR segment related to fault strength and earthquake decay rate of seismic sequences. Detachment faults associated to a asymmetrical mode of spreading have a faster decay rate. Abyssal hill faulting associated to o asymmetrical mode of spreading have a slower decay rate of earthquakes. Stars represent seismic sequences.	116
1	MAR's Mantle Bouguer Anomaly. White segments represent MAR's segmentation. MAR Segmentation following <i>Maia et al.</i> (2007), <i>Smith et al.</i> (2008) and <i>Thibaud et al.</i> (1998).	141
2	1999 04 06 seismic sequence	145
3	1999 04 06 seismic sequence	146
4	1999 04 06 seismic sequence	147
5	2000 02 18 seismic sequence	148
6	2000 02 18 seismic sequence	149
7	2000 02 18 seismic sequence	150
8	2000 10 05 seismic sequence	151
9	2000 10 05 seismic sequence	152
10	2000 10 05 seismic sequence	153
11	2001 01 12 seismic sequence	154
12	2001 01 12 seismic sequence	155
13	2001 01 12 seismic sequence	156
14	2001 02 28 seismic sequence	157
15	2001 02 28 seismic sequence	158
16	2001 02 28 seismic sequence	159
17	2001 03 16 seismic sequence	160
18	2001 03 16 seismic sequence	161

19	2001 03 16 seismic sequence	162
20	2001 07 13 seismic sequence	163
21	2001 07 13 seismic sequence	164
22	2001 07 13 seismic sequence	165
23	2001 11 12 seismic sequence	166
24	2001 11 12 seismic sequence	167
25	2001 11 12 seismic sequence	168
26	2001 12 13 seismic sequence	169
27	2001 12 13 seismic sequence	170
28	2001 12 13 seismic sequence	171
29	2002 03 24 seismic sequence	172
30	2002 03 24 seismic sequence	173
31	2002 03 24 seismic sequence	174
32	2003 08 27 seismic sequence	175
33	2003 08 27 seismic sequence	176
34	2004 04 16 seismic sequence	177
35	2004 04 16 seismic sequence	178
36	2004 04 16 seismic sequence	179
37	2007 04 16 seismic sequence	180
38	2007 04 16 seismic sequence	181